UNIVERSITY OF OKLAHOMA

GRADUATE COLLEGE

DEVELOPMENT OF SOIL-PILE INTERACTION MODELS IN IMPROVED SOILS USING CENTRIFUGE TEST DATA AND SYSTEM IDENTIFICATION METHODS

A DISSERTATION

SUBMITTED TO THE GRADUATE FACULTY

in partial fulfillment of the requirements for the

Degree of

DOCTOR OF PHILOSOPHY

By

HODA SOLTANI
Norman, Oklahoma
2016

DEVELOPMENT OF SOIL-PILE INTERACTION MODELS IN IMPROVED SOILS USING CENTRIFUGE TEST DATA AND SYSTEM IDENTIFICATION METHODS

A DISSERTATION APPROVED FOR THE
SCHOOL OF CIVIL ENGINEERING AND ENVIRONMENTAL SCIENCE

BY

_____
Dr. Kanthasamy K. Muraleetharan, Chair

_____
Dr. Thordur Runolfsson

_____
Dr. Gerald A. Miller

_____
Dr. Amy B. Cerato

_____
Dr. Sivalingam Sritharan

This dissertation is dedicated

to my parents and to my husband Joe.

Acknowledgements

I am thankful to my advisor and dissertation committee chair Prof. Muraleetharan; he gave me a big problem to work on and stuck with me for six years solving it. He offered many valuable suggestions and guidance during my research. Despite the fact that he smiles at everyone all the time, he made me tough! And he backed me up when it really counted! I am especially grateful to him for supporting me while I pursued my interests in system identification. I want to thank Professors Miller and Cerato for serving on my committee and providing their expertise in many areas including foundation design and testing. I am thankful to Prof. Sritharan at Iowa State University for giving me technical guidance and for sharing the findings from his full-scale tests. Prof. Runolfsson's courses introduced me to system identification and I am grateful to him for spending many hours teaching me the finer points of the field and for his contributing ideas, insights, and new ways of thinking that helped me to better understand the problem at hand.

From earliest childhood I have memories of watching my father as he developed structural designs in his home office and of him giving me little computations to do to "help." He took me to construction sites and let me record measurements for him. I spent hours gazing at the "tools of the trade" from every angle: his German drawing tools, drafting table, his nice calculator and so on. Later, he made sure that I excelled in mathematics and science, especially geometry. I became a Civil Engineer because of him, as did my brother. I am grateful to him and to my mother for loving me, for motivating me, and for supporting me while I pursued my educational goals so far away from our home.

I would like to thank my husband for being a great support, both emotionally and technically. He listened to me when I was frustrated, overwhelmed, and exhausted. His unconditional love and continuous encouragement over the years allowed me to devote so much of my time and energy to this work.

I am grateful to all my friends in Geotechnical Engineering Group. The intellectual and social interaction with them helped me through many of the challenges I faced during these six years. Some of my fondest memories I will treasure forever have been of the times I spent with them in our offices.

I would also like to thank Dr. Chunyang Liu for conducting the centrifuge tests in the Geotechnical Centrifuge facility at University of California-Davis.

The research presented in this dissertation was supported in part by a U.S. National Science Foundation (NSF) George E. Brown, Jr. Network for Earthquake Engineering Simulation Research (NEESR) grant (Grant No. CMMI-0830328). Any opinions, findings, and conclusions or recommendations expressed in this paper are those of the author and do not necessarily reflect the views of the National Science Foundation.

I am honored and grateful to the Provost's Office for selecting me as a recipient of the Nancy Mergler Dissertation Completion Fellowship which supported me during the final nine months of my work.

Table of Contents

List of Tables

List of Figures

Abstract

Documented distresses in pile foundations in soft soils during past earthquakes have shown that piles founded in soft soils undergo large lateral deformations during seismic loading. Improving the soil surrounding the piles is an effective strategy to improve the behavior of pile foundations in soft soils. Many fundamental mechanisms determining the interaction between the improved soil and piles have, however, not been fully understood. This has led to limited applications of soil improvement around piles in seismic regions and excessive conservatism in designs.

This dissertation assessed the static and seismic responses of single piles in improved and unimproved soft clays using data from a series of centrifuge tests. The centrifuge model contained a number of single piles embedded in a soft clay layer overlying a dense sand layer. The soft clay near the ground surface surrounding some of the piles was improved to various dimensions with cement.

Experimental results were used to extract the p-y curves for both the improved and unimproved soils and these curves were compared with the curves currently used in practice. A new feature was added to the traditional bending moment curve fitting methods accounting for the discontinuities in the distributions of shear force and soil reaction along the piles at the interface between the improved and unimproved soil. The p-y curves currently used in practice were found to be accurate for cases with medium and large improved zones. Although the theory assumes that the p-y curve at a given depth is entirely controlled by soil at that depth, influence of adjacent soil layers were observed on the experimentally derived p-y curves.

System identification methods were employed to extract the natural frequencies, damping ratios, and mode shapes of the unimproved soil system. The identified parameters were validated against those estimated from analytical methods and employed to synthesize prediction models which were subsequently used to simulate the soil response for three successive base motions. The identified models captured acceleration time-histories reasonably well in the small and moderate shaking events. The influence of the improved zone size was reflected on the identified natural frequencies of the soil-pile-top mass systems.

Seismic interactions between the soil and pile were simulated by adapting a hysteretic model that integrated phenomena such as soil-pile separation, material degradation, and radiation damping. The developed interaction elements calibrated for one shaking event were deployed to predict the soil reactions in another shaking event. The predicted soil reactions compared reasonably well with those obtained from the measured results.

CHAPTER 1: INTRODUCTION

1.1 Motivation

The performance of pile-supported structures such as highway bridges, port wharves, off-shore oil and gas production platforms, and towers under lateral loadings depends on the interaction of soil and piles as well as the interaction between piles and the superstructures. Common sources of lateral loads are earthquakes, ocean waves, wind, ship impact and traffic. Vast documentation of pile distresses and failure in bridge structures during past earthquakes (Finn, 2005) has shown that piles in competent soils generally perform satisfactorily, while the excessive deformation of piles in soft and liquefied ground such as in port areas can cause severe structural damage. A wide range of methods and technologies have been developed to provide adequate lateral resistance where the foundation soil is incompetent.

Cement-mixing soil improvement methods are often applied to enhance the bearing capacity of foundation soils by increasing the soil strength against deformation, liquefaction, and sliding (Bouassida and Porbaha, 2004; Lai et al., 2006; Namikawa et al., 2007; Siddharthan and Porbaha, 2008; Raju and Yandamuri, 2010; Barron et al., 2006; Yamashita et al., 2012). Modifying the soil strength has proved in many cases to be more economically efficient than modifying the structural elements of foundations (Ohtsuka et al., 1996; Rollins et al., 2010). Cement Deep Soil Mixing (CDSM) is a ground improvement technique that has been widely applied in supporting embankments and excavations, in sites susceptible to lateral spreading, in slope stabilization, and in seismic retrofitting of foundations (Kitazume and Terashi, 2013). In the CDSM method, a shaft is advanced into the ground, and a cement slurry is injected and mixed with the in situ

soil using rotary mixing tools. The single column of treated soil resulting from this process can be repeated with or without overlaps to produce a zone of improved soil. Recently, special attention has been paid to the application of soil mixing methods, both to enhance the performance of existing pile foundations and to aid in the design of new piles against lateral loads. However, researchers have not yet thoroughly examined the effects of ground improvement on pile response, nor have they validated or modified the existing computational models. Therefore, simplified and optimized design procedures for piles in improved ground have not yet been established.

Only a few studies have been conducted to date on insitu and centrifuge testing of piles in cement-improved ground; one is the work of Tomisawa and Miura (2007), who investigated the static and dynamic behavior of piles under lateral loads and offered design methods concerning the necessary range of ground improvement. To evaluate the effectiveness of this ground improvement technique and to modify the available design procedures, Tobita et al. (2008) investigated the impact of ground improvement in liquefiable soils on the response of full-scale pile groups subjected to lateral loading. Rollins et al. (2010) evaluated the effect of different soil improvement methods on the ultimate strength of full scale pile groups. They found that mass mixing and jet grouting beneath and in front of the pile cap can increase the ultimate strength three- to five-fold over that of unimproved soils. The outcomes of these tests resulted in a simplified design method that can be used to determine the lateral extent of the improved zone. Bao et al. (2012) modeled the seismic behavior of a group-pile foundation with partial ground improvement at some depth below the ground surface by conducting a series of shaking table tests. Most recently, a combination of static and dynamic pile load tests were

performed by Fleming et al. (2015) on a full scale single pile where the ground was improved by CDSM. Comparing the results of the improved and unimproved cases showed that the pile lateral strength increased by 42% and the effective elastic stiffness increased by 600%.

Examination of the current literature shows a dearth of experimental data to help advance the fundamental understanding of the complex mechanisms of interaction between the improved soil and pile–superstructure system. For this reason, the CDSM-improvement technique is not widely used in earthquake-prone regions, even though this method shows great potential for retrofitting aging and degrading structures. Resolving these uncertainties through comprehensive experimental and analytical investigations could be an important step in earthquake hazard mitigation.

The use of geotechnical centrifuges is well established as an experimental testing framework for earthquake studies where the dynamic response of reduced-scale models can be modeled under increased gravitational fields. Many physical model studies have reported dynamic and static lateral behavior of piles through centrifuge testing, for example, Finn and Gohl (1987), Ting et al., (1987), Scott (1994), Wilson (1998), Brandenberg et al., (2005), Banerjee (2009), Ashlock and Pak (2009), Zhang et al., (2011). These test results have been used to calibrate available commercial finite element or finite difference software using the concept of Beam on Nonlinear Winkler Foundation (BNWF) model, which is acknowledged by practicing engineers to be simple and computationally efficient. The BNWF theory simplifies the interaction mechanisms between the soil and pile under lateral loads by modeling the pile as a series of beam elements and idealizing the adjacent soil continuum with discrete springs, also called

interaction elements, distributed along the pile. The force-displacement relationships of these springs at a certain depth is represented by a p-y curve that describes the lateral soil resistance per unit length of pile (p) mobilized by lateral pile displacement (y). It is assumed that the discrete soil reactions at different depths are uncoupled. When the BNWF model is applied to problems involving cyclic and dynamic loading, it is important to properly formulate phenomena such as degradation of the improved zone, energy dissipation and soil-pile separation (Matlock et al., 1987; Boulanger et al., 1999; Gerolymos and Gazetas, 2005; Allotey and El Naggar, 2008a and 2008b). Integrating these components into the interaction elements is a very complex and challenging task even when the soil system is homogeneous. In the case of improved soil systems, which are notably inhomogeneous, the accuracy of the BNWF approach can suffer significantly.

For several reasons, this is an area with great potential for further research. First, only limited numerical and physical data are available from previously published studies of soil improvement methods for deep foundations engineering. Second, it is inherently difficult to generalize the published results to other soil types and improvement methods. Third, there is a high level of uncertainty that makes it difficult to select optimal dimensions for the improved zone for a given design load.

1.2 Research objectives

This dissertation presents the results and interpretations of pseudo-static and seismic lateral load tests on centrifuge model piles in soft clay where the top layers of the soil were improved by CDSM. This study is part of the NEES-pilEs (The George E. Brown, Jr. Network for Earthquake Engineering Simulation-piles in low E soils), where E stands for Young's modulus.

The pile models are intended to cover a significant range of practical ground improvement dimensions. The current philosophy for designing bridges against earthquake loads demands plastic regions in piles to form above the soil surface. The reason for this restriction is that it is not feasible to identify piles with damage below the soil surface. The size of the improved zone can be determined by studying the soil and the pile behavior where the lateral and vertical extents of the improved zone gradually increase. The improved zone for which the nonlinrearity starts to concentrate in the pile is typically the optimum improved zone. This study intends to address how different degrees of ground improvement affect the lateral response of single piles and how these effects can be incorporated into computational models. This investigation provides insight into the mechanisms of soil-pile interaction in cement-improved soft clay by

- Assessing the applicability of popular p-y models for the soft and cement-improved clays in reproducing the pile response to pseudo-static load tests utilizing LPILE (Ensoft, Inc., 2004; a finite-difference-based software for modeling pseudo-static soil-pile interaction). The conventional p-y models are based on the results of field experiments on full scale piles, and they have proved to be reliable and accurate where only one type of soil is prominent. Because ground improvement introduces a strong heterogeneity in the soil profile, it is necessary to reevaluate the existing models.
- Deriving the p-y curves directly from the centrifuge experiments and evaluating the validity of the extracted curves.
- Improving the quality of the back-calculated p-y curves by incorporating the discontinuities imposed by the soil layer interfaces on lateral soil pressure

distribution along the piles at locations where significant changes in soil stiffness properties occur.

- Comparing the p-y curves obtained from the pseudo-static loads tests and the seismic load tests.
- Commenting on the effects of the improved zone size on the characteristics of the p-y curves.
- Estimating the modal characteristics of the soil at free-field and of the piles in both improved and unimproved soils using spectral analysis and state space system identification methods. Changes in the stiffness of the soil-pile system introduced by the improved soil affect the fundamental frequency of the system.
- Validating the identified modal parameters using the published analytical methods and closed-form solutions.
- Using the identified modal parameters as a way of explaining the size impacts of the improved zone on the modal parameters of the soil-pile systems.
- Developing a representative macro-element model for the hysteretic p-y behavior of the cement-improved soil under seismic excitations while accounting for factors such as soil-pile separation, soil strength and stiffness degradation, and damping associated with outgoing stress waves that the piles transmit into the soil (radiation damping).
- Exploring the possibility of calibrating the macro-element models using the measured soil properties.
- Providing recommendations for the seismic and static designs of single pile foundations in CDSM-improved soft clay.

1.3 Dissertation organization

Chapter 2 describes the details of the centrifuge model, including the model layout, model preparation, construction of the cement-improved zones, properties of the soils, structural properties of the piles, and layout of the sensors placed in the soil and attached to the piles.

Chapter 3 starts with a review of the BNWF model. This chapter then describes the bending moment curve-fitting procedure adopted to back-calculate the experimental p-y curves that account for the discontinuity of the shear force in the pile and the lateral soil pressure acting on the pile at the interface of different soil layers. The p-y curves are derived for piles with different degrees of soil improvement and compared with one another. This chapter also assesses the applicability of the conventional models in predicting the pile behavior when subjected to static loads. This is followed by a discussion about estimating the parameters required by these models. The reliability of the implemented curve-fitting procedure was evaluated by integrating the derived p-y curves into the LPILE computer code.

Chapter 4 extends the bending moment curve-fitting method developed in Chapter 3 to the seismic data. Free-field lateral displacement is derived using the accelerometers in the soil, and p-y traces are back-calculated where the y component represents the pile displacement relative to the free-field soil. This chapter also explores tracking of the excess pore pressure at various levels over time and discusses correlations between the soil response and pore pressure.

Chapter 5 provides technical background on state space identification and spectral analysis which are used to estimate the modal parameters of the soil and pile system. It

includes the estimation of the modal characteristics of the unimproved soil at free-field using accelerometer recordings and the data-driven subspace state space system identification (4SID) method. The estimated natural frequencies and the normal mode shapes are compared with closed-form solutions obtained from the one-dimensional shear wave propagation equation. The identified modal parameters are then employed to synthesize state space prediction models, which are subsequently used to simulate the soil response to three successive base motions. This chapter also presents an examination of the transfer functions calculated using spectral methods on the pile head, soil surface, and base motion accelerations, and estimates the natural frequencies of the soil-pile systems.

Chapter 6 provides a detailed review of previous studies in developing macro-element models for seismic/dynamic p-y behaviors with a focus on mathematical formulation and components. A review of the Bouc-Wen hysteresis model and its application in structural and geotechnical systems is also presented. This model was selected due to its power in simulating the soil-pile separation and the degradation in soil stiffness and strength. This chapter provides details about the formulation of the Bouc-Wen model and explains the procedure for calibrating its parameters to reproduce the p-y traces obtained in the improved zones. Chapter 6 also considers combination of the nonlinear hysteretic spring and a viscous damper for modeling the radiation damping.

Chapter 7 summarizes the outcomes of the research and shows how the research objectives have been achieved. Recommendations for future work are presented with regards to the issues and problems encountered in this research.

CHAPTER 2: CENTRIFUGE TESTING

2.1 Geotechnical centrifuge testing

The centrifuge tests reported here were conducted at the NEES@UC Davis centrifuge facility (Liu et al., 2010). The major components of the centrifuge system are a container wherein the soil model is built, a platform accommodating the container, a shaking table, and a reaction mass (Figure 2.1). The radius from the center of rotation to the platform is 9 m. More detailed information about the UC Davis centrifuge can be found in Wilson et al. (1997).

The centrifuge model was constructed in a Flexible Shear Beam (FSB) container with inside dimensions of 1.722 m long, 0.697 m deep, and 0.684 m wide and a weight of 846.3 kg. The container is made of five hollow aluminum rings separated by durometer neoprene layers and a base plate form as shown in Figure 2.2. Shear stiffness of the container increases with depth. In horizontal vibration where the behavior of soil/structure systems under vertically propagating shear waves is investigated, it is essential to provide suitable boundary conditions so that the container moves with the soil profile and shear deformation prevails. The column bending of soil is minimized by complementary shear stresses provided by shear rods (see Figure 2.3). During consolidation, they were separated from the clay layers by a thin aluminum plate that was removed after consolidation. Other important aspects of dynamic centrifuge modeling have been explored by Wilson et al. (1997) and Ilankatharan and Kutter (2008) including dynamic characteristics of the container, soil-container interaction, undesirable vertical motions, and model uniformity.

The tests were performed at a centrifugal acceleration of 30 g. Therefore, prototype dimensions can be obtained by multiplying the model dimensions by 30. In addition to scaling the physical dimensions of a scaled centrifuge model, other quantities should be scaled according to the relations given in Table 2.1. These scale factors can be derived using either dimensional analysis or the governing differential equations (Taylor, 1995). All the measurements reported hereafter will be in prototype units unless stated otherwise.

2.2 Model preparation

The centrifuge model layout is shown in Figure 2.4. The soil profile consisted of four horizontal clay layers underlain by two sand layers. Sand layers were dense Nevada sand, a fine uniform sand with D_{50} = 0.15 mm, e_{max} = 0.887, e_{min} = 0.511, and G_s = 2.67. The soft clay mixture was made using commercially available kaolin (No. 1 Glaze Clay from Old Hickory Clay Company in Hickory, Kentucky) and a fine sand (D_{50} = 0.14 mm) from George Townsend Co., Inc., in Oklahoma City (Quikrete Commercial Grade Fine White Sand, No. 1961-55). The mixture consisted of 1:1 kaolin/sand by dry weight mixed at a water content of 64% (twice the liquid limit). The sand was added to the soft clay mixture to increase the coefficient of consolidation of the mixture, which was found to be about 4.5×10^{-8} m^2/s. The liquid limit and the plasticity index of the mixture were 32 and 17, respectively. Additional laboratory test results, including triaxial test results, for this mixture can be found in Thompson (2011).

Two layers of dense Nevada sand were prepared via pluviation through air. In this method, the sand is "rained" from a calibrated height through a slotted plate attached to the bottom of a suspended box while the box moves with a certain speed above the

centrifuge container (Figure 2.5). Different densities can be achieved by changing the height of the sand box and the opening size of the slotted plate. After the sand layers were constructed and instrumented, the container was sealed and the air inside the model was replaced with carbon dioxide. Then the sand layers were saturated with deionized water under a vacuum.

After the sand layers were saturated, a soft clay mixture for the first clay layer was poured into the container and was consolidated in a press under a vertical effective stress of 190 kPa. To accelerate the consolidation process, filter papers were placed between the sand and the first clay layer and between the subsequent clay layers, as shown in Figure 2.6. After consolidation of each clay layer, the vertical load was removed and instruments were placed within the clay layer. The vertical effective stresses were chosen to make each clay layer lightly overconsolidated under the centrifugal acceleration of 30 g. The initial stress states of the clay layers are shown in Figure 2.7. Using the information in Figure 2.7 and the laboratory oedometer test results for the clay shown in Figure 2.8, the initial state (stress, void ratio, and overconsolidation ratio) at any given point within the clay layer can be calculated.

The improved soil, which simulates CDSM in the centrifuge test, was created as follows. First, the 1:1 (by weight) kaolin/sand dry soil mixture was created as mentioned above and then water was added to prepare a soft clay mixture at a water content of 34%, which represented the average water content of the centrifuge model clay layer after consolidation. Then a cement (Type I Portland Cement) slurry was prepared with 10% cement (by dry soil weight) and 1:1 cement/water (by weight) ratio. This slurry was finally added to the soft clay mixture to create a uniform cement-mixed soil. The final

mix design described above was determined after testing various cement contents and water cement ratios (Thompson, 2011),

Ground improvement around the single piles consisted of one large (17D×17D×12D), two medium (13D×13D×9D), and two small (9D×9D×6D) zones, where D is the outer diameter of the pile (= 0.286 m). The dimensions of the improved zone are given as (length×width×depth). Due to limited available space in the container, only one pile was constructed in the large improved zone. Having two identical models for the piles improved by the small and medium zones allowed us to study the pseudo-static and seismic responses on separate piles.

After consolidation and instrumentation of the last clay layer, excavation was carried out for improved zones using molds made of thin aluminum sheets (Figure 2.9a). The instrumented piles were driven into the center of the excavation, and then the cement-mixed soil was placed within the excavations around the piles (Figure 2.9b). The piles were fabricated using small steel tubes that closely matched the elastic and inelastic behavior of the steel pipe piles used in seismic regions by the California Department of Transportation (Caltrans). The yield and ultimate flexural moments of the steel tube, which are listed in Table 2.2, closely matched those of Caltrans pile PP14. The cement-mixed soil was cured in situ for 10-16 days before being subjected to lateral loads. The variation in the shear strength of the cement-mixed soil with curing time is shown in Figure 2.10. In addition to five improved piles, two piles were placed in the unimproved soil. The water table was maintained at 1 cm (model scale) above the soil surface.

2.3 Instrumentation

In the centrifuge model, a number of pore pressure transducers and accelerometers were placed in the soil deposit, as shown in Figures 2.11 and 2.12. Figure 2.11also shows the accelerometers attached to the top masses that were mounted on piles during the seismic load tests. Displacement transducers used to measure settlement at the soil surface and the lateral deflections of piles in seismic tests are depicted in Figure 2.13. Each pile was instrumented with a pair of strain gages in the half-bridge configuration at six different levels to quantify the bending moments along the pile. The locations of these strain gages, shown in Figures 2.14, were determined by performing preliminary analyses using the computer code LPILE to accurately capture the moment profile along the pile (Kirupakaran et al., 2010). The improved piles were labeled to indicate the depth of the improved zones (6D, 9D, 12D) as 6D-EF, 6D-GH, 9D-KL, 9D-IJ, and 12D-MN. The unimproved piles were called UI-AB and UI-CD (see Figure 2.4).

2.4 Loading tests

2.4.1 Pseudo-static loading tests

The pseudo-static lateral loading tests were performed with an actuator in a displacement-controlled mode in multiple steps. The loading started by moving the pile head from the initial position to a target displacement on the right side (which is towards the north side of the container in about 10 to 15 seconds) and maintaining this displacement for several minutes in order to send the command for the next step to the actuator. In the following step, the pile head was moved to the opposite side. Moving the pile from one side to the other side in one loading step took about 10-15 seconds, while a two- to three-minute pause between the loading steps was involved to set up the actuator for the next deflection.

Bending moments along each pile were measured using the calibrated strain gages, with one pair above the soil surface. The lateral deflection of pile outside the soil layer was measured at three different levels using three displacement transducers: one embedded in the actuator mounted on the piles top and two below the actuator and above the soil surface. The lateral load was measured by a load cell in the actuator. During pseudo-static loading, however, the piles in the large improved zones were subjected to limited displacements without inducing any damage to the pile or the improved soil so that the shaking test could be performed for the same pile. Pseudo-static lateral loading tests were conducted on piles UICD, 6DGH, 9DKL, 12DMN before the seismic testing and on UIAB, 6DEF after performing the seismic tests, because the bending moment measurements from the pseudo-static load tests on pile UICD and 6DGH were not collected due to an error in the first loading phase. The maximum displacement applied to 12D-MN was 0.2 m, about a third of the maximum displacements applied to other piles. This was done to prevent any damage to the ground improvement around this pile during pseudo-static loading and to preserve the system for seismic testing. After the third shaking event, piles UIAB and 6DEF were tested for pseudo-static loads. The results of these tests are presented in Chapter 3.

2.4.2 Seismic loading tests

After pseudo-static load testing, seismic masses (listed in Table 2.3) were attached to the top of the piles and the models were subjected to a series of base motions. The seismic masses shown on top of the piles in Figure 2.11 were attached to the piles to simulate the inertial loads from the superstructure during the seismic loading tests. The seismic masses were steel hollow cylinders made up of two halves bounded with two expansion screws.

Three base motions, with increasing intensity, were applied in sequence. Enough spinning time was allowed between shakes to dissipate the excess pore water pressure generated during shaking. The first two base motions were a scaled version of the 1989 Loma Prieta earthquake in California, while the third base motion was the scaled 1995 Kobe earthquake in Japan. The acceleration time histories of the base motions measured on the east and west sides of the container base plate were nearly identical. Figure 2.15 presents the acceleration time histories of the three shaking events recorded on the west side of the container. Data measured during the shaking events are presented in Chapters 4 and 5.

Table 2-1 Centrifuge Scaling Factors at a Centrifugal Acceleration of 30 g

Quantity	Prototype scale/model scale
Length	30
Time	30
Frequency	1/30
Acceleration	1/30
Mass	30^3
Force	30^2
Moment	30^3
Stress or pressure	1
Density	1

Table 2-2 Pile Properties

Material	Outside Diameter, *D* (m)	Wall Thickness, (m)	Length (m)	Young's Modulus, *E* (GPa)	Yield Strength (MPa)	Yield Bending Moment (kN.m)
Steel tubes (A513 Type 2, Grade 1010)	0.286	0.027	20.40	192.5	260.0	305

Table 2-3 Top Masses

Piles	UIAB	6DEF	9DIJ	12DMN
Top masses (kg)	661.5	656.1	661.5	664.2

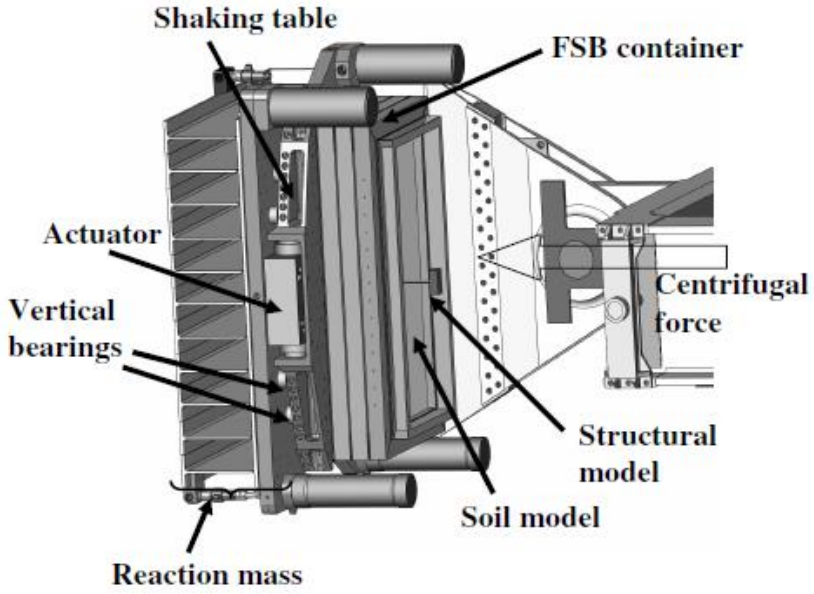

Figure 2.1 Components of a centrifuge shake table (Ilankatharan and Kutter, 2008)

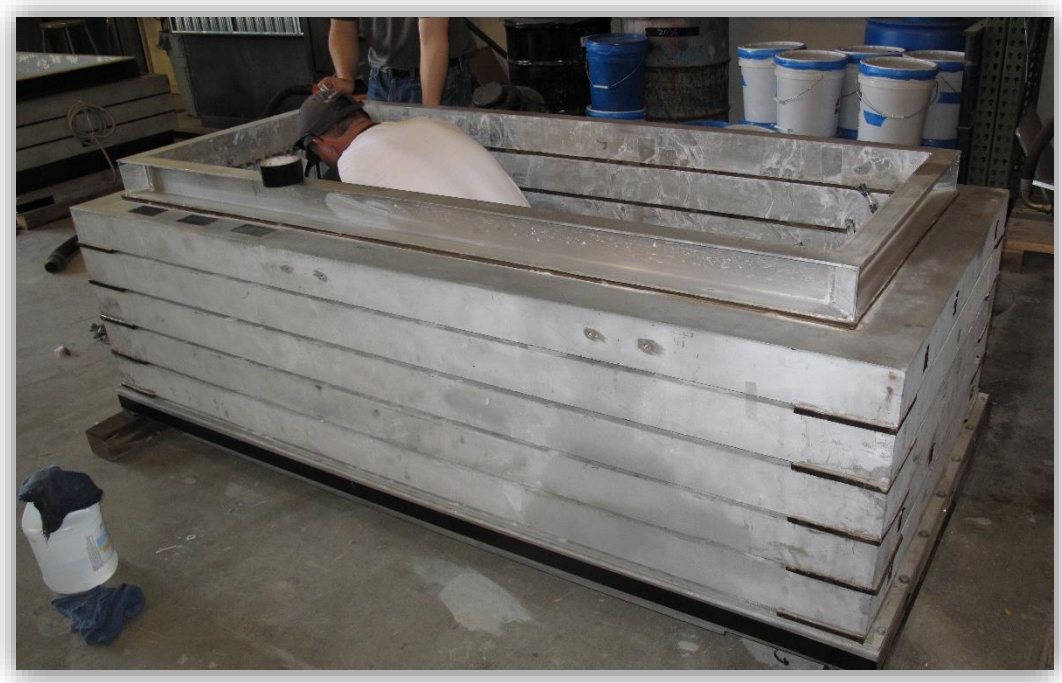

Figure 2.2 Flexible shear beam container

Figure 2.3 Shear rods located at both ends of the container

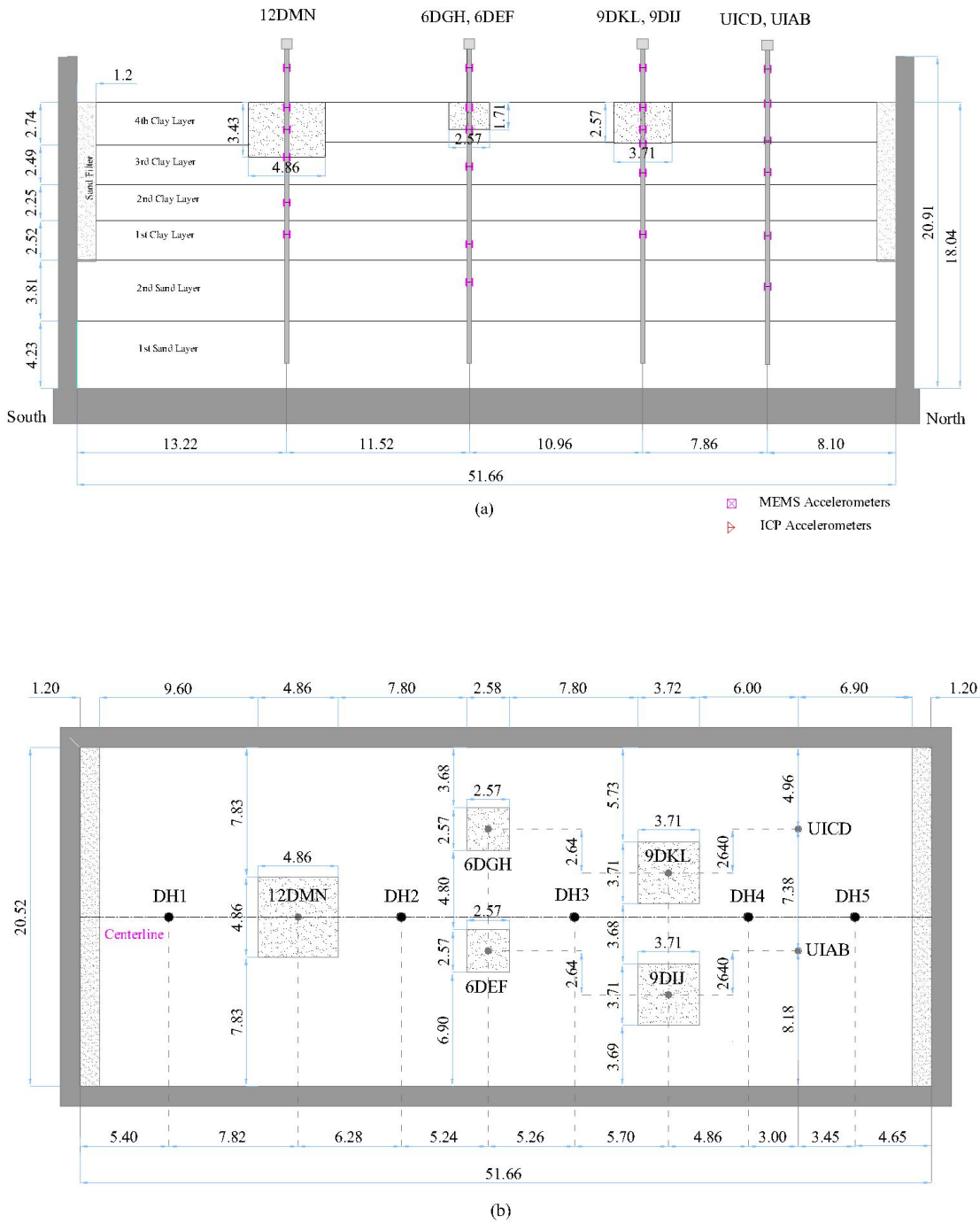

Figure 2.4 Centrifuge model layout (a) plan view (b) side view (in prototype dimensions)

Figure 2.5 Sand pluviation

Figure 2.6 Preparation of a clay layer

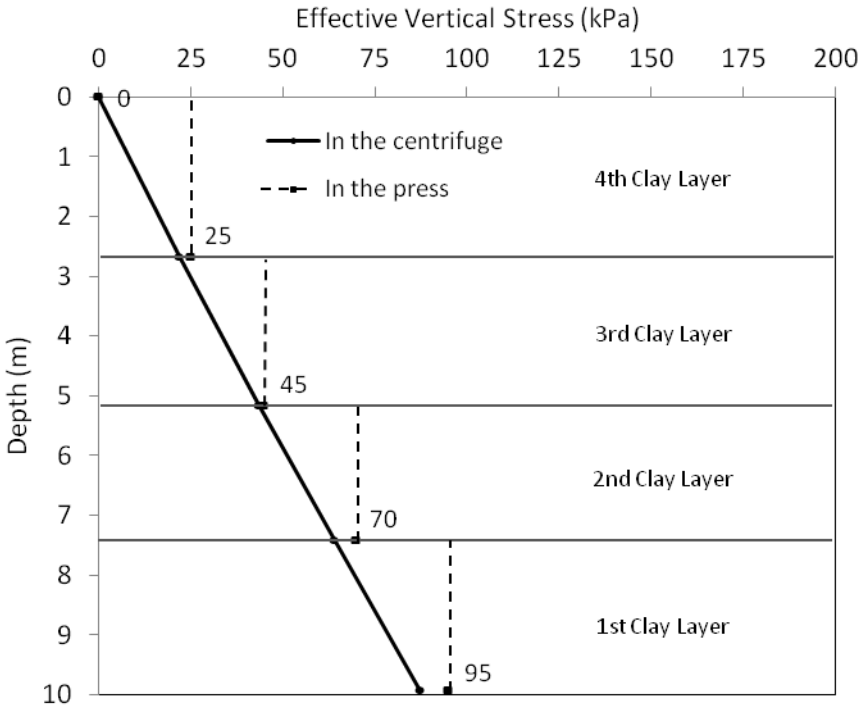

Figure 2.7 Stress state in the clay layer

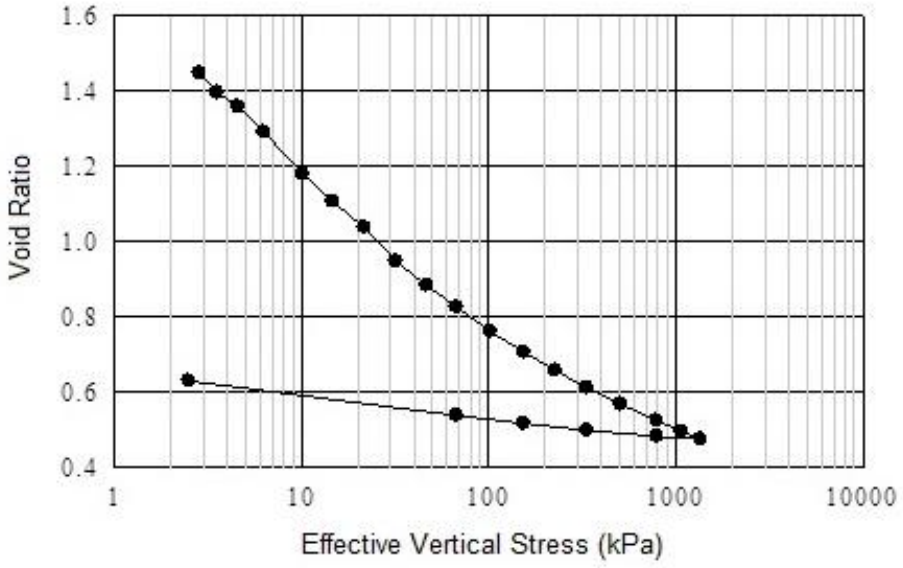

Figure 2.8 Oedometer test result on soft clay

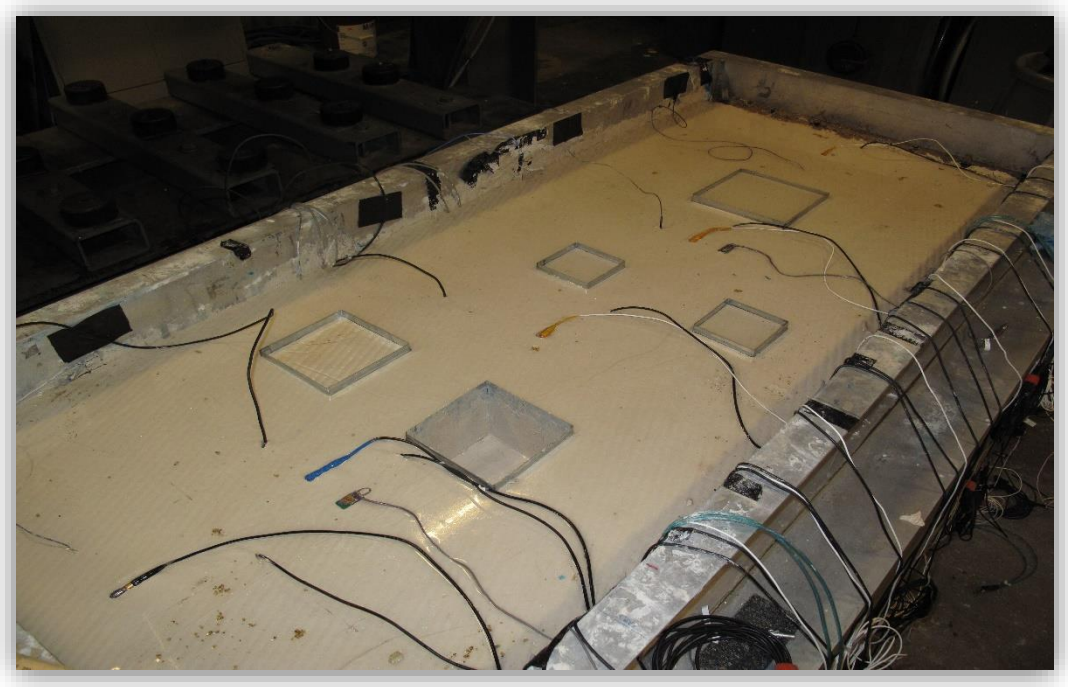

(a)

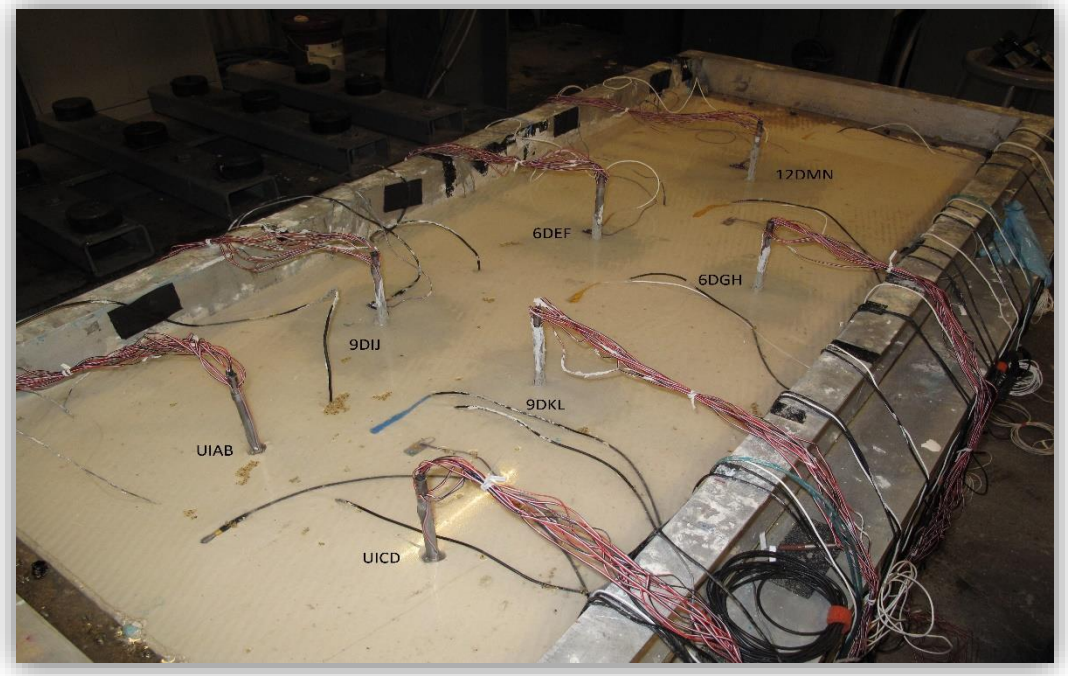

(b)

Figure 2.9 Construction of the improved zones (a) excavation (b) curing

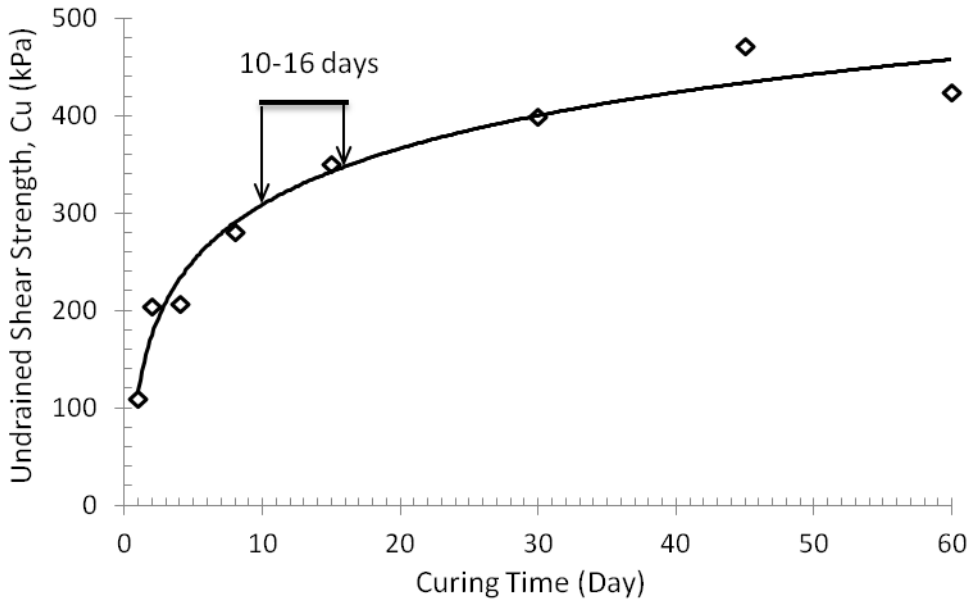

Figure 2.10 Undrained shear strength vs. curing time for the improved soil

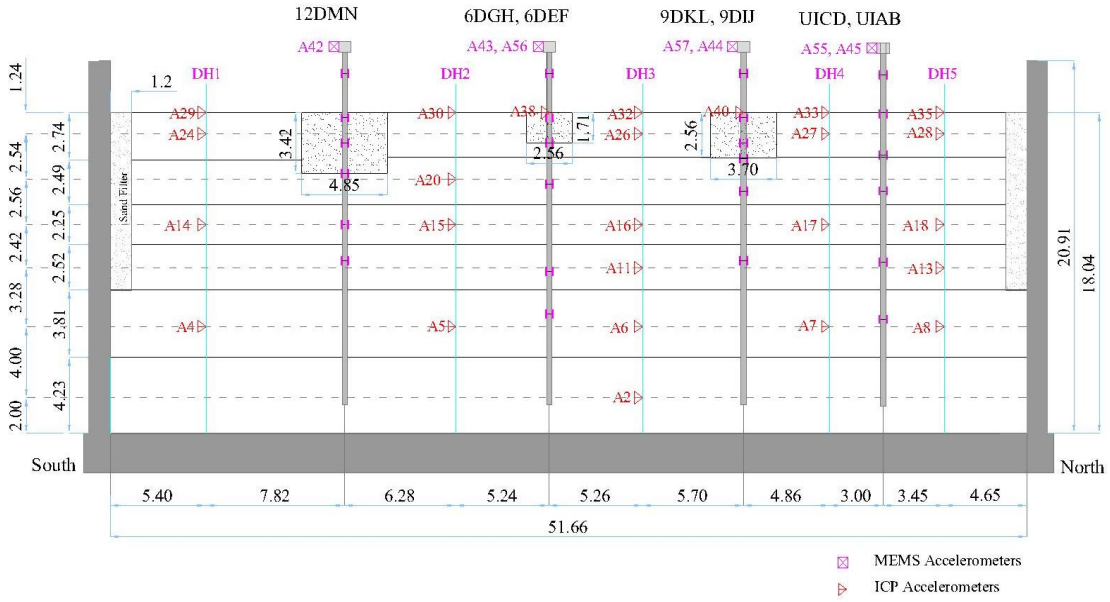

Figure 2.11 Accelerometer locations

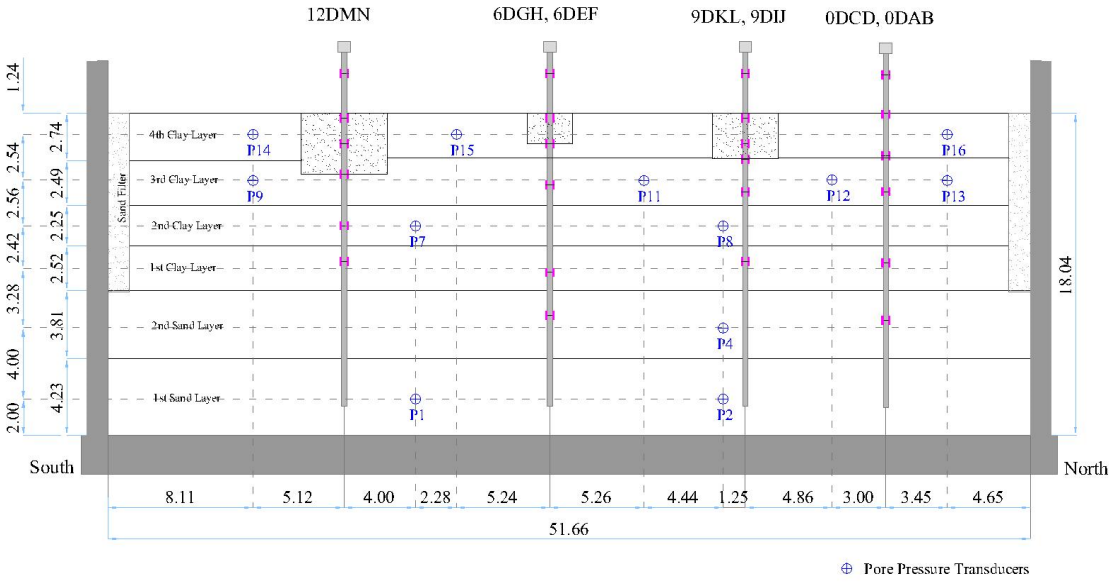

Figure 2.12 Pore water pressure transducer locations

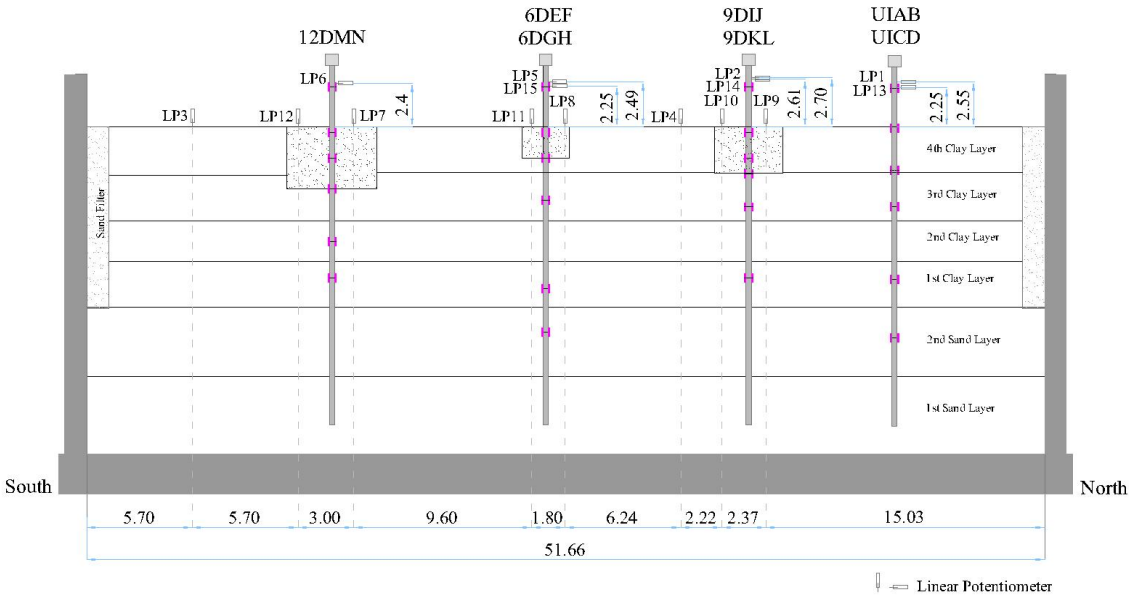

Figure 2.13 Displacement transducer locations

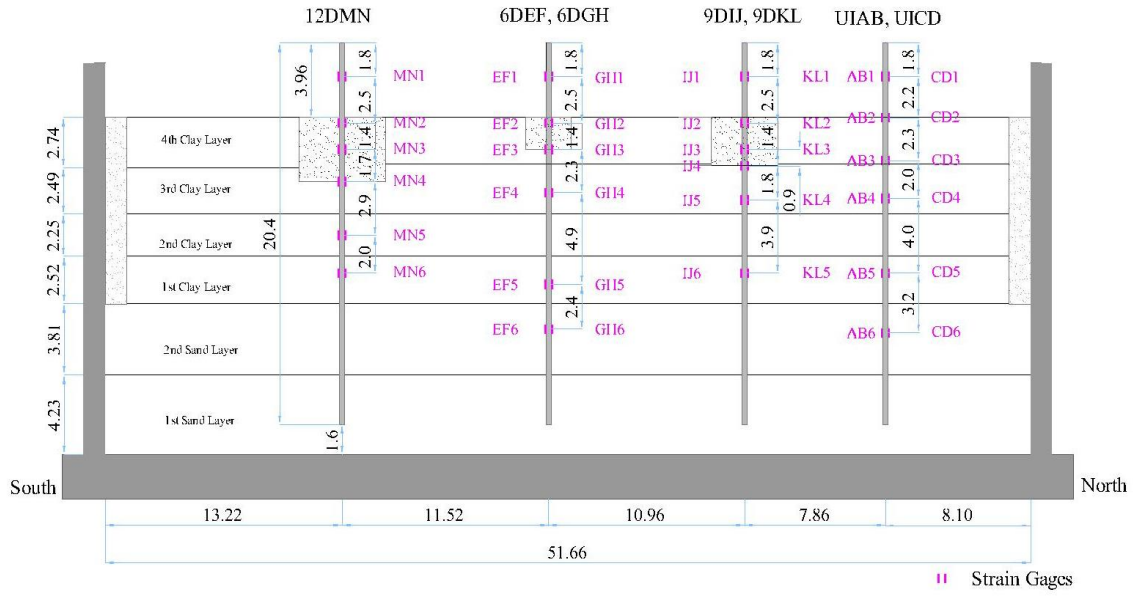

Figure 2.14 Strain gage locations

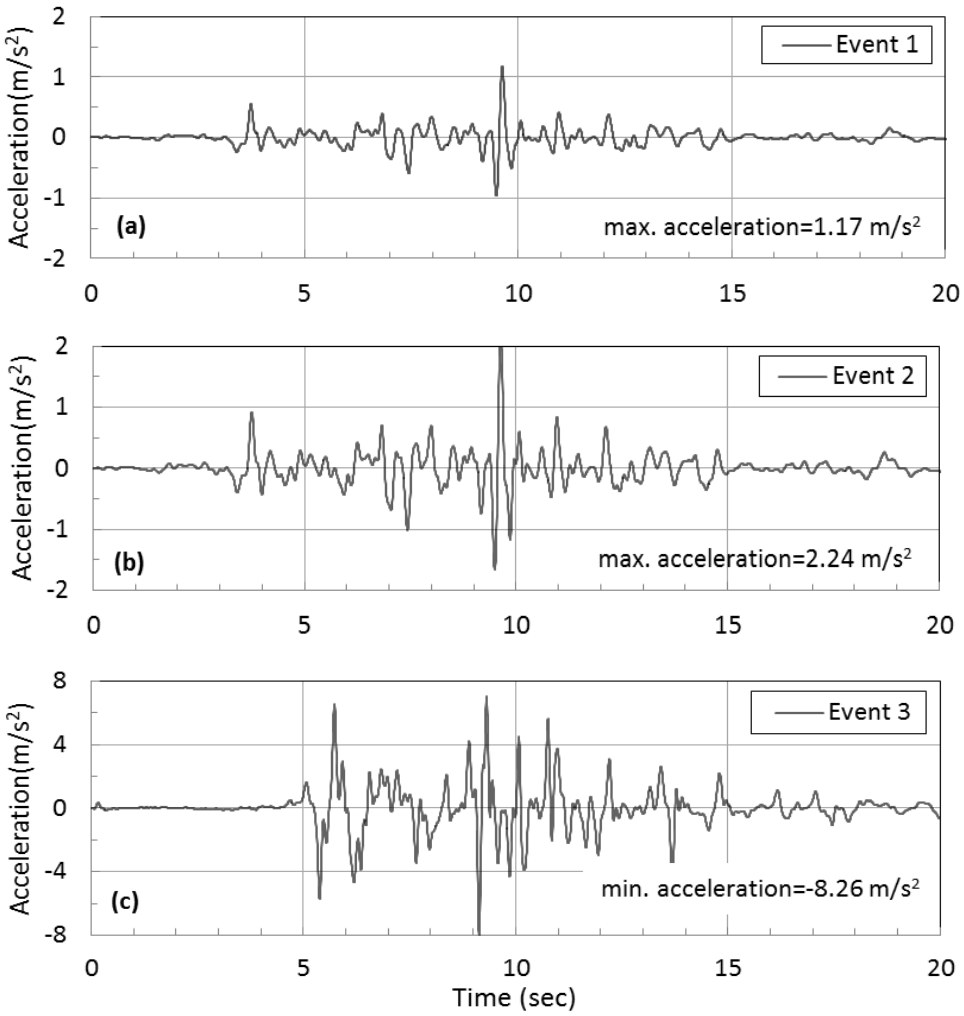

Figure 2.15 Acceleration-time histories of the base motion in the shaking events

CHAPTER 3: DEVELOPING P-Y CURVES FROM PSEUDO-STATIC LOADING EXPERIMENTS

3.1 Previous work on the derivation of p-y curves

In Beam on Nonlinear Winkler Foundation (BNWF) models, a pile is modeled as a beam resting on a bed of independent and closely spaced nonlinear springs whose force-displacement relationships are expressed with p-y curves. Here, "p" represents soil reaction distributed along a unit length of the pile, and "y" is the lateral pile deflection. Observations from pile head load tests on full- or reduced-scale pile models were the primary sources used in developing mathematical expressions for the p-y curves. Despite the simple and convenient application of the BNWF model in commercial finite element or finite difference software, this approach has limitations with regard to the adequate modeling of the continuity of the soil mass, the shear transfer between the springs, and the vertical shear stresses induced between the soil and the sides of the pile (Gazioglu and O'Neill, 1984; Murchison and O'Neill, 1984).

The most popular p-y models employed in engineering practice were established by Matlock (1970) for soft clay, by Reese and Welch (1975) and Reese and Cox (1975) for stiff clay, and by Reese et al. (1974) for sand, based on the results of field experiments on full-scale models of flexible piles with diameters up to 2 m. The derived curves were functions of depth, soil properties, and pile characteristics (diameter, material, and flexural stiffness). The conventional models have undergone extensive examination, and certain strengths and weaknesses in these models have been determined (Gazioglu and O'Neill, 1984; Murchison and O'Neill, 1984). A large majority of the published work on experimentally extracted p-y curves has been focused on piles embedded in homogenous

deposits (Ting et al., 1987; Dunnavant and O'Neill, 1989; Georgiadis, 1992a and 1992b; Dou and Byrne 1996; Wilson, 1998; El Naggar and Wei, 1999; Cho et al., 2007; Kim et al.,2009, Rovithis and Kirtas, 2009; Brandenberg et al., 2010).

Georgiadis (1983) was one of the earliest researchers to offer a solution to the problem of modeling the layered soil by introducing the concept of equivalent depth. Another notable contribution to the problem of layered soil profiles has been reported by Yang and Jeremic (2005). Through a finite element study, they observed that the p-y curves close to the interface of intermediate layers between two sand layers and two clay layers were significantly different from those in homogenous soils. Movement of the soil at the interfaces into the upper and lower layers was identified as a major factor in propagating the layering effects further away from the interface. Ground improvement introduces a strong heterogeneity in the soil system, which introduces discontinuities in the soil reaction at the interface of the improved and unimproved soil. As described in the following sections, the proposed moment curve-fitting procedure in this study includes a new feature that accounts for the discontinuity of the shear forces in the pile and the lateral soil reaction acting on the pile at the interface of the layers with significantly different stiffness values.

Soil reaction, p, and pile deflection, y, can be calculated using elastic beam theory, provided that the distribution of the bending moment is available and the pile behavior is within the elastic range. Interpolation techniques have been used to fit continuous functions to the discrete bending moment measurements, depending on the number and spacing of the measurements, criteria defined at boundaries, and the quality of the measurements. For instance, the derived pile deflection using polynomial functions can

deviate widely from known pile behavior below the level of the last measuring point (Scott, 1979). On the other hand, third-order polynomials used by El Naggar and Wei (1999) and Rovithis et al. (2009) resulted in reasonable lateral soil reaction distributions. Oldham (1984) and Geordiadis et al. (1992a) used fifth-order and fourth-order splines for laterally loaded piles in sand. The cubic spline fitting method was also used by Dou and Byrne (1995) to study the soil-pile interaction in a uniform sand under lateral base shaking. Different methods of curve fitting were compared by Brandenberg et al. (2010), who found that the weighted-residual method and cubic spline curve fitting yielded better results than polynomial regression. Ting et al. (1987), Sousa Coutinho (2006), and Brandenburg et al. (2010) have reported analytical problems with empirically derived p-y curves such that any slight error in the bending moment data becomes greatly magnified during differentiation. Moreover, the centrifuge scaling exacerbates any uncertainties in the measurements.

3.2 Proposed method for bending moment curve fitting

Pile deflection, y, and soil reaction per unit length of the pile, p, as functions of depth, z (measured from the soil surface), can be obtained using the following equations.

$$\frac{1}{EI}\int\left(\int M(z)\,dz\right)dz = y(z) \tag{3.1}$$

$$\frac{\partial^2 M(z)}{\partial z^2} = p(z) \tag{3.2}$$

where EI is the flexural stiffness of the pile.

In this study, the embedded length of the piles was divided into segments depending on the number of serviceable strain gages and the location of the soil layer interfaces between the improved clay and soft clay and between the soft clay and sand.

The traditional cubic spline curve fitting splices together third-order polynomials, provided that the continuity conditions are satisfied (Soltani and Muraleetharan, 2015). Adopting this method, bending moment within segment *i* at depth *z* was interpolated using a third-order polynomial, as presented by

$$M_i(z) = a_i(z - z_i)^3 + b_i(z - z_i)^2 + c_i(z - z_i) + d_i, \quad (3.3)$$

where a_i, b_i, c_i and d_i are constant coefficients and z_i is the distance between the pair of strain gages at the upper boundary of segment *i* and the soil surface. Various constraints can be incorporated into the procedure to solve for the unknown values (i.e. four constant coefficients of Eq. 3.3, in addition to e_i and f_i introduced later by twice integrating the bending moment in each segment to obtain pile deflection). At the layer interfaces, the distribution of soil reaction and shear force along the pile is not continuous. It was assumed in this study that the soil reaction at the interfaces is proportional to the soil layers modulus of elasticity and governed by the following equations

$$(a)\ \frac{p_{clay}(z_{interface})}{p_{sand}(z_{interface})} = \frac{E_{clay}}{E_{sand}} = 0.12;\ (b)\ \frac{p_{CDSM}(z_{interface})}{p_{clay}(z_{interface})} = \frac{E_{CDSM}}{E_{clay}} = 13.2 \quad (3.4)$$

where E_{clay}=6215 kPa, E_{CDSM}=82217 kPa, and E_{sand}=51164 kPa are the modulus of elasticity of the soft clay, improved clay, and the dense sand, respectively. The values for these moduli were determined using both laboratory tests conducted in this project and values reported in the literature. As for the boundary conditions, bending moment, shear force, and deflection associated at the pile toe along with the soil reaction were assumed to be zero. Applying the measurements regarding the pile displacement above the soil surface as additional constraints resulted in distortion of the interpolated bending moment around the pile toe and unusual shapes for the deflected piles. Therefore, the freestanding

portion of the pile above the soil surface was not included in the curve fitting process; however, the associated measurements were considered for validation of the derived deflection, as will be discussed in the next section. Boundary conditions at the soil surface were considered as a shear force equal to the applied lateral force and a bending moment calculated from the strain gage data at a depth of 35 cm within the improved soil. Because precise measurements regarding the location of the lateral force in the centrifuge model were not available, the bending moment derived from the lateral force was found to be inaccurate, even though it was used for pile UIAB with no serviceable strain gages close to the soil surface. The lateral soil reactions acting on the pile were estimated by twice differentiating the bending moment with respect to depth. Pile deflections were estimated by twice integrating the bending moment with depth.

3.3 Details of the testing procedure

The pseudo-static lateral loading test was performed with an actuator in a displacement-controlled mode in multiple steps. The loading started by moving the pile head from the initial position to a target displacement on the right side (towards the north side of the box) and maintaining this displacement for several minutes in order to send the command for the next step to the actuator. In the following step, the pile head was moved to the opposite side. The applied displacements at the end of each step are shown in Table 3.1 for pile 6DEF. Other piles followed the same loading pattern and target top displacements. The piles were subjected to a sequence of pseudo-static lateral loads applied incrementally to the pile head until a target deflection was achieved at the location of a loading point about 3.94 m above the soil surface (Figure 3.1). The positive displacement is to the right side. The deflections induced in the freestanding length of the

piles were measured at three levels using displacement transducers. In the next loading step, the pile head was moved to the opposite side. Moving the pile from one side to the other in one loading step took about 10-15 seconds, whereas a pause of two to three minutes between loading steps was required to set up the actuator for the next deflection. To derive the bending moments, data were collected from a group of electrical-resistant strain gages distributed along the piles: five pairs located below the soil surface and one pair above the soil surface.

The improved and unimproved piles 6DEF, 9DKL, 12DMN, and UIAB experienced 0.606 m, 0.632 m, 0.189 m, and 0.594 m deflection on the right side of the piles, respectively at the piles tops, 3.94 m above the soil surface, in response to a maximum applied load of 143 kN, 188 kN, 120 kN, and 63 kN, respectively. The required lateral force for inducing nearly the same amount of top deflections increased as the improved zone became larger in size. Pile 12DMN was subjected to smaller displacements compared to other piles to prevent significant damage to the pile and the surrounding improved soil since there was only one pile with 12D improvement and this pile had to be protected for seismic loading.

3.4 Primary results: distributions

Lateral force-displacement curves measured at the pile tops for selected loading steps are shown in Figure 3.2. The arrows in these figures show the direction of the pile head displacement. The envelop curves shown in Figure 3.3 were generated by plotting the peaks of the load-displacement traces at the end of each loading step. The curves obtained from testing 6DEF and UIAB after seismic loading match those obtained before the shakings (UICD and 6DDGH) and confirm the visual observations that the piles and

CDSM block around 6DEF sustained no damage during shaking. Small-strain lateral stiffness values (at a lateral displacement of 0.05 m) for unimproved (UIAB), small improvement (6DEF), medium improvement (9DKL), and large improvement (12DMN) were 400 kN/m, 600 kN/m, 760 kN/m, and 880 kN/m, respectively. The ultimate lateral resistance (at a displacement of 0.6 m) of the unimproved pile was about 50 kN, whereas that of the pile in the medium improved zone was about 200 kN. Although the load-displacement curves for 12DMN and 9DKL improvements appear similar up to 0.2 m of lateral displacement, the 12DMN pile likely would have provided somewhat higher load resistance than the 9DKL pile if the loading continued. The closeness of these two curves indicates that the full benefit of ground improvement may be achieved around 17D×17D×12D improvement. That is, further ground improvement beyond this region will produce only negligible benefit to the lateral loading behavior of the pile for this soil-pile system.

The distributions of pile bending moments with depth are shown in Figure 3.4. The measured bending moments are shown by discrete points in these figures. The curves indicate that the piles in both improved and unimproved soils reached the yield bending moment (YBM) of 305 kN.m. The maximum bending moments for the unimproved pile UIAB occurred at 3 to 4 m below the ground surface. The maximum bending moments and shear forces (Figure 3.5) in the improved soil occurred within the improved zone. For a lateral displacement of about 0.2 m, the maximum bending moments in the unimproved as well as small, medium, and large improvement zones were, 184 kN.m, 238 kN.m, 460 kN.m, and 616 kN.m, respectively. For the same lateral displacement, maximum shear forces were, 36 kN, 76 kN, 188 kN, and 376 kN. For a lateral force of about 60 kN, the

piles deflection at the soil surface were, 0.298 m, 0.015 m, 0.011 m, and 0.010 m, respectively while the measured displacement at the piles tops were, 0.510 m, 0.141 m, 0.070 m, and 0.066 m, respectively as depicted in Figure 3.6.

3.5 Secondary results: p-y curves

The p-y curves were generated by plotting the peaks of the soil reaction–pile deflection traces at various depths. Figure 3.7 shows the derived curves at a depth of 0.5 m (1.75D). The loading steps in which the bending moment along the pile passed the yield point of 305 kN.m are shown with large red circles. The loading steps beyond the yield points are removed, so the observed nonlinearity in the derived p-y curves is most likely due to the nonlinear soil-pile interaction rather than nonlinearities in the pile behavior. The lateral loads causing the bending moments in the piles to reach the yield moment are reported in Figure 3.7. In this figure, the curves on the right side of zero deflection are different from their counterparts on the left side. For a given displacement, more soil reaction develops on the right side than on the left side. The asymmetric response of the pile on the left and the right side of the center line can be explained by observed crack patterns in the CDSM block, as shown in Figures 3.8 and 3.9. These photographs were taken after stopping the centrifuge following the last loading step (Loading Step No. 20, Table 3.1). On the right half of the improved zone, a diagonal crack developed. On the left half, two perpendicular cracks can be seen; they appear to separate almost a quarter of the CDSM block from the rest of the improved zone. It is very likely that the separated zone provided less resistance during movements to the left side. Relaxation of the pile under sustained top deflection at the end of each step caused a gradual drop in the lateral soil reaction, as can be detected on the curves derived for 6DEF. Unlike piles 6DEF and 9DKL, no degradation in the

improved zone was observed, other than a slight separation of pile for 12DMN, as shown in the pictures in Figure 3.10. It should be noted here that the lateral displacements applied to pile 12DMN are much smaller than those applied to 6DEF and 9DKL.

Figures 3.11 through 3.14 portray the p-y curves at various depths in the improved clay and soft clay. The extracted p-y curves are compared with conventional curves proposed by Reese and Welch (1975) for stiff clay with no free water within the improved zone, and by Matlock (1970) for soft clay, respectively. The conventional curves were drawn using the associated models available in LPILE (Ensoft, Inc., 2004) and referred to as the "built-in models." Even though the centrifuge model was kept saturated by maintaining a one-centimeter-deep layer of free water above the soil surface, it was believed that the water could not cause considerable material degradation in the cemented soil and particularly in the gap between the improved soil and pile induced by repeated loading. Furthermore, the proposed p-y curves for stiff clay with free water by Reese and Cox's (1975) showed that at a particular deflection the ultimate soil resistance was developed and beyond this point there was a reduction in soil resistance with continued deflection which did not agree with the characteristic shapes of the derived curves in the pseudo-static centrifuge tests.

The results for each pile will be discussed below

- **Pile UIAB**: The extracted p-y curves in soft clay within the top 1.5 m of the surface soil were difficult to interpret. At deeper layers, they exhibited hyperbolic shapes, as shown in Figure 3.11. The initial stiffness and the ultimate strength increased with depth. The conventional p-y curves using Matlock's soft clay model underestimated the

ultimate strength and overestimated the initial stiffness at depths of 3.5 m and 5 m. The derived p-y curve at a depth of 2 m matched the conventional model at a depth of 3.5 m.

- **Pile 6DEF**: The conventional model for stiff clay with no free water produced p-y curves that varied proportionally with depth (i.e., both stiffness and strength increased with depth). Contrary to expectations, the ultimate strength of the p-y curves derived from experiment in the improved zone was inversely related to depth. Direct comparison of the derived p-y curves with the ones generated by the stiff clay model implies that the conventional model with the selected parameters, which will be discussed in detail in the next section, consistently overestimated the experimentally derived curves. Nonetheless, the characteristic shape of the p-y curves generated by the model agreed with those from the experiment, especially the point at which the curves reached their plateaus, near 0.05 m. Below the interface of the improved and soft clay, the extracted p-y curves appear as expected, stiffer and stronger with depth. Similar to the UIAB, the soft clay model overestimated the soil reaction for pile deflections smaller than 2 cm. However, the congruity between the model and the experimental results increased at greater depths. The p-y curves derived from testing 6DEF in soft clay appear to be softer than their counterparts obtained from testing UIAB.

- **Pile 9DKL**: Extending the treated zone around the pile to larger lateral and vertical extents does not affect the curves produced by the stiff clay model, because the improved soil is treated as a semi-infinite layer in the conventional model. On the other hand, the experiment-based curves showed a stiffer and stronger behavior compared to 6DEF curves (Figure 3.13a). The conventional model still overestimated the stiffness and ultimate strength. For example, the soil reaction at a depth of 0.5 m on pile 6DEF

increased from 150 kN/m to 280 kN/m on pile 9DKL. The inverse relationship with depth was also observed in the improved zone. Due to difficulties in interpreting the data for pile deflections smaller than 1 cm, the p-y curves in soft clay were plotted only at two depths, 3.5 m and 5 m, as shown in Figure 3.13(b). Interestingly, the conventional model underestimated the soil reaction in soft clay. It appears that the presence of the improved zone affected the behavior of the underlying soft clay and induced p-y curves stiffer and stronger than the curves at the same depths back-calculated for UIAB and 6DEF. Figures 3.12 and 3.13 also show a smooth transition from the p-y curves in the improved zone (close to the interface of the improved zone and the soft clay) to the ones within the soft clay right below the interface (e.g. at depths of 2 m and 3 m, respectively for piles 6DEF and 9DKL). This is likely due to the fact that as the depth increases, the soil reactions are likely to be influenced more by the soft clay below the CDSM block. In other words, "p" values at a given depth do not depend only on the soil at that depth, as assumed by the theory, but also are affected by adjacent soil layers. This phenomenon is not captured by the conventional models.

- **Pile 12DMN**: As was explained in Section 3.3, pile 12DMN experienced only very small loads, the largest of which was 130 kN. The derived p-y curves should represent the material behavior in the linear range within small displacements of up to 3 cm at the soil surface. At a depth of 0.5 m, for displacements smaller than 0.01 m, a close agreement between the curves resulting from the experiment and from the stiff clay model was observed. Because the induced pile deflections inside the soft clay layer were less than 0.001 m, it was difficult to provide a meaningful interpretation of the results.

- For the sand layers (whose results are not shown here), where the pile deflection was less than 0.01 cm, the conventional model proposed by Reese et al. (1974) overestimated the derived curves, although both showed linear behavior.

3.6 Validation of the conventional models

This section details the implementation of the conventional and the experimentally derived p-y models in simulating the pile response under static top load in improved and unimproved soil using LPILE. The simulation results are compared with the bending moment and the deflection measured in the centrifuge tests.

3.6.1 LPILE simulations using the conventional p-y curves

The improved soil was modeled with Reese and Welch's (1975) model for stiff clay with no free water. The underlying soft clay and sand were modeled using the p-y curves proposed by Matlock (1970) and Reese et al. (1974), respectively. Based on the available data and upon the judgment of the authors, the input values of these built-in models were selected following the recommendations available in the LPILE program manual. The soil was modeled as a horizontally layered system (an LPILE assumption). As a result, it did not allow for proper consideration of the improved zone's lateral dimensions.

In the conventional model calibration, ε_{50}, the strain corresponding to one-half of the maximum deviatoric stress in triaxial tests, was selected as 0.002 and 0.004 for the unimproved and improved soft clay, respectively, according to the recommendations in the LPILE manual. The selected values were quite close to the results of triaxial tests, as plotted in Figure 3.15 (Thompson, 2011). The selected values for ε_{50} happened to agree with the values suggested in the LPILE manual. As explained in Section 2.2, the soft clay layer consists of four sublayers that were consecutively placed and consolidated during

construction of the centrifuge model. The required parameters concerning the effective unit weight, the consolidation stress, and the undrained shear strength of each soil layer are listed in Table 3.2. The undrained shear strength, C_u, of the soft clay was estimated based on the correlation relation proposed by Ladd and Foot (1974) as

$$C_u = 0.22 * \acute{\sigma_v} * OCR^{0.8} \quad (3.5)$$

where $\acute{\sigma}_v$ is the effective vertical stress. OCR at the top and the bottom of each soil layer was calculated using the effective stress applied to the soil layers during the consolidation phase of the centrifuge model preparation and the state of stress in the centrifuge. Shear strength of the improved soil was estimated as 330 kPa, based on the unconfined compressive strength of cured samples measured in laboratory tests (Figure 2.10). The subgrade coefficient and the friction angle of the dense sand layer was selected, respectively, as 33900 kN/m^3 and 38 degrees, based on the recommendations in the LPILE manual.

3.6.2 LPILE simulations using the user-defined p-y curves

The experimental p-y curves (see Figures 3.11 to 3.14) were assigned as user-defined curves to the soil layers in LPILE models at various depths. In LPILE simulations utilizing both the user-defined and the built-in p-y curves, the upper boundary condition was defined as a pure lateral force at 3.94 m above the soil surface, which is consistent with the boundary conditions assumed in the bending moment curve-fitting.

Simulated bending moment, shear force, soil reaction, and pile deflection for a lateral force of 60 kN are plotted in Figures 3.16 through 3.19. Simulations were performed considering a lateral force of 60 kN, which seemed to be a reasonable choice

for comparing the behavior of unimproved and improved piles without yielding the pile itself. Therefore, the pile behavior was limited to the elastic region (Figure 3.7). Curves labeled “No. 1” and “No. 3” are associated with the built-in and the experimentally extracted p-y curves, respectively. Curves marked “No. 2” were back-calculated using the spline curve fitting of bending moments described in Section 3.4. The actual measurements are marked with filled squares on the graphs of bending moment and pile deflection. Curves marked ”No. 4” represent the simulation results where the E ratio in Eq. 3.4 was set to 1, which will be discussed in Section 3.7.

The back-calculated p-y curves for UIAB predicted deflections in the freestanding length of the pile matching the values measured by the displacement transducers at two levels, as shown in Figure 3.16, whereas the Matlock soft clay model resulted in larger deflections. In general, the predicted bending moment, shear force, and soil reaction using the back-calculated p-y curves are consistent with those generated using the built-in models, except at the interface of the soft clay and sand, where the built-in models produced lower soil reaction. It should be noted that the sign convention used indicates that positive soil pressure is directed from left to right. The associated pile deflections at the soil surface were found to be compatible with the soil reactions which means a positive pile displacement to the right side generates a negative soil reaction and vice versa.

Figure 3.17 shows that, for pile 6DEF, the simulated deflections outside the soil layer using the back-calculated curves lay between the measured values and the values predicted by the built-in models. For the zone of smallest improvement, the conventional models create a stiffer pile, because the LPILE models do not include the lateral extent

of the improved zone as an influencing factor on the overall stiffness. Because no measurement of bending moment was available within the improved zone, a linear distribution of soil reaction was obtained from the spline curve fitting (curve No. 2), which differs from the S-shaped distribution of the soil reaction produced by the built-in models (curve No. 1).

The measured and LPILE-predicted deflections for 9DKL using the derived p-y curves compared quite well, as can be seen in Figure 3.18. Slight underestimation of the conventional models is believed to be related to the non-inclusion of the lateral extent of the improved zone. The sudden change in the soil reaction distribution at the interface of the improved and unimproved soft clay produced by LPILE and represented by curve No. 1 is compatible with our assumption on the discontinuity of the soil pressure in Eq. 3.4.

As depicted in Figure 3.19, the excellent match between the measured and the predicted deflections for pile 12DMN suggests that, for this configuration of the improved zone, practically identical results can be produced for the experimentally derived p-y curves and those based on the Reese and Welch model for stiff clay with no free water.

Ultimately, for all piles in the improved soil, the LPILE-predicted bending moments using the conventional models at the interface of the improved and soft clay was smaller than the measured values. In addition, the predicted shear force in the improved zone using the conventional models was consistently higher than that of the user-defined curves. The under- and over-estimation of the conventional models might be of concern where they are employed for design purposes. Another important observation from the simulated responses is that the presence of the improved soil altered the distribution of the bending moment, shear forces, soil reaction, and pile deflection.

The maximum values were concentrated in the improved zones. The case with the zone of smallest improvement (6DEF) can be considered as a hybrid case, having the components of the unimproved and improved soils.

3.7 Sensitivity analysis

Increasing and decreasing the *E* ratio in part (b) of Eq. 3.4 by a factor of five in all improved cases did not noticeably affect the simulated pile responses except for pile 9DKL. Setting the *E* ratios at the soil layer interfaces equal to one had minor effects on the distributions for piles UIAB, 6DEF, and 12DMN, as represented by curve No. 4 in Figures 3.16, 3.17 and 3.19. However, it significantly influenced the distributions for pile 9DKL such that the pile deflection at the soil surface no longer agreed with the measurements above the soil surface (Figure 3.18). The insensitivity of the responses of piles 6DEF and 12DMN might be related to the smaller spacing between the strain gages and the location of the strain gages within the improved zone, which is another influencing factor that imposes constraints on the estimated bending moment distribution. The sensitivity analysis results confirmed that introducing discontinuities at the soil layer interfaces improved the quality of the derived quantities, including the pile deflections.

3.8 Summary of the observations and conclusions

- The bending moment curve-fitting procedure developed in this chapter takes into account the soil layering effects by including sharply varying soil reactions at the interface of improved and soft clay layers. This is a novel feature of the proposed approach. The close agreement of the estimated pile deflections with measurements confirmed that the adopted method significantly improved the accuracy of the

estimations, especially when the spacing between the strain gages was large, as was the case with pile 9DKL.

- The one-dimensional soil model created in LPILE was not capable of incorporating the limited lateral extent of the improved zones; as a result, the built-in models overestimated both the stiffness and the ultimate strength of the improved soft clay for piles 6DEF and 9DKL. However, the agreement between the derived p-y curves and the conventional model curves and also the agreement between the measured and LPILE-simulated responses became closer as the size of the improved zone increased, such that close matches were observed for pile 12DMN. This behavior is expected because the one-dimensional soil model generated by LPILE can represent the behavior of the improved soil in the centrifuge experiment more accurately as its lateral extent increases and the influence of the surrounding soft clay vanishes as it moves deeper within the soil profile.

- The conventional curves compared reasonably well with the derived curves in soft clay.

- An inverse relationship of the derived curves with depth within the improved soil was observed for piles 6DEF and 9DKL.

- As the size of the improved zone increased, more lateral resistance was provided inside the improved zone at the same lateral deflection.

- The study evaluated the merits and limitations of the conventional p-y methods in modeling the pile behavior in three different configurations of the improved soil. The conventional models were found to be accurate for predicting the deflection response of

piles of 9D and 12D improvements, but inaccurate for 6D. The conventional models accuracy improves as the lateral extent of the treated zone increases.

- Maximum bending moments and shear forces within piles was observed in the improved zones. The design implication of these findings is that for a given lateral load, ground improvement around a pile in soft clays can be used to reduce the corresponding lateral displacement considerably. The bending moments and shear forces generated within the piles for a given lateral displacement, however, will be significantly increased, especially within the improved soil regions. Therefore, appropriate dimensions for the piles should be selected so that any significant yielding or premature failure of the pile can be prevented, as assumed in routine seismic design practice, and the full potential of a pile can be realized.

- The closeness of these force-displacement curves at pile tops indicates that the full benefit of ground improvement may be achieved in improvement zones of approximately 17D×17D×12D in size. That is, further ground improvement beyond this region will produce only negligible benefit to the lateral loading behavior of the pile for this soil-pile system.

- Depending on the vertical and horizontal extents of the ground improvement area, the small-strain lateral stiffness and load resistance of a pile in improved soil subjected to cyclic loading increased from 2 to 8 times and 4 to 5 times, respectively, from those of a pile in the unimproved soil.

- For a given lateral force, lateral displacements in improved soil can be reduced as much as 8 times compared to those in unimproved soil during cyclic loading.

- On the other hand, for a given lateral displacement, for a pile in improved soil, the maximum bending moments in piles increased by as much as 3 times, and the shear forces increased as much as 8 times, over that for a pile in unimproved soil.
- Soil reaction at a given depth do not depend only on the soil properties at that depth, as assumed by the theory, but also are affected by adjacent soil layers. This phenomenon is not captured by the conventional models.

Table 3-1 Target Displacement on the Left and Right Sides for the Piles

Lateral displacement	
Right side (m)	**Left side (m)**
(1) 0.039	(2) 0.049
(3) 0.057	(4) 0.067
(5) 0.077	(6) 0.087
(7) 0.094	(8) 0.106
(9) 0.142	(10) 0.148
(11) 0.189	(12) 0.205
(13) 0.287	(14) 0.300
(15) 0.382	(16) 0.397
(17) 0.511	(18) 0.525
(19) 0.606	(20) 0.619

Table 3-2 Input Parameters Used in LPILE Simulations

Soil Layer	Thickness (m)	Effective unit weight (kN/m^3)	Consolidation stress (kPa)	Undrained shear strength (kPa)	ε_{50}
Improved soft clay	6DEF=1.71 9DKL=2.58 12DMN=3.42	8.69	-	330	0.004
Clay layer 4	2.742	8.18	25	Top=2.78 Bottom=5.38	0.002
Clay layer 3	2.490	8.68	45	Top=8.61 Bottom=9.86	0.002
Clay layer 2	2.250	9.05	70	Top=14.03 Bottom=15.15	0.002
Clay layer 1	2.520	9.28	95	Top=19.34 Bottom=20.57	0.002
Sand	6.396	10.88-10.44	-	-	-

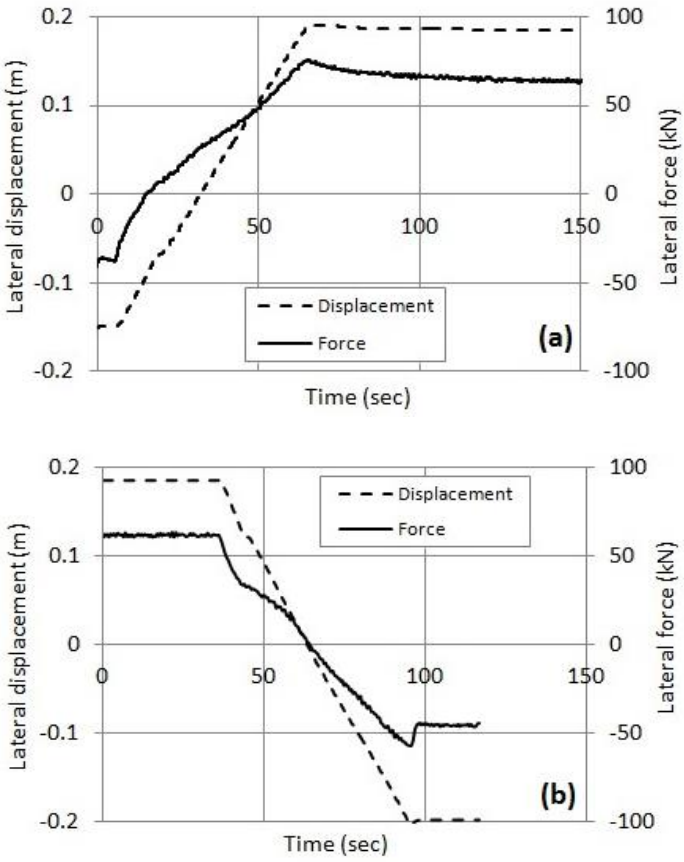

Figure 3.1 Time histories of top displacement and the applied force for pile 6DEF in loading steps: (a) No. 11 and (b) No. 12

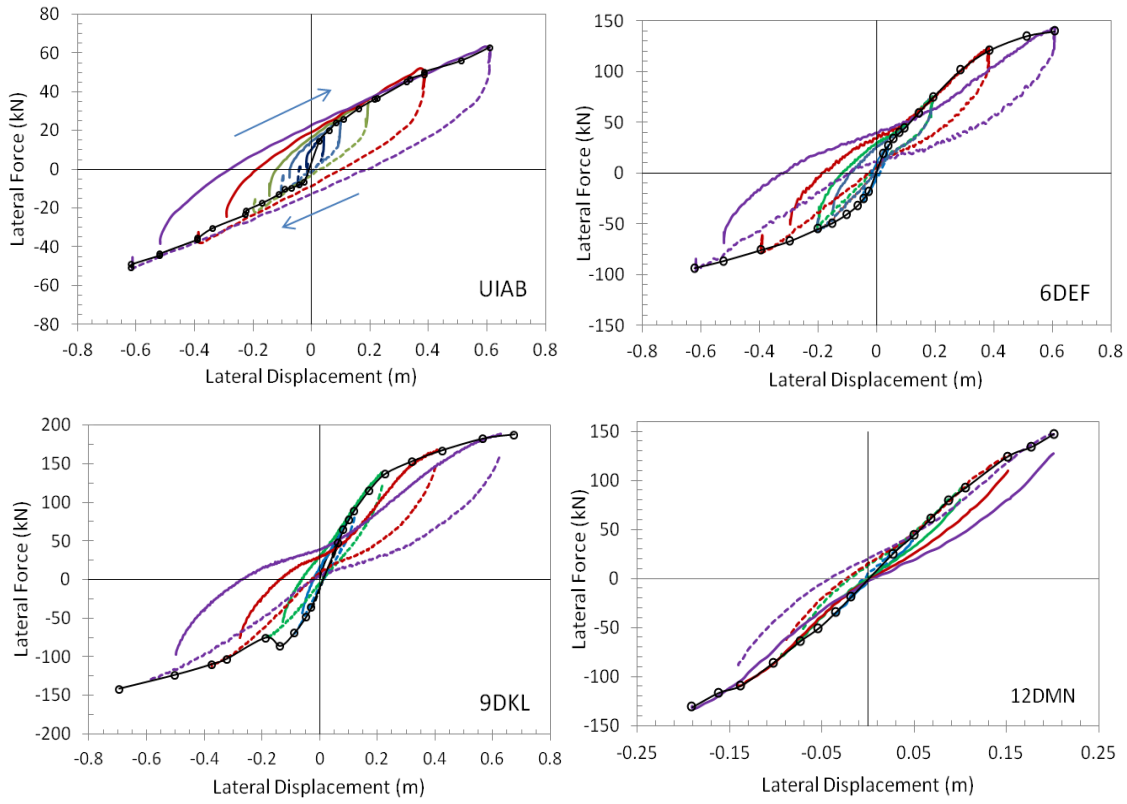

Figure 3.2 Lateral force-displacement curves measured at the pile tops for selected loading steps

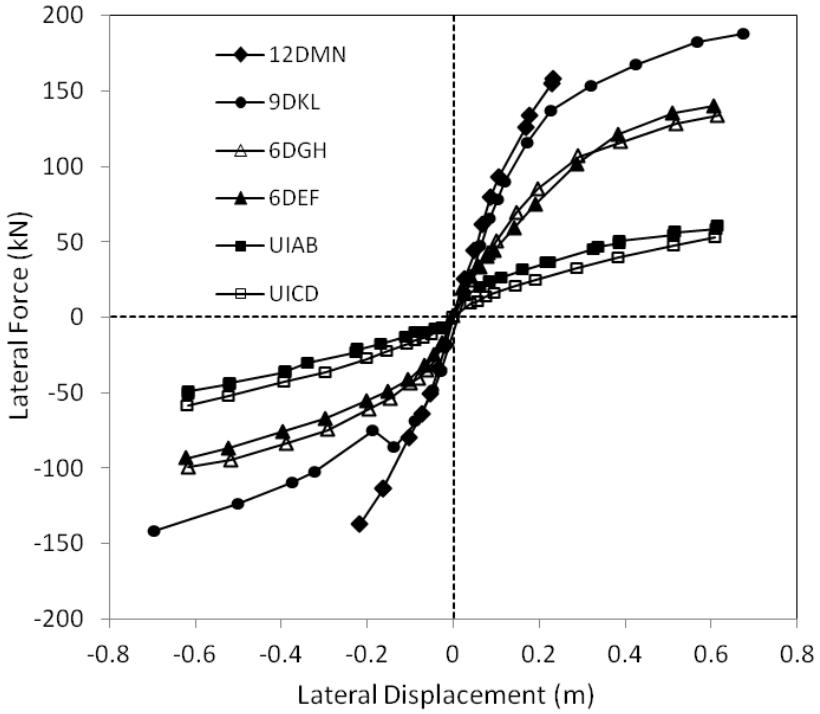

Figure 3.3 Envelopes of the lateral load-displacement curves at the pile tops

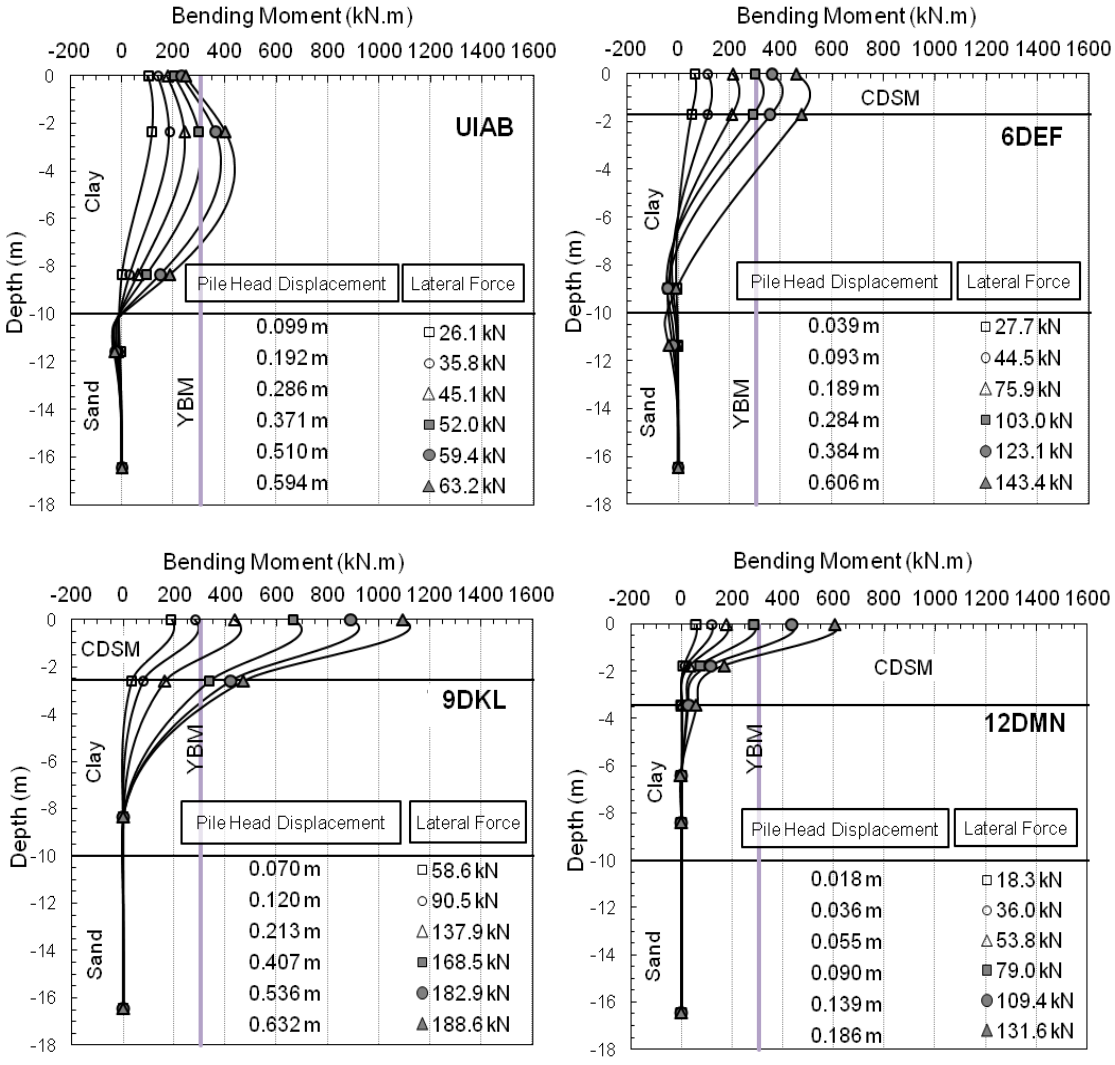

Figure 3.4 Distribution of bending moment along the piles

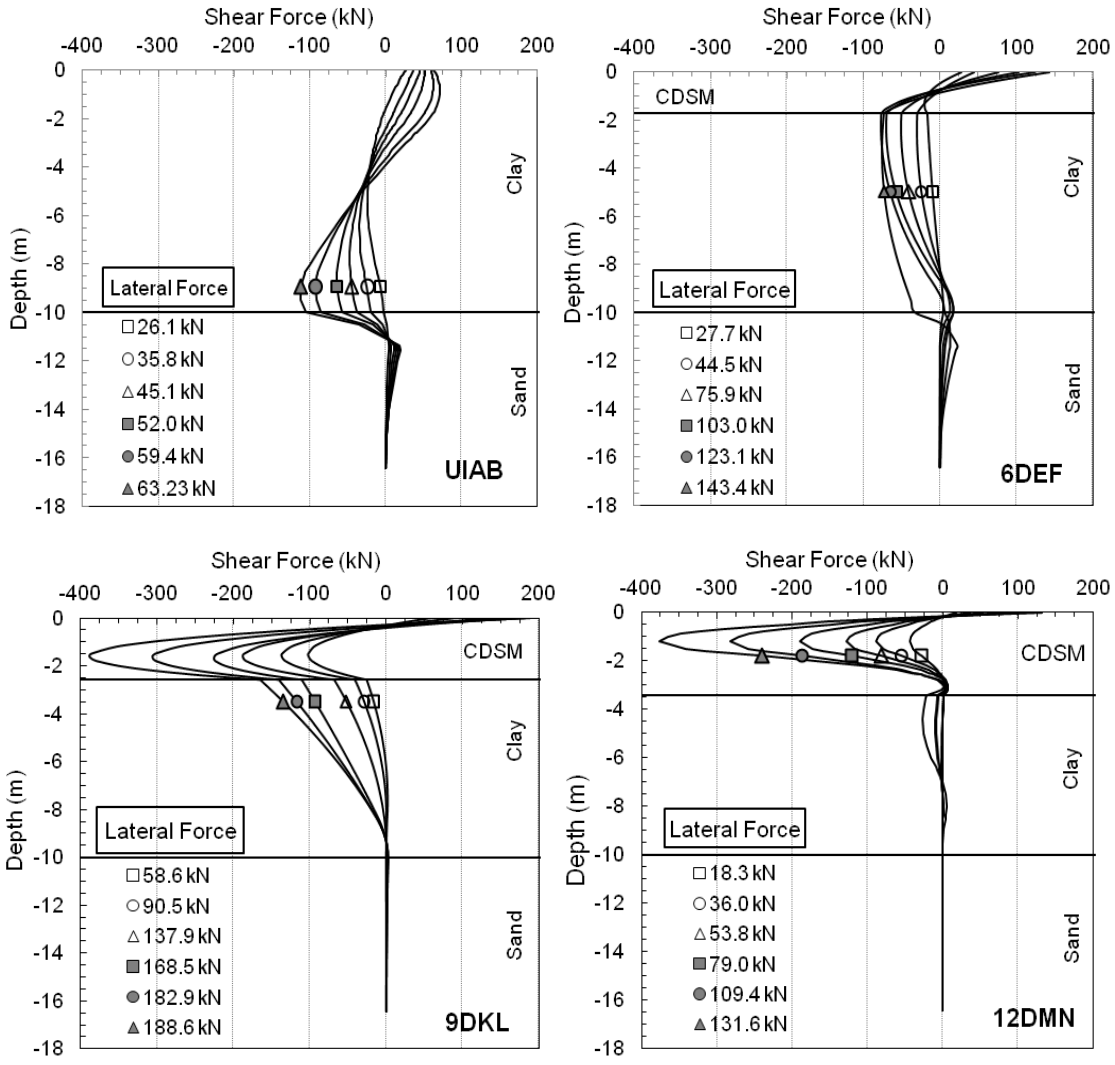

Figure 3.5 Distribution of the shear force along the piles

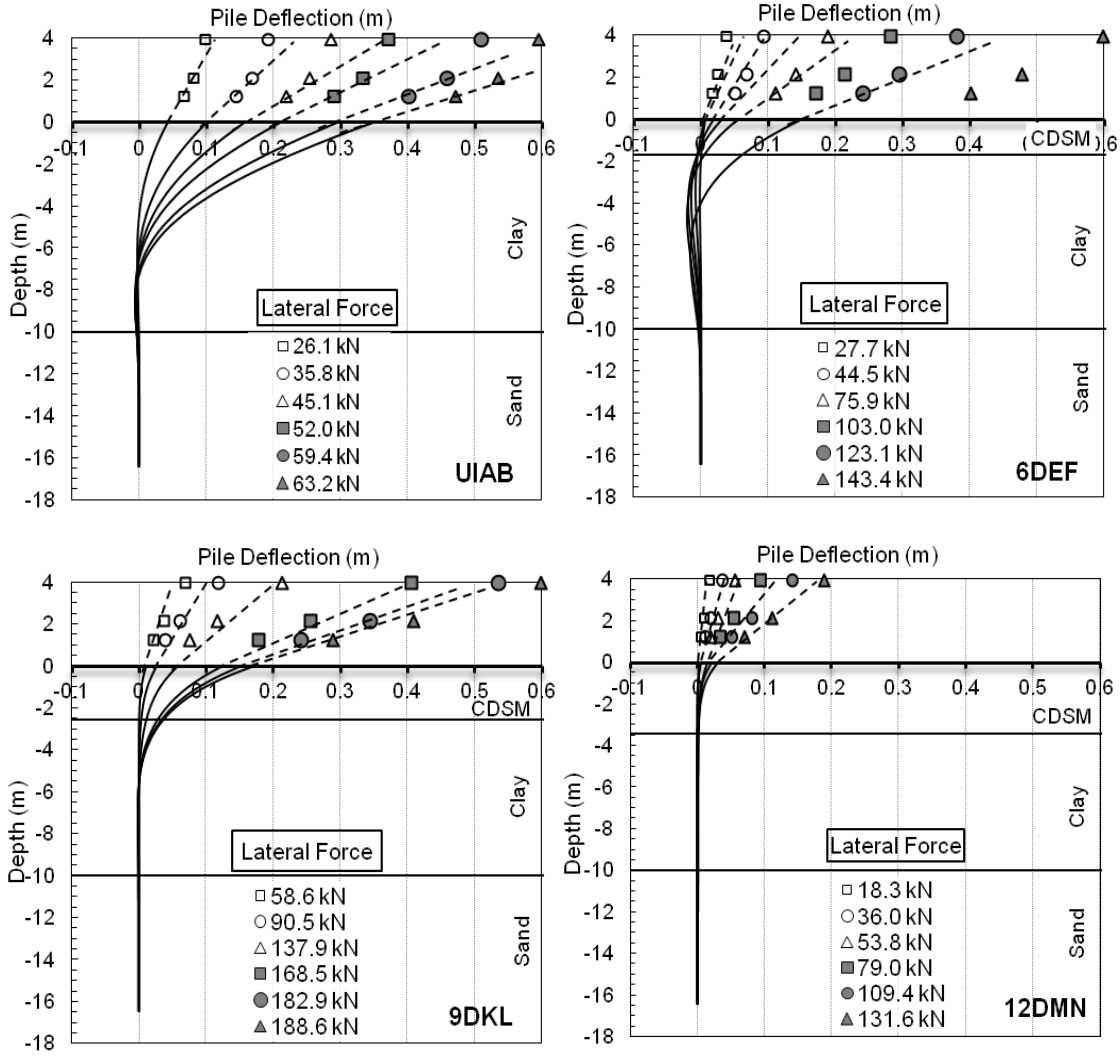

Figure 3.6 Distribution of pile deflections

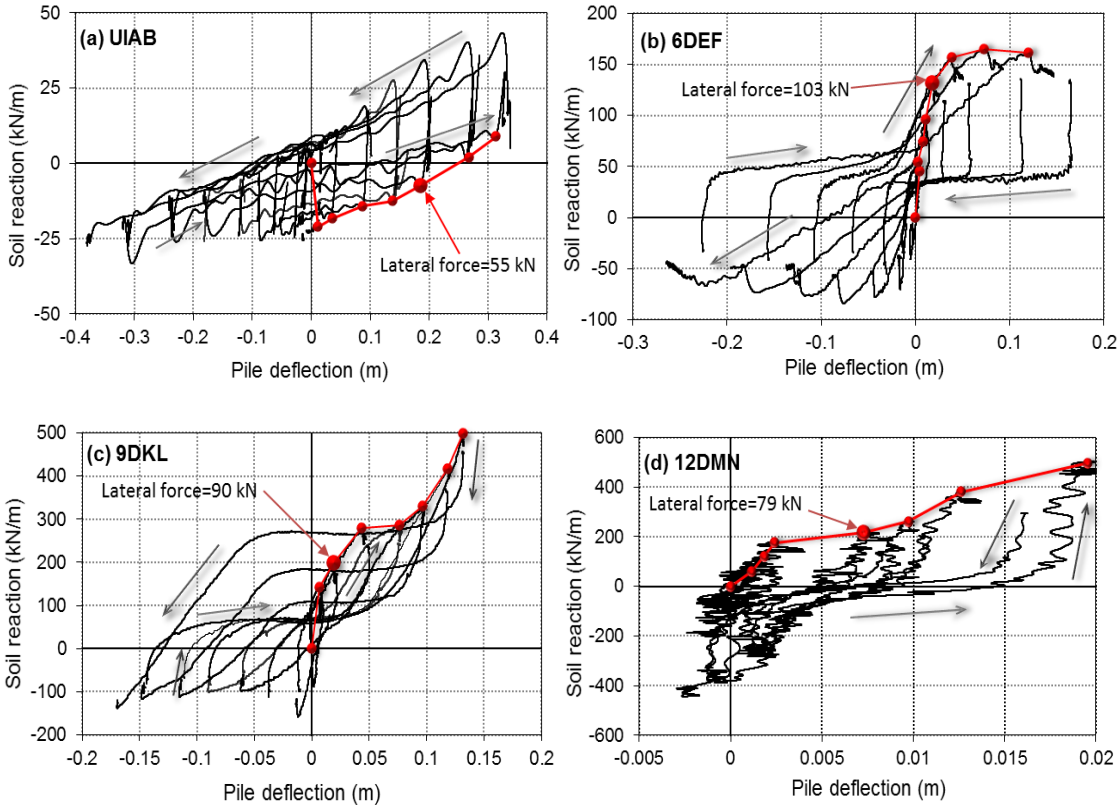

Figure 3.7 Soil reaction-pile deflection traces at the depth of 0.5 m (1.75D)

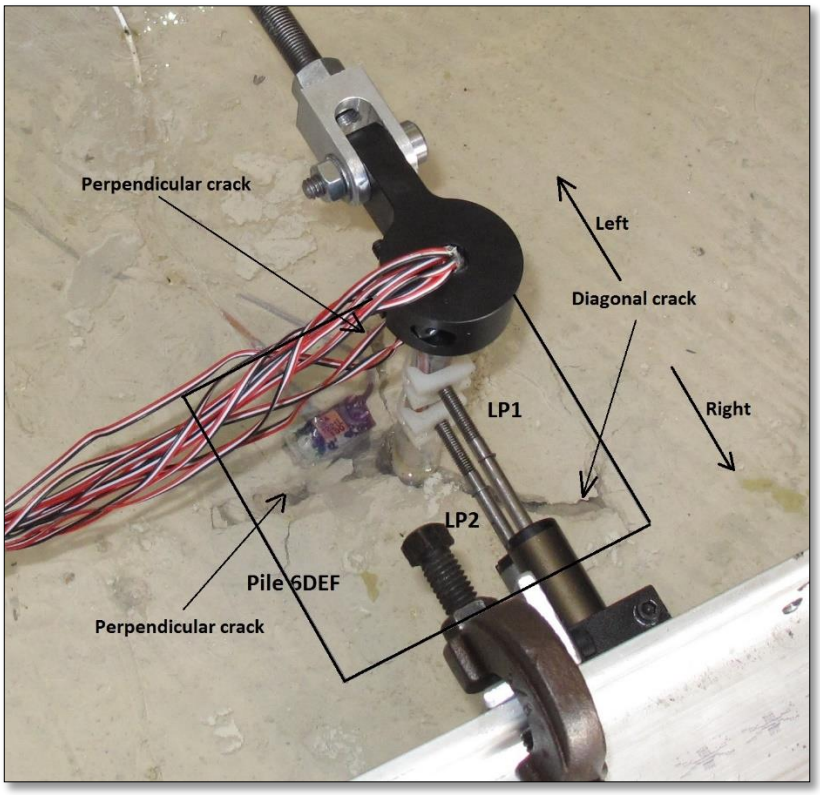

Figure 3.8 Location of the cracks in the cement treated zone around 6DEF

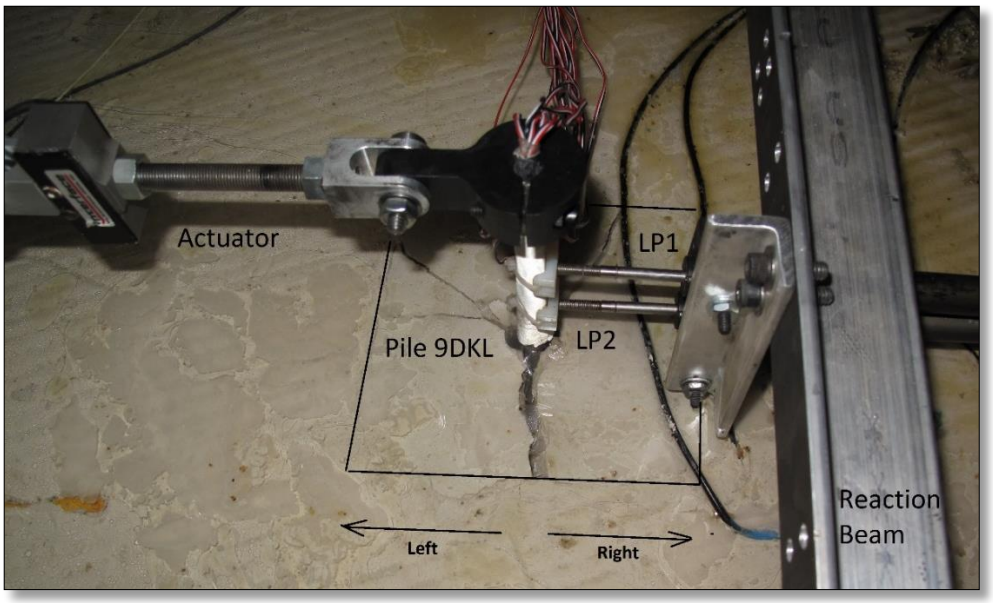

Figure 3.9 Deterioration in the improved soil around pile 9DKL

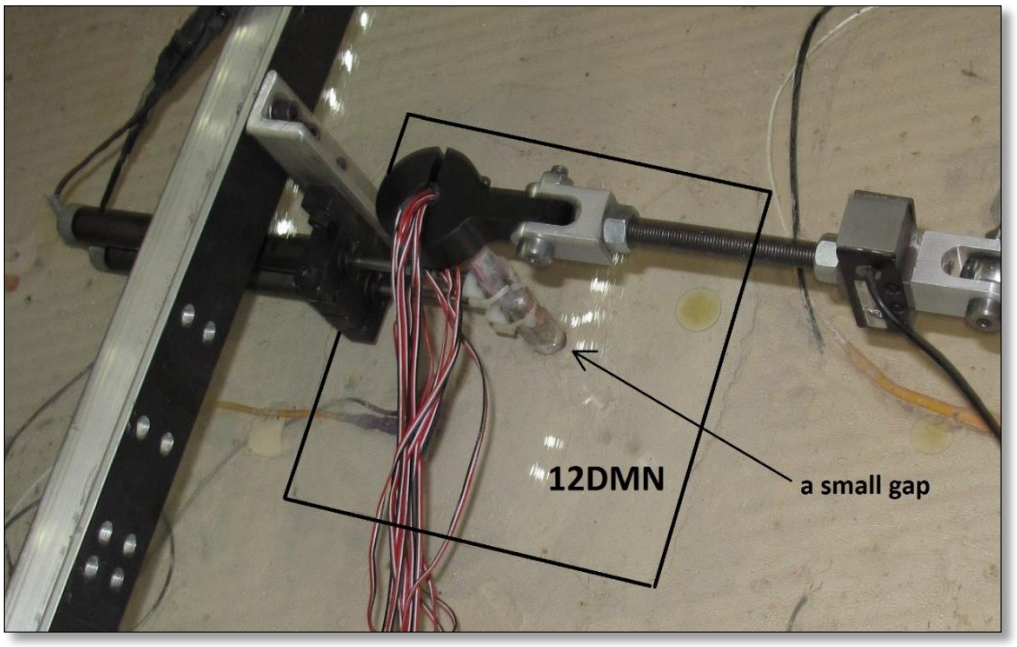

Figure 3.10 Pile 12DMN after pseudo-static loading tests

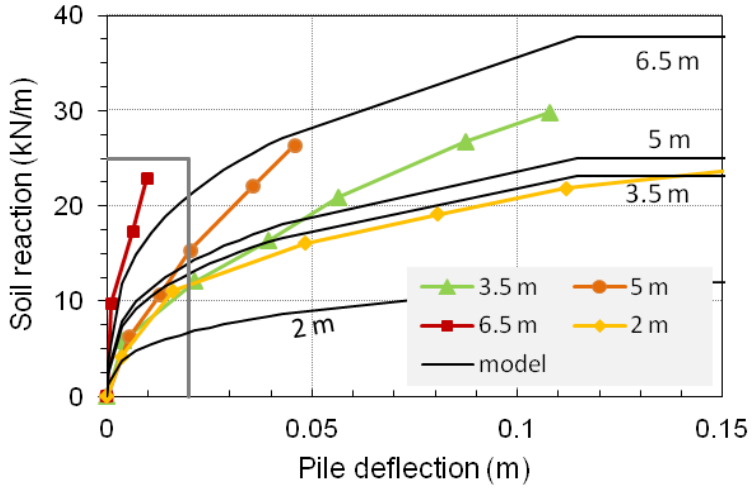

Figure 3.11 p-y curves derived from the experiment and the conventional model-Pile UIAB
(Solid black lines represent the conventional model for soft clay.)

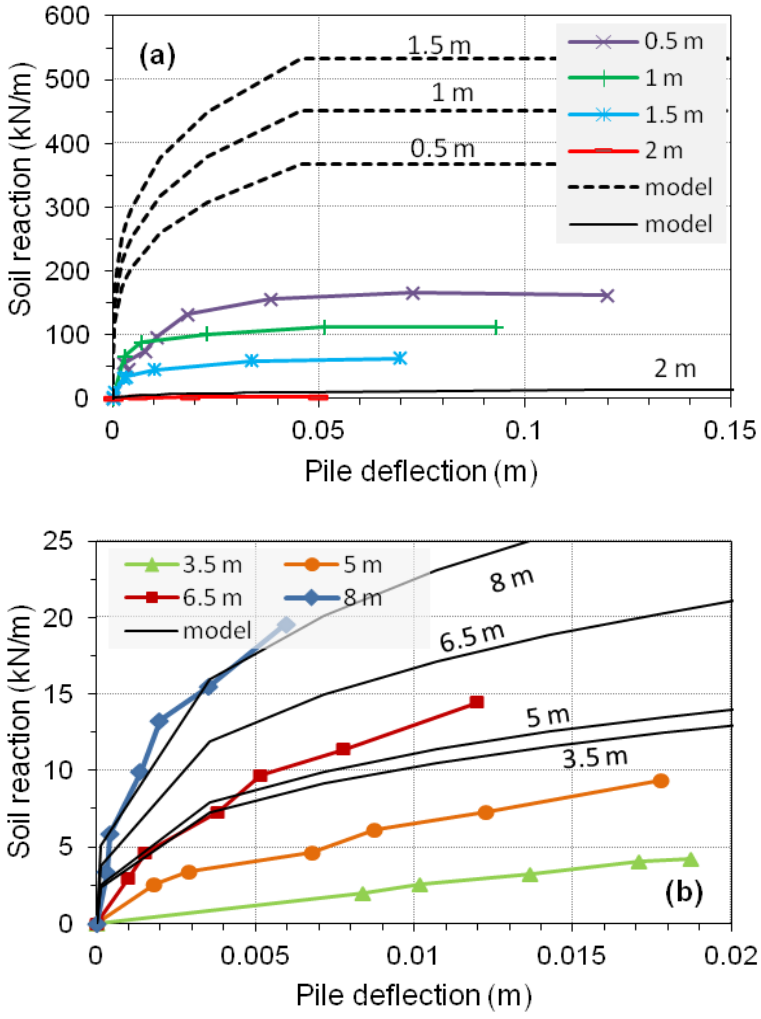

Figure 3.12 p-y curves derived from the experiment and the conventional models-Pile 6DEF
(a) in improved clay (b) in soft clay (depth of improvement=1.71 m)
(Broken lines represent the conventional model for stiff clay, and solid black lines represent the conventional model for soft clay.)

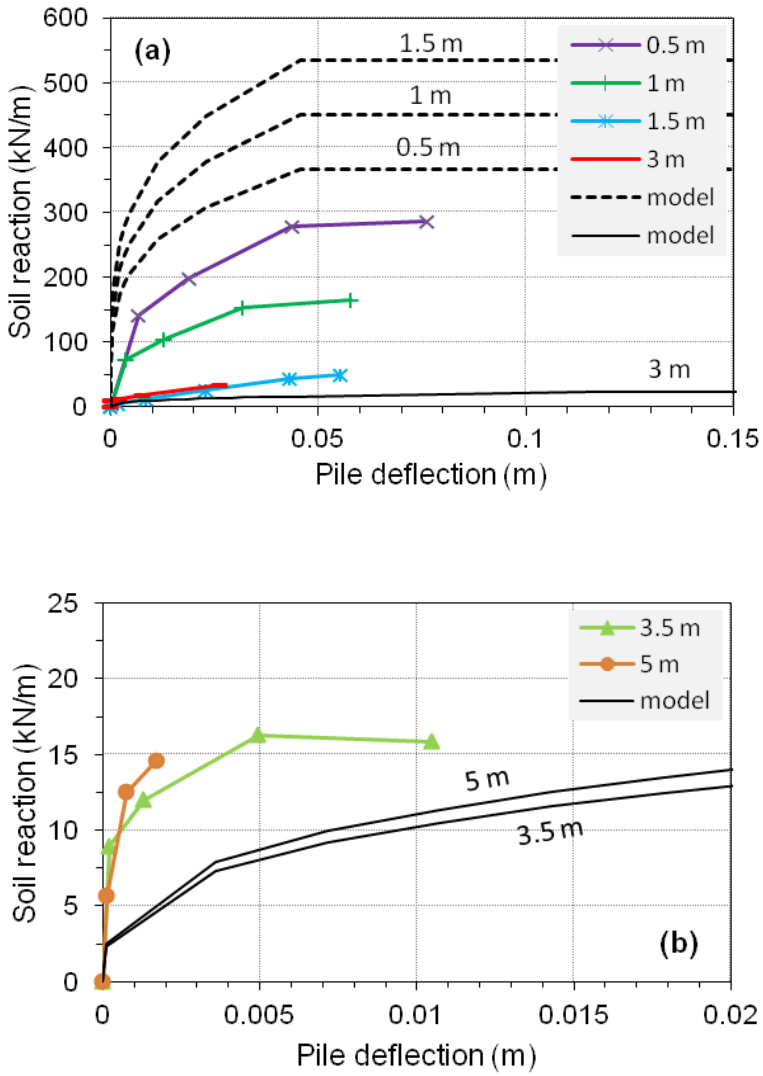

Figure 3.13 p-y curves derived from the experiment and the conventional models- Pile 9DKL
(a) in improved clay (b) in soft clay (depth of improvement=2.57 m (Broken lines represent the conventional model for stiff clay, and solid black lines represent the conventional model for soft clay.)

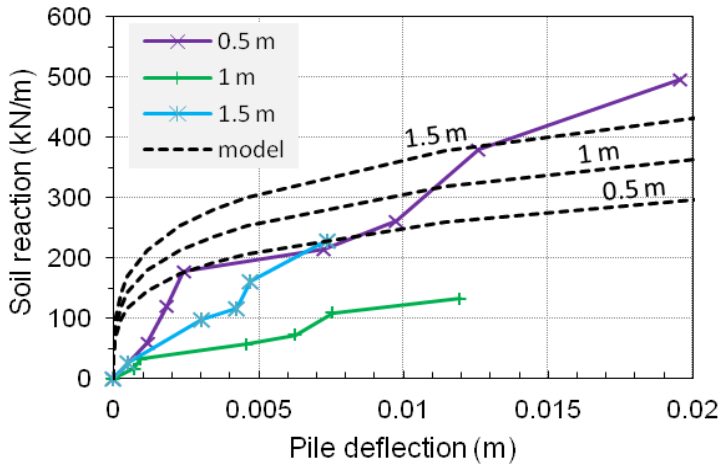

Figure 3.14 p-y curves derived from the experiment and the conventional models- Pile 12DMN
(Broken lines represent the conventional model for stiff clay.)

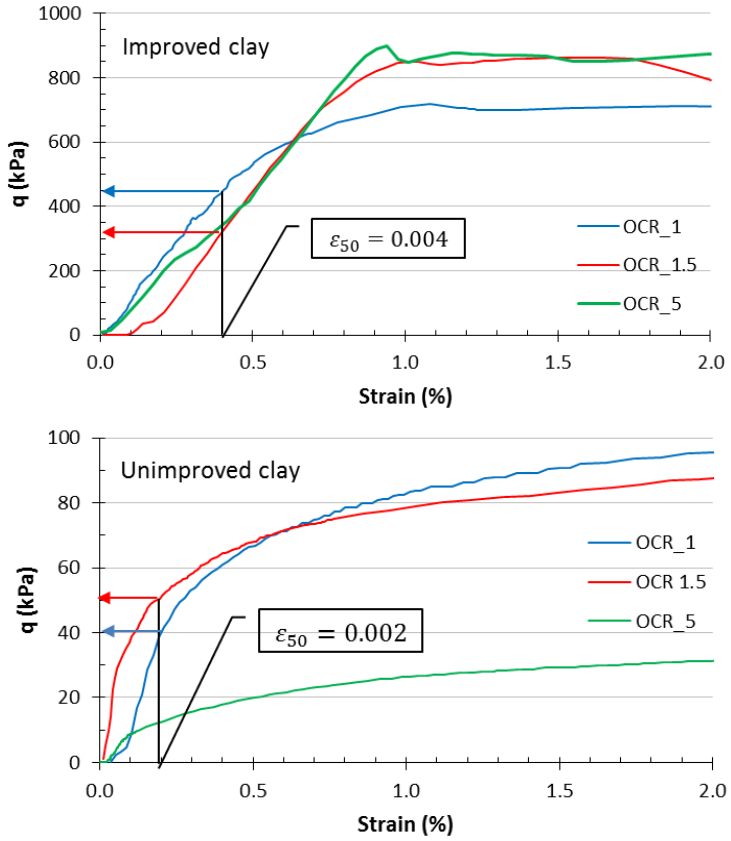

Figure 3.15 Results of the triaxial tests on unimproved and the improved soft clay (Thompson, 2011)

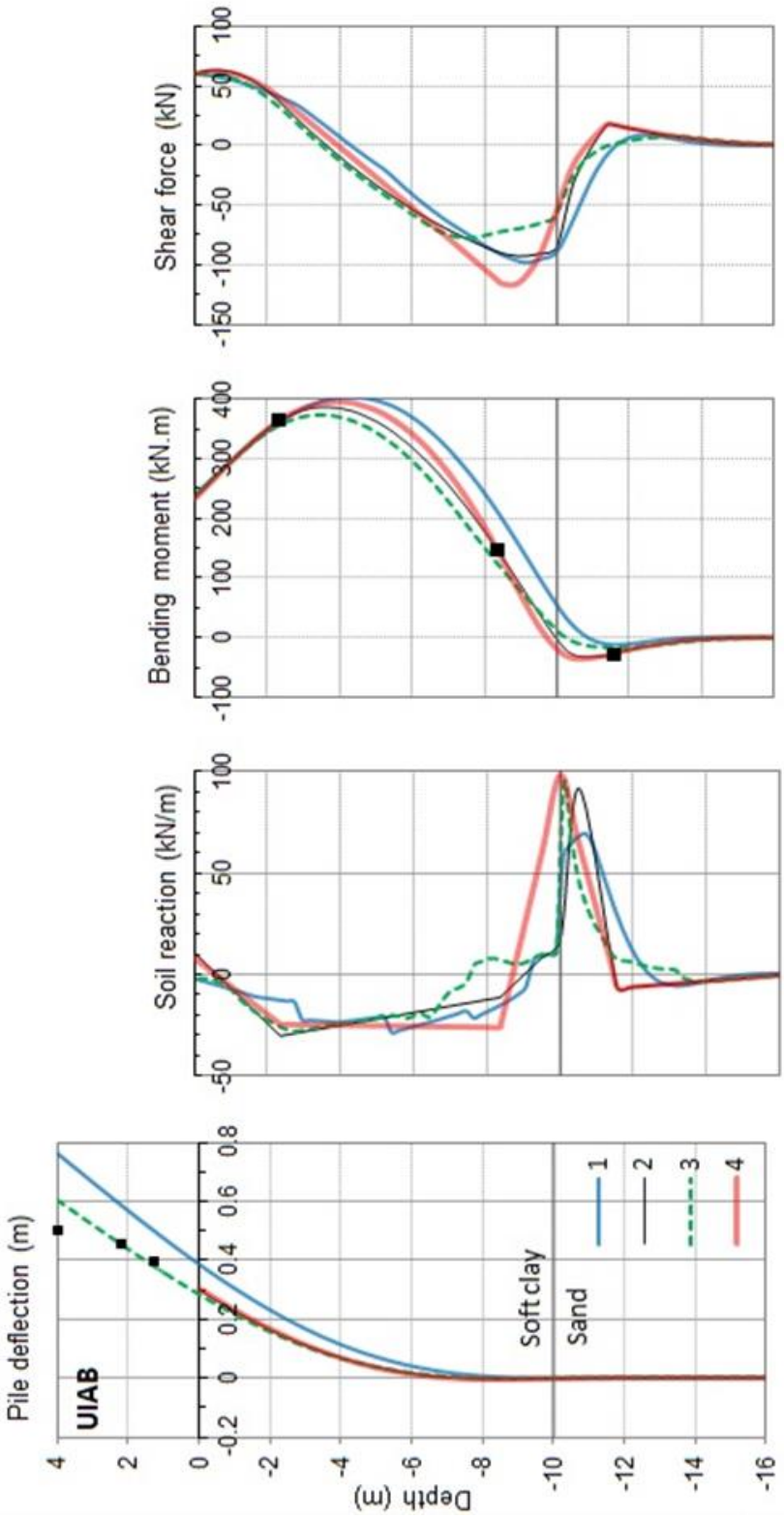

Figure 3.16 Distribution of pile deflection, bending moment, shear force, and soil reaction induced by lateral force=60kN on pile UIAB

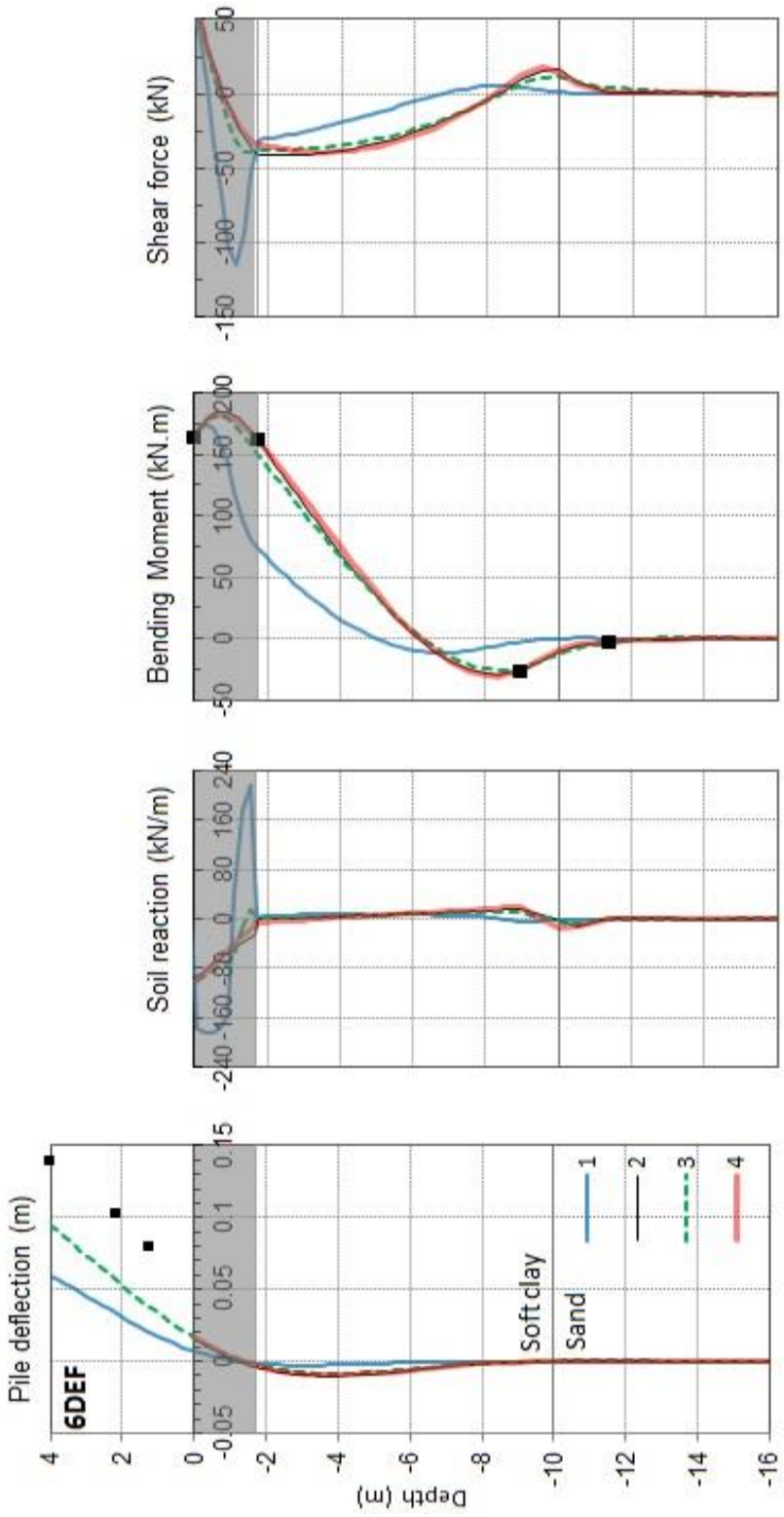

Figure 3.17 Distribution of pile deflection, bending moment, shear force, and soil reaction induced by lateral force=60kN on pile 6DEF

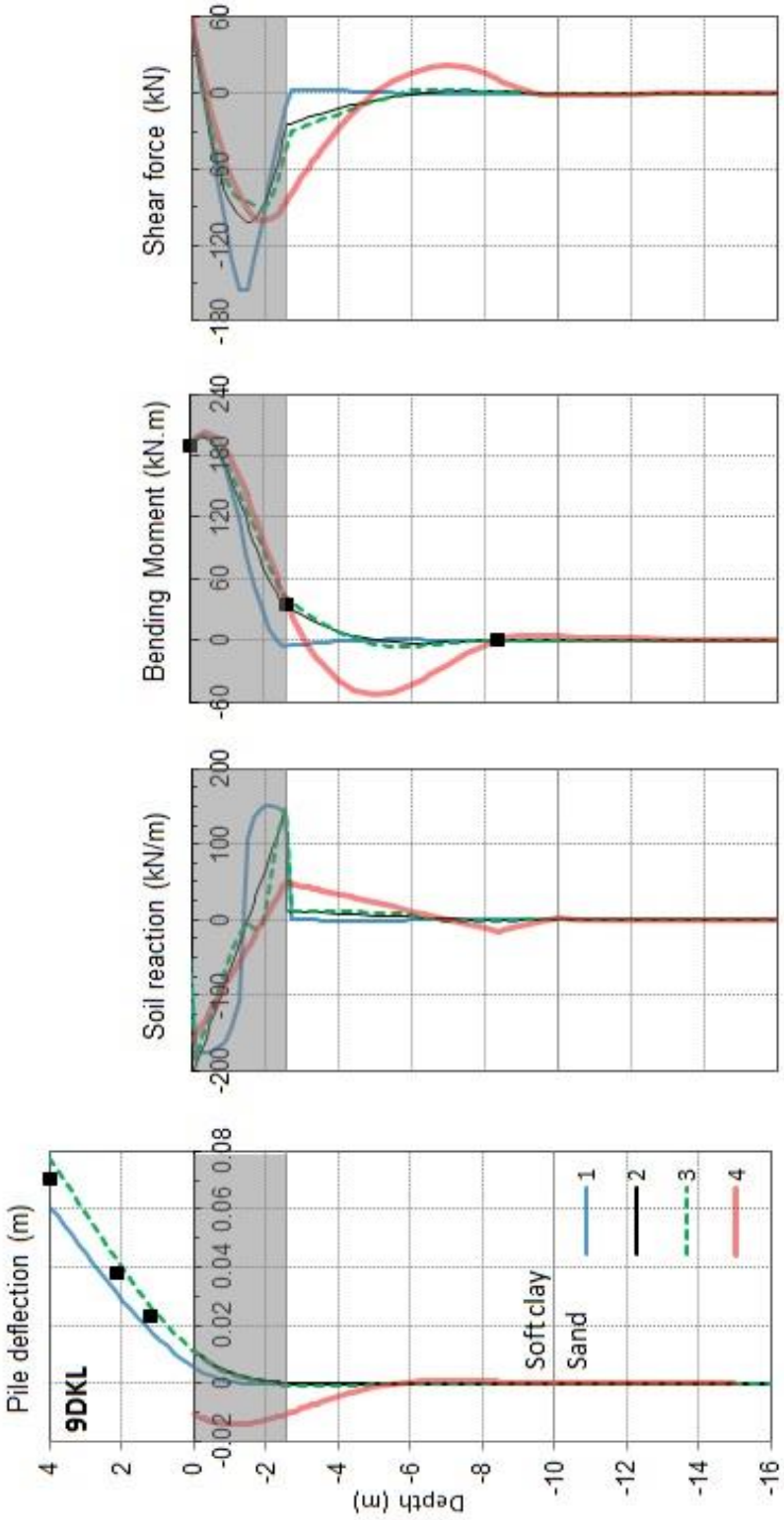

Figure 3.18 Distribution of pile deflection, bending moment, shear force, and soil reaction induced by lateral force=60kN on pile 9DKL

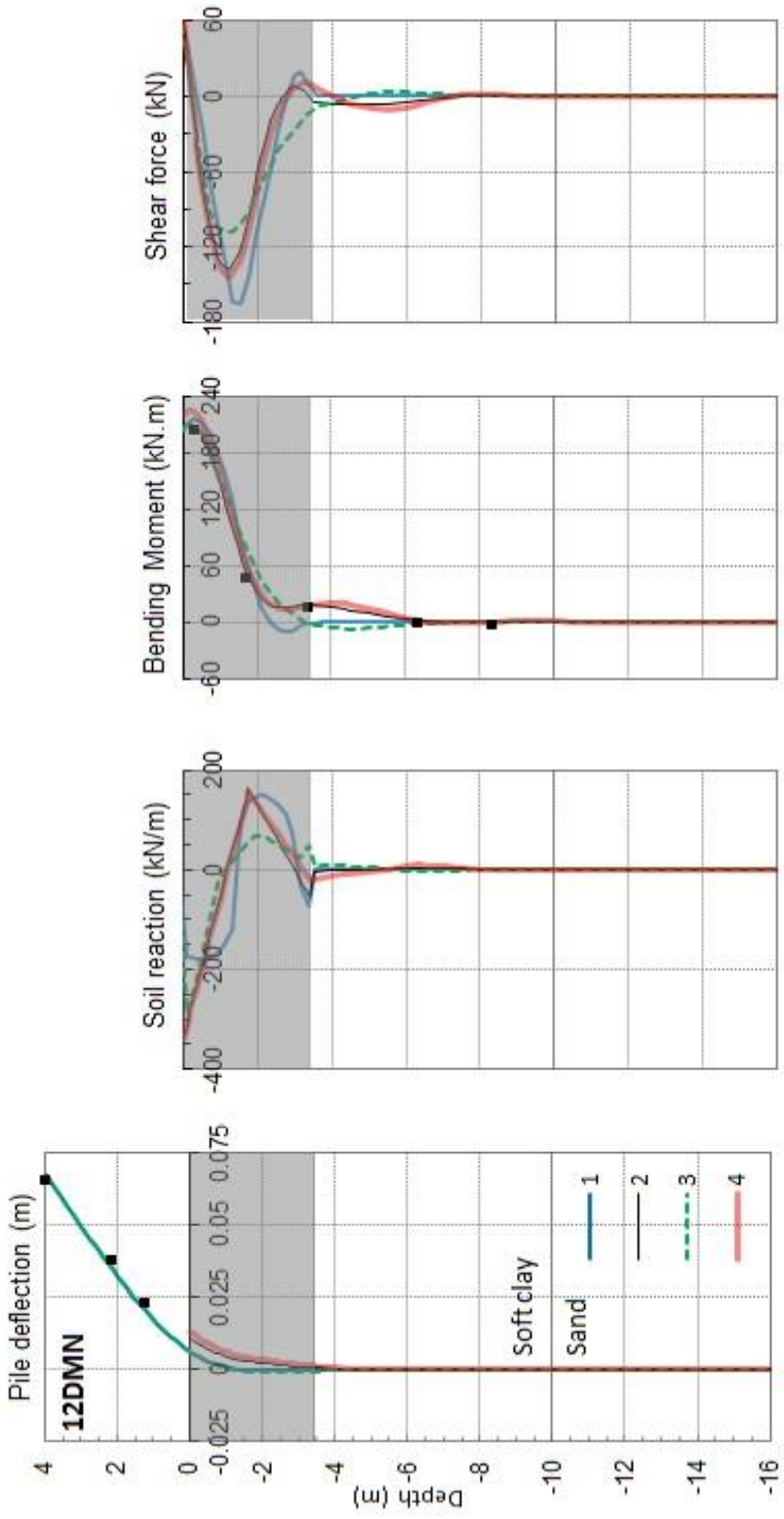

Figure 3.19 Distribution of pile deflection, bending moment, shear force, and soil reaction induced by lateral force=60kN on pile 12DMN

CHAPTER 4: OBSERVATIONS AND INTERPRETATION OF SEISMIC TESTS RESULTS

The measured data from the seismic testing of piles in unimproved and improved soft clay are discussed in this chapter. Also included in this chapter are an interpretation of the raw data and the back-calculated and derived quantities. The observations provide further insight into the load transfer mechanism between pile foundations and the improved ground.

4.1 Model container effects

The influence of the model container on the motion of the soil, particularly the motion of the surface layers, is an important consideration in centrifuge modeling. The container effects and the level of coherency of motion across the soil model and the container were evaluated by comparing the acceleration time histories recorded on the five rings of the container and the soil close to the south and north walls of the container. The rings shown in Figure 2.2 are stacked up in such a way that Ring 1 and Ring 5 are, respectively, the lowest and the highest ones above the baseplate. The container and the soil had similar responses to the applied excitations, as shown in Figure 4.1 for the third event, except for clay layer 4, where the maximum acceleration of the soft clay was three to four times smaller than that of the container at that level. In addition, at the surface, the soil motion had a lower frequency content compared to the container. Reduction in accelerations in clay layer 4 is likely due to softening of this layer during the strong third event. The acceleration response of A13 close to the shear rods on the north side showed several spikes that are likely due to the sand and soft clay boundary effects and the effects of the shear rods.

4.2 Top masses accelerations

The peak superstructure acceleration has been employed to estimate inertial loads imposed on pile heads in static-seismic/pseudo-static design analysis (Abghari and Chai, 1995; Liyanapathirana and Polous, 2005; Tabesh ans Poulos, 2001). Seismic masses (also called top masses) simulated the inertial effects of superstructures on the centrifuge model piles. Acceleration time-histories measured on the seismic masses during the three shaking events are shown in Figures 4.2 through 4.4. During Events 1 and 2 (Figure 2.15), the improvement around 9DIJ and 12DMN reduced the maxima of the top mass accelerations compared to the unimproved case. Conversely, the acceleration of the top mass mounted on 6DEF was amplified. Possible reasons for this unexpected behavior will be explained in Chapter 5 utilizing modal analysis methods. For the third shaking event, the maximum acceleration of top mass on UIAB, reached at 6 seconds, was reduced in all of the improved piles, but for pile 12DMN, significant amplification with respect to the unimproved pile was apparent at 10 to 12 seconds. Moreover, the accelerations of the top masses on piles 12DMN and 9DIJ had higher frequency content than the piles 6DEF and UIAB. The maximum accelerations measured on the seismic masses during the three events are compared in Figure 4.5, which shows that the efficiency of the ground improvement becomes more pronounced as the shaking event intensity increases. Various causes might have contributed to this behavior. Softening of the top clay layers could be the most likely reason. Another reason is believed to be the frequency content of the input motion and the natural frequencies of the piles; this will be explored in detail in Chapter 5. At this point, with regard to maximum accelerations, pile 9DIJ seems to have shown overall the best performance.

4.3 Pile deflections measured by displacement transducers

The lateral deflection of the free length of the piles outside of the soil was measured by one displacement transducer. Because the transducers were supported by a reaction beam clamped to the uppermost ring of the container, the values recorded by these sensors represent the relative displacement between the piles and the last ring of the container (as shown in the photograph in Figure 4.6).

Figures 4.7 through 4.9 compare the lateral deflection of the piles already subjected to pseudo-static loads with their counterparts saved for the seismic load tests. In these figures, DSS stands for the distance of the sensors from the soil surface. Notably larger displacements were recorded on the tested piles for the first and second events. However, in the third event, close displacement behavior was observed for the two groups of piles. This is likely due to the reason that during the stronger third event undisturbed soil was engaged by all the piles. In the first and second events, the largest displacement was recorded on 6DEF (Figure 4.10), whereas the second largest displacement was produced by UIAB. In the third event, the smallest displacements were recorded on piles 9DIJ and 12DMN. Although the transducer measurements for 6DEF and 9DIJ look the same, 9DIJ's was located at a higher elevation than 6DEF's. Therefore, by comparison, 9DIJ reduced the lateral deflection. The data acquired from the displacement transducers confirmed that improvement zones with depths of 9D and 12D can effectively reduce the pile displacements.

Pile displacements above the soil surface also can be obtained from the measured acceleration of the top masses. After the base acceleration was subtracted from the top masses absolute accelerations shown in Figures 4.2 through 4.4, the relative accelerations

were double-integrated and drift-corrected using fourth-order band-pass Butterworth filters with cut-off frequencies in the range of approximately 0.3-8 Hz to obtain the displacement histories shown in Figures 4.11 through 4.13. Double integration gives only the dynamic component of the displacement. Permanent displacement is inherent in the low-frequency part of the acceleration signal, which was filtered out due to noise corruption. The acceleration-based displacement values shown in Figures 4.11 through 4.13 represent the pile displacement with respect to the container base. To correct the displacements recorded by LPs attached to the pile tops to compensate for the motion of Ring 5, the relative displacement between the ring and the container base was calculated using the recorded accelerations of the ring and the base. Then, the derived displacements were added to the transducers' measurements. In these figures, y(0) is the pile displacement at the soil surface which was be back-calculated from the bending moment measurements as discussed in Section 4.6.

Because the accelerometers were located at higher elevations than the displacement transducers (as can be seen in the photograph in Figure 4.6), it was expected that the acceleration records would indicate larger displacements. However, the displacement derived from double integration of the filtered acceleration records was consistently smaller than the one derived from the LPs. It is to be noted that the acceleration-derived displacement contained only the transient component of the motion since the permanent component was filtered out. This complicates the interpretation of the derived displacements. Nevertheless, the displacements obtained from two different sensors compared reasonably well in terms of following the same trends as shown in Figures 4.11 through 4.13.

The derived displacements from LPs and top mass accelerometers again highlighted the poor performance of 6DEF in Events 1 and 2 and UIAB in Event 3 in reducing the lateral displacements.

It should be noted that, during the third event, the pile head displacements did not exceed the largest displacement experienced by the piles in pseudo-static loads except in pile 12DMN. As mentioned earlier in Section 3.3, the improved and unimproved piles 6DEF, 9DKL, 12DMN, and UIAB experienced 0.606 m, 0.632 m, 0.189 m, and 0.594 m deflection at the pile tops, 3.94 m above the soil surface, in response to maximum applied loads of 143 kN, 188 kN, 120 kN, and 63 kN, respectively. The maximum deflection for pile 12DMN derived from LP6 (slightly below the pile head) was 0.4 m which was almost twice the maximum pseudo-static displacement.

The maximum inertial loads exerted by the top masses on piles in Event 3 (the largest shaking event) were 3.0 kN, 2.2 kN, 3.2 kN, and 4.3 kN, respectively, which were much smaller than the pseudo-static loads. This confirms the dominance of kinematic contributions for these piles in generating large top displacements during seismic shaking.

4.4 Bending moment measurements

Due to a malfunction in the data acquisition system, no data were recorded from the strain gages on piles UIAB, 6DEF, and 9DIJ in the first and the second shaking events. Figures 4.14 and 4.15 show the time-histories of bending moments derived from the strain gages attached to pile 12DMN in the first two events. The maximum bending moment in the first event was observed at a depth of 3.46 m within the improved zone, whereas in the second event, the maximum value was pushed down deeper to a layer within the soft clay at a depth of 8.38 m, close to the interface of clay and sand. In the third event, the

maximum moment occurred at a depth of 3.46 m in 12DMN and at a depth of 8.35 m in 6DEF and UIAB, while all happened around 7 seconds (Figures 4.16 through 4.18). In 12DMN and 6DEF the bending moments at 0.34 m below the soil surface and 2.15 m above the soil surface contained higher frequencies.

4.5 Dynamic BNWF

The BNWF concept was extended to seismic problems as the decoupled analysis of near-field soil-structure interaction response and free-field response. Two important features of seismic response are the kinematic interaction between the pile and the soil, and the inertial interaction consisting of the transferred superstructure inertial forces to the pile foundations. The presence of stiff foundation within the soil causes the foundation motions to deviate from the free-field motions. Scattering of seismic waves off of corners and asperities of the foundation can potentially contribute to such deviations. Therefore, the rigidity and size of the pile foundation as well as the spatial variation of earthquake ground motion are among the most influencing parameters. At a large distance from the foundations, soils are less affected by the structures, and the behavior of the soil can efficiently represent the soil response to one-dimensional shear wave propagation. The ground motion time histories along the depth of the free-field soil profile are applied to the support of the interaction springs/elements (Figure 4.19).

In this study, the vertical array of accelerometers at the center of the container (DH3 in Figure 2.11) included the largest number of sensors and was at a large distance from the model boundaries. For these reasons, DH3 was employed to obtain the free-field soil displacement profile. Since DH3 lacked the acceleration data for the third clay layer, the data from A20 in the nearby array DH2 was employed to increase the resolution of

the free-field soil displacement profile. By subtracting the base motion acceleration from the recorded accelerations at the locations of the accelerometers in soil, relative accelerations of free-field motion with respect to the base were obtained. Then, the soil displacements with respect to the base of the model were calculated by double integration of the derived relative acceleration time-histories. As shown in Figure 2.11, the sensor numbers and the depths of these accelerometers are: A2, z=16.03 m; A6, z=12.04 m; A11, z=8.74 m; A16, z=6.34 m; A20, z=3.79 m; A26, z=1.24 m; and A32, z=0.2 m. In Figures 4.20 through 4.24, the free-field soil displacements (curves drawn with solid lines) along with the piles displacements (curves drawn with broken lines), which will be discussed in Section 4.6 are plotted. The maximum displacement at the soil surface was 2 cm, 4 cm, and 25 cm in the first, second, and the third events, respectively.

4.6 Back-calculation of soil reactions and pile deflections

The methodology described in Chapter 3, Section 3.2, was adopted to curve-fit the bending moment data measured during the base shaking events. The upper boundary condition, the shear force in the pile at the soil surface level, was set to the inertial loading of the top mass: the product of the top mass and its absolute acceleration. The boundary conditions at the pile tip were defined as zero for bending moment, shear force, soil reaction, and pile deflection with respect to the soil. However, it was assumed that the sand around the pile tip 1.6 m above the base followed the same motion as the base.

In Dynamic BNWF, the soil exerts resisting forces against lateral pile movement, applied through distributed interaction elements, combinations of springs and dashpots, as will be explained in Chapter 6. Dynamic equilibrium of a pile resting against a uniform

distribution of the interaction elements can be expressed by a fourth-order partial differential equation as

$$EI\frac{\partial^4 y_p(z,t)}{\partial z^4} + m\frac{\partial^2 y_p(z,t)}{\partial t^2} + F_e\left(y_p - y_s\right) = 0 \quad (4.1)$$

Here, y_p is the transverse deflection of the pile and y_s is the soil displacement with respect to the base. F_e is the soil reaction per unit length of the pile which is a function of pile-soil relative displacement. $EI = 3.54\times10^4$ (kN.m^2) is the flexural stiffness of the pile, m is the mass per unit length of the pile, and z denotes the depth measured from the soil surface. Double integration of bending moment gives the displacement of the pile with respect to the pile tip. As can be inferred from Eq. 4.1, the first term can be obtained by multiple differentiation of $y_p(z)$ derived from curve-fitting of the bending moment, called p in Chapter 3. However, in using the same methodology for curve fitting, it should be noted that the derived p for seismic loading is in equilibrium with inertial load of the pile itself and the forces in the interaction elements. In this study, it was assumed that the effects of pile masses were insignificant, and therefore the second term of Eq. 4.1 was neglected.

The derived pile deflection at the soil surface $y(0)$ was compared with the measured deflections by LPs in Figures 4.11, 4.12, and 4.13. As the results show, the estimated pile deflections at the soil surface followed the trends in LPs measurements. The pile deflection at the soil surface derived for 12DMN in the third event (20 cm) was half that of piles 6DEF and UIAB (40 cm). The soil improvement apparently reduced the pile deflection at the soil surface, with the lowest deflection belonging to pile 12DMN.

It was expected that pile deflections at the soil surface would be smaller than the LP's measurements; however, in the first and second events, the deflection of pile

12DMN at the soil surface exceeded the LP's measurements. It is not clear why the estimated pile deflections were larger. In the third event, the difference between the estimated pile deflection at the soil surface and the LPs' measurements increased as the improved zone became larger. The data acquired from two pairs of embedded strain gages on 9DIJ had a very small signal-to-noise ratio. As a result of the missing measurements, no estimation for y(0) could be provided for pile 9DIJ. The back-calculated pile deflection at the soil surface, y(0), for piles UIAB and 6DEF were the first and second largest values, respectively in Event 3 which agreed with the results of Figure 4.5.

Free-field soil was found to move in the same direction as the piles down to depth 6.34 m. However, at the depth of 8.74 close to the interface of the soft clay and sand layers they became out of phase (Figures 4.20 through 4.24). Time histories of soil reactions and pile deflections shown in Figures 4.25 to 4.27 are in phase at some depths and out of phase at some other depths.

4.7 Distributions

Distributions of bending moment, shear force, soil reaction, and the displacement profile of the free-field and the piles are plotted in Figures 4.28 through 4.33 for the timing of peaks in the positive and negative peak base accelerations (T_b (P)=9.32 s; T_b (N)=9.14 s), in the free-field displacement (T_f=6.97 s), and in the inertial forces induced by the top masses (T_m (UIAB)=5.97 s; T_m (6DEF)=9.55 s; T_m (12DMN)=10.69 s). In pseudo-static foundation design approach (Abghari and Chai, 1995; Tabesh and Poulos, 2001), it is important to estimate the timing of the maximum inertial forces transmitted from the superstructure onto the head of the pile and the timing of the peak kinematic loads induced by the ground motions.

At time T_b (N)=9.14 s (Figure 4.28) and at time T_b (P)=9.32 s (Figure 4.29) the soil and pile displacements are 180 degrees out of phase. Disagreements between the displacements of the piles and the soil profile is a sign for the kinematic interaction. Disagreement between the pile displacements at the soil surface and LP measurements was observed at T_b (N)=9.14 s (Figure 4.28), at T_b (P)=9.32 s (Figure 4.29), and at T_m (6DEF)=9.55 s (Figure 4.32).

Maxima of bending moments and shear forces appear to occur at different locations. The maximum soil reaction occurred at the interface of the improved and soft clay at T_f =6.97 s, T_m (UIAB)=5.97 s, and T_m (12DMN)=10.69 s and , whereas it moved further down, close to the interface of the soft clay and sand, at T_b (P)=9.32 s, T_b (N)=9.14 s, and T_m (6DEF)=9.55 s. Comparing the distributions associated with the static and seismic loadings revealed that the direction of the dynamic soil reaction is not necessarily compatible with the direction of the pile-soil relative displacement at a given level.

The envelopes of the maximum pile deflection, bending moment, shear force, and soil pressure for Event 3 are shown in Figure 4.34. As seen in this figure, the improved clay effectively restrained the motion of pile 12DMN for the positive deflections, whereas pile 6DEF followed the same deflection as the unimproved pile UIAB. The bending moment envelop for pile UIAB showed one broad peak approximately at the middle of the soft clay. The improved pile 6DEF's peak bending moment occurred about 2 m above the clay-sand interface. Pile 12DMN showed an additional larger peak at the interface of improved and soft clay, which is where the pile started to yield. The maximum of the shear force in pile UIAB appeared to be close to the soil surface and the clay-sand interface, whereas it moved to the middle of the improved zone for the improved piles

6DEF and 12DMN, although a second, smaller peak appeared in the middle of soft clay. The maxima of soil reaction occurred for the improved and unimproved piles at the interface of the improved and soft clay, and 2 m above and below the interface of clay and sand, respectively. Unlike in the static case, the clay-sand interface happened to be the location for some of the maxima. The active length of the piles also tended to increase beyond the static values. It is believed that in kinematic interaction dominated vibration, deeper parts of the piles were involved.

Nikolaou et al. (2001) observed that maximum kinematic bending moment occurs at the interface between two consecutive soil layers with considerable contrast in stiffness. The peak bending moment happens when the lateral ground displacements and the inertia loads are both large and act in the same direction, which is dependent on the natural period of the soil and structure. The timing of the peak bending moments in the piles which was around 7 s in Event 3 agreed with that of the free-field soil peak acceleration, T_f=6.97 s. This finding shows that the interaction between the soil and piles was controlled by the soil motion known as kinematic interaction. In this study, the seismic masses were not large enough to appreciably contribute in deforming the piles through inertial interaction. The dependency on the natural period of the soil and structure will be investigated in Chapter 5.

4.8 Seismic load transfer curves

Soil-structure interaction can be evaluated by back-calculating the p-y loops. Figure 4.35 illustrates the soil reaction vs. relative pile-soil displacement in Event 3 at the depths of free-field accelerometers for a time window starting at 5 seconds and ending at 15 seconds, containing the peaks of the base acceleration. Inside the improved soil, piles

6DEF and 12DMN showed S-shaped pinched hysteresis p-y loops at depths of 0.2 m and 1.24 m. The nearly flat part in the middle is an indication of pile-soil separation. The load-transfer curves for pile 12DMN showed more stiffness than pile 6DEF.

At a depth of 3.79 m in soft clay, load-transfer curves derived for 6DEF became very irregular. Oval-shaped loops were observed for 6DEF and 12DMN at deeper layers in soft clay, at depths of 6.34 m and 8.74 m. Significant softening behavior was observed on the curves for 6DEF at the depth of 6.34 m whereas the loops for 12DMN showed much stiffer behavior at the same depth. This behavior might be explained by the fact that the p-y springs cannot be considered as uncoupled elements, because the improved clay with the depth of 12D affected the load-transfer behavior of the underlying soft clay. A transition from oval-shaped loops in the soft clay to bilinear loops in the dense sand was observed in the loops at the depth of 12.04 m.

A comparison of the experimentally derived p-y curves in the improved soil from pseudo-static load tests on pile 6DEF shown by red lines in Figure 4.35 and the seismic p-y curves showed that the back-bone curves of the seismic loops were much softer reflecting significant material deterioration occurring in the shaking events. On the other hand, the conventional p-y curves for soft clay appeared to be a reasonable representative for the back-bone curves of the loops derived for 12DMN at the depth of 6.34 m and for 6DEF at the depth of 8.74 m. The conventional model for sand highly overestimated the stiffness. The discrepancy between the static and dynamic p-y curves was also observed by Brandenburg et al. (2005) and Rovithis et al. (2009), who obtained, respectively, softer and stiffer dynamic back-bone curves compared to the static curves.

4.9 Pore water pressure data interpretation

Generation and dissipation of excess PWP due to seismic loading affects the stiffness and strength of the soil. Here, the magnitude of the excess PWP is expressed as the ratio of excess PWP over the initial effective vertical stress $\acute{\sigma}_{v0}$; this is called the PWP ratio.

In the first and second events, PWP in the third clay layer close to the container walls (P9, P13) was 180 degree out of phase. That is, during the main excitation, one showed positive excess PWP while the other one showed a negative value (Figures 4.36 and 4.37). PWP records showed that the ratio in the surface clay layer close to the container's wall, P14 and P16 (Figure 2.12), was quite high in all three earthquake motions. In calculating $\acute{\sigma}_{v0}$ for the surface layer errors are likely due to small variations in the recorded depth of the transducers. The high PWP in the upper-most soft clay layer close to the wall could also be explained by the discrepancy between the accelerations of the soil and the container observed in Figure 4.1. Large acceleration spikes appearing on the acceleration-time history recorded by A13 (Figure 4.1) could be tracked by simultaneous drops in PWP in the vicinity of the wall (Figure 4.38).

Although the PWP showed a monotonic accumulation of pressure, with some transient drops and oscillations in sand layers (P1, P2, P4), the PWP in clay layers showed almost no accumulation) Excess pore pressure increased rapidly in sands over the first few cycles of the motion and leveled off at an excess PWP ratio of 0.6 and 0.8 (Figure 4.38) in the first and second sand layers, respectively, during the last event. The PWP dissipated at a slow rate after the main excitation. No liquefaction was induced in the sand layers, although the PWP ratio reached the maximum of 0.8. The cyclic component of the PWP time histories in soft clay was a feature distinguishing the PWP trends in clay from

those of sand. Continuous oscillation between the positive and negative values was observed.

It was revealed that the load-transfer curves reversal points in clay were correlated with the local peaks and drops in the PWP time histories. In addition, soil reaction and PWP followed a very similar trend though they were more in phase for 12DMN than for 6DEF and UIAB as depicted in Figure 4.39. Due to the similarity between the load-transfer curves of 6DEF and UIAB at the depth of 6.34 m only the curves for 6DEF are shown. The phase difference between the soil reaction and the PWP could be a possible reason for the softening behavior observed in the load-displacement loops of 6DEF and UIAB. On the other hand, as expected the maxima of PWP and the free-field soil displacement at this level happened almost at the same time (Figure 4.39).

4.10 Summary and conclusions

- The maximum values of static bending moment and soil reaction were concentrated within the improved zones, whereas distribution of these quantities along the pile during seismic loading showed that the peaks occurred at the interface of the improved and unimproved soil as well as within a region around the interface of the soft clay and dense sand.
- The experimentally derived p-y curves in the improved soil from static loading tests appeared to represent a stiffer behavior than those of the p-y traces in the seismic loading. However, the conventional model seemed to be able to represent the back-bone curves of the derived seismic loops in soft clay.

- The directions of estimated soil reaction along the piles was found to be incompatible with the corresponding estimated relative pile-soil displacement at the same depth.
- The influence of the improved zone on the behavior of the underlying soft clay layer and vice versa was detected, suggesting that the p-y springs close to soil layer interfaces functioned as coupled elements.
- The similar seismic performance of 9DIJ and 12DMN indicates that the full benefit of ground improvement may be realized in improvement zones with depths of 9D and 12D. Although it is possible for ground improvement around a pile to produce larger pile top accelerations and lateral displacements, as observed for 6DEF, they generally will be smaller in the improved soil-pile system.
- In the uppermost clay layer close to the container wall, the PWP ratio was quite high in all shaking events.
- The load-transfer curves' reversal points are correlated with the local peaks and drops in the PWP time histories.
- The accelerations of the top masses on piles 12DMN and 9DIJ had higher frequency content than the piles 6DEF and UIAB.
- The maximum moment occurred at a depth of 3.46 m in 12DMN and at a depth of 8.35 m in 6DEF and UIAB, while all happened at 7 seconds which agreed with the free-field soil peak acceleration time, T_f=6.97 s. This finding shows that the interaction between the soil and piles was controlled by the soil motion known as kinematic interaction. In this study, the seismic masses were not large enough to appreciably contribute in deforming the piles through inertial interaction.

- The bending moment envelop for pile UIAB showed one broad peak approximately at the middle of the soft clay. The improved pile 6DEF's peak bending moment occurred about 2 m above the clay-sand interface. Pile 12DMN showed an additional larger peak at the interface of improved and soft clay, which is where the pile started to yield.
- The maximum of the shear force in pile UIAB appeared to be close to the clay-sand interface, whereas it moved upward to the middle of the improved zone for the improved piles 6DEF and 12DMN, although a second, smaller peak appeared in the middle of soft clay.
- Inside the improved soil, piles 6DEF and 12DMN showed S-shaped pinched hysteresis p-y loops at depths of 0.2 m and 1.24 m. The nearly flat part in the middle was an indication of pile-soil separation.

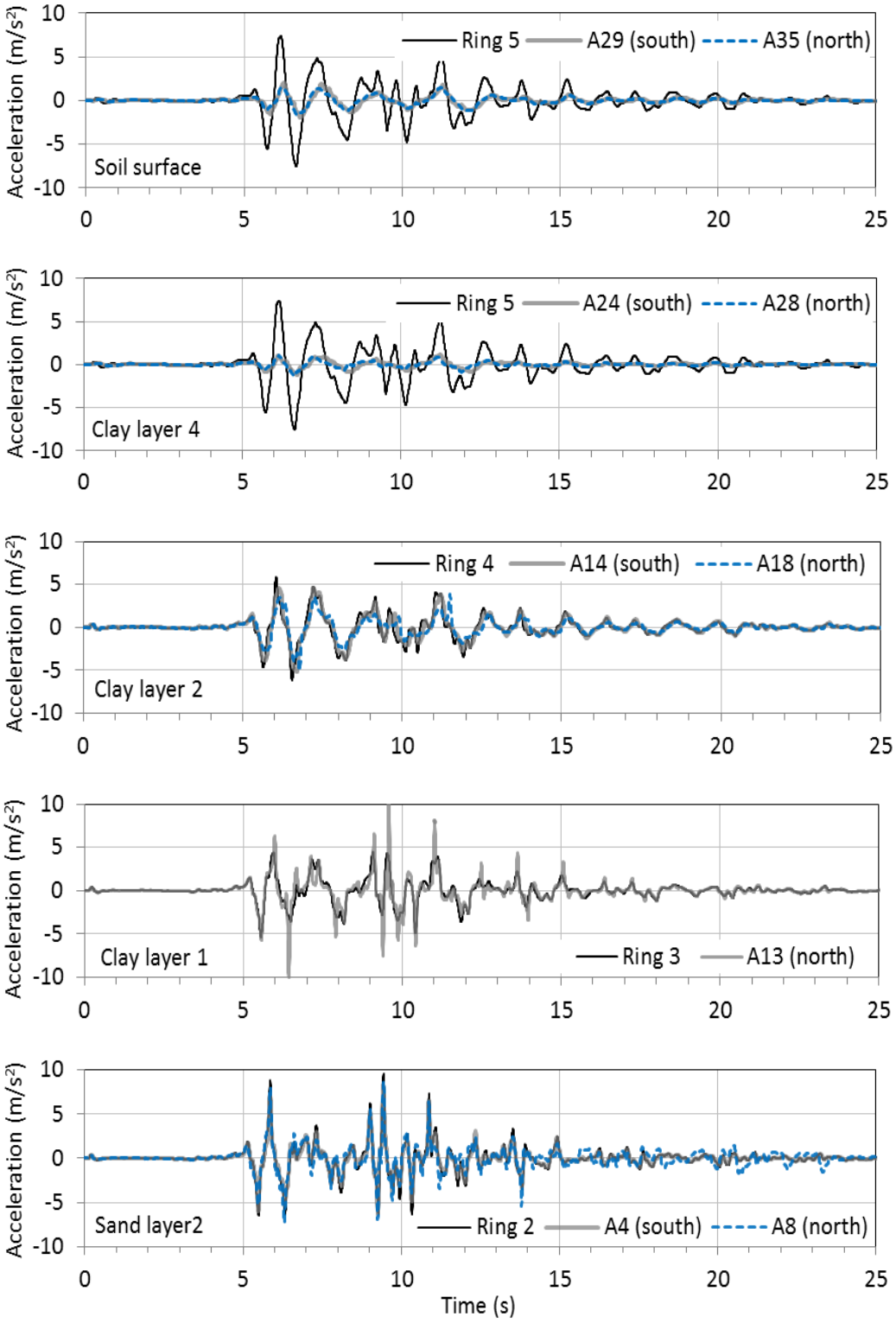

Figure 4.1 Absolute acceleration-time histories of the container rings and the soil close to the south and north walls in Event 3

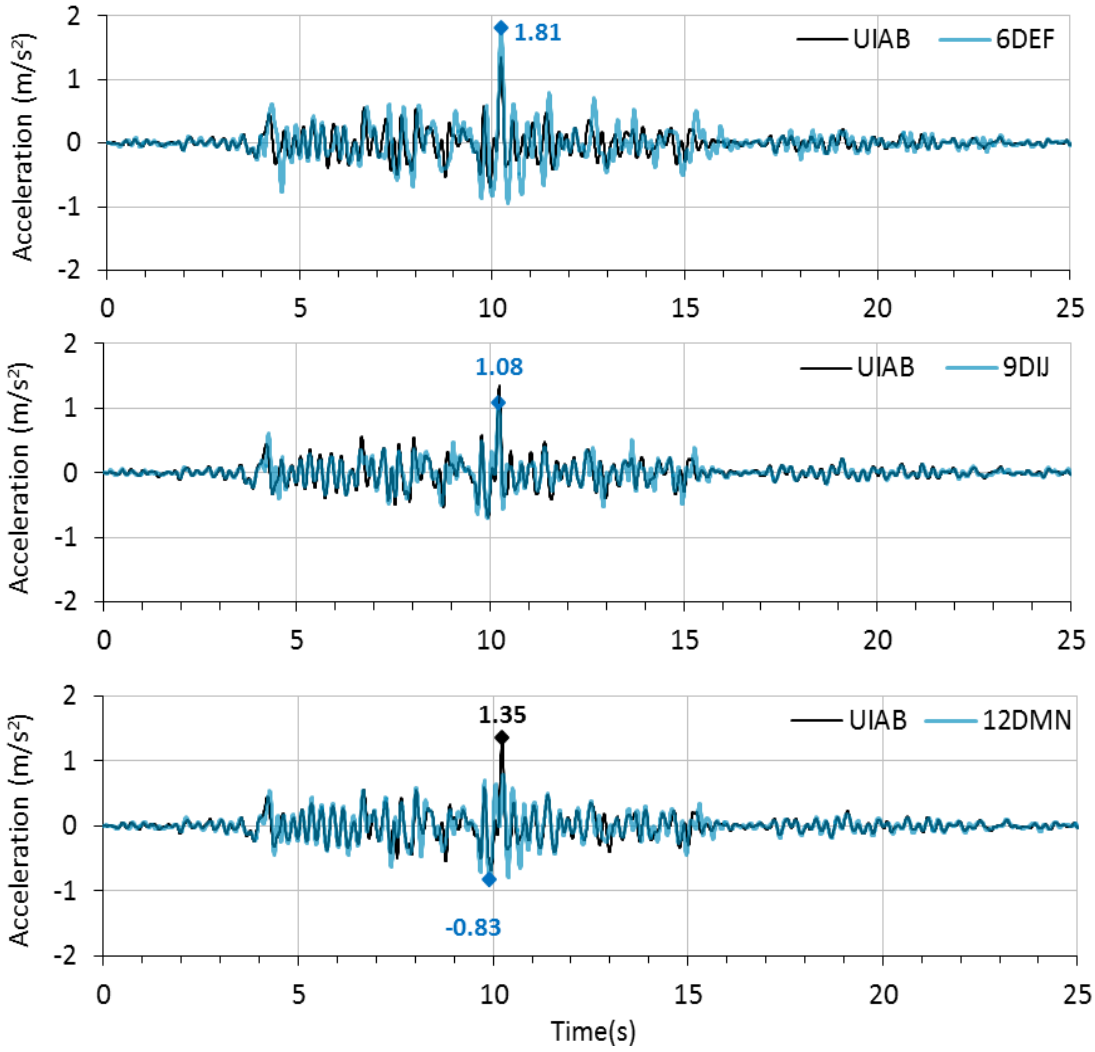

Figure 4.2 Acceleration time-histories of the seismic masses (Event 1)

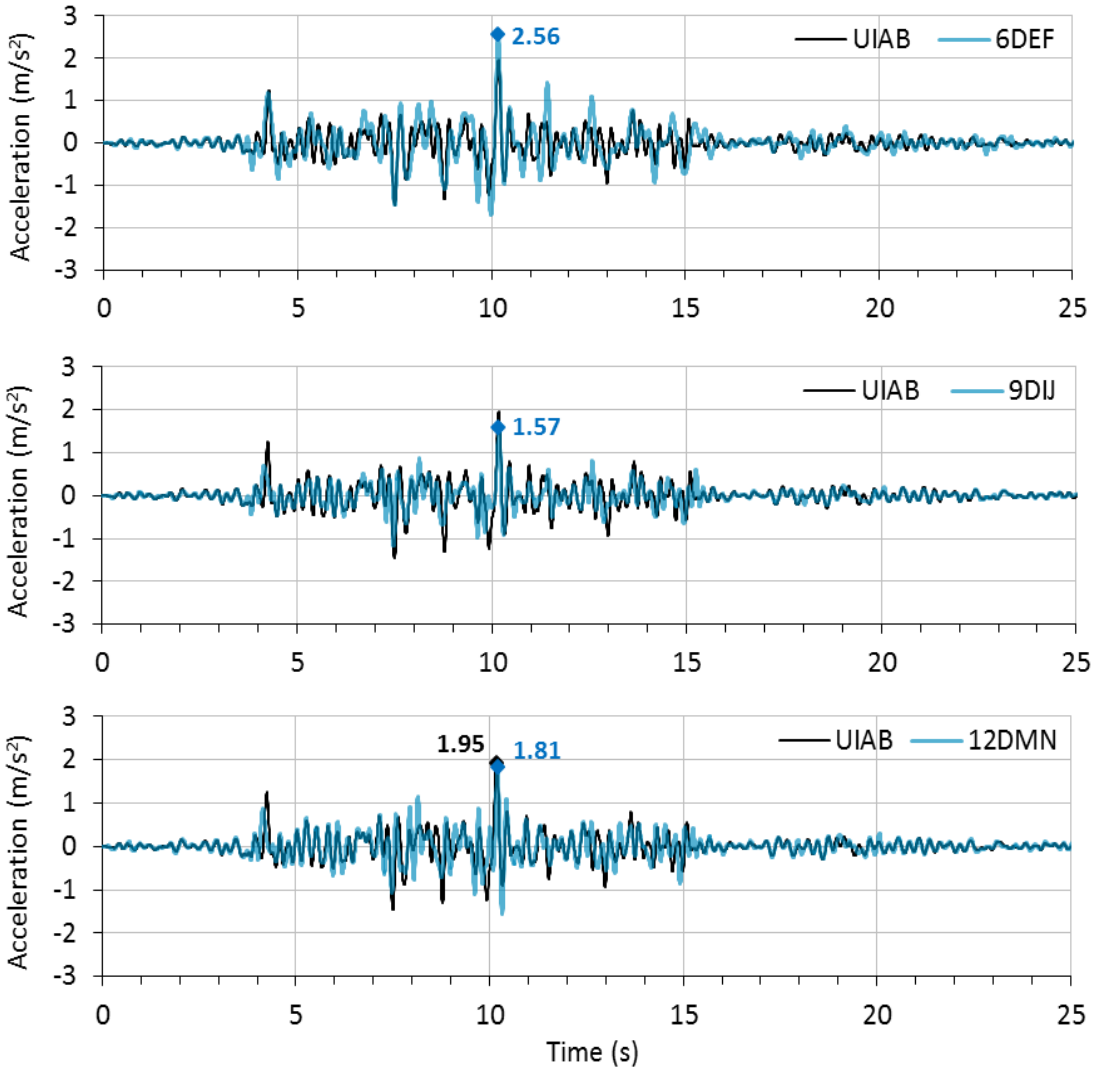

Figure 4.3 Acceleration time-histories of the seismic masses (Event 2)

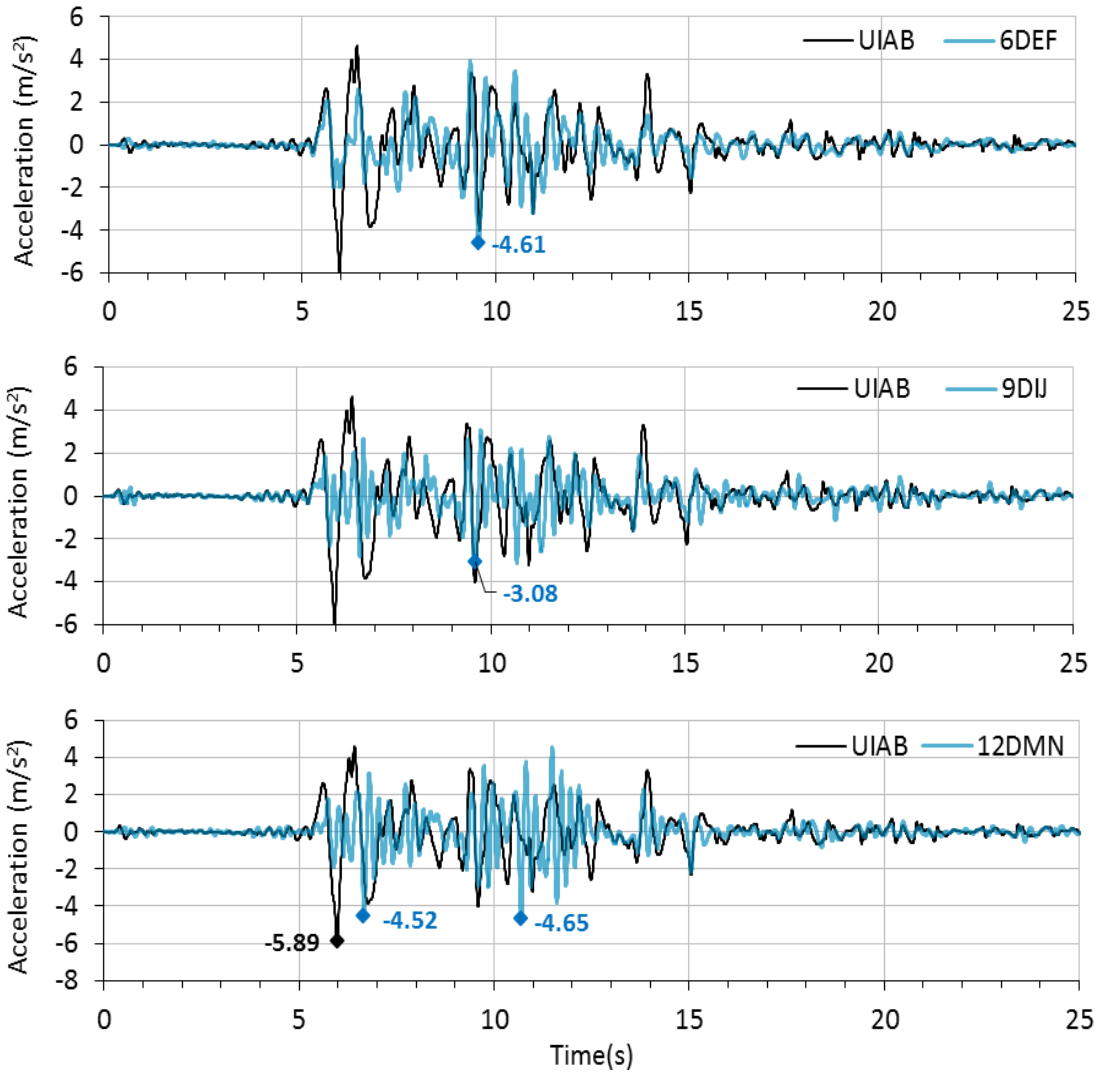

Figure 4.4 Acceleration time-histories of the seismic masses (Event 3)

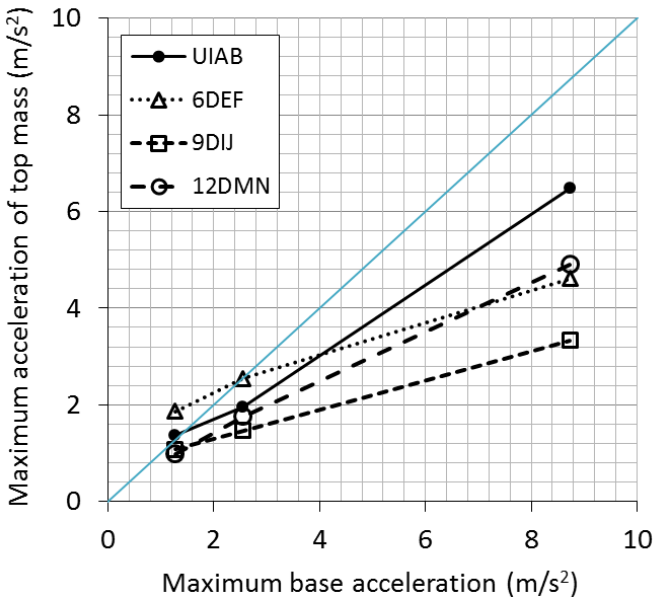

Figure 4.5 Maximum horizontal pile top accelerations in all shaking events

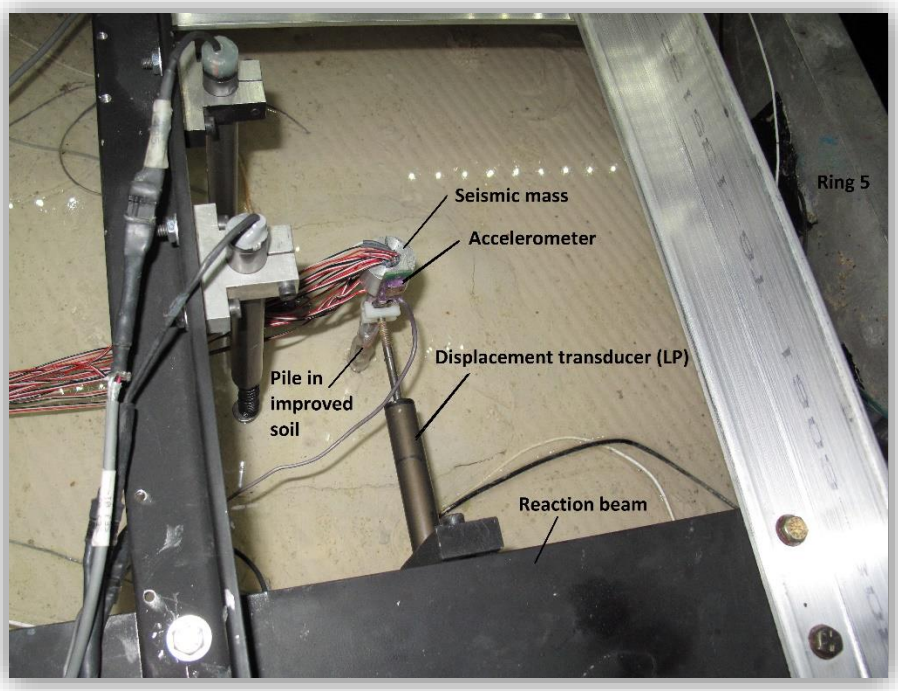

Figure 4.6 Displacement transducer setup in the seismic loading events

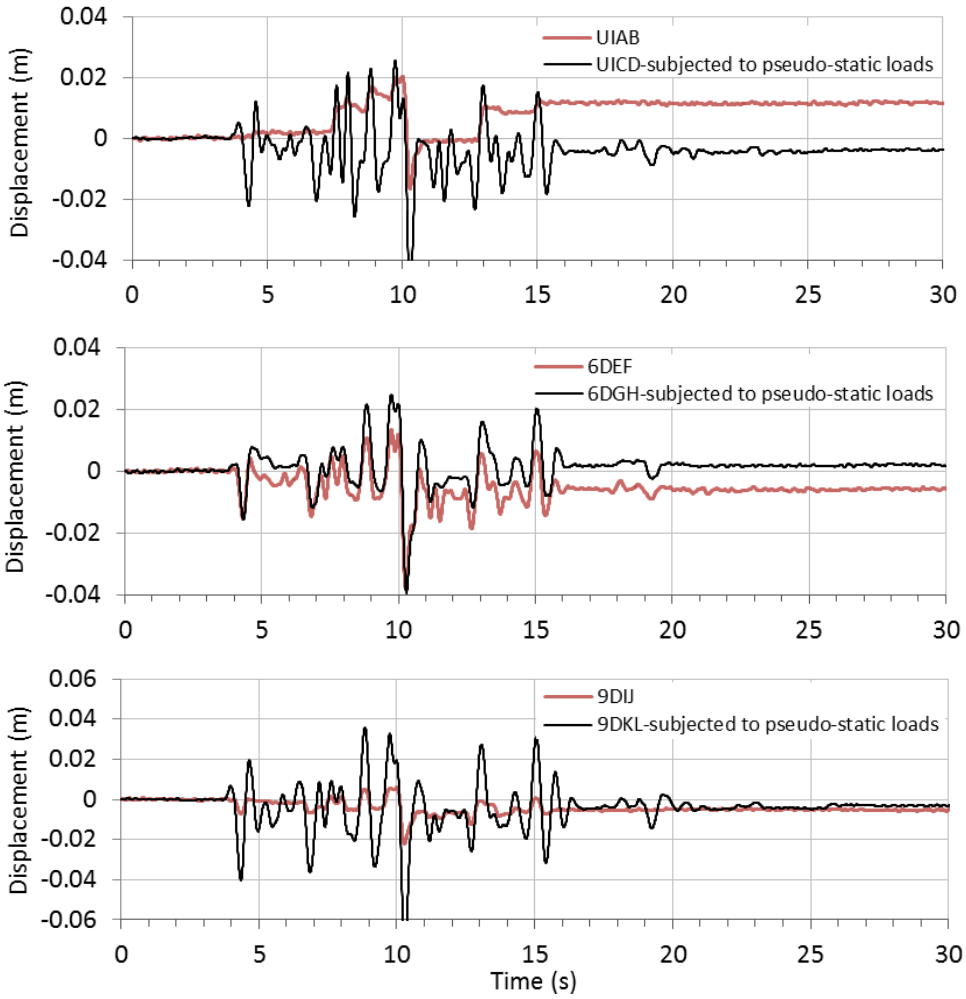

Figure 4.7 Comparison of seismic displacement-time histories (transducer readings) of piles tested in prior pseudo-static loading with those not subjected to prior loading-Event 1 (DSS=Distance from the Soil Surface)

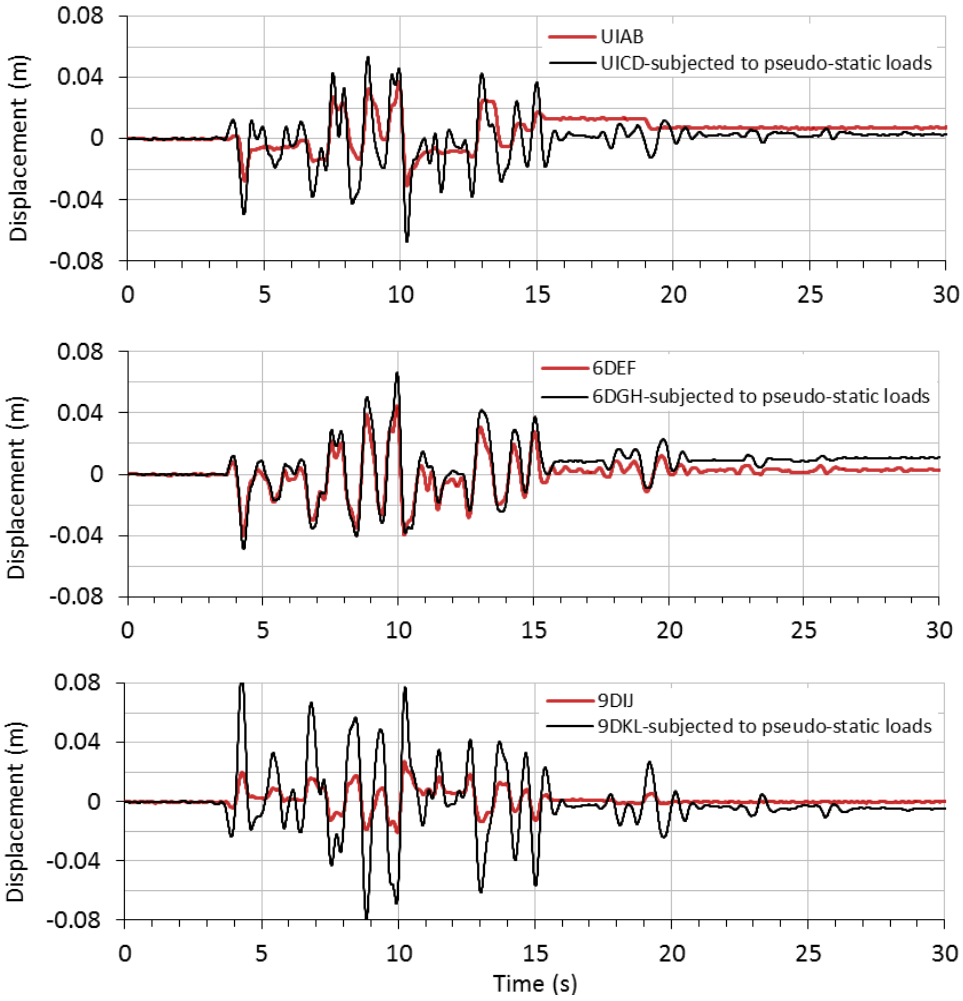

Figure 4.8 Comparison of seismic displacement-time histories (transducer readings) of piles tested in prior pseudo-static loading with those not subjected to prior loading-Event 2 (DSS=Distance from the Soil Surface)

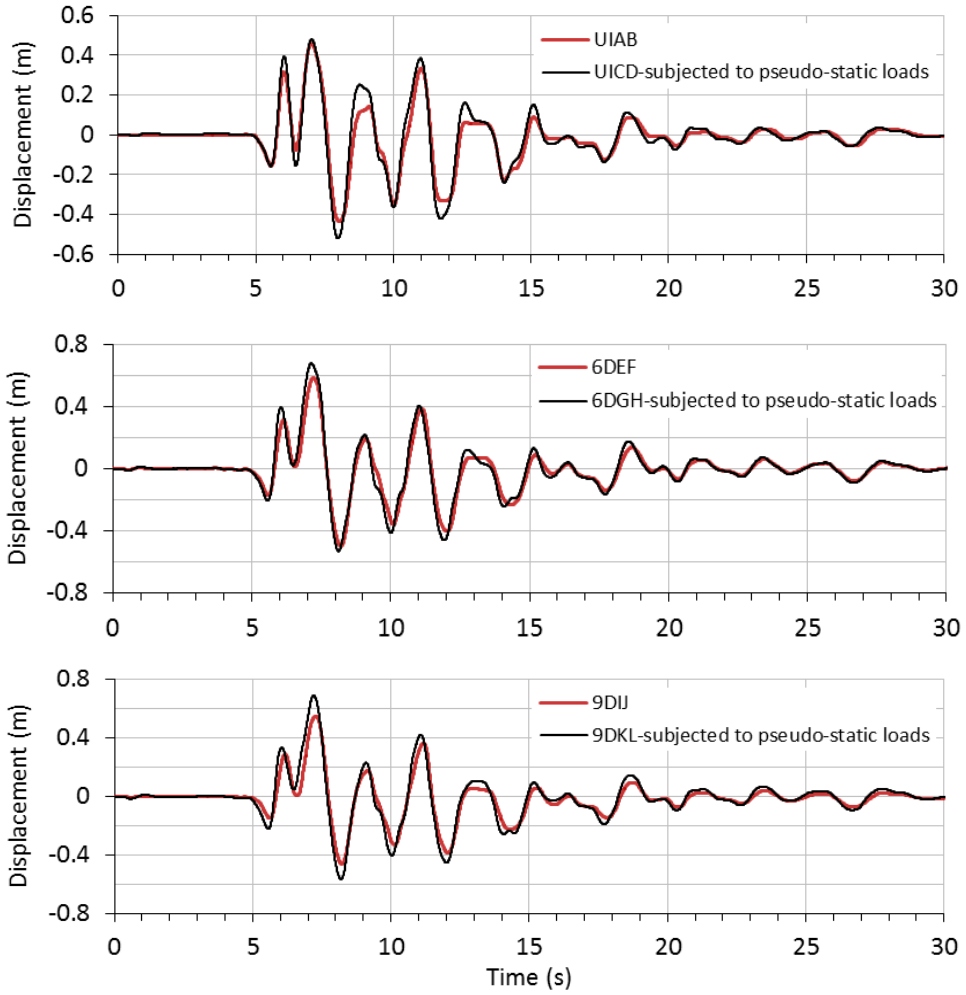

Figure 4.9 Comparison of seismic displacement-time histories (transducer readings) of piles tested in prior pseudo-static loading with those not subjected to prior loading-Event 3 (DSS=Distance from the Soil Surface)

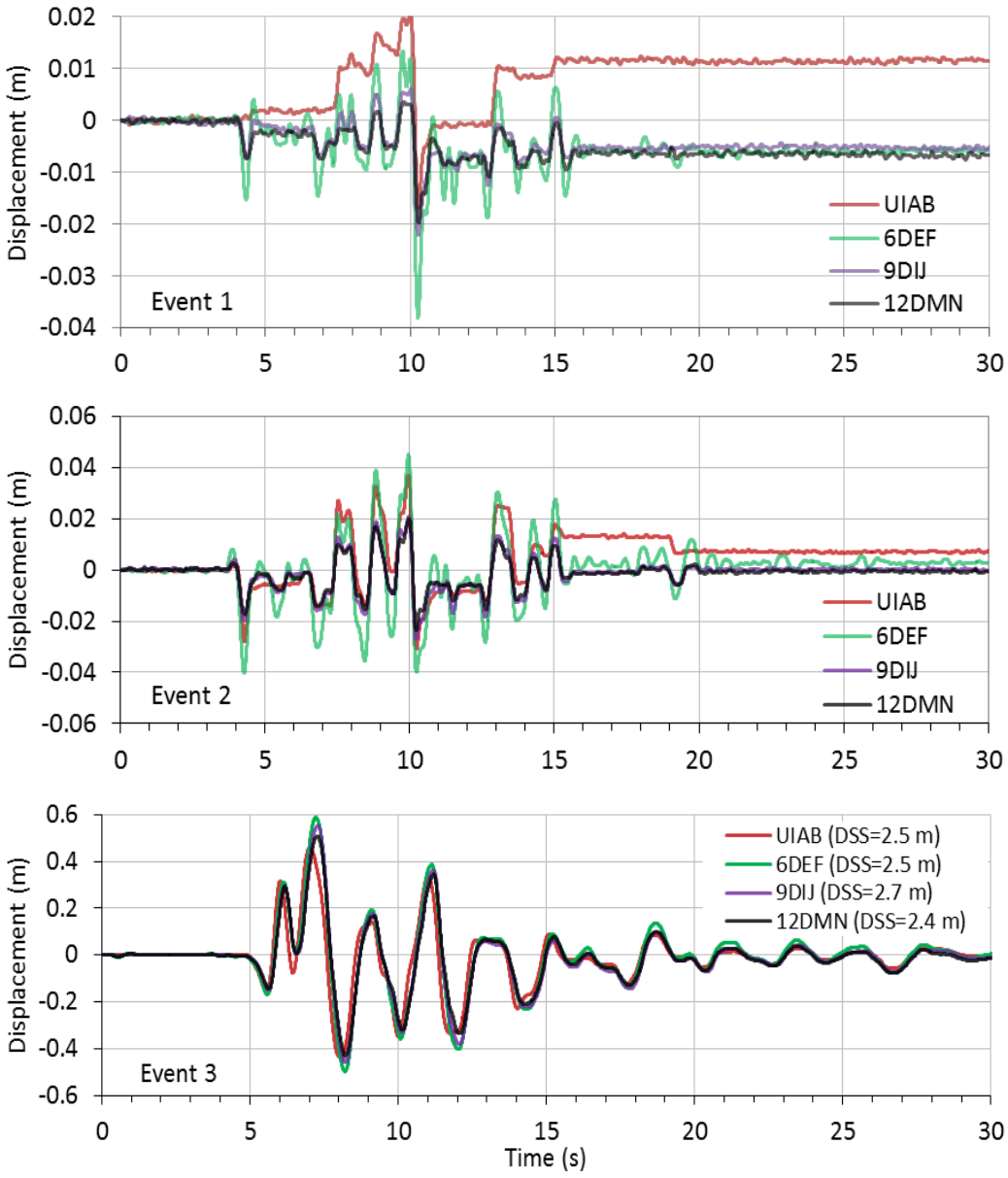

Figure 4.10 Time histories of the displacements recorded by transducers in all shaking events (DSS=Distance from the Soil Surface)

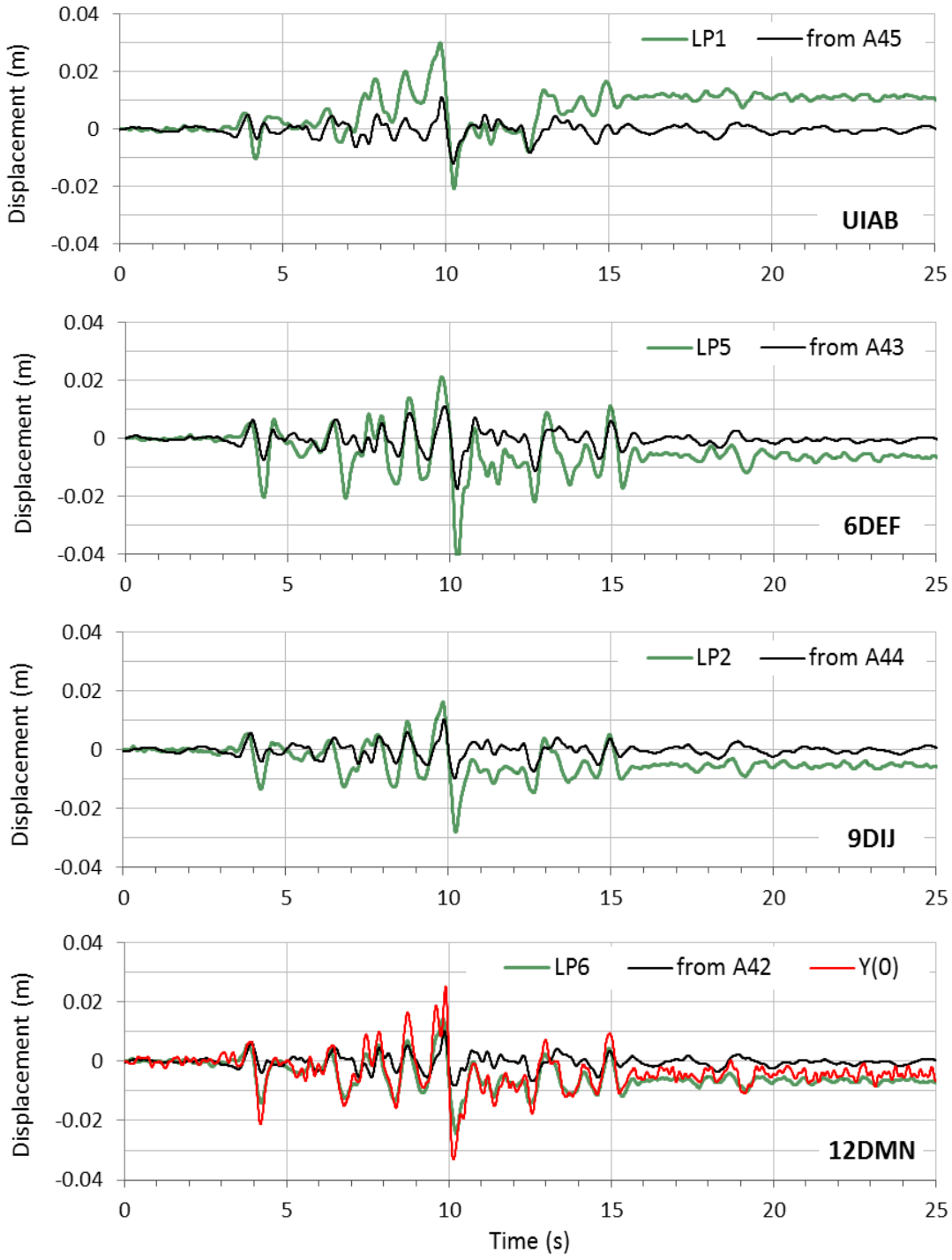

Figure 4.11 Displacements with respect to the base derived from displacement transducers and top mass accelerometers (Event 1)

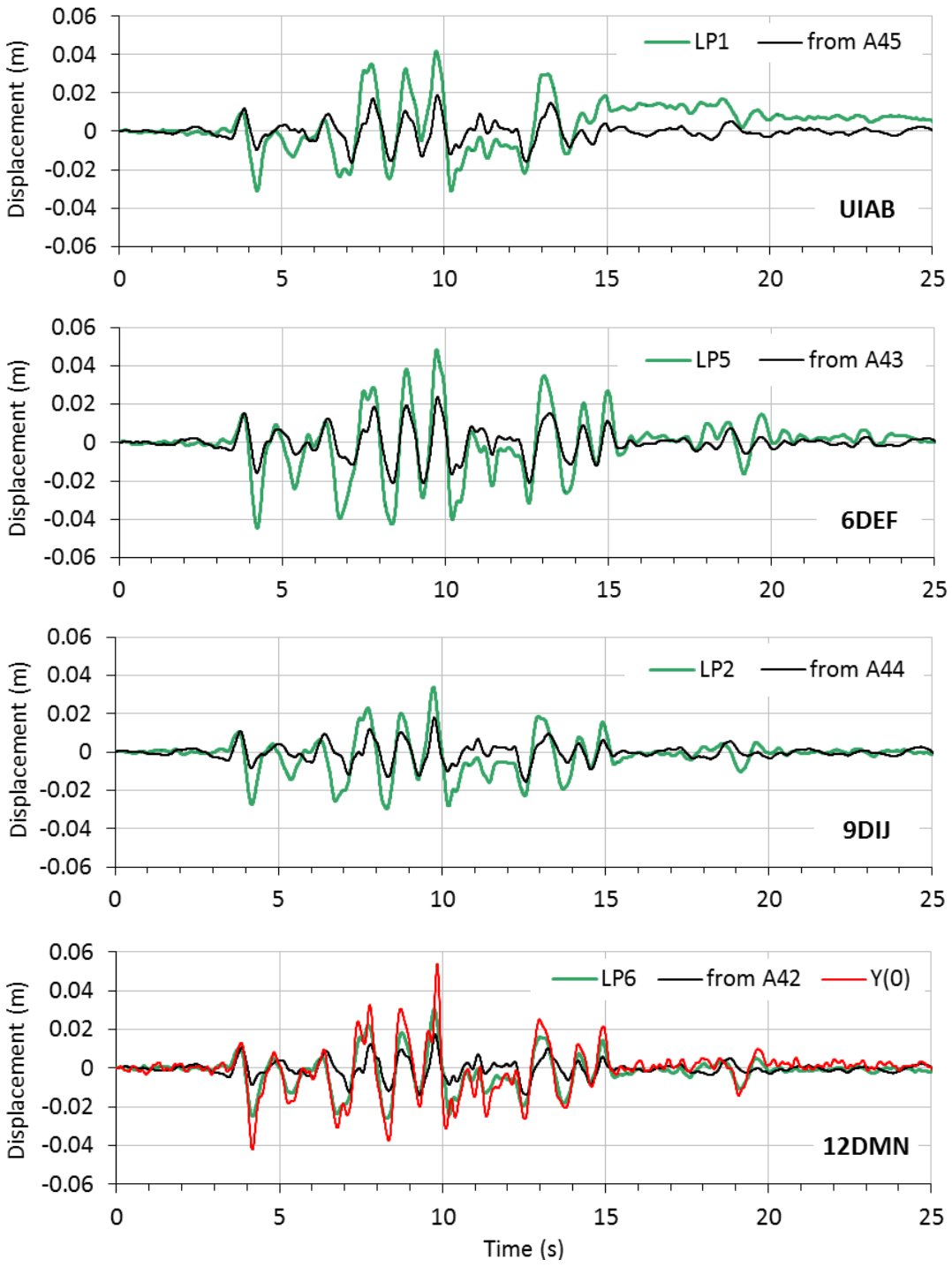

Figure 4.12 Displacements with respect to the base derived from displacement transducers and top mass accelerometers (Event 2)

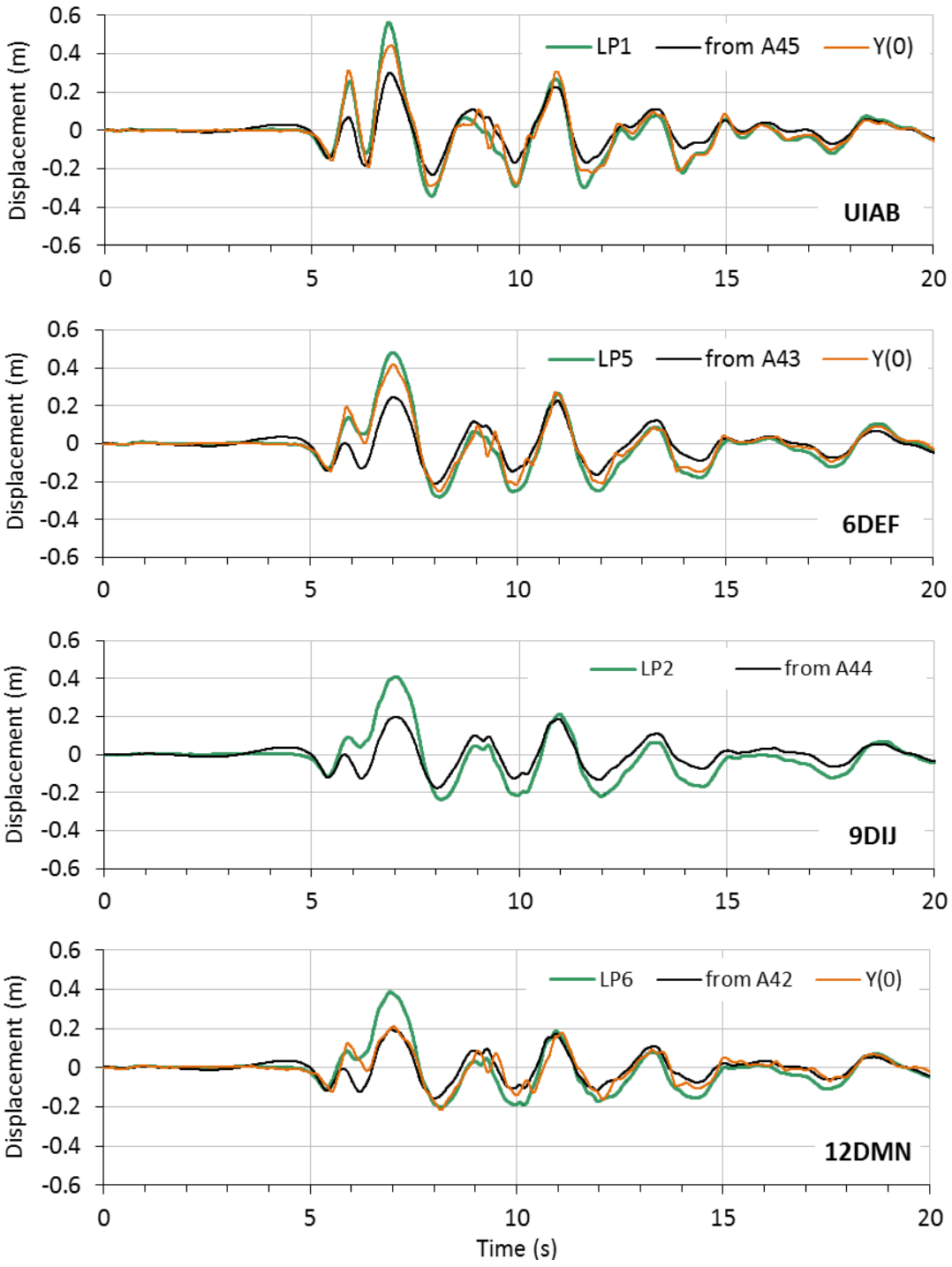

Figure 4.13 Displacements with respect to the base derived from displacement transducers and top mass accelerometers (Event 3)

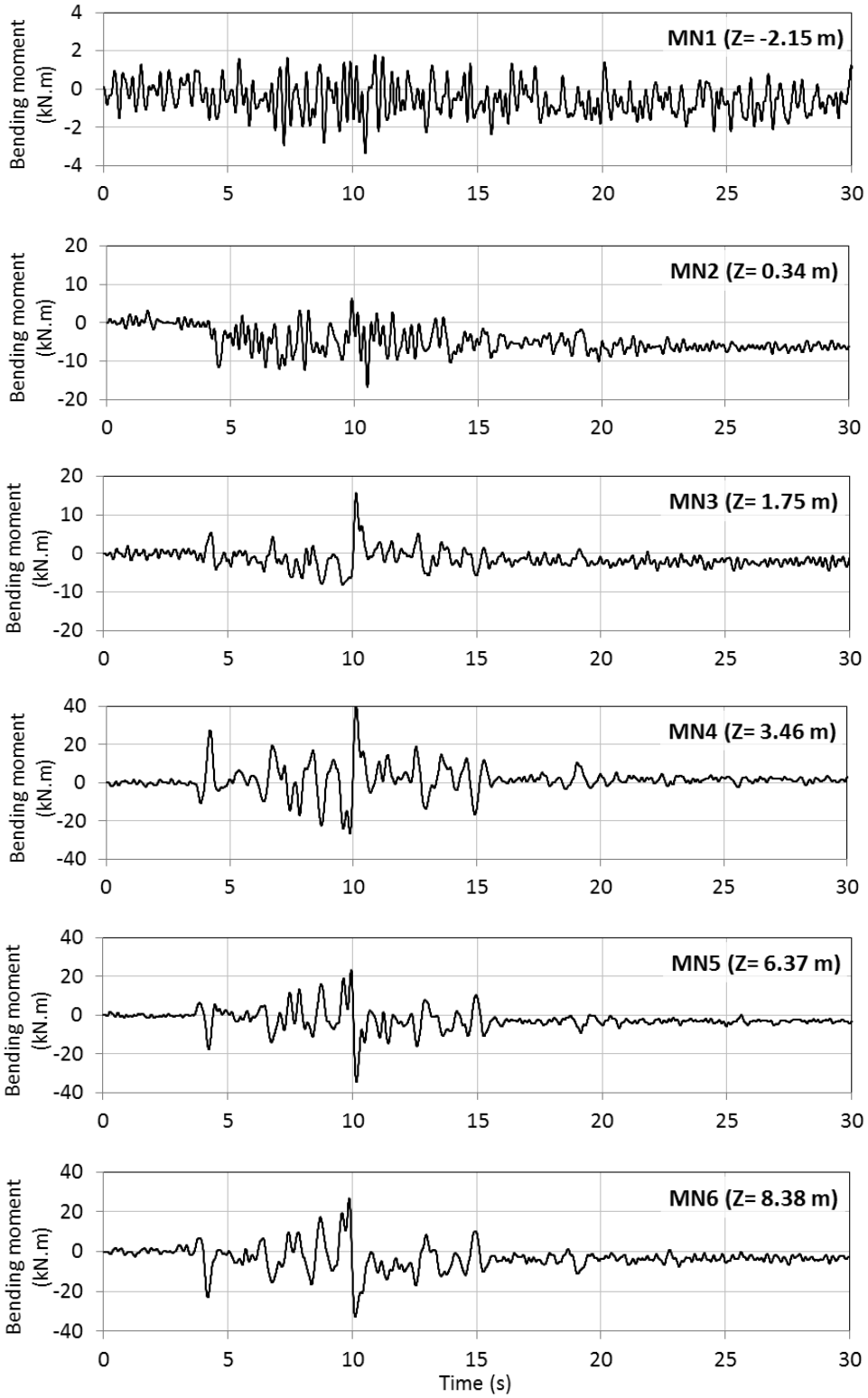

Figure 4.14 Time histories of bending moments measured along pile 12DMN-Event 1
(z is depth from the ground surface; negative value implies above the ground.)

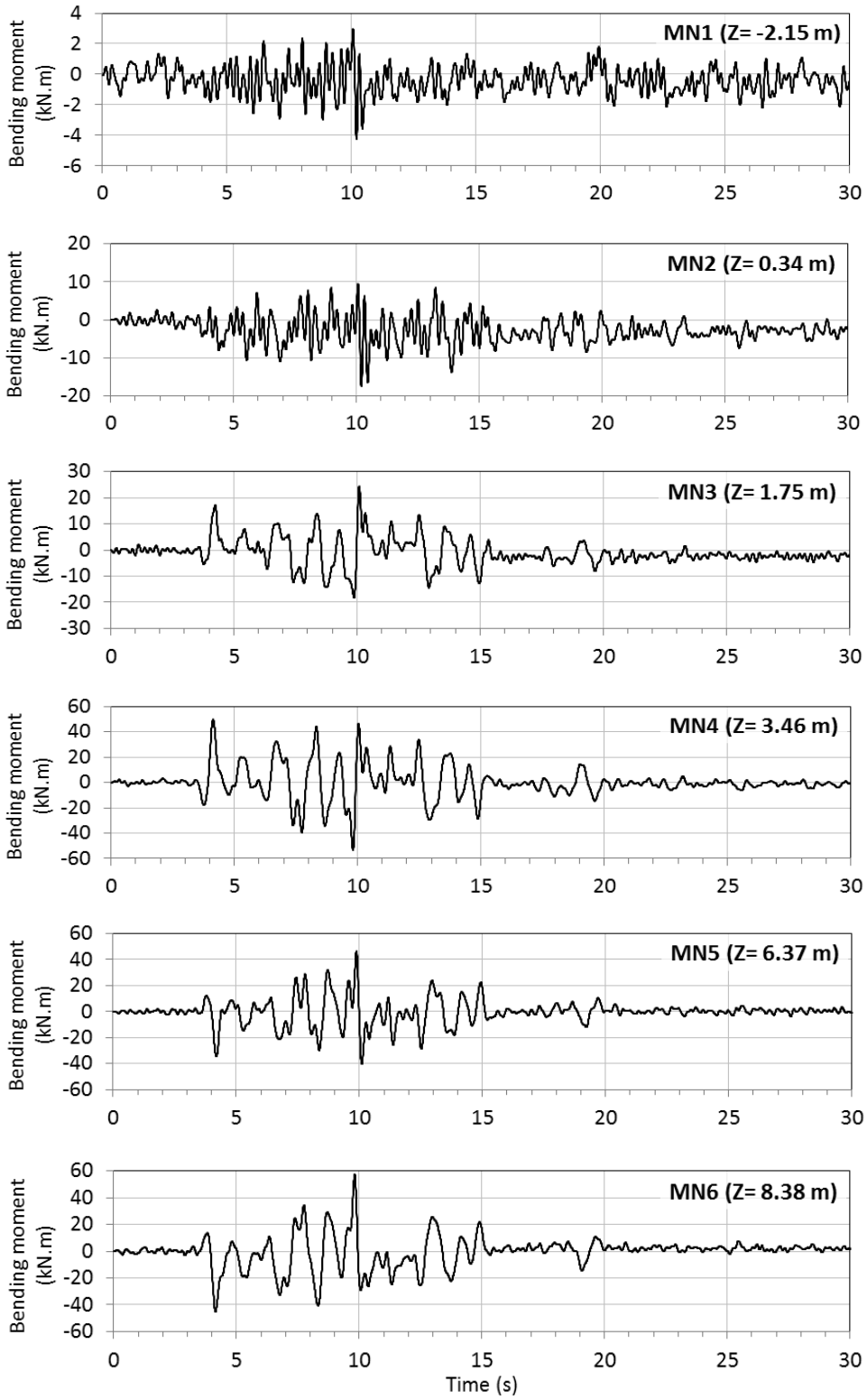

Figure 4.15 Time histories of bending moments measured along pile 12DMN-Event 2
(z is depth from the ground surface; negative value implies above the ground.)

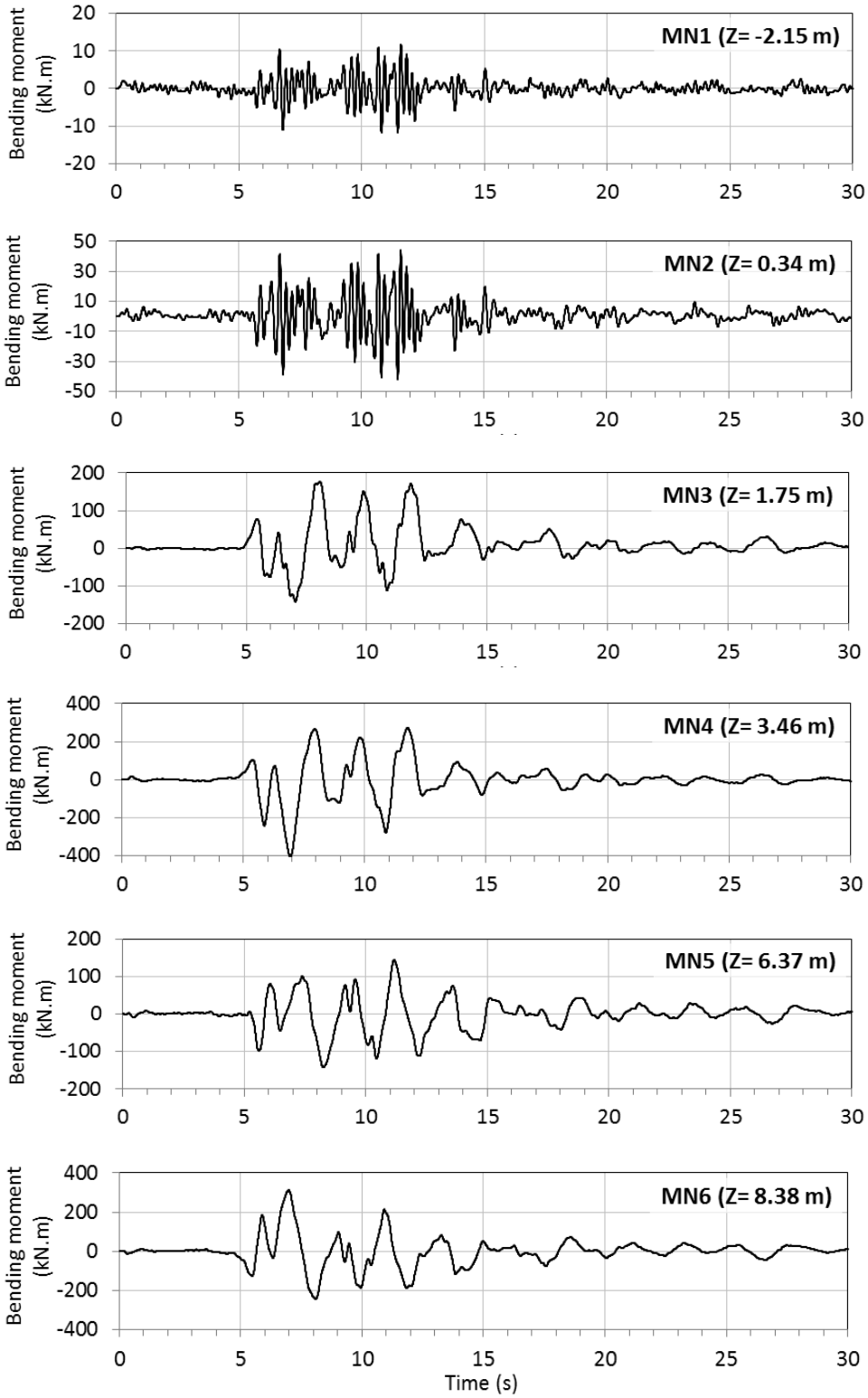

Figure 4.16 Time histories of bending moment measured along pile 12DMN-Event 3
(z is depth from the ground surface; negative value implies above the ground.)

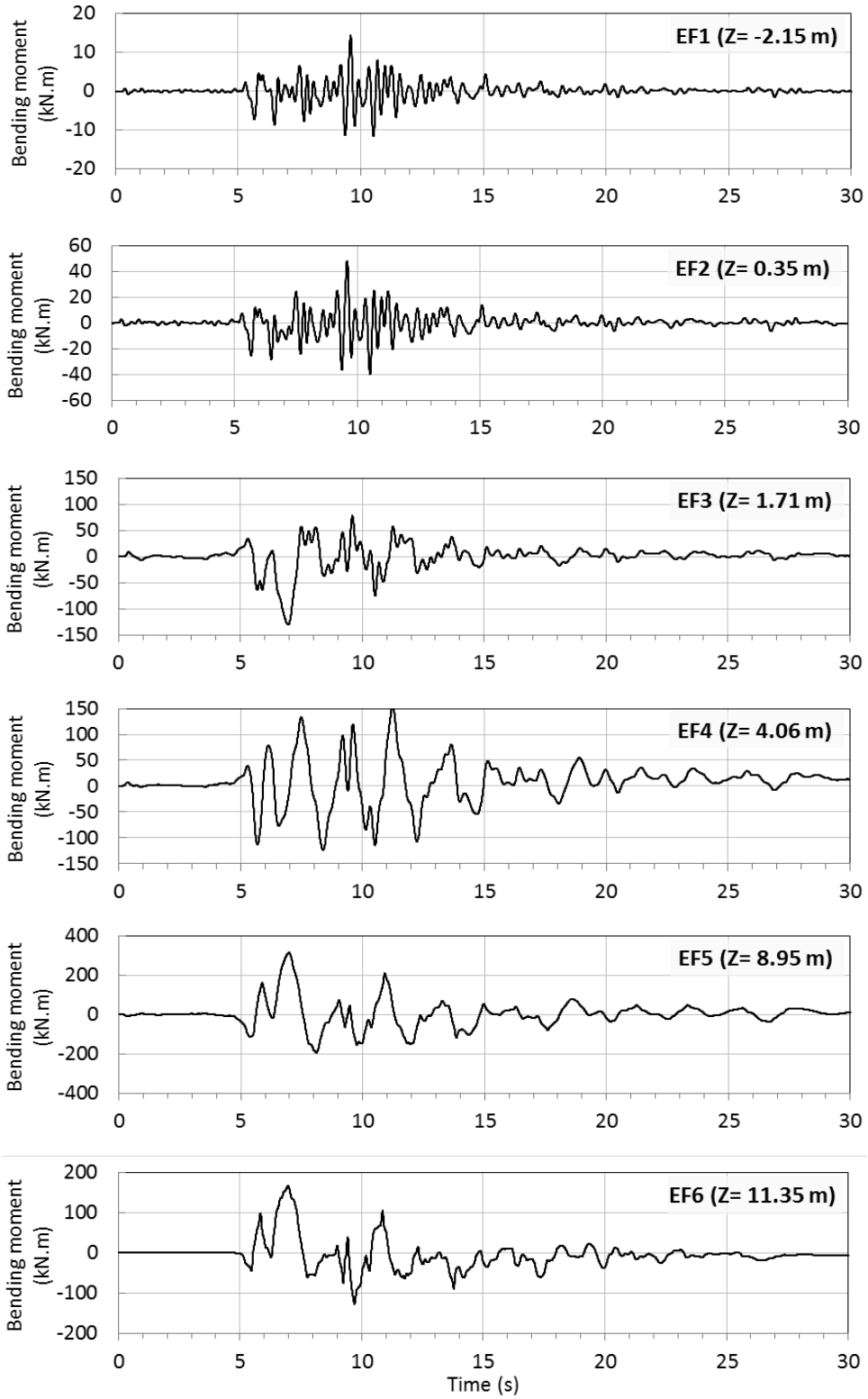

Figure 4.17 Time histories of bending moment measured along pile 6DEF-Event 3 (z is depth from the ground surface; negative value implies above the ground.)

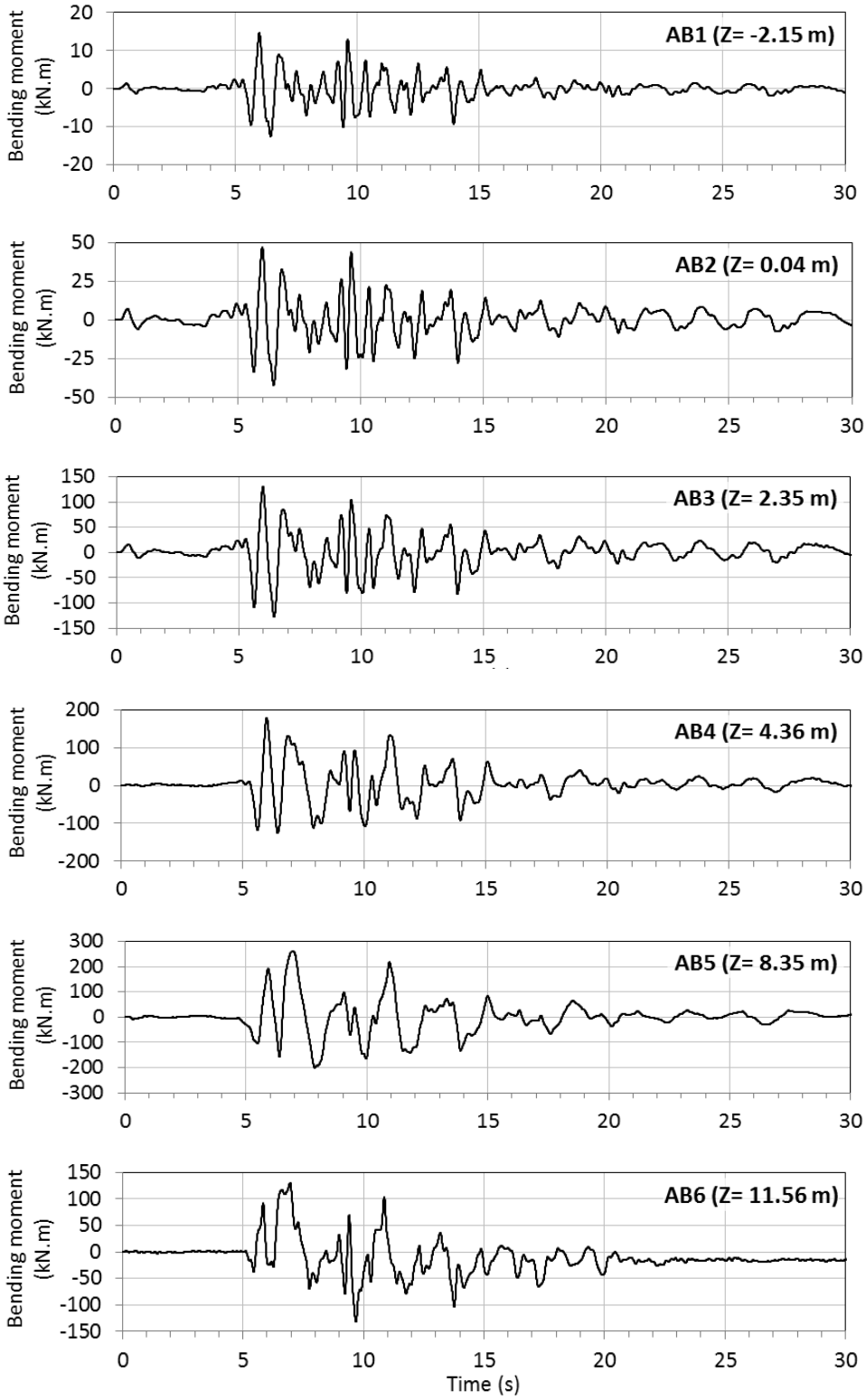

Figure 4.18 Time histories of bending moment measured along pile UIAB-Event 3 (z is depth from the ground surface; negative value implies above the ground.)

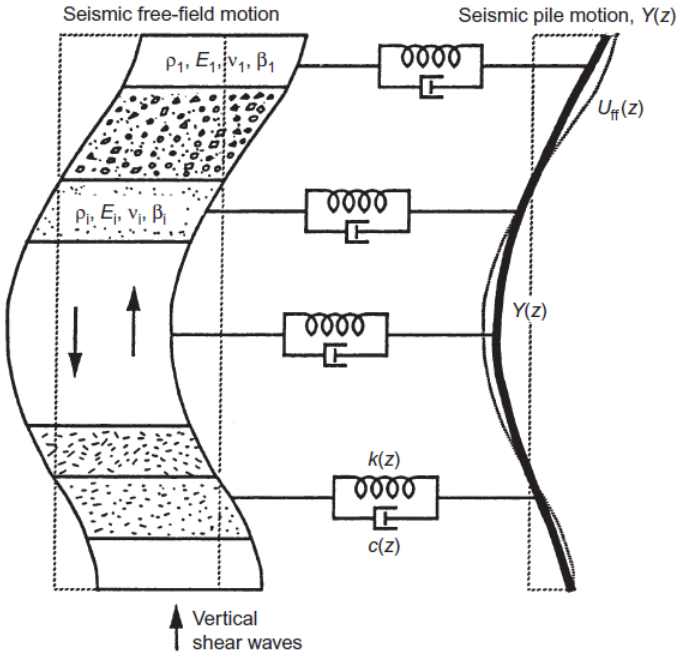

Figure 4.19 BNWF model for a pile excited by vertically propagating shear waves (Nikolaou et al., 2001)

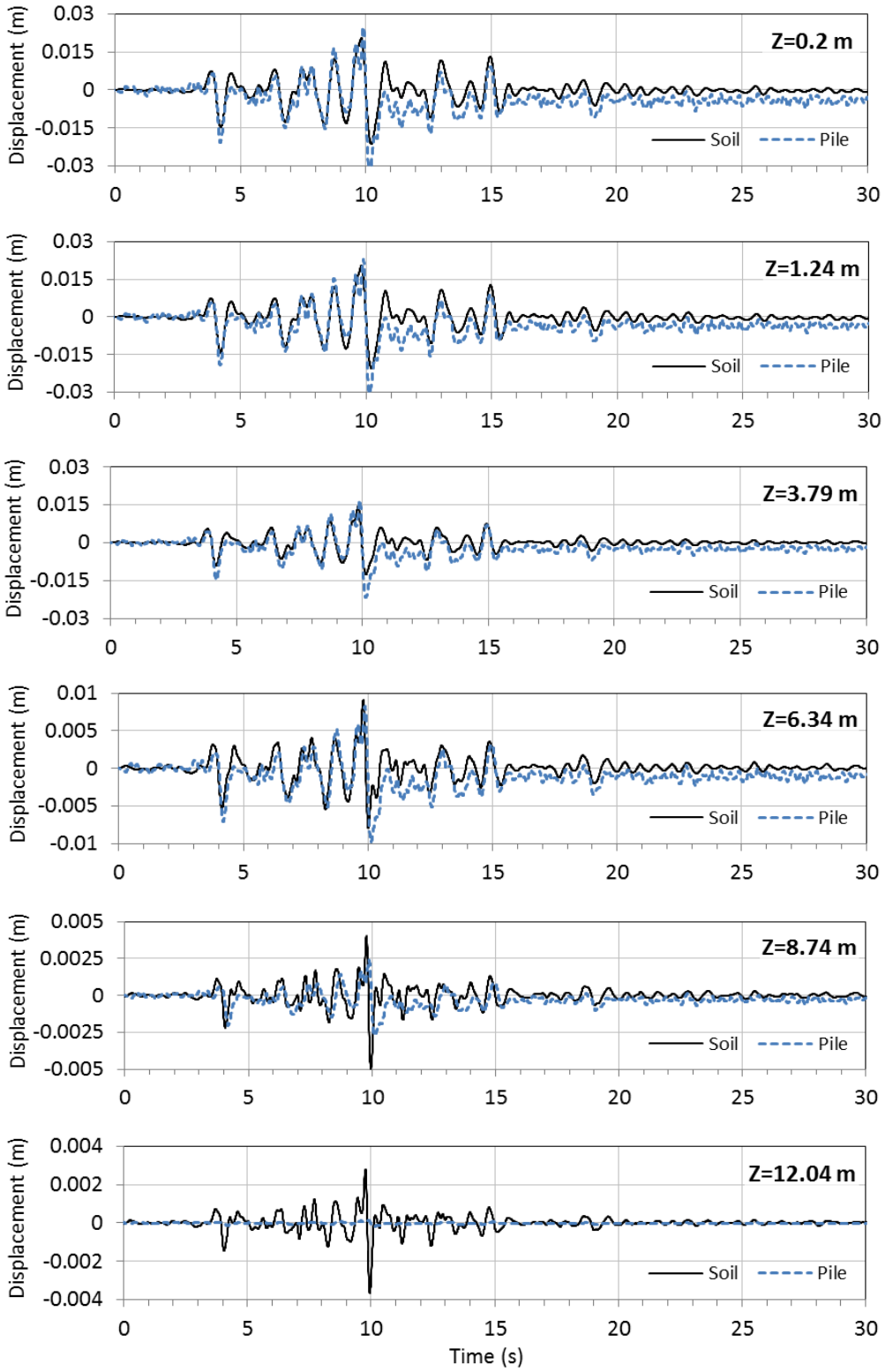

Figure 4.20 Soil and pile displacements with respect to the base 12DMN (Event 1)

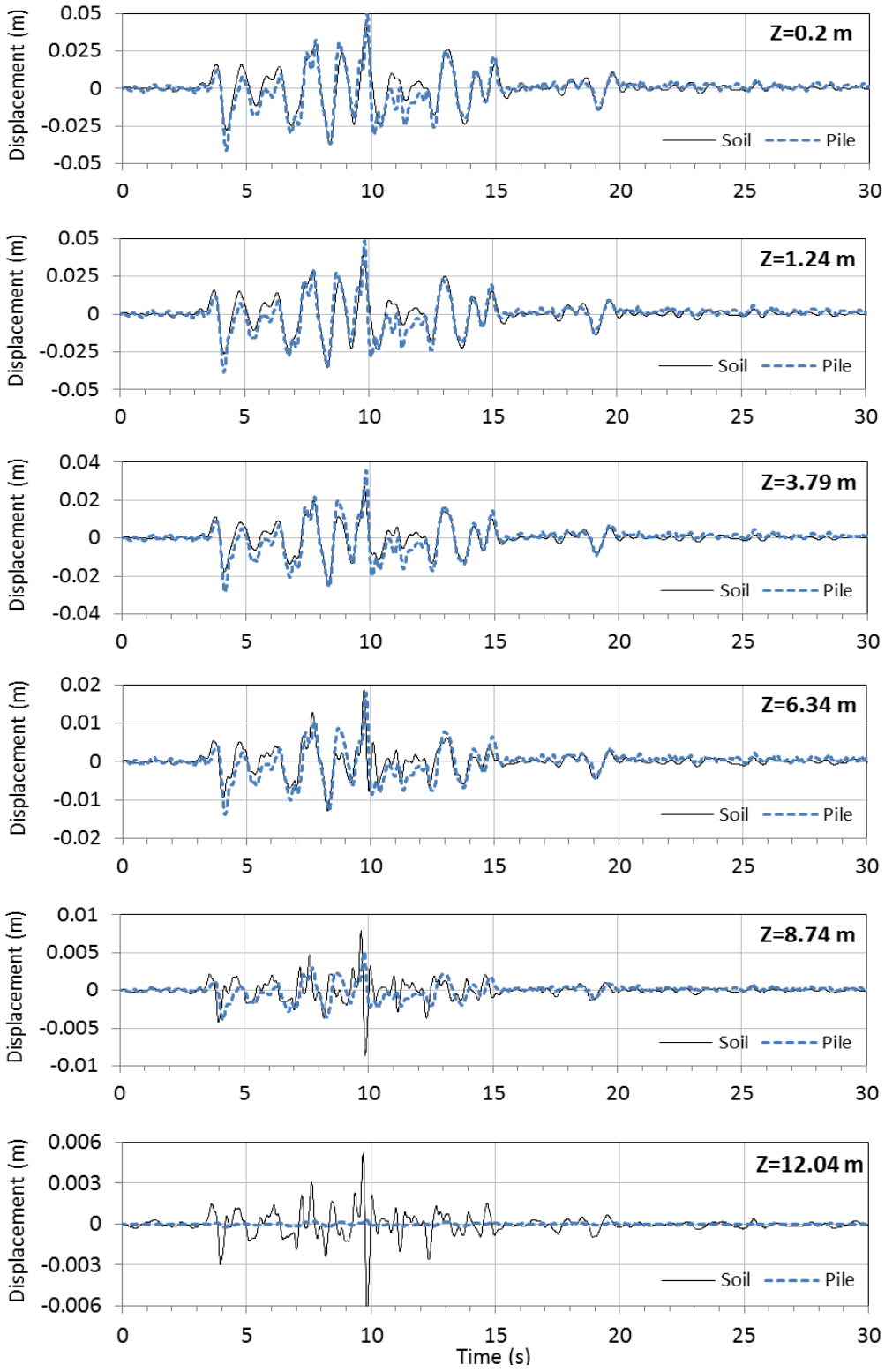

Figure 4.21 Soil and pile displacements with respect to the base 12DMN (Event 2)

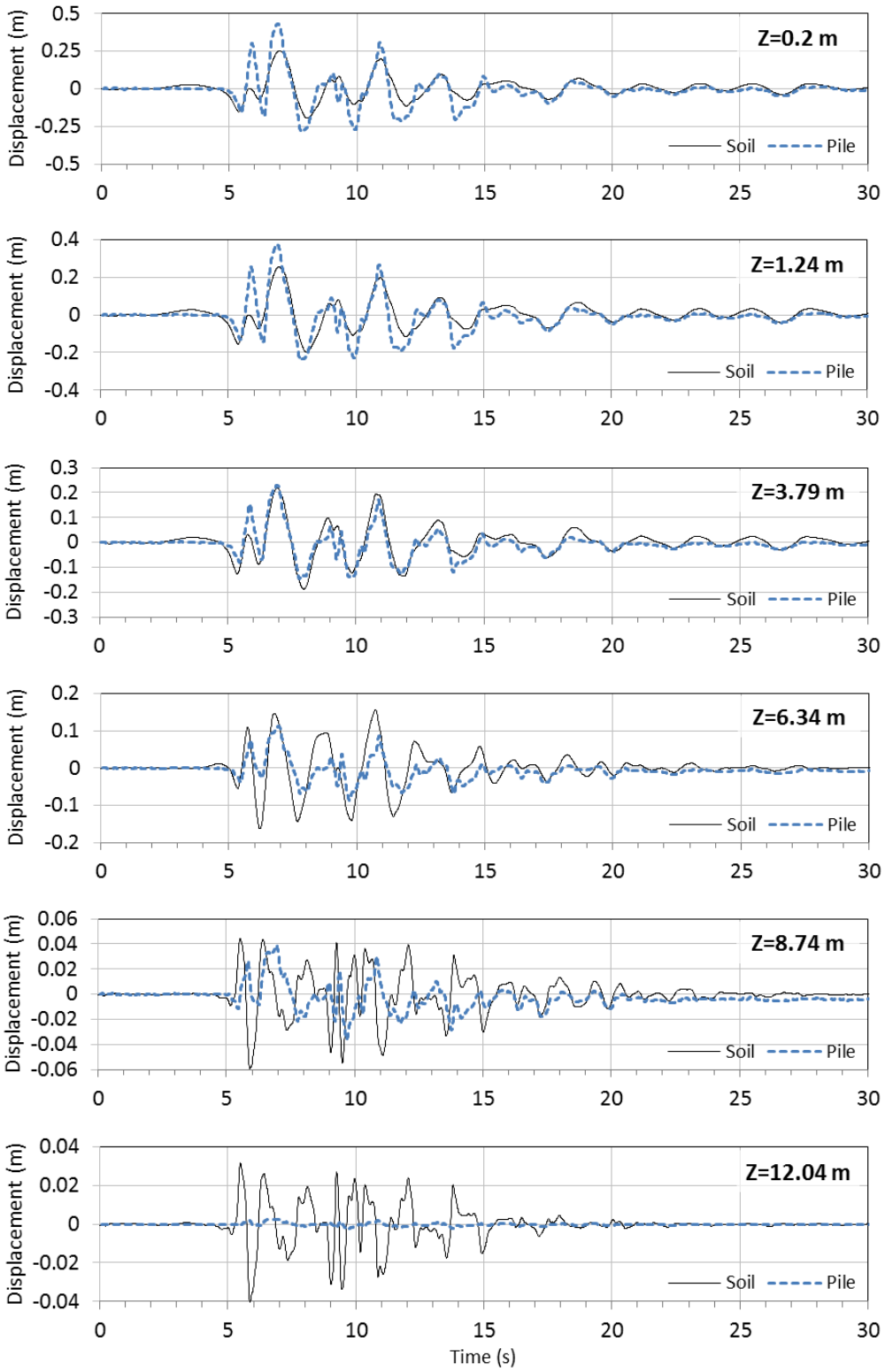

Figure 4.22 Soil and pile displacements with respect to the base UIAB (Event 3)

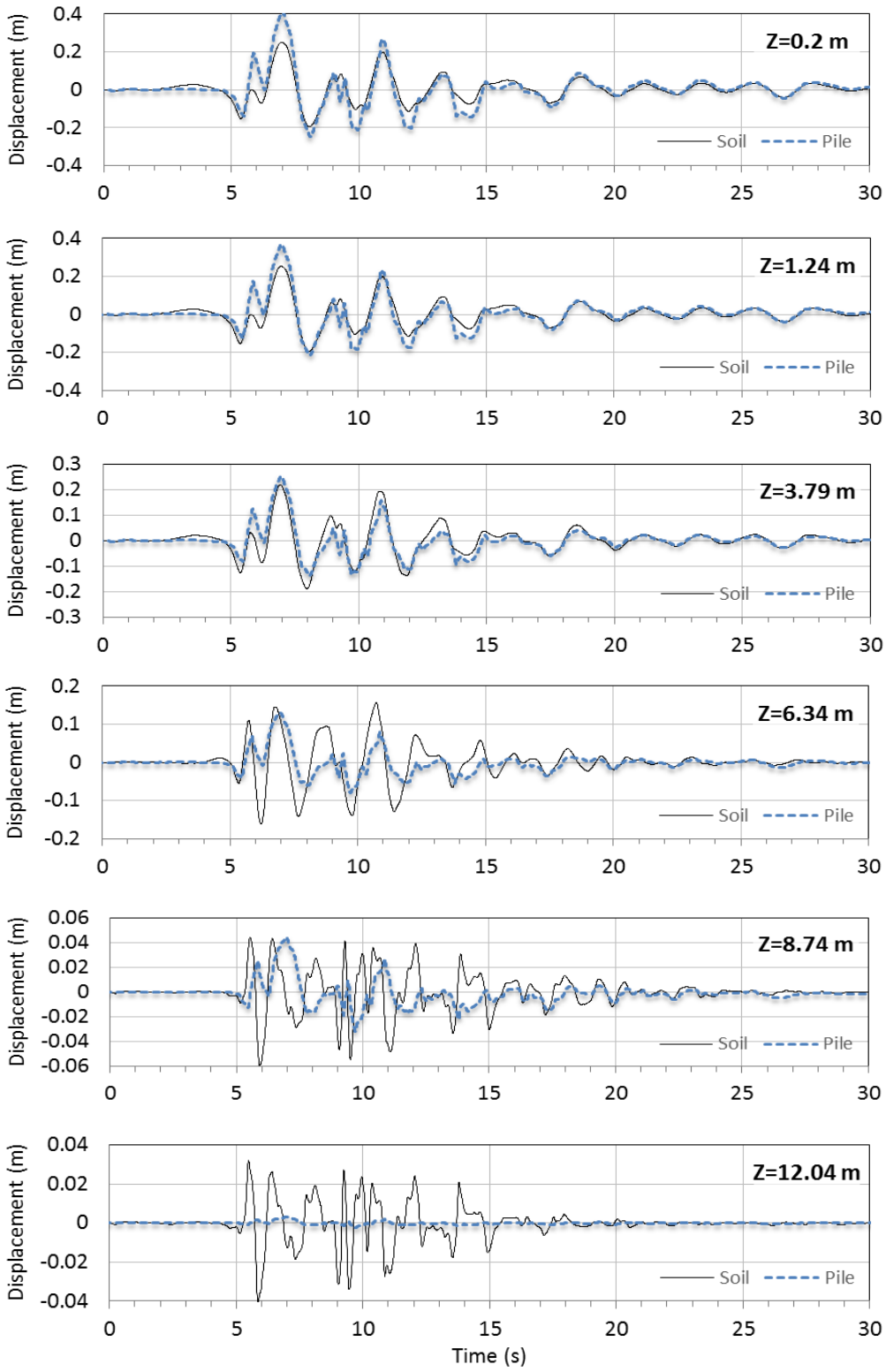

Figure 4.23 Soil and pile displacements with respect to the base 6DEF (Event 3)

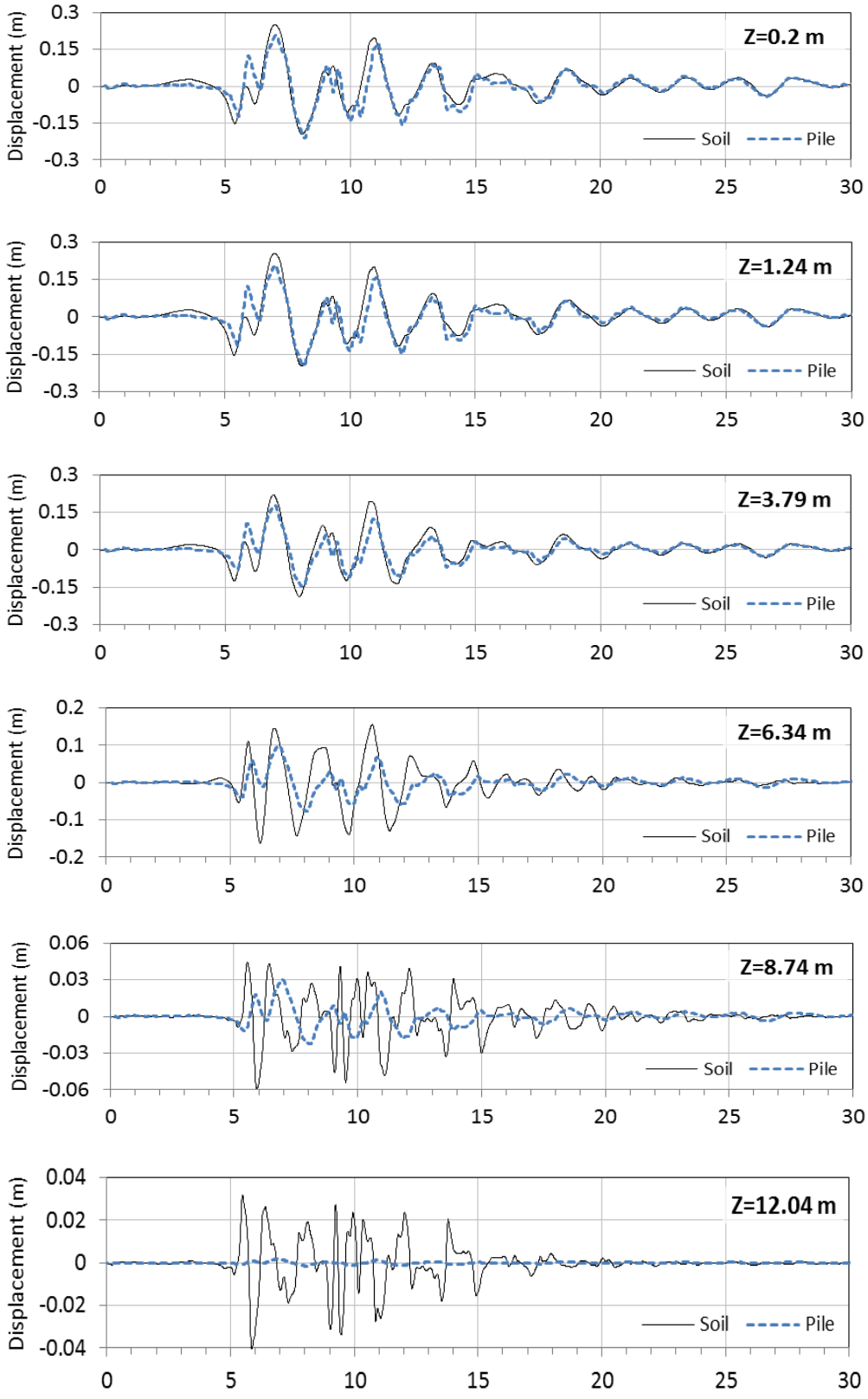

Figure 4.24 Soil and pile displacements with respect to the base 12DMN (Event 3)

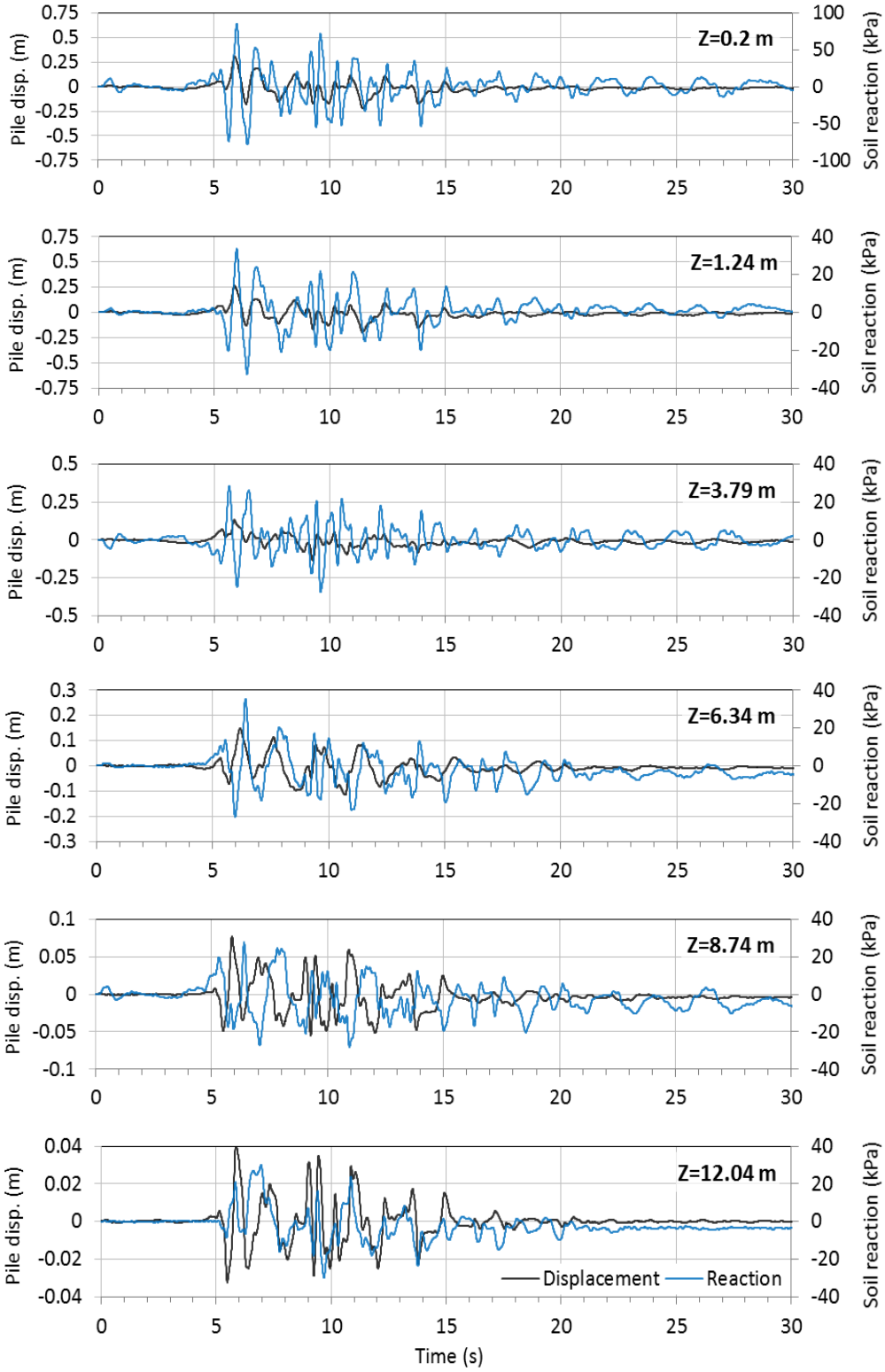

Figure 4.25 Time histories of soil reaction on UIAB-Event 3 (Pile displacements are with respect to the free-field)

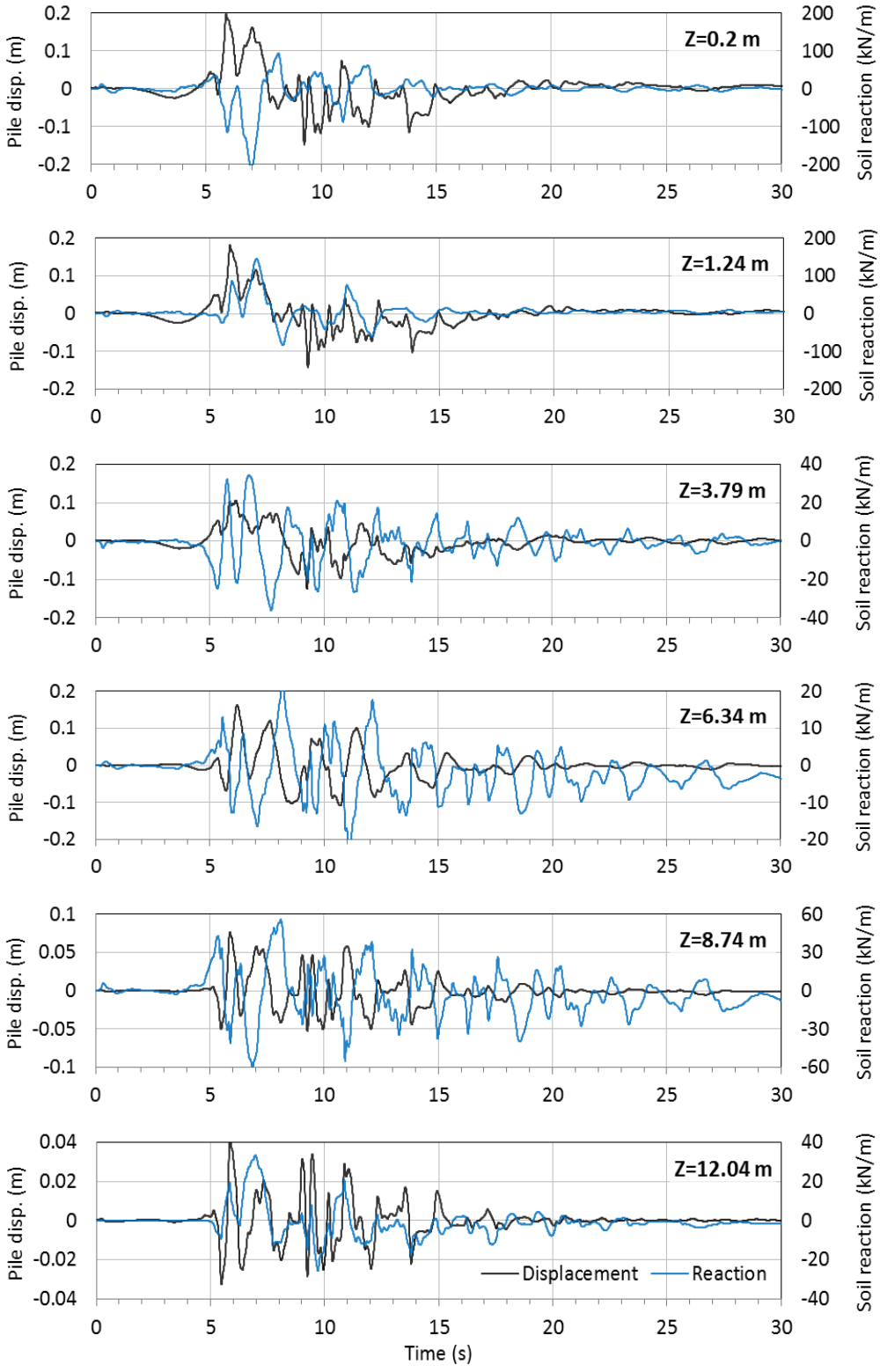

Figure 4.26 Time histories of soil reaction on 6DEF-Event 3 (Pile displacements are with respect to the free-field)

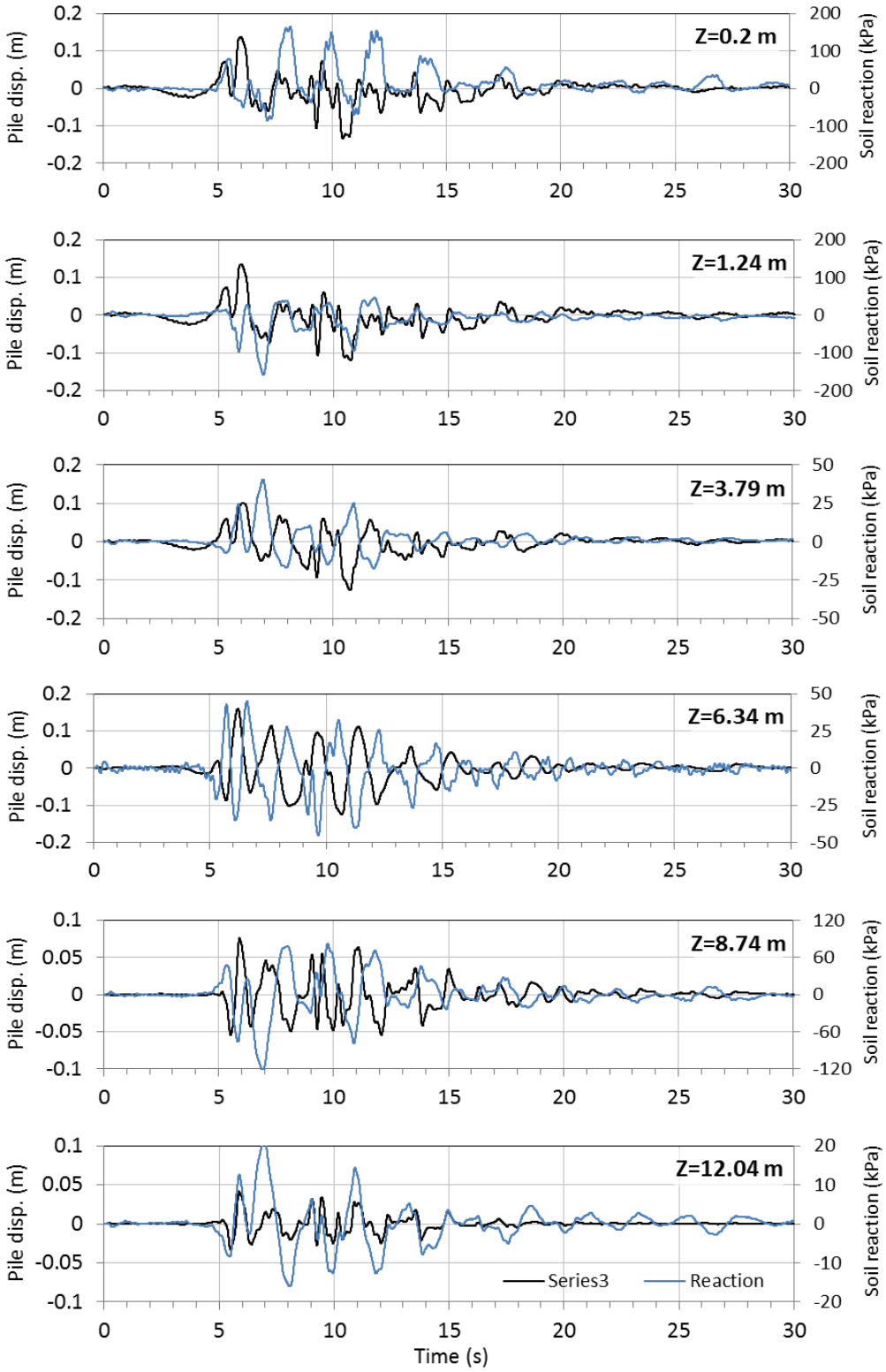

Figure 4.27 Time histories of soil reaction on 12DMN-Event 3 (Pile displacements are with respect to the free-field)

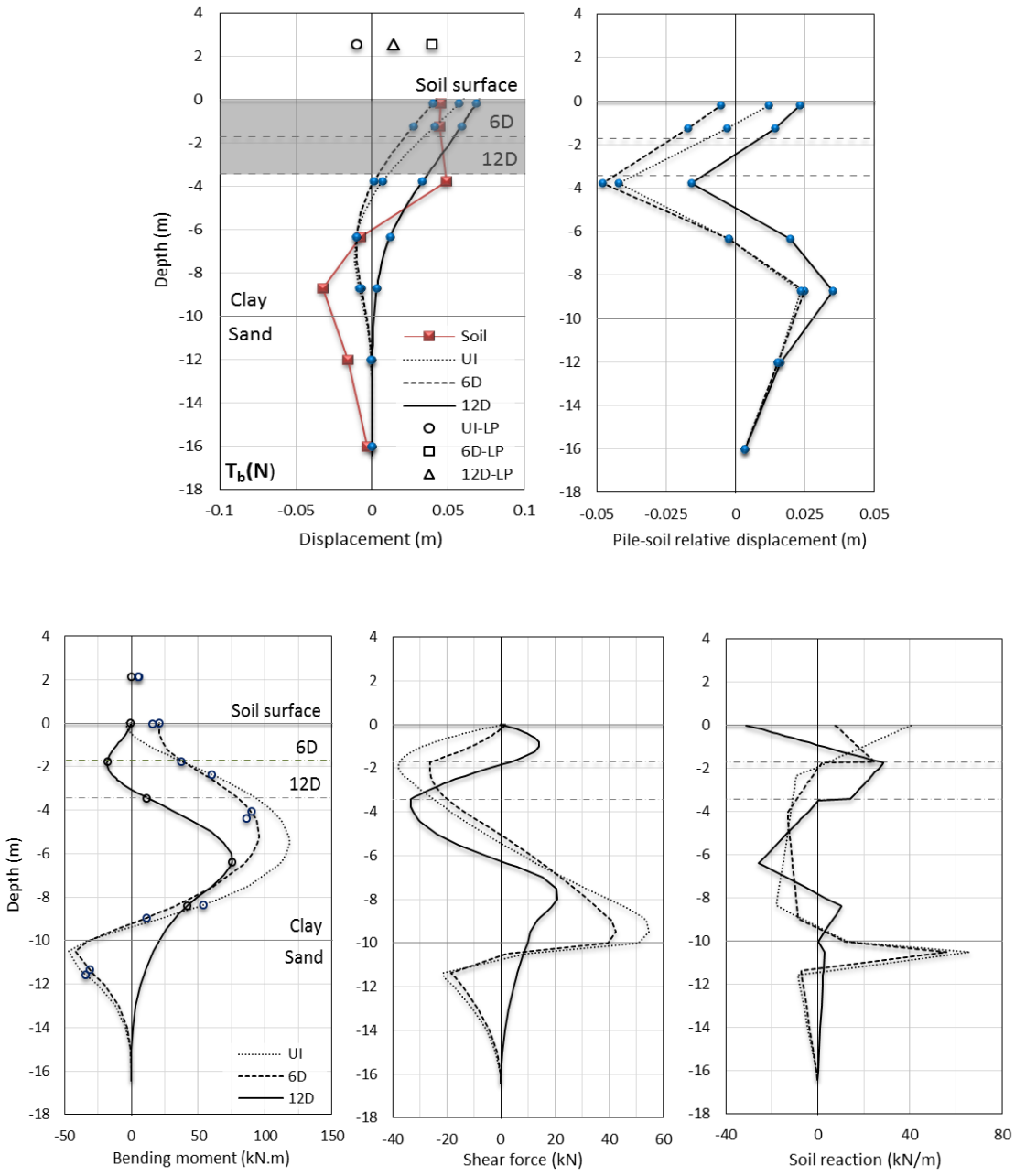

Figure 4.28 Bending moment, shear force, soil reaction and pile displacement profiles at the time instant corresponding to the negative peak of base acceleration T_b(N)=9.14 s (Event 3)

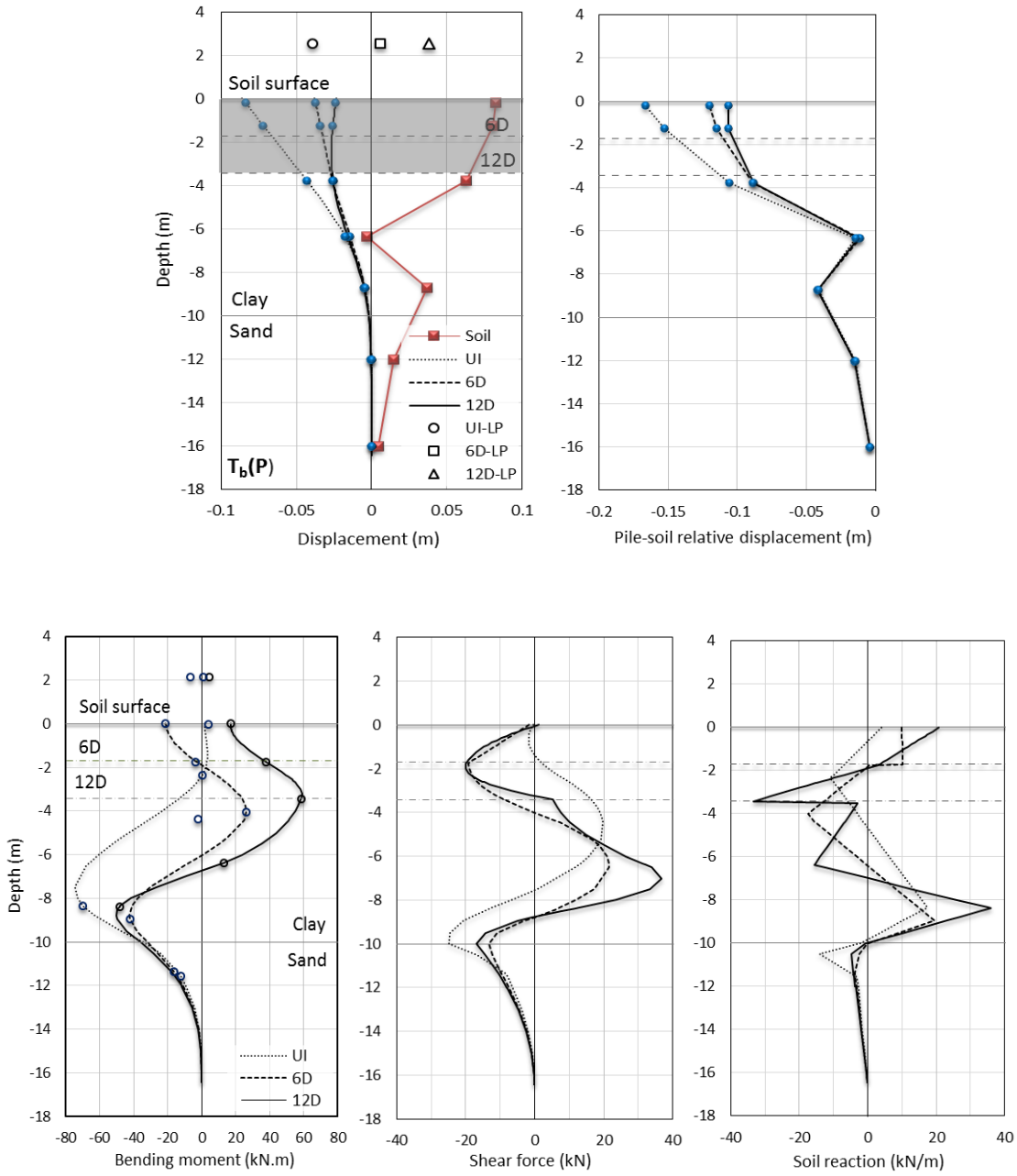

Figure 4.29 Bending moment, shear force, soil reaction and pile displacement profiles at the time instant corresponding to the positive peak of base acceleration $T_b(P)$=9.32 s (Event 3)

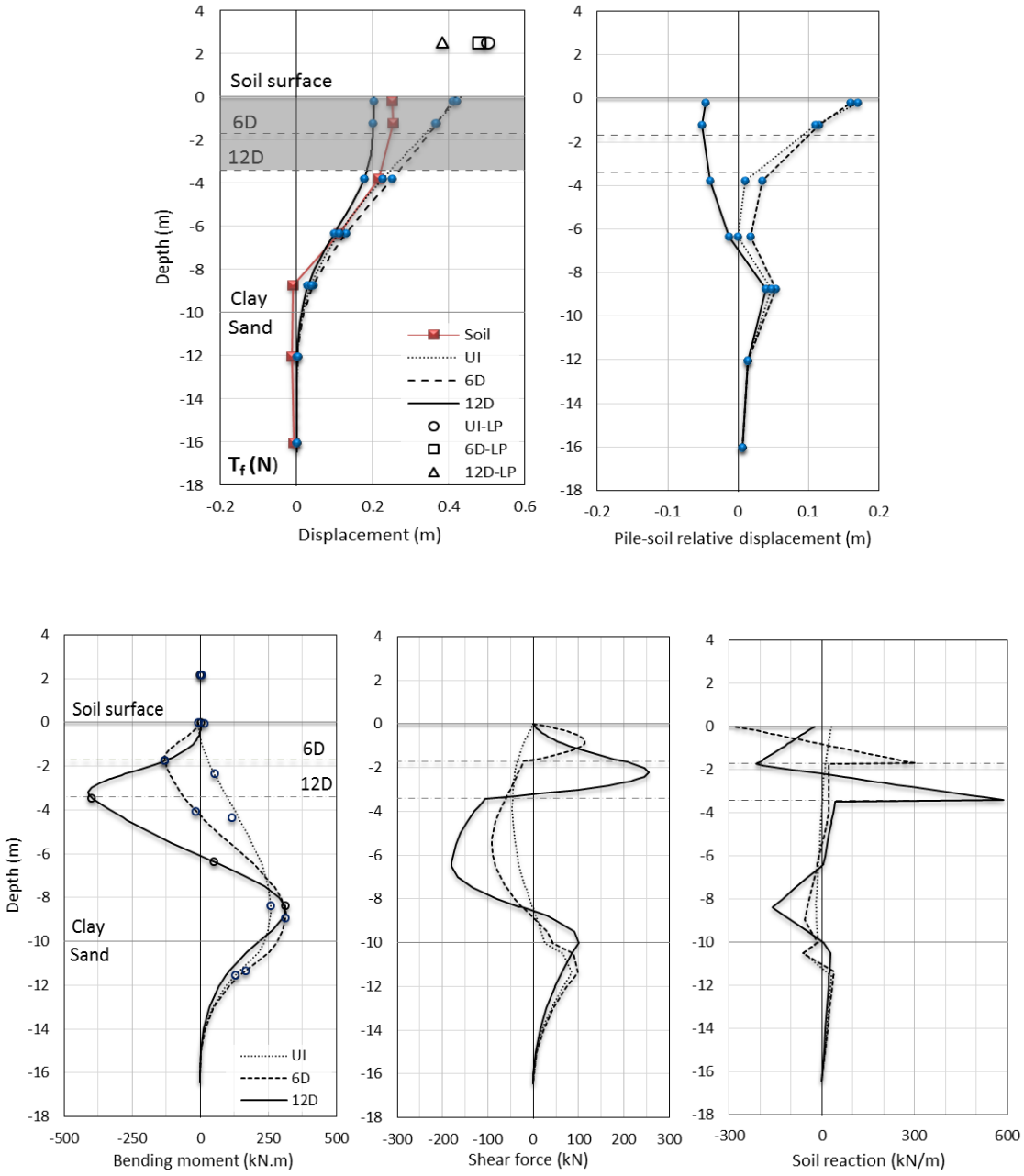

Figure 4.30 Bending moment, shear force, soil reaction and pile displacement profiles at the time instant corresponding to the peak free-field displacement T_f =6.97 s (Event 3)

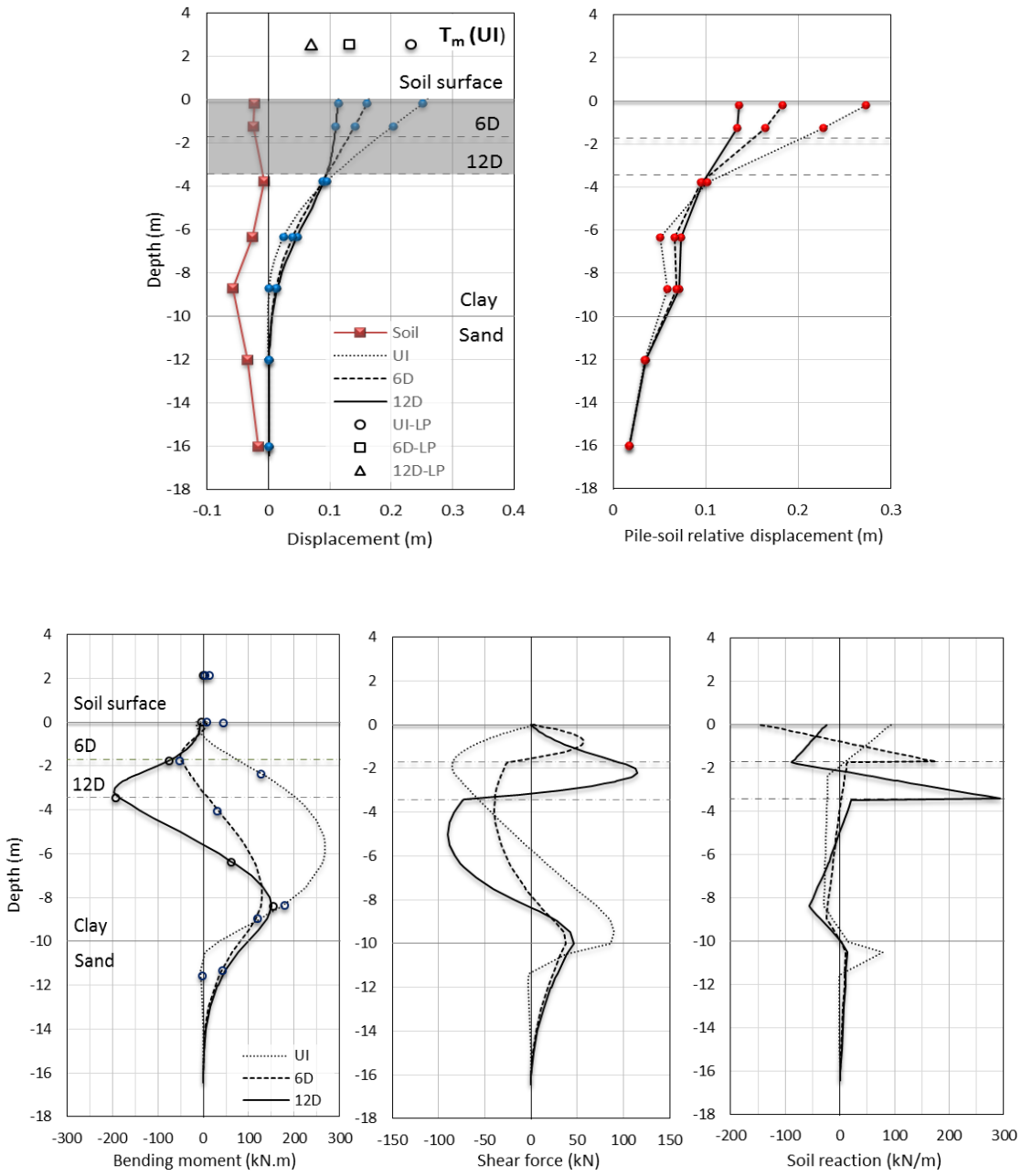

Figure 4.31 Bending moment, shear force, soil reaction and pile displacement profiles at the time instant corresponding to peak top mass acceleration T_m (UIAB)=5.97 s (Event 3)

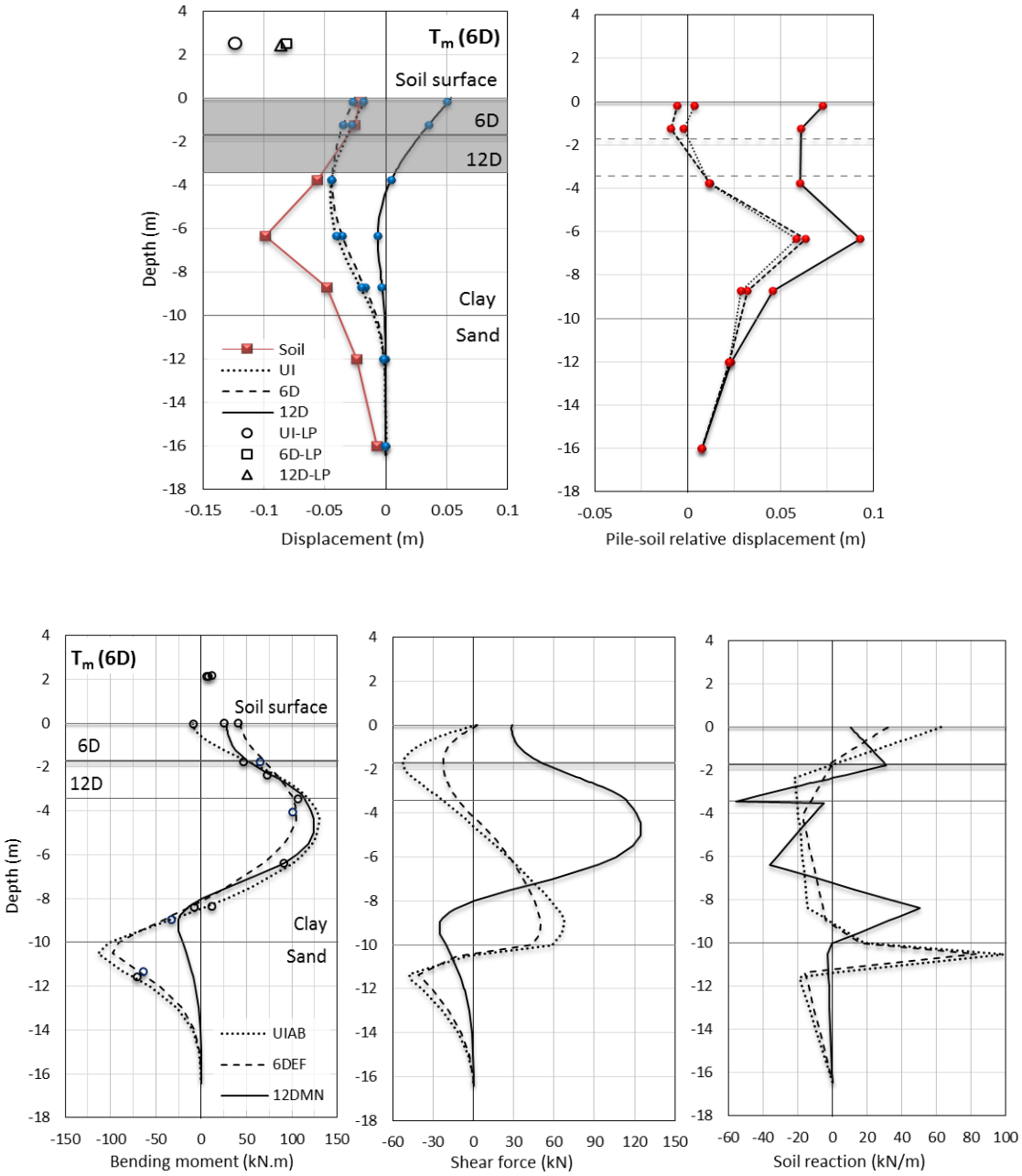

Figure 4.32 Bending moment, shear force, soil reaction and pile displacement profiles at the time instant corresponding to peak top mass acceleration T_m (6DEF)=9.55 s (Event 3)

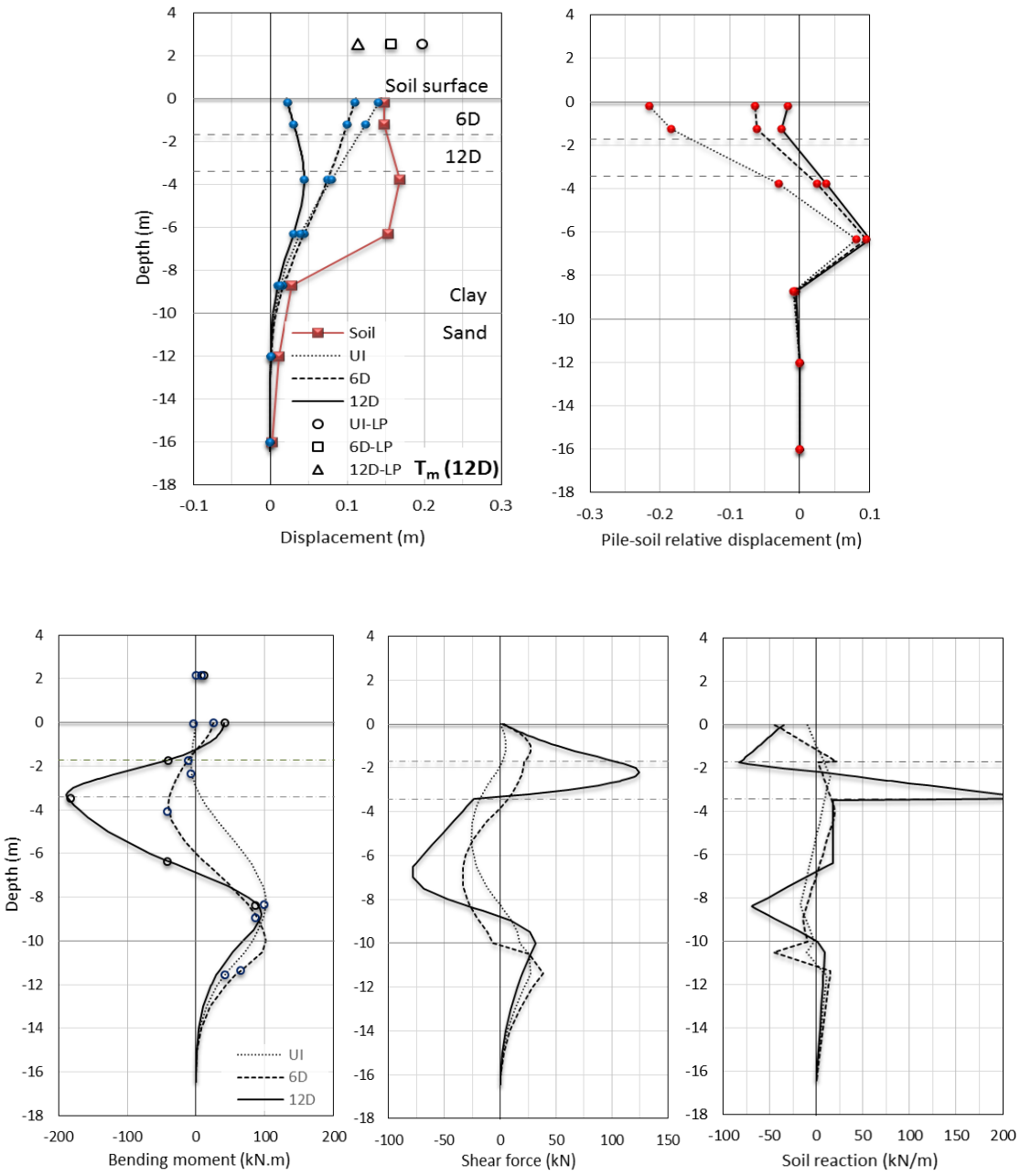

Figure 4.33 Bending moment, shear force, soil reaction and pile displacement profiles at the time instant corresponding to peak top mass acceleration T_m (12DMN)=10.69 s (Event 3)

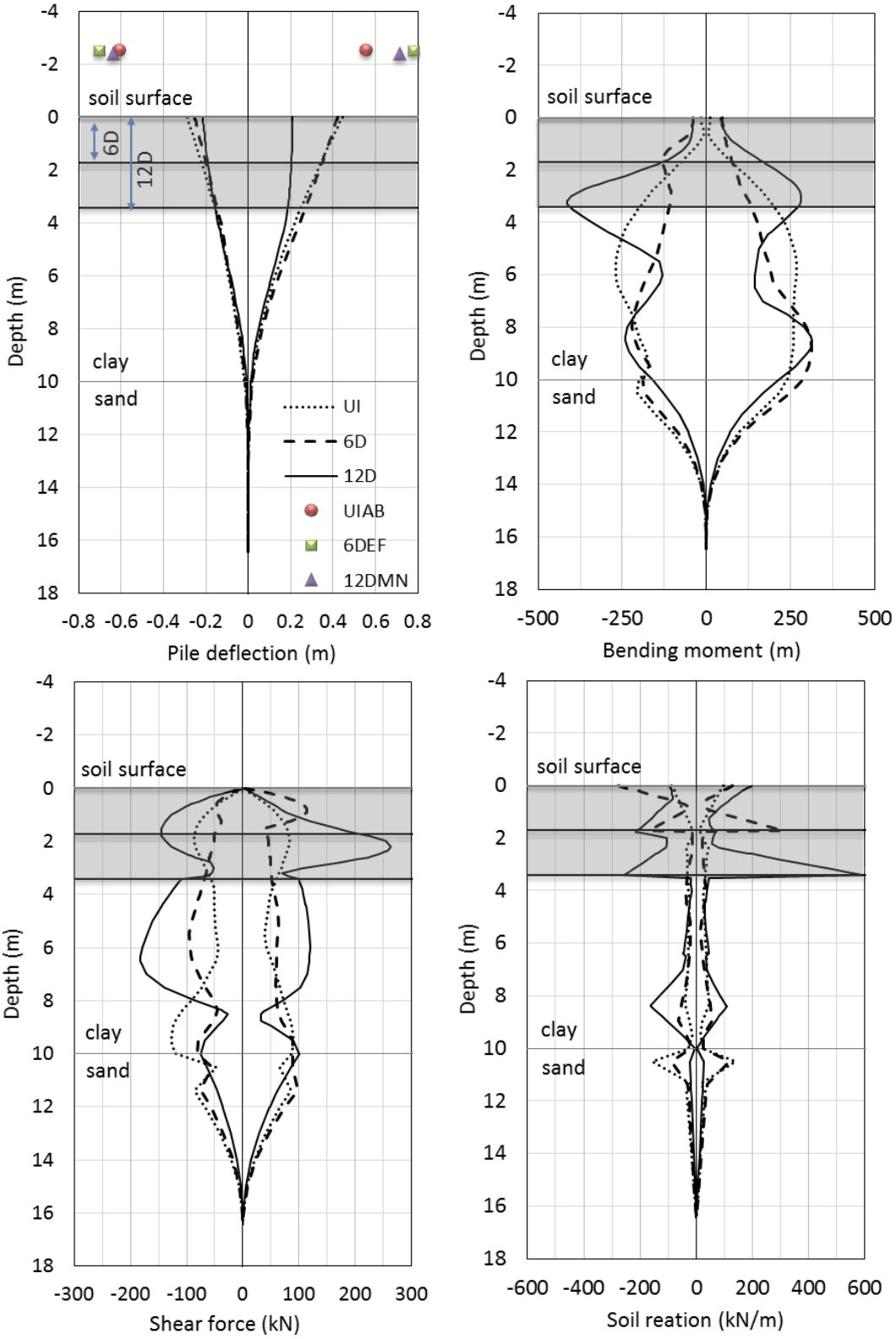

Figure 4.34 Envelopes for Event 3

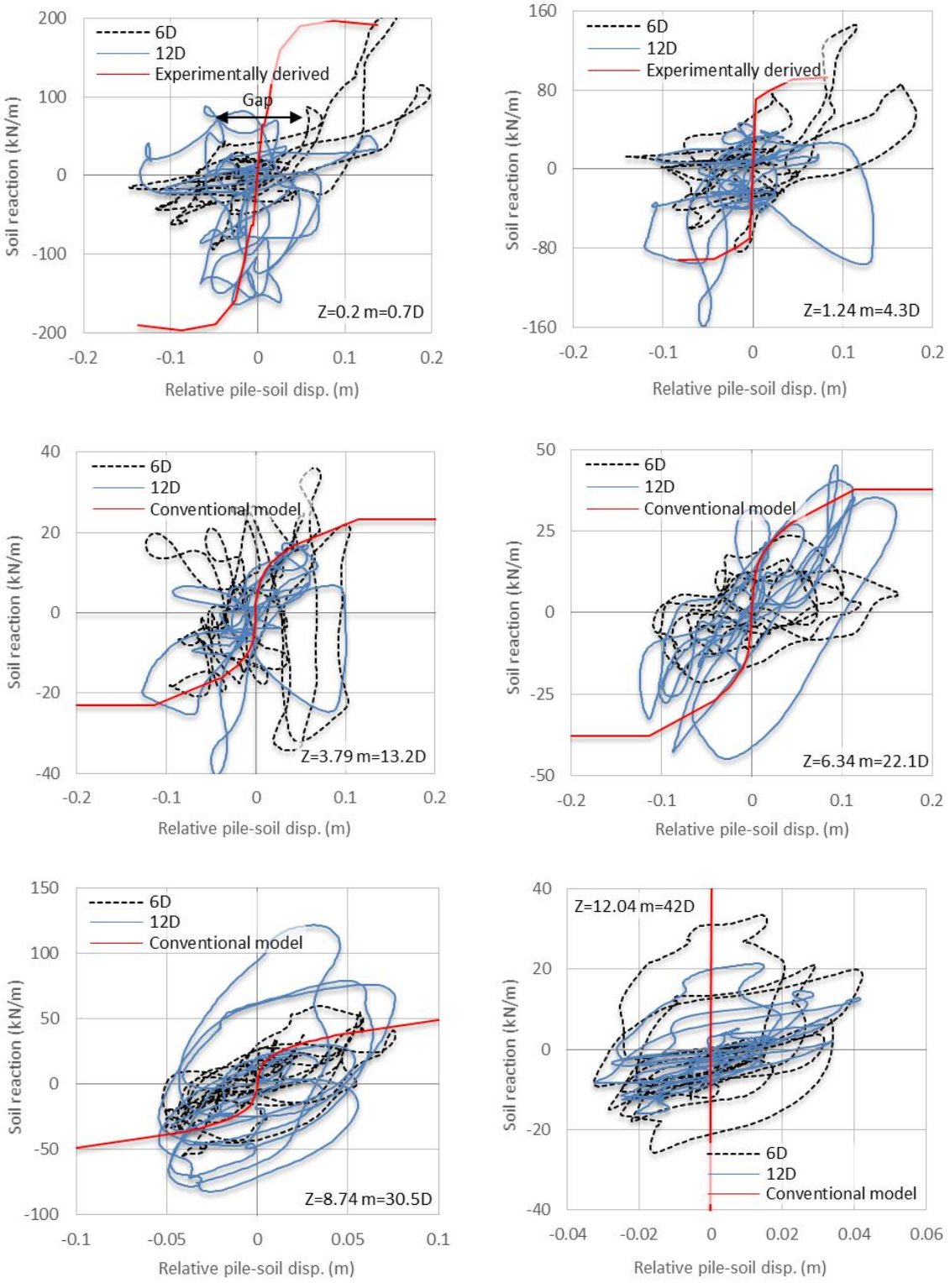

Figure 4.35 Load transfer curves at the depths of free-field accelerometers-Event 3

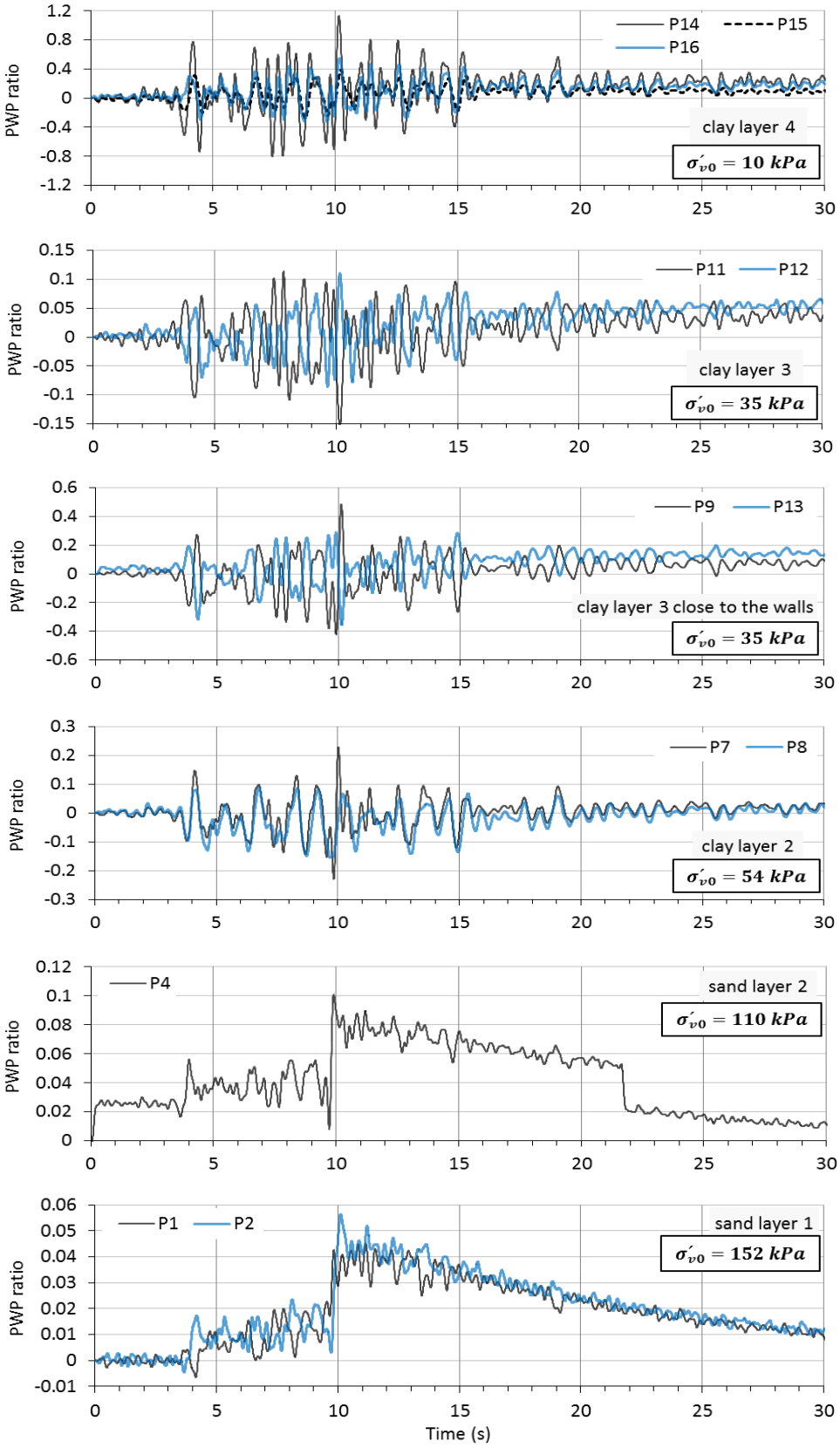

Figure 4.36 PWP time histories-Event 1

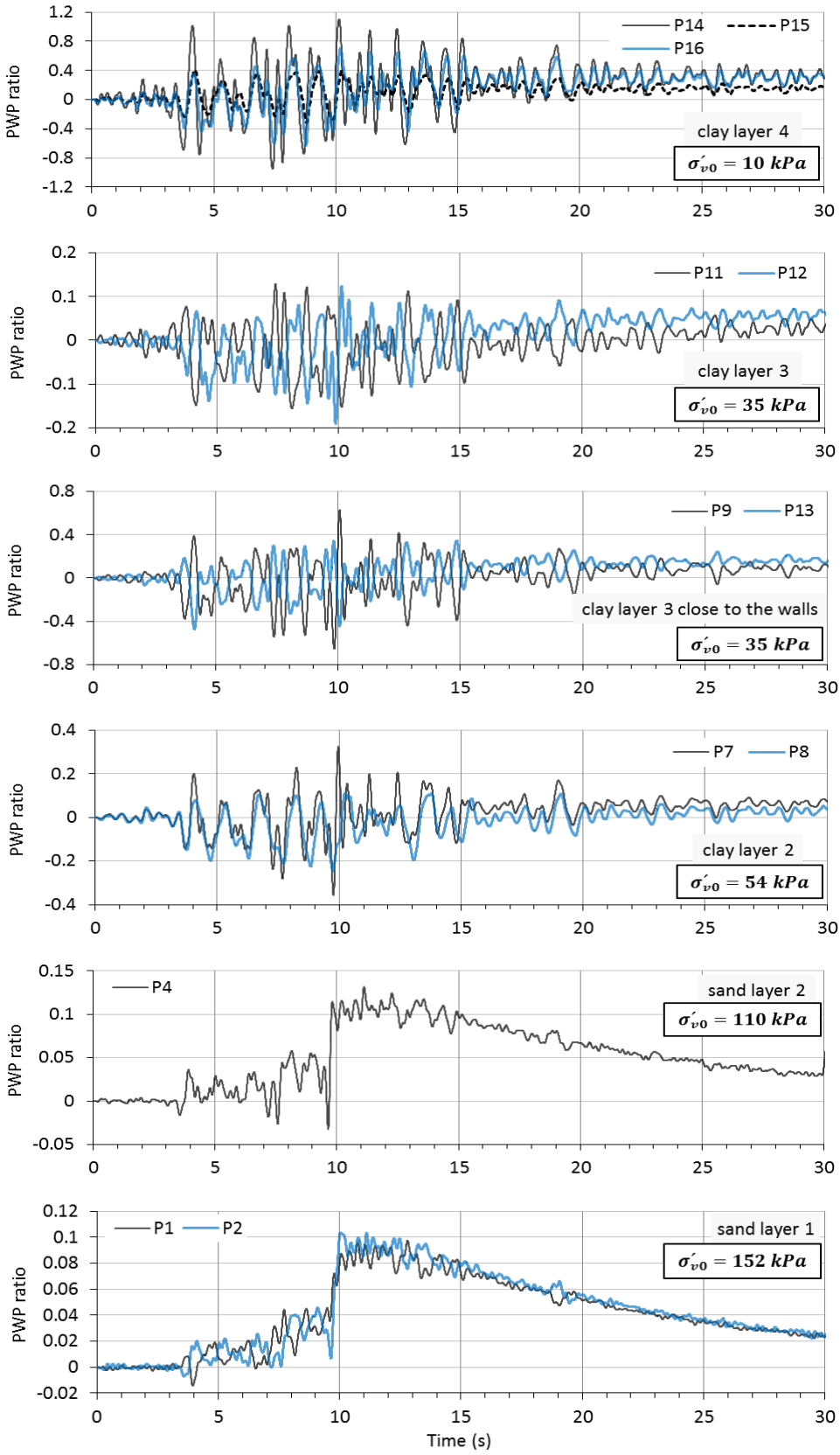

Figure 4.37 PWP time histories-Event 2

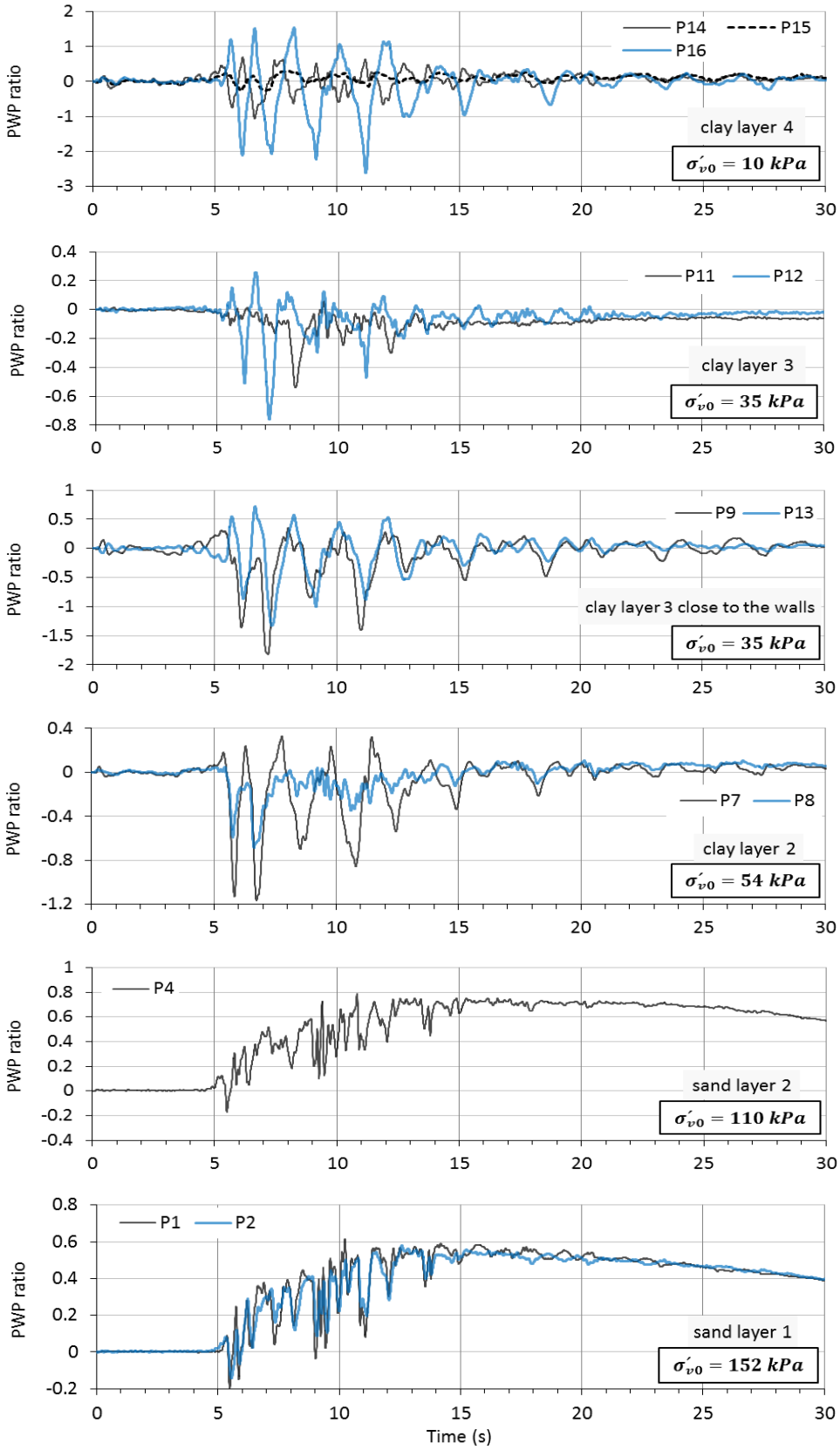

Figure 4.38 PWP time histories-Event 3

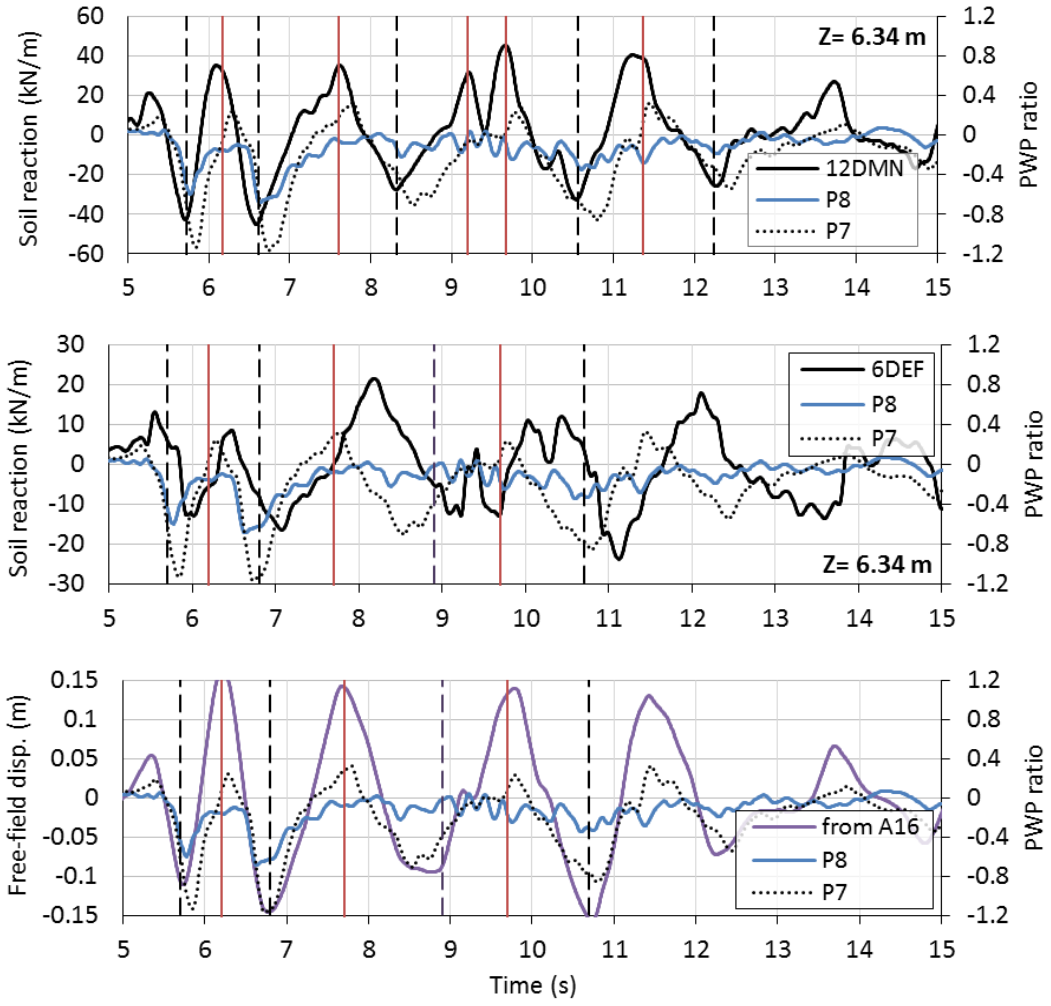

Figure 4.39 Timing of the load-transfer curves reversal points

CHAPTER 5: MODAL IDENTIFICATION OF SOIL-PILE-SUPERSTRUCTURE SYSTEM

5.1 Overview

Modal analysis of vibrating structures has been widely applied in diverse areas including aerospace and aeronautical engineering, civil engineering, and the automotive industries. The objective of modal analysis is to identify the modal parameters of a structure, including natural frequencies, modal damping ratios, and mode shapes, from measurements of its response to an external excitation.

Over the past 20 years, system identification has received increasing attention in experimental and operational modal analysis of instrumented bridges and buildings. Many parametric and nonparametric system identification methods have been well-stablished and applied successfully to structural systems (Alvin et al., 2003). The fundamental objective of any system identification analysis is to evaluate the properties of an unknown system given a known input into, and output from, that system. In most of these methods, the structural response recorded during vibrations induced by wind, traffic, earthquake, impact loads, etc. is employed to identify a predicting mathematical model from which the modal parameters are extracted. The mass, stiffness and damping properties of the structure required for many analytical models can also be estimated using system identification methods (Alvin and Park, 1994; Lus et al., 1999).

One important application of modal parameters is in model validation. For example, analytical or numerical models such as finite element models are often validated by comparing their modal data with those acquired from system identification results (Mottershead, 1993). In designing a vibrating system, it is required to prevent the

coincidence of the system modal frequencies and its operational frequencies such as the case with machine foundations and wind turbines. Similar guidelines are available for structures designed to resist earthquakes, winds, and ocean waves. In other words, modal identification helps in reducing the damage accumulation due to amplifications likely to occur during lifetime of a structure. Another benefit of the modal analysis is that the response to an arbitrary excitation can be obtained simply by super position of the significantly contributing modes. This has been done by synthesizing predicting models using the modal parameters (Alvin et al., 2003). Studying the variations in modal parameters over a structure's lifetime induced by material aging and severe excitations has been considered as an effective tool in health monitoring and assessment (Arici and Mosalam, 2005; Fraraccio et al., 2008).

Susceptibility of a structure to dynamic loads is not only determined by the modal characteristics of the structure itself, but also by the modal characteristics of the underlying soil. The natural frequencies and damping properties of the soil become extremely important in evaluating vibration-induced interactions between the soil, foundation, and superstructure. Many analytical and experimental identification methods have been developed to find reliable estimations of soil modal properties. This chapter provides a brief background on the theory of spectral analysis and subspace-state space system identification methods which are employed later in the analyses of the free-field soil and soil-foundation-structure (SFS) systems. The identified values are validated using available analytical methods.

5.1.1 System identification methods applied to soil systems

In site response analysis, a great deal of effort has been invested to estimate the soil modal parameters from vertical accelerometer array data acquired in seismically active regions or in simplified models used in centrifuge and shake table tests (Dobry and Whitman, 1969; Gazetas, 1982; Zeghal and Elgamal, 2000; Elgamal et al., 1996 ;Hadjian, 2002; Brennan at al., 2005; Conti and Viggiani, 2012; Afacan et al., 2014). The most widely used methods in this area include traditional correlation analysis, spectral analysis, and the shear beam method. These techniques estimate the natural frequencies and damping coefficients using data from a pair of accelerometers, where both accelerometers may be embedded in the soil or one may be embedded with the other placed at the surface. The magnitude of the soil surface acceleration, amplification or attenuation, is of great importance in free-field analysis.

Glaser (1996) and Glaser and Baise (2000) advocated the application of system identification techniques through implementing a variety of time invariant and time varying parametric models where the estimated model parameters were mapped to the mechanical parameters of a lumped-mass oscillator. These models proved surprisingly effective for predicting soil response to earthquakes. However, it should be noted that model order selection was difficult in these methods and only was achieved by empirically matching the model response to recorded data. Another interesting feature of this method is that the modal parameters of systems with general viscous damping can be identified, thereby providing a more realistic approximation of the damping mechanism in layered soils.

5.1.2 Modal identification methods applied to SFS systems

Various methods have been proposed to determine the natural frequencies and damping properties of soil-foundation-superstructure (SFS) systems through experimental, numerical, and simplified analytical modeling. The experimental methods consist mainly of free-vibration and forced-vibration tests that excite either the entire SFS system (e.g., by seismic loading) or only the superstructure. The structural response in time or in frequency domain is then used to identify the modal parameters of the SFS system. Several analytical procedures are also available for computing the modal properties of structures supported on shallow or deep foundations; many of these results are summarized in a report by Stewart et al. (1998). In the case of deep foundations, the basic concept is to replace the pile/pile group with springs and dashpots at the soil surface on which the foundation slab of the superstructure is situated, as illustrated schematically in Figure 5.1. The stiffness and damping of the springs and dashpots in the translational, rotational, and coupled vibration modes are expressed as functions of loading frequency and are called the impedance functions. The dynamic stiffness of a single pile is formulated as the product of the static stiffness and a dynamic modifier. The static stiffness of the pile head at the soil surface depends on the ratio of the pile's Young's modulus to that of the soil, the ratio of the pile length to the diameter (which has been often called the slenderness ratio), and some weighting factors (Poulos and Davis,1980; Scott, 1981; Mylonakis, 1995). The dynamic modifier, on the other hand, is a function of the soil's and the pile's mass densities and elastic moduli, as well as a dimensionless frequency parameter that itself depends on the loading frequency and the soil shear velocity. After the stiffness vlaues of the springs have been determined, the modal

parameters of the structure can be modified accordingly. Veletsos' (1977) two-DOF model is among the most widely used simplified solutions for investigating the effect of soil–structure interaction (SSI) on the frequency content of recordings in the superstructure. The period-lengthening phenomena is, in fact, a result of incorporating the foundation flexibilities into the equations used for calculating the fundamental period of the superstructure.

Dou and Byrne (1995) and Damgaard et al. (2014) performed modal identification in time domain by carrying out free-vibration tests on scaled model piles in sand. The natural frequencies of the soil-pile system was found to be dependent on the amplitude of the vibration. A vast body of literature is available regarding identification methods in the frequency domain. For example, an early study by Gazetas (1984) using FE analyses employed the ratios of pile motion to bedrock and free-field motion to identify resonance frequencies. The results showed that the frequency range between the fundamental frequencies of the soil and the superstructure was substantially amplified. Flores-Berrones and Whitman (1982) and Mylonakis et al. (1997) employed steady-state transfer functions relating bridge and foundation response amplitudes to those of the rock outcrop and the free-field. The resulting transfer functions indicated a resonance at the fundamental frequency of the soil stratum. Makris (1997) used the ratio of pile displacement at various depths to ground motion amplitude where the model was subjected to harmonic motions in shake table tests. Two major peaks were observed, one at the natural frequency of the soil deposit and the other at the natural frequency of the superstructure. Stewart and Fenves (1998) considered parametric and non-parametric system identification methods using the motion records at the free-field, building roof,

and foundation level to estimate the modal parameters associated with fixed-base and flexible-base conditions.

Ashlock and Pak (2009) identified vertical, horizontal, and rocking modes of single piles through small-strain forced vibration tests with random and impact loads. The modal parameters, including the natural frequencies and the associated damping ratios, were estimated by deriving the "accelerance functions," i.e., the ratio of pile acceleration to the applied force in the frequency domain. The peaks of these functions represented the natural frequencies of the SFS system. The derived accelerance functions shared similar features: a sharp peak in the low-frequency range and a gentle broad peak at higher frequencies. A similar methodology was employed by Lombardi and Bhattacharya (2014) to identify the natural frequencies of soil-pile-top mass systems under vertical vibration. Observations showed that the first natural frequency of the system was reduced as the shaking intensified and there was a progressive reduction of soil stiffness due to liquefaction. Ashford and Juirnarongrit (2003) used the same method to analyze the vibration-induced responses of cast-in-drilled-hole piles with various diameters. Rovithis et al. (2009) introduced the notion of two dominant frequencies—effective natural frequency and pseudo-natural frequency—and discussed these frequencies' role in the seismic response of pile foundations. At the effective natural frequency, the pile response was amplified, whereas at the pseudo-natural frequency, a significant de-amplification of the pile head motion with respect to the free-field was observed.

In analyzing the piles dynamic response, the non-parametric identification method (spectral analysis method) proposed by Stewart et al. (1998) will be employed (see Section 5.3.2) because it was found to be very effective in answering some of the

questions that arose in Chapter 4 regarding the unexpected displacement and acceleration responses of piles UIAB and 6DEF.

5.2 Methods of modal identification

5.2.1 Spectral analysis method

To provide context, it is helpful to begin with a brief overview of spectral analysis method used for estimating the transfer functions. Transfer functions (commonly referred to as frequency response functions) are used to examine the response of dynamic systems and are estimated given a pair of input-output signals. Transfer function of a system shows how the magnitude and phase of the input signal in the frequency domain are changed by the system. The plot of the transfer function magnitude depicts those frequencies that were amplified or attenuated by the system and thereby allowing for identification of the natural frequencies. That is why it is sometimes called the amplification function.

In principle, a single-input/single-output linear time-invariant dynamic system can be characterized completely by its transfer function $H(\omega)$ given by

$$H_F(\omega) = \frac{Y(\omega)}{U(\omega)}, \text{ or} \tag{5.1}$$

$$|H_P(\omega)| = \frac{PSD_y(\omega)}{PSD_u(\omega)}. \tag{5.2}$$

Fundamentally, $H_F(\omega)$ in Eq. 5.1 represents the ratio of the Fourier transform of the output signal $y(k)$ to that of the input signal $u(k)$. Here, *k* denotes the time instant. It is assumed that the input and output signals are deterministic discrete-time data sequences with length *N*. The *N*-point Fourier transform of the output signal is defined as

$$Y(n) = \sum_{k=1}^{N} y(k)e^{-i\omega k}, \quad \omega = \frac{2\pi}{N}n, \quad k=1, 2, 3 \ldots N; \tag{5.3}$$

the input Fourier transform is defined analogously. The physical frequency Ω with units of cycle per sampling interval (T_s) is related to ω as

$$\Omega = \omega/T_s. \tag{5.4}$$

For a random input signal it is very likely that its Fourier transform does not exist (i.e. zero amplitude) or is very small at some frequencies, causing the $H_F(\omega)$ ratio to be undefined or unreasonably large. For this reason, transfer function is usually computed from power spectral density (PSD) functions of the input and output signals, which always exist (Pandit, 1991). The magnitude of the transfer function as expressed in Eq. 5.2 is the ratio of the power spectral density of the output signal $PSD_y(\omega)$ and that of the input signal $PSD_u(\omega)$. The PSD is real-valued, positive and even, and it gives the distribution of energy per unit of frequency. Here, PSD is defined as the Fourier transform of the auto-correlation function $r(k)$:

$$PSD(\omega) = \sum_{k=-(N-1)}^{N-1} r(k)e^{-i\omega k}\ , \tag{5.5}$$

where the auto correlation function for the output signal is given by

$$r(k) = \sum_{i=1}^{N} y(i)y(i-k)\ . \tag{5.6}$$

The autocorrelation of the input is defined similarly. The statistical variability of the estimated PSD due to poor accuracy of the auto correlation function for large time lags close to the signal length can be alleviated by forcing the end of the correlation function to zero. This can be achieved by windowing the auto correlation function in the time domain using a lag window (Safak, 1997; Stoica and Moses, 2005; Mikami et al., 2008). In the frequency domain, this is equivalent to applying a locally weighted average of the PSD around a certain frequency. This can be achieved by implementing the Blackman-Tukey Spectral estimator (Stoica and Moses, 2005) as follows:

$$PSD_w(\omega) = \sum_{k=-(N-1)}^{N-1}[w(k)r(k)]e^{-i\omega k} = 2Re\left\{\sum_{k=0}^{N-1}[w(k)r(k)]e^{-i\omega k}\right\} - w(0)r(0) \quad (5.7)$$

where $w(k)$ is the lag window with length $2M+1$ such that $w(0)=1$ and $w(k)=0$ for $|k| \geq M$. It can be thought of as a moving average filter by assigning a weighted sum of $2M+1$ values around a certain point. The smaller the length of the lag window in time domain, less band limited the smoothing window would be in frequency domain. Many smoothing windows are popular, including Parzin, Hanning, Hamming, and Bartlett (Stoica and Moses, 2005). Figure 5.2 compares the two transfer functions obtained implementing Eqs. 5.1 and 5.2 and labeled as unsmoothed and smoothed, respectively, on earthquake induced input and output signals. Small frequency content of the input signal at certain frequencies caused spurious peaks in the transfer function spectra using Eq. 5.1 which were removed applying a smoothing window.

Despite the easy implementation of the methods described for deriving the transfer functions, there exist a number of potential issues such as leakage due to non-periodicity of the signal and sensitivity to the measurement noise. Moreover, with spectral analysis, a successful identification cannot be guaranteed unless excitations are wideband and rich in frequency stationary signals (Glaser, 1995). It should be emphasized that spectral analysis methods result in accurate estimations provided that the system behavior remains linear during low amplitude excitations and the peaks of the transfer function are well separated. Resonant frequencies of system appears around the peaks of the transfer function amplitude. The associated damping can be calculated using the half-power bandwidth method; however, poor estimation of damping is expected due to the sensitivity of the transfer functions to the shape and the length of the smoothing windows.

Consequently, alternative methods have been proposed to overcome these inherent problems of the frequency domain techniques such as state-space identification methods. The following section briefly reviews the theoretical foundations of state-space modeling as applied to general mechanical systems and introduce the well-known subspace state space system identification (4SID) algorithm that will be used in Section 5.4 to identify the modal parameters of the free-field soil.

5.2.2 Subspace state-space system identification method

State space techniques for representing general mechanical systems are briefly reviewed in Section 5.2.2.1 followed by the theory of 4SID method in Section 5.2.2.2.

5.2.2.1 State space representation of equation of motion in mechanical systems

The coupled second-order differential equations for the motion of a mechanical system with *N* DOFs (i.e., $\boldsymbol{M}\ddot{d}(t) + \boldsymbol{L}\dot{d}(t) + \boldsymbol{K}d(t) = \boldsymbol{\beta}u(t)$) can be represented by a collection of first-order differential equations called "state equations." By defining a physical state vector $x_p(t) = [d(t)^T \quad \dot{d}(t)^T]^T \in \mathbb{R}^{2N}$ containing the displacement $d(t) \in \mathbb{R}^N$ and velocity $\dot{d}(t)$ of all DOFs, the corresponding state space representation becomes

$$\begin{bmatrix} \boldsymbol{L} & \boldsymbol{M} \\ \boldsymbol{M} & \boldsymbol{0} \end{bmatrix} \dot{x}_p(t) = \begin{bmatrix} -\boldsymbol{K} & \boldsymbol{0} \\ \boldsymbol{0} & \boldsymbol{M} \end{bmatrix} x_p(t) + \begin{bmatrix} \boldsymbol{\beta} \\ \boldsymbol{0} \end{bmatrix} u(t), \tag{5.8}$$

with mass matrix $\boldsymbol{M} \in \mathbb{R}^{N\times N}$, damping matrix $\boldsymbol{L} \in \mathbb{R}^{N\times N}$, and stiffness matrix $\boldsymbol{K} \in \mathbb{R}^{N\times N}$. The input influence matrix $\boldsymbol{\beta} \in \mathbb{R}^{N\times r}$ relates the excitation forces in vector $u(t) \in \mathbb{R}^r$ to the corresponding DOFs (Alvin et al., 2003). The response of the mechanical system $y(t)$ measured at *m* DOFs can be expressed in terms of $m \times N$ displacement, velocity and acceleration output influence matrices $\boldsymbol{H_d}$, $\boldsymbol{H_v}$, and $\boldsymbol{H_a}$ according to

$$y(t) = [\boldsymbol{H_d} - \boldsymbol{H_a}\boldsymbol{M^{-1}}\boldsymbol{K} \quad \boldsymbol{H_v} - \boldsymbol{H_a}\boldsymbol{M^{-1}}\boldsymbol{L}]x_p(t) + \boldsymbol{H_a}\boldsymbol{M^{-1}}\boldsymbol{\beta}u(t). \tag{5.9}$$

In cases, where only acceleration measurements are acquired, $\boldsymbol{H_d}$ and $\boldsymbol{H_v}$ become identically zero. The order of the state space model is defined as the number of state variables in the state vector, i.e. two times the number of DOFs.

The modal parameters of the system can be obtained by solving the symmetric eigenvalue problem associated with Eq. 5.8. The eigenvalue problem can be diagonalized simultaneously if the eigenvectors are normalized with respect to the physical properties of the system i.e., $\boldsymbol{M}$, $\boldsymbol{L}$, and $\boldsymbol{K}$. The resulting diagonal matrices are given by

$$\begin{bmatrix} \boldsymbol{\psi} \\ \boldsymbol{\psi\Lambda} \end{bmatrix}^{\mathbf{T}} \begin{bmatrix} \boldsymbol{L} & \boldsymbol{M} \\ \boldsymbol{M} & \mathbf{0} \end{bmatrix} \begin{bmatrix} \boldsymbol{\psi} \\ \boldsymbol{\psi\Lambda} \end{bmatrix} = \boldsymbol{I} \tag{5.10}$$

$$\begin{bmatrix} \boldsymbol{\psi} \\ \boldsymbol{\psi\Lambda} \end{bmatrix}^{\mathbf{T}} \begin{bmatrix} -\boldsymbol{K} & \mathbf{0} \\ \mathbf{0} & \boldsymbol{M} \end{bmatrix} \begin{bmatrix} \boldsymbol{\psi} \\ \boldsymbol{\psi\Lambda} \end{bmatrix} = \boldsymbol{\Lambda}, \tag{5.11}$$

where $\boldsymbol{\Lambda} \epsilon \mathbb{C}^{2N \times 2N}$ is a diagonal matrix with complex eigenvalues λ_i, and $\boldsymbol{V} = [\boldsymbol{\psi^T} \quad (\boldsymbol{\psi\Lambda})^{\boldsymbol{T}}]^{\boldsymbol{T}}$ is a $2N \times 2N$ matrix containing the corresponding complex eigenvectors $\psi_i, i = 1 \ldots 2N$. Other forms of scaling the eigenvectors are discussed in Balmes (1997). By changing the state vector to $\eta(t)$ given by $x_p(t) = [\boldsymbol{\psi^T} \quad (\boldsymbol{\psi\Lambda})^{\boldsymbol{T}}]^{\boldsymbol{T}} \eta(t)$ the system states are transferred to the modal space. The system equations in the modal form become

$$\dot{\eta}(t) = \boldsymbol{\Lambda}\eta(t) + \boldsymbol{\psi}^T \boldsymbol{\beta} u(t), \tag{5.12}$$

$$y(t) = \boldsymbol{H_a \Lambda^2 \psi} \eta(t) + \boldsymbol{H_a M^{-1} \beta} u(t), \tag{5.13}$$

where $\boldsymbol{H_a}$ is an identity matrix for the case of acceleration measurements at all DOFs. The columns of $\boldsymbol{\psi}$ in Eqs. (5.12) and (5.13) are the complex displacement mode shapes. For underdamped systems, modes appear in complex conjugate pairs. A complex conjugate pair of eigenvalues accompanied by the corresponding complex conjugate pair of eigenvectors belong to one vibration mode. From the complex conjugate eigenvalue

pairs the natural frequencies f_i and damping ratios ξ_i of each mode can be retrieved using the following equations (Alvin et al., 2003)

$$f_i = \frac{|\lambda_i|}{2\pi}, \tag{5.14}$$

$$\xi_i = \frac{-Re(\lambda_i)}{|\lambda_i|}. \tag{5.15}$$

The real-valued undamped or normal mode shape $\boldsymbol{\phi}$ can be extracted from the complex eigenvector $\boldsymbol{\psi}$ given in Eqs. (5.12) and (5.13) (Alvin et al., 1997). To this end, we assume that the external forces in $u(t)$ are imposed on the system at r DOFs. However, in base excitation problems the external force at each DOF is modeled as a mass at that DOF multiplied by the base acceleration in the opposite direction. Thus, in Eq. 5.8, $\boldsymbol{\beta}$ becomes a vector containing the masses of all DOFs and $u(t)$ is simply the negative of the base acceleration. As a result, $y(t)$ in Eq. 5.13 represents the acceleration with respect to the base. In the next section, we will show how the state space model described in Eqs. (5.12) and (5.13) can be identified provided that the mass matrix, the base acceleration, and the structural response are available.

5.2.2.2 Subspace state space system identification (4SID)

In control and system theory, dynamic systems are modeled by differential or difference equations in the time domain. The system may be interpreted simply as a block that executes a prescribed set of mathematical operations on externally supplied inputs to calculate the outputs. The measured inputs and outputs of a discrete-time, linear, time-invariant, system can be fit into a discrete-time state space model

$$x(k+1) = \boldsymbol{A_d}x(k) + \boldsymbol{B_d}u(k) \tag{5.16}$$

$$y(k) = \boldsymbol{C_d}x(k) + \boldsymbol{D_d}u(k), \tag{5.17}$$

where $\boldsymbol{A_d} \in \mathbb{R}^{n\times n}$ is the state matrix, $\boldsymbol{B_d} \in \mathbb{R}^{n\times r}$ is the input matrix, $\boldsymbol{C_d} \in \mathbb{R}^{m\times n}$ is the output matrix, $\boldsymbol{D_d} \in \mathbb{R}^{n\times r}$ is a matrix through which inputs are directly fed into the outputs, and subscript $\boldsymbol{d}$ denotes discrete time. The state vector $x(k) \in \mathbb{R}^n$ includes n state variables that describe the internal states of the system. The input is a deterministic vector $u(k) \in \mathbb{R}^r$ including r input measurements at time instant k and $y(k) \in \mathbb{R}^m$ is the corresponding output vector including m output measurements at the same time.

The goal of system identification is to determine the constant matrices $\boldsymbol{A_d}$, $\boldsymbol{B_d}$, $\boldsymbol{C_d}$ and $\boldsymbol{D_d}$ given $u(k)$ and $y(k)$ measured in an experiment. For state space identification of a controllable and observable system, a wide variety of methods are available (Viberg, 1995). In this dissertation the focus will be on 4SID, a relatively new technique which has been successfully employed recently in modal identification of a variety of complex structures including bridges (Peeters and Ventura, 2003; Siringoringo and Fujino, 2008; Weng et al., 2008; He et al., 2009). The objective in this section is not to provide a rigorous detailed treatment of 4SID, but rather to convey the basic ideas of the approach in an accessible way. Interested readers are referred to work of Viberg (1995) for a comprehensive overview of data-driven or direct subspace identification methods and to the book published by Van Overschee and De Moor (1996) for a detailed treatment of 4SID.

Subspace state space methods begin by constructing the block Hankel matrices from the measured data samples. The past input and the past output block Hankel matrices are defined by

$$\boldsymbol{U}_{0|i-1} = \begin{bmatrix} u_0 & u_1 & \dots & u_{j-1} \\ u_1 & u_2 & \dots & u_j \\ \vdots & \vdots & \vdots & \vdots \\ u_{i-1} & u_i & \dots & u_{i+j-2} \end{bmatrix}, \boldsymbol{Y}_{0|i-1} = \begin{bmatrix} y_0 & y_1 & \dots & y_{j-1} \\ y_1 & y_2 & \dots & y_j \\ \vdots & \vdots & \vdots & \vdots \\ y_{i-1} & y_i & \dots & y_{i+j-2} \end{bmatrix}, \tag{5.18}$$

respectively. The block Hankel matrix of the future inputs $\boldsymbol{U}_{i|2i-1}$and the future outputs $\boldsymbol{Y}_{i|2i-1}$ are formed in a similar way by adopting proper indices where the first number specifies the subscript of the entry in the first row of the first column while the second number specifies the subscript of the entry in last row of the first column. On the other hand, the subscript of the matrix entries identifies the data sample number. It is to be noted that each column is a time-shifted version of the previous column, and the distinction between the past and future can be assessed by checking the corresponding columns of $\boldsymbol{U}_{0|i-1}$ and $\boldsymbol{U}_{i|2i-1}$ that they have no common entries. Here, i is the number of block rows in the block Hankel matrices and is a user defined parameter. The value of this parameter is selected to be greater than the model order, but much smaller than the number of columns, j (Van Overschee and De Moor, 1996). The number of columns can be calculated known i and the total number of time samples. By stacking the block Hankel matrices corresponding to the past data over the ones associated with the future data, $\boldsymbol{U}$ and $\boldsymbol{Y}$ matrices are constructed as

$$\boldsymbol{U} = \begin{bmatrix} \boldsymbol{U}_{0|i-1} \\ \boldsymbol{U}_{i|2i-1} \end{bmatrix}, \qquad \boldsymbol{Y} = \begin{bmatrix} \boldsymbol{Y}_{0|i-1} \\ \boldsymbol{Y}_{i|2i-1} \end{bmatrix}. \tag{5.19}$$

For consistent identification of a linear system it should be verified whether the input signal is persistently exciting. This condition is satisfied if the rank of $\boldsymbol{U}$ is equal to $2ir$ (Van Overschee and De Moor, 1996). The performance of 4SID algorithm heavily relies on the assumptions imposed on the input data. A broadband and stationary signal with a high signal to noise ratio is ideal for a successful identification. Therefore, checking the input data for these assumptions is a crucial step.

System identification using subspace methods implements two approaches to estimate the matrices in the state space model defined by Eqs. (5.16) and (5.17): the shift

invariance approach and the least-squares estimates of the system matrices provided that the state sequence $\boldsymbol{X}_i = [x_i \quad x_{i+1} \quad \cdots \quad x_{i+j-1}]$ is known. Geometric operations of subspaces spanned by the column or row vectors of block Hankel matrices formed by the input and output data is used to estimate the state sequence. In this study, the latter method where $\boldsymbol{Y}$ is decomposed into orthogonal matrices one of which is the product of the extended observabiliy matrix and the state sequence is used. Singular value decomposition (SVD) of the product of the extended observabiliy matrix and the state sequence determines the optimal order of the system. For an ideal noise-free data, the number of singular values greater than zero is the minimum model order whereas for noise-corrupted data with a low level of noise, the number of singular values above a noise threshold specifies the system order. Once the state sequence is estimated the system matrices $\widehat{\boldsymbol{A}}_{\boldsymbol{d}}$, $\widehat{\boldsymbol{B}}_{\boldsymbol{d}}$, $\widehat{\boldsymbol{C}}_{\boldsymbol{d}}$, and $\widehat{\boldsymbol{D}}_{\boldsymbol{d}}$ can be extracted from

$$\begin{bmatrix} x_{i+1} & x_{i+2} & \cdots & x_{i+j} \\ y_i & y_{i+1} & \cdots & y_{i+j-1} \end{bmatrix} = \begin{bmatrix} \widehat{\boldsymbol{A}}_{\boldsymbol{d}} & \widehat{\boldsymbol{B}}_{\boldsymbol{d}} \\ \widehat{\boldsymbol{C}}_{\boldsymbol{d}} & \widehat{\boldsymbol{D}}_{\boldsymbol{d}} \end{bmatrix} \begin{bmatrix} x_i & x_{i+1} & \cdots & x_{i+j-1} \\ u_i & u_{i+1} & \cdots & u_{i+j-1} \end{bmatrix}. \tag{5.20}$$

When the number of data points $j \to \infty$ the optimization problem of determining the system matrices is solved in a least squares sense. A finite number of data points, presence of high noise level or over estimation of the system order might give rise to unstable models. For the detailed explanation of the identification algorithm and the geometric interpretation of the subspace method the readers are referred to Van Overschee and De Moor (1996) and Kim and Lynch (2012a).

The estimated system matrices can be transformed to their continuous time counterparts $\boldsymbol{A}_{\boldsymbol{c}}$, $\boldsymbol{B}_{\boldsymbol{c}}$, $\boldsymbol{C}_{\boldsymbol{c}}$ and $\boldsymbol{D}_{\boldsymbol{c}}$ using the zero-order hold assumption (Juang, 1993) in order to be consistent with the state space representation of the physical system in Eqs. (5.8) and (5.9). Note that $\boldsymbol{C}_{\boldsymbol{c}} = \widehat{\boldsymbol{C}}_{\boldsymbol{d}}$ and $\boldsymbol{D}_{\boldsymbol{c}} = \widehat{\boldsymbol{D}}_{\boldsymbol{d}}$. Using the eigenvectors of $\boldsymbol{A}_{\boldsymbol{c}}$, denoted

by $\boldsymbol{\varphi_c}$, the identified continuous time system can be converted to its modal coordinates $\mu(t)$ as defined by $x(t) = \boldsymbol{\varphi_c}\mu(t)$

$$\dot{\mu}(t) = \boldsymbol{\Lambda_c}\mu(t) + \boldsymbol{\varphi_c}^{-1}\boldsymbol{B_c}u(t), \tag{5.21}$$

$$y(t) = \boldsymbol{C_c}\boldsymbol{\varphi}_c\mu(t) + \boldsymbol{D_c}u(t), \tag{5.22}$$

where $\boldsymbol{\Lambda_c}$ is a diagonal matrix containing eigenvalues of $\boldsymbol{A_c}$. The eigenvalues of the continuous time model λ_c are related to the eigenvalues of the discrete time model λ_d through

$$\lambda_c = \ln(\lambda_d)/T_s. \tag{5.23}$$

where T_s is the sampling interval. However, both the discrete and continuous time models have the same set of eigenvectors (Juang, 1993). It worth mentioning that the eigenvectors of the state space model represented by Eqs. (5.12) and (5.13) are normalized with respect to the mass matrix. De Angelis and Imbimbo (2012) showed that in base excitation problems, scaling the mode shapes can be performed having the mass of one DOF known a *priori*. The proposed scaling approach also demands a complete set of mode shapes in which the number of sensors or the elements in each mode shape vector is equal to the number of identified modes. For lumped-mass systems, this implies that all vibration modes are adequately excited and identified. Once the eigenvectors are scaled, the entire mass matrix as well as the stiffness and damping matrices of the system can be derived as (De Angelis et al., 2002)

$$\boldsymbol{M} = (\boldsymbol{\psi\Lambda\psi}^T)^{-1}, \boldsymbol{L} = -\boldsymbol{M\psi\Lambda}^2\boldsymbol{\psi}^T\boldsymbol{M},\ \boldsymbol{K} = -(\boldsymbol{\psi\Lambda}^{-1}\,\boldsymbol{\psi}^T)^{-1}. \tag{5.24}$$

5.3 Application of system identification procedures-Spectral analysis

5.3.1 Free-field soil system

Soil motion at seven different depths recorded by accelerometers A2, A6, A11, A16, A20, A26, and A32 (Figure. 2.11) were selected as outputs, and the base acceleration measured by A46 was introduced as input. The transfer functions were computed from the power spectral density (PSD) of the soil acceleration at a specific depth (i.e. the output) over the PSD of the base motion (i.e. the input). Small frequency content of the input base motion at certain frequencies (Figure. 5.3) caused spurious peaks in the transfer function spectra as already shown in Figure 5.2. Bartlett lag windows with lengths 700 were employed to remove the fictitious peaks in the transfer functions.

As shown in Figure 5.3, the first and second events are characterized by a predominant frequency at 2.4 Hz. However, in the third event the majority of the base motion energy is carried by the harmonic components with lower frequencies between 0.5 to 1.5 Hz. The frequency at which the spectral peaks occur, referred to as the predominant frequency of ground motion which is generally controlled by the tectonic regime, earthquake magnitude, and site-source distance in real world.

The transfer function amplitude for each pair of base and soil acceleration data acquired from the first and second events are shown in Figure 5.4a and 5.4b, respectively. Two important observations can be made from these graphs. First, the amplification in deeper layers occurs at frequencies greater than 2 Hz, while in the uppermost layer amplification is pronounced at lower frequencies around 1 Hz. This behavior is expected since soil layers act as low-pass filters removing the high frequencies in the propagating waves. The natural frequencies of the soil system are identified as the peaks of the transfer

functions at 1 Hz, 2.8 Hz and in the frequency range of 5-6 Hz. The transfer function for the pair A46-A2 and pair A46-A6 have values close to unity, indicating a negligible amplification of response within the dense sand layer. The above observation implies that the soil profile is likely responding as a single inhomogeneous layer where the response is dominated by the upper soft clay layer.

The transfer function spectra obtained for the second and third shaking events depicted in Figure 5.4 showed noticeable changes compared to the first event reflecting the nonlinearity in the soil system. For instance, the second and third natural frequencies in the first event around 2.8 Hz and in the range of 5-6 Hz were shifted towards lower frequencies of 2.2 Hz and 4-5 Hz. Moreover, transfer functions in the third event differ from the first two in that there is essentially only one significant peak in the first two events while in the third event, multiple peaks with nearly the same magnitude were observed. Transfer functions at deeper layers (i.e. TF A46-A2, TF A46-A6, TF A46-A11) peaked at 1.5 Hz, 3.5 Hz, 5.7 Hz, 6.7 Hz, and 9 Hz whereas the ones corresponding to the surface layers showed only one peak at about 0.3 Hz.

5.3.2 Soil-pile-top mass system

Under seismic excitations, two different interaction mechanisms, known as inertial and kinematic interactions, can be idealized between the superstructure above the ground surface and the foundation at or below the soil surface. This an idealization. In reality these two effects are always present and coupled together. Inertia developed in the superstructure due to its own vibrations gives rise to base shear and over-turning moment at the interface of the superstructure and the foundation. Those in turn lead the foundation to experience translational and rotational displacements relative to the free-field.

Kinematic interaction, on the other hand, involves the response of a hypothetical system different from the actual system in that the superstructure and the foundation slab are assumed to be massless. The presence of a stiff foundation on or within the soil causes the foundation motions to deviate from the soil motions in free-field. The response of the superstructure can be estimated by superposition of these two effects even in the presence of slight nonlinearities (Stewart et al., 1998).

In analysis of superstructures supported on "fixed bases," zero displacements and zero rotations are assumed at the foundation level. Approximate methods based on the equivalent single degree of freedom (SDOF) models have been used to effectively demonstrate the interaction mechanisms in SFS systems, as illustrated schematically in Figure 5.5 (Rovithis et al., 2009). The lateral deflection of a SDOF fixed-base structure with respect to an inertial frame of reference U_s consists of the displacement relative to the base $U_{s,rel}$ and the displacement of the free-field soil U_{ff} (Figure 5.5a). The superstructure stiffness determines the value of $U_{s,rel}$. The ground motions U_{ff} can be measured directly in the free-field or predicted by estimating the rock motion for the site and then performing a site response analysis. In contrast, in analyzing structures with "flexible bases," the foundation is allowed to have translational displacement U_p and rotational displacement θ_p with respect to the free-field, which contribute to the superstructure's total displacement (Figure 5.5b). In calculating the superstructure motion, pile-head motion (calculated through kinematic interaction analysis) is applied to the support ends of the foundation springs and dashpots (as discussed earlier) as the foundation input motion. This analysis assumes that foundation input motion is not altered by inertial effects of the superstructure.

Stewart et al. (1998) introduced three sets of input–output data that can be used to estimate the natural frequencies of a superstructure associated with a flexible-base, a pseudo-flexible base, and a fixed-base (Table 5.1). The pseudo-flexible-base case applies to conditions of partial base flexibility and considers only the effects of foundation rocking at the soil surface. This case is important because the actual flexible-base parameters are often well-approximated by pseudo-flexible-base parameters, especially when the free-field motion is not available. Stewart et al. (1998) noted that the flexible-base first modal frequency is smaller than the pseudo-frequency, and the pseudo-frequency is smaller than that of the fixed-base. Because it is assumed that the behavior of the entire system remains in the elastic realm, the results should be the same regardless of whether displacement or acceleration data are used.

5.3.2.1 Application

By assigning the absolute acceleration of free-field soil measured by A32 as the input (Figure 5.6) and that of the top masses as the outputs (Figures 4.2-4.4), the flexible-base transfer functions were derived for all three shaking events. However, because direct measurements of pile displacements (or accelerations) and rotations at the soil surface were not available, the transfer functions associated with the pseudo-flexible base and the fixed-base were not estimated. The results are discussed in the following section.

5.3.2.2 Observations and interpretation of results

Before discussing the transfer functions, it is worth examining the frequency contents of the base motion along with those of the input and output signals. It is to be noted that the selected frequency bandwidth of the filters used in processing the accelerometer data was 0.3 Hz to 7 Hz in the first and second events, whereas it was expanded to approximately

0.25 Hz to 10 Hz in the third event due to different characteristics of the noise present in the measurements which were found to be dependent on the excitation level.

The compatibility of the soil motion recorded at the surface and at a depth of 0.2 m was inspected by comparing the frequency contents of the acceleration records at the corresponding locations. As Figure 5.7 shows, similar trends with slight differences between the maximum values were observed, confirming the adequacy of A32 in the vertical array of DH3 as a representative for free-field soil motion.

As shown in Figure 5.8, in the first event, significant de-amplification of the motion on top masses with respect to the free-field motion is evident for all piles in the frequency range of 0.3-2.2 Hz, but with a lower extent for 6DEF. In other words, if a harmonic excitation with a frequency in this range is introduced as the free-field motion, the amplitude of the motion on the top masses will be reduced. The fundamental frequency of the soil system also emerged in this range (Figure 5.4). It is noteworthy that the frequency content of the free-field soil and top masses were almost identical from 2.2 Hz to 3.4 Hz except in the case of 6DEF, which showed considerable amplification. Amplification in the other piles occurred at higher frequencies: for UIAB, a sharp peak appeared at 3.8 Hz; and for 12DMN, multiple peaks occurred in the range of 3.6 Hz to 4.2 Hz. For 9DIJ, mild amplification was noticed, with several peaks in a wider range of 3.5 Hz to 7 Hz (the higher half of the frequency range of interest).

In the second event, the same patterns of de-amplification and amplification were observed (Figure 5.9). The highest peaks of the Fourier spectra were observed at 4.1 Hz for UIAB, 9DIJ, and 12DMN, and at 2.5 Hz for 6DEF. The common peak at 4.1 Hz was in the vicinity of the third vibration mode of the soil system, which will be estimated

analytically later in Section 5.5.1. A second peak with smaller magnitude was also detected in both UIAB and 6DEF around 3.4 Hz. In general, in the first two events, no amplification appeared in the vicinity of the first mode of the soil about 1.2 Hz; however, in this frequency range, the smallest de-amplification occurred in 6DEF. On the other hand, significant amplification in 6DEF occurred at frequencies that coincided with the second mode of the free-field soil at around 2.8 Hz while amplification in other piles took place in higher frequencies and around higher vibrational modes of the free-field soil.

In the third event, the Fourier transform of the free-field soil motions (Figure 5.7c) showed that most of the incident energy was carried by the harmonic components with frequencies smaller than or about 1.6 Hz. For frequencies exceeding 1.6 Hz, the free-field input motion became very weak. As evident in Figure 5.10, significant amplifications occurred for UIAB in the frequency range of 0.2 Hz to 2 Hz, including its highest peak at 1 Hz. Within the same frequency range, weaker or even no amplifications were observed for 6DEF, 9DIJ and 12DMN. Another observation from this figure is that the frequency range carrying the main part of the motion energy was gradually shifted towards higher frequencies as the size of the improved zone increased.

The frequency content of the top mass motions with respect to the free-field motion revealed that the role of the soil's fundamental frequency (at 1.2 Hz) was less significant in the first and the second events (excluding 6DEF) compared to the third event, where the response of UIAB appeared to be dominated by the soil characteristics. This might explain the amplified acceleration response of UIAB in the third event and of 6DEF in the first and second events. The amplified frequencies are summarized in Table 5.2.

Although not measured in this experiment, the response of the improved soil (ground) to earthquake motion far away from the piles could be very insightful in defining the appropriate free-field motion. A question that naturally arises here is, if the input motion is set to be the base motion, how will this change the main characteristic features of the top mass acceleration responses relatively? The main and seemed to be the only difference recognized by inspecting Figures 5.11 through 5.13 was that the significant de-amplification in the frequency range of 0.3-2.2 Hz previously observed for the first and second events vanished and instead, remarkable amplification happened for 6DEF. However, outside of this range, the peak values were quite the same as the values reported in Table 5.2. The reason that 6DEF showed the largest acceleration and displacement responses in the first and second events (Figures 4.5 and 4.10) is most likely related to the vicinity of the first and second natural frequencies of the free-field soil and those of the soil-pile 6DEF-top mass system. In the third event, almost no amplification was shown for 9DIJ. This justifies the desirable performance of 9DIJ in comparison with the other piles, as observed in Figure 4.5. In contrast, the amplification of motion in piles UIAB and 12DMN, respectively around the first (1 Hz) and the second (2.8 Hz) modes of the soil system, explains their amplified responses in the third event.

Investigation of the Fourier spectra of the input and output motions provided insights in interpreting the associated transfer functions, as presented in Figures 5.14 to 5.15. First, the flexible-base transfer functions (Table 5.1) are discussed; these are drawn as black lines in the figures.

- In the first and second events, the transfer functions for unimproved pile peaked at 3.9 Hz and 4.1 Hz, respectively, which agrees with the values in Table 5.2. An

additional peak occurred at 6.2 Hz, which is suspected to be related to the one of the vibration modes of the soil that will be estimated as being close to 6.2 Hz in Sections 5.4 and 5.5.1 using the identification methods and an analytical solution, respectively. This peak was not visually detected in the previous investigation of the Fourier spectra. In addition to the peaks close to the vibration modes of the soil, an additional peak with smaller amplitude was detected in the second event at 3.3 Hz.

- Multiple peaks with the same amplitude appeared in the transfer function of 6DEF in the first event with the lowest frequencies of 2.9 Hz and 3.4 Hz. However, two peaks were observed in the second event at 3.1 Hz and 4.1 Hz. A broad peak with a lower amplitude was detected in the frequency range of 5 Hz to 7 Hz.
- For 9DIJ, the highest peaks in the frequency range of 0 Hz to 7 Hz emerged at 5.9 Hz in the first event and at 6 Hz in the second event. A second peak with a smaller amplitude at 4.2 Hz was also present.
- In the transfer function derived for 12DMN for the first event, the peaks at 3.6 Hz and 4.1 Hz appeared to be the highest in the first event, whereas in the second event, in addition to the peak at 4.2 Hz, another peak with slightly larger amplitude arose at 5.7 Hz.
- In the second event, an increase in the size of the improvement zone resulted in a gradual shift of the transfer function peak located at 6.2 Hz for UIAB towards smaller frequencies such as 5.7 Hz in the case of 12DMN.
- In the third event, two major peaks were observed in transfer functions for all piles. The first peak within lower frequencies showed a gradual shift from 2.8 Hz

for UIAB, to 3.4 Hz for 6DEF, to 4 Hz for 9DIJ, and finally to 4.2 Hz for 12DMN; this reflects the direct effect of the improvement zone size on the magnitude and frequency of the lower frequency peak. However, the opposite was observed on the second peak as it moved from 8.2 Hz for UIAB towards the lower frequencies to 7 Hz for 12DMN as the improvement zone became larger in size. The intensity of the second peak was also reduced compared to the first peak, to the extent that the transfer function for 12DMN could be effectively characterized by only one relatively sharp peak at 4.3 Hz. The derived transfer functions for soil shown in Figure 5.4 suggest that the second peak could be a result of the soil vibration modes in the frequency range of 5 Hz to 10 Hz. The first mode of vibration became more prominent when soil was improved and when the size of the soil improvement zone was increased. Shifting of the second mode to the lower frequencies was also observed in the second test.

- The top mass transfer functions with respect to the base excitation are depicted in the same figures by orange lines. Several observations were made from these figures. First, in the first and second events, changing the input to the base acceleration caused the first two natural frequencies of the soil deposits to emerge on the graphs. Second, both groups of transfer functions showed peaks at 4 Hz, with an especially good agreement for all piles in the second event.

In summary, the flexible-base modal frequencies of the soil-pile-top mass systems appeared to be approximately the same as the modal frequencies of the free-field soil. In the second event, modal frequencies at about 4 Hz and 6 Hz appeared in all transfer functions with nearly the same amplitudes for each pile. The amplitudes increased with

the size of the improved zone, except for 6DEF, where the highest amplitude peak occurred at 3.1 Hz. This mode with a lower amplitude was also identified for UIAB. The results suggest that a lower frequency mode (at about 3.1 Hz) contributed to the response of UIAB and 6DEF; this does not seem to have been in effect in determining the responses of 9DIJ and 12DMN. This mode is close to the second mode of the soil. Introducing the CDSM apparently filtered out this low-frequency mode. There was also observed an evolving mode in the first and second events moving from 6.2 Hz to 5.8 Hz with increase in size of the improved zone. In the third event, this mode moved from 8 Hz for UIAB to 7 Hz for 12DMN. The identified natural frequencies of the flexible-base transfer functions are listed in Table 5.3.

5.3.3 Soil-pile-top mass system-simplified methods

The fundamental frequency of the super structure can be estimated using a SDOF fixed-base idealized model as depicted in Figure 5.5. The super structure is characterized by its mass, m_{str}, its height, H_{str}, and its bending stiffness, $(EI)_{str}$. The natural frequency of a fixed-base structure depends exclusively on the structure's mass and stiffness as

$$f_{fixed} = \frac{1}{2\pi}\sqrt{\frac{k_{str}}{m_{str}}}\,. \tag{5.25}$$

Using the deflection formula of a cantilever beam subjected to a concentrated transverse force (Beer et al., 2008), the stiffness k_{str} was estimated as

$$k_{str} = \frac{3\,EI_{str}}{{H_{str}}^3} = 173 \times 10^4\ (\frac{kN}{m}) \tag{5.26}$$

where $EI_{str} = 3.54 \times 10^4$ kN.m^2 based on the pile properties in Table 2.2 and H_{str}=3.94 m, the distance of the top mass center from the soil surface. After substituting k_{str} and

m_{str} (reported in Table 2.3) in Eq. 5.25 the fundamental frequency of the fixed-base superstructure was obtained as 8 Hz.

In another approach, k_{str} was obtained from the force-displacement relationships at the piles' top resulting from the pseudo-static loading tests (Figure 3.3). Lateral stiffness of the soil-pile systems estimated at the displacement of 5 cm along with the associated fundamental frequencies are listed in Table 5.5. Comparing these values with those estimated from the flexible-base transfer functions summarized in Table 5.3 showed that the SDOF model with the lateral stiffness estimated from the pseudo-static tests results over estimated the lowest natural frequency of the soil-pile-top mass systems by 40% for the unimproved soil and about 35% for the improved soils.

5.4 Application of system identification procedures-4SID

As the first step, the input data Hankel matrices $\boldsymbol{U}_{0|i-1}$ and $\boldsymbol{U}_{i|2i-1}$ were constructed using the base acceleration recorded by A46 according to Eq. 5.19. In a similar way, the acceleration time histories of the embedded sensors (A2, A6, A11, A16, and A26) with respect to the base were used to form the Hankel matrices of the past and future output data, $\boldsymbol{Y}_{0|i-1}$ and $\boldsymbol{Y}_{i|2i-1}$, respectively. A32 at the soil surface was not included in the analysis due to its vicinity to the soil surface. Since A20 was not aligned with the other accelerometers in DH3 it was excluded as well.

Implementing 4SID requires two parameters to be determined a priori: the number of block rows i and the appropriate model order n. Examining the rank of the input Hankle matrix $\boldsymbol{U}$ in Eq. 5.19 for different values of the block rows showed that row blocks higher than 12 would result in rank deficient $\boldsymbol{U}$ matrix; therefore, i was selected as 12. The performance of the state space identification methods depends greatly on how well

the input excitation meets the underlying assumptions. When the excitation is narrowband and non-stationary, which is the case for earthquake excitations, the identified values depend on the length of the data used in the identification (Lus et al., 1999; Siringoringo and Fujino, 2008). Herein, different lengths of data were used in the identification. The number of columns j depends on the number of selected data points contained in the Hankel matrices. In order to determine the model order, which corresponds to twice the number of structural modes, we started by inspecting the singular values of the product of the extended observabiliy matrix and the state sequence. From the singular values plot in Figure 5.16, it is clear that the number of significant singular values is not sensitive to the number of data points. These graphs show that except the fourth or fifth singular value, the rest are of very small values suggesting that two or three modes are present in the data.

In modal analysis, when trying to estimate the modal parameters from real data, especially in experimental modal analysis of large scale structures where the selection of the model order is difficult, it is a standard practice to over specify the model order above what is implied by the singular value plot (Reynders, 2012). This helps to detect the weakly excited system modes that appear only in systems with high orders. Although over specification helps to capture all the excited modes and reduces the bias in the estimated parameters, it creates a set of non-physical or mathematical modes due to the measurement noise or nonlinearities in the system. To distinguish between the true modes and the spurious modes, stabilization diagram were introduced which are the plots of modal parameters identified from the state space models with increasing order against the corresponding model order. These diagrams have been widely used in modal

identification of bridges and shear-frame structures (Lus et al., 1999; Siringoringo and Fujino, 2007; Fraraccio, 2008; He et al., 2009; Peeters and Ventura, 2003; Reynders and De Roeck, 2008; Kim and Lynch, 2012a, 2012b). Not only the effect of the model order on the identified modal parameters is explored in these graphs, but also the effect of data length is considered as studied in (Lus et al., 1999; Siringoringo and Fujino, 2007). In stabilization diagrams a true mode of the system lines up along the nearly same frequency as the model order increases. It also shows up with consistent damping and mode shapes. On the other hand, spurious modes are expected to show erratic behavior. These modes can be detected and removed by setting a validation criterion such that if the difference between the eigen frequencies of the two consecutive model order is larger than a pre-set value, these modes can be marked as spurious modes.

In developing the stabilization diagrams, discrete-time state space models with the model order changing from 2 to 12 (corresponding to systems with 1 to 6 modes) were identified while the model order was increased in steps of 2. The upper bound limit on the model order was imposed by the maximum number of rows in the Hankel matrix $\boldsymbol{U}$. In addition, the effect of data length was also studies by increasing the number of time samples introduced to the identification algorithm counted from the beginning of the excitation. The natural frequencies f_i and damping ratios ξ_i were extracted using Eqs. 5.14 and 5.15. As the number of time samples increased, the identified parameters became stabilized at certain frequency ranges as shown in Figure 5.17. The number of stable modes in models with the order of 4 and 6 were so small that no stabilization diagram could be created. Therefore, only the parameters of the models with orders 8, 10 and 12 are presented in the figure. The magnitude and phase of the associated complex mode

shapes are depicted in Figure 5.18. In order to improve the clarity of these diagrams, the unstable modes with negative damping ratios and modes with frequencies higher than 7Hz (i.e. the upper cutoff frequency of the applied Butterworth filter) were excluded. It is a well known fact that constraints such as finite number of the samples/data points, modeling errors, plant and measurement noise can result in unstable modes and therefore unstable $\widehat{\mathbf{A}}_{\mathbf{d}}$ matrix (Eq. 5.20), even though the system being modeled in real world is stable. According to the definition (Juang, 1993) a discrete state space model is stable if and only if all the poles or the eigenvalues of matrix $\widehat{\mathbf{A}}_{\mathbf{d}}$ lie inside the unit circle. To date, various methods have been proposed to force a stable identification of $\widehat{\mathbf{A}}_{\mathbf{d}}$ (Lacy and Bernstein, 2003) which is not the focus of this study.

5.4.1 Observations and interpretation of results

The diagrams for natural frequencies in Figure 5.19 imply that three modes around 1 Hz, 3 Hz and in the frequency range of 5-6 Hz were excited. There is a good agreement between the results of two different identification approaches, 4SID in the time domain and the spectral analysis using the transfer functions in the frequency domain. The stabilization diagrams for modal damping ratios (Figure 5.17) show higher uncertainties in the estimated values. Difficulties in identification of modal damping ratios has been experienced and commonly reported in the structural identification literature (Lus et al., 1999; Siringoringo and Fujino, 2007; He et al., 2009; Reynders and De Roeck, 2008; Kim and Lynch, 2012a and 2012b). In all these studies it was found that the uncertainty in estimation of damping ratios is high relative to the uncertainty in estimated natural frequencies. As stated in the aforementioned studies, small valued damping ratios are sensitive to non-stationary nature of seismic excitation and the presence of noise. This

can partly explain the observed scatter in the damping ratio stabilization diagram. In order to facilitate easy interpretation of the stabilization diagrams of natural frequencies and damping ratios, modal parameters associated with a certain model order that varied between appropriately chosen threshold values as a result of increase in data length were grouped together. A total of 15 groups were detected including 3 groups of the identified vibration modes around 1 Hz, 7 groups around 3 Hz, and 5 groups in the frequency range of 5-6 Hz. From each group one representative complex mode shape was selected and used in the validation phase of this study as reported later in Section 5.5.2.

5.5 Validation

5.5.1 Natural frequencies of free-field soil

The identified natural frequencies were verified against the natural modes of an inhomogeneous viscoelastic soil layer over a rigid rock. Various research efforts on response of continuously inhomogeneous soils to vertically propagating shear waves have resulted in closed-form solutions for natural frequencies, mode shapes and base-to-surface amplification functions (Dobry et al., 1976; Schulze, 2005; Rovithis et al., 2011; Vrettos, 2013). Exponential and power law variations of the shear wave velocity with depth are the special cases that simplify the solutions of the wave propagation differential equation in terms of Bessel functions or power series solutions. The shear wave velocity profile calculated from the cross-correlation of all combinations of two embedded accelerometers in the soil model (shown by circles) is shown in Figure 5.20. This profile suggests that an exponential function can reasonably represent the variation in the shear wave velocity or the shear stiffness with depth z as

$$V_s(z) = V_0 e^{az}. \tag{5.27}$$

Velocity at the soil surface V_0 and the inhomogeneity rate parameter a were estimated using the least squares fit as 11.43 m/s and 0.24, respectively.

The response of a viscoelastic soil layer to a harmonic base motion with circular frequency ω is governed by the following differential equation

$$\frac{d}{dz}\left(G(z)\frac{du}{dz}\right) + \rho\omega^2 u = 0 \tag{5.28}$$

where u is the horizontal displacement of the soil at a certain depth; $G(z)$ is the continuously varying shear modulus with depth which can be obtained from the shear wave velocity profile knowing the soil mass density ρ using

$$V_s = \sqrt{\frac{G}{\rho}} \tag{5.29}$$

The solution of Eq. 5.28 is provided by Schulze (2005) where it is assumed that the mass density of the soil is constant throughout the layers. A mass density of 973 kg/m^3 was estimated based on the weighted average mass density of the soil layers. The material damping is accounted for by replacing $G(z)$ by its complex counterpart as

$$G(z) \rightarrow G(z)(1 + 2\beta i) \tag{5.30}$$

where β is the linear hysteresis damping coefficient which was assumed as a constant for the entire soil profile. The natural frequencies are determined by assuming zero displacement at the interface of the soil and the bedrock. The natural frequencies of the soil model in the frequency range of interest 0-7 Hz (i.e. the band-pass frequency of the filters used to process the acceleration data in soil in the first event) were calculated solving

$$J_1\left(\bar{f}_n \frac{\pi}{2}\frac{1}{\bar{a}}\right) N_0\left(\bar{f}_n \frac{\pi}{2}\frac{e^{\bar{a}}}{\bar{a}}\right) - J_0\left(\bar{f}_n \frac{\pi}{2}\frac{e^{\bar{a}}}{\bar{a}}\right) N_1\left(\bar{f}_n \frac{\pi}{2}\frac{1}{\bar{a}}\right) = 0 \tag{5.31}$$

for the normalized frequency $\overline{f_n} = \frac{2}{\pi}\, k_n H e^{-\bar{a}}$ (Schulze, 2005). Here, $\bar{a} = aH$, where H is the soil layer thickness, and $k_n = \frac{\omega_n}{V_0}$, where ω_n is the soil natural frequencies. $J_0()$ and $J_1()$ denote the Bessel functions of the first kind of order 0 and 1, respectively. Similarly, $N_0()$ and $N_1()$ denote the Bessel functions of the second kind.

The amplification function of the soil model was obtained using the following equation

$$\mathcal{A} = \frac{2a}{\pi k_0 e^{-aH}\left[J_1\left(\pm\frac{k_0}{a}e^{-aH}\right)N_0\left(\frac{k_0}{a}\right) - J_0\left(\frac{k_0}{a}\right)N_1\left(\pm\frac{k_0}{a}e^{-aH}\right)\right]} \tag{5.32}$$

which expresses the ratio of the displacement at the soil surface to that of the base (Schulze, 2005).

In the analytical method, all modes possess the same damping ratio. Implementing Eqs. 5.31 and 5.32 the first five natural frequencies were calculated as 1.08, 2.48, 3.90, 5.34, 6.76 Hz for the selected values of the fitting parameters V_0 and a. However, the exponential analytical model of shear wave velocity in Eq. 5.27 is very sensitive to the values of the parameters V_0 and a. The estimated value of V_0 (i.e. 11.43 m/s) is quite low for real soils. Therefore, a sensitivity analysis was performed by increasing the shear velocity estimated at the soil surface from 12 to 20 while a was changed accordingly to produce the best match with the original least-squares fit. The calculated shear wave velocity profiles for five different combinations of V_0 and a are shown in Figure 5.21.

The impacts of the fitting parameters variation on the estimated natural frequencies can be observed on the corresponding amplification functions plotted in Figure 5.22. The resulting functions showed that slight changes in the fitting parameters can cause significant changes in the natural frequencies (i.e. the peaks of the amplification

functions). An increase in V_0 shifts the natural frequencies towards higher frequencies while it spread the same number of modes over a broader frequency band such that for the case with V_0 = 20 m/s only three modes with frequencies of 1.60, 3.68, and 5.79 Hz were situated within the frequency range of interest. Among the various cases considered in the sensitivity analysis, the case with V_0= 14 m/s and a = 0.235 produced the closest match with the first and the second identified frequencies as 1.25 Hz and 2.89 Hz from 4SID and the peaks of the transfer function in Figure 5.19; therefore, the parameters of the shear wave velocity model were updated to V_0= 14 m/s and a = 0.235.

Amplification functions for various damping coefficients: β=0.01, 0.02, 0.05, and 0.1 are plotted in Figure 5.23. The stabilization diagram and the transfer functions for deeper layers such as TF A46-A6, TF A46-A11, and TF A46-A16 in the first drew attention to existence of some mode(s) in the frequency range of 4-6.5 Hz. However, due to the multiband-band limited nature of the applied earthquake motion and its low frequency content in this range the third and the forth analytical modes at 4.53 and 6.18 Hz were not adequately excited to be identified with confidence.

5.5.2 Mode shapes of the free-field soil

The validity of the identified complex mode shapes and be validated by extracting their real-valued counterparts known as normal mode shapes and compare them against those calculated using available closed-form solutions proposed for simplified soil models in literature (Dobry et al. 1976; Schulze, 2005; Rovithis et al., 2011; Vrettos, 2013). Normal modes are defined for structures with no damping or small damping. The phase angle distribution along the modal vector is either zero or 180 degree. The computation of normal modes from the identified complex modes for lightly damped structures or

structures with proportional damping is a straight forward task as detailed in Alvin et al., (1994) and Alvin et al., (1997). The challenge arises when the system is non-proportionally damped, and/or the set of identified modes is incomplete. Many studies have been published on non-proportionally damped systems where the number of DOFs and the identified modes were equal (Balmes, 1997; De Angelis and Imbimbo, (2012). Incomplete sets of identified modes are commonly encountered in the analysis of continuous structures. In principal, all structures are considered as spatially distributed systems with an infinite number of DOFs. When a distributed system is approximated by a lumped parameter system with countable number of DOFs, various incompleteness issues are often encountered as stated in Mukhopadhyay et al. (2014). Since it is not feasible to instrument all the DOFs, the identified mode shapes are only available at the measured DOFs. It is also possible that some modes are not excited or observed properly at the measuring points along the structure. Therefore, the number of identified modes could be larger or smaller than the number of sensors. The measurement locations certainly affect the quality and the spatial resolution of the identified mode shapes. The sensor location selection is an active research topic in modal testing, and well-studied methods have been published in this area Udwadia (1994). The optimal sensor selection is not within the scope of this study; however, some attention will be paid to this subject. A review on the existing methods treating different cases of incompleteness can be found in the work of Ibrahim (1983), Ibrahim and Fuellekrug (1990), Alvin et al. (1995), Lus et al. (2003a, 2003b), and Fuellekrug (2008). All the proposed methods for extracting the normal modes from an incomplete set of identified complex modes are approximate to some extent. In this study, a reduction transformation proposed by Ibrahim and

Fuellekrug (1990) and Fuellekrug (2008) was implemented to estimate the normal modes from the three identified complex modes measured at five locations (A2, A6, A11, A16, A26). Herein, the number of sensors was higher than the number of identified modes. The reduction transformation solves the problem of modal truncation by reducing the number of eigenvector elements to the number of identified modes. The transformation matrix is obtained using the SVD technique which helps in finding and extracting the linear dependencies in the identified mode shapes.

As explained earlier, the identified modes were divided into 14 groups based on the similarities between their frequencies. Using a representative from each group, a total of 32 sets of complex mode shapes with 3 members were created so that each member falls into one of the three groups of identified modes around 1 Hz, 3 Hz and in the frequency range of 4.5-6.5 Hz. Using the reduction transformation the associated normal mode shapes were estimated, and it was found that only the normal mode shapes of the first two identified modes associated with lower frequencies could be estimated with reasonable accuracy as plotted in Figure 5.24 labeled with "I". In another attempt, two-member sets with complex modes belonging to the first and second modes around 1Hz and 3 Hz were considered and the third mode in the frequency range 4.5-6.5 Hz was ignored. No two-member set was able to yield a reliable estimate of the second mode shape which implies that although the third identified mode was weakly excited it has a significant impact on the identification of the second mode. Of these 32 sets, one set was qualified upon evaluating the response prediction of the soil system as will be discussed in details in the Section 5.4. In this set the first and the second modes were selected from the diagrams for the model order 8 while the third mode was selected from the diagrams

for the model order 12 where 2000 samples were used in the identification. The selected modal parameters listed in Table 5.5 show that the complex displacement mode shapes at the sensor locations are neither in phase nor 180-degrees out of phase. The associated normal modes extracted by implementing the reduced transformation are drawn with markers at the accelerometers locations in Figure 5.24. The mode shape amplitudes at soil surface was obtained by extrapolation.

The analytical normal mode shapes of displacement were calculated using the following equation

$$\Phi_n(z) = \frac{\pi k_{0n} e^{-az}\left[J_1\left(\pm\frac{k_{0n}}{a}e^{-az}\right)N_0\left(\frac{k_{0n}}{a}\right) - J_0\left(\frac{k_{0n}}{a}\right)N_1\left(\pm\frac{k_{0n}}{a}e^{-aH}\right)\right]}{2a} \tag{5.33}$$

derived by Schulze (2005). Comparing the identified normal modes with the analytical mode shapes $\Phi_n(z)$ labeled with "A" in Figure 5.24 revealed that the first and second modes of the layered soil resembled the first and the second modes of the inhomogeneous soil model. However, the peak displacement for the second identified mode shape occured in deeper layers compared with its analytical counterpart. Sparse instrumentation in the upper soil layers specifically between A16 and A26 forced the peak of the second identified mode shape to occur at the location of A16. Insufficient number of sensors in the upper soil layers where the third and higher analytical modes show a great deal of variation in the amplitude and sign can explain the reason why the third analytical mode was missed out by the 4SID algorithm. This emphasizes the impact of spatial distribution of sensors on the quality of the identified mode shapes. Another difference between the analytical mode shapes and their identified counterparts was observed as small fluctuations in the identified mode shapes close to the interface of the clay and sand layers. This is likely due to the strong stiffness contrast between the soft clay layer and

the underlying dense sand layer as reflected in the shear wave velocity profile shown in Figure 5.20. Also it should be noted that in obtaining the analytical mode shapes identical damping ratios was assumed for all modes (1%) while the damping ratio of the first and second identified modes was estimated as 13% and 36%, respectively. The analytical mode shapes were found to be less sensitive to the variations in the parameters of the exponential model of the shear wave velocity profile as opposed to the analytical natural frequencies. Changing V_0 from 12 to 20 m/s did not cause a significant change in the location of the maximum displacements as illustrated by the curves in Figure 5.24.

Validation of the identified parameters presented in this section highlights the benefit in considering a combination of analytically and experimentally identified models for validating the results and thereby avoiding the missing modes.

5.6 Prediction models

In synthesizing the state space prediction model described in Eqs. 5.12 and 5.13 from the identified modes two obstacles were confronted. First, the set of the identified complex mode shapes as mentioned in the previous section was incomplete and as a result the scaling of the complex mode shapes in Eqs. 5.3 and 5.4 could not be performed. Second, the input influence matrix $\boldsymbol{\beta}$ containing the lumped masses at the measured DOFs was unknown. The first issue was overcome by taking only three elements of the complex eigenvectors (Table 5.5) into account as if the soil response was recorded by only three sensors. Accordingly, eight different sensor combinations named as Trials 1-8 listed in Table 5.6 were selected. As shown by De Angelis and Imbimbo (2012) a complete set of mode shapes can be scaled provided that the mass of only one DOF is known. A *priori* knowledge of the mass matrix, even partially, was also realized by Kim and Lynch

(2012b) for conversion of an identified black-box state space model to its physically meaningful gray-box model. In this regard, to treat the second issue, the lumped mass at only one sensor location was approximated based on the unit weight and the thickness of the corresponding soil layer. Following the procedure detailed in De Angelis and Imbimbo (2012), the resultant mass matrices estimated from the scaled mode shapes as stated in Eq. 5.24 for all trials appeared with one or two negative diagonal entries. This implies that the selected set of measurements in the trials could not be generated by a 3DOFs lumped mass system. In other words, synthesizing the state space prediction model using the incomplete set of modal parameters results in a model which may not correspond to a physical system. This depends on the contribution of the missed out modes in the system response. Yet, using the calculated mass matrix containing the negative entries and the scaled complex mode shapes, the state space model of each trial was synthesized and utilized to predict the soil response at the selected sensor locations as depicted in Figure 5.25.

Those models that reproduced the peak accelerations within 5-10 % error and the lowest root mean square of the residual between the measured and predicted values were selected as successful trials. As can be seen in Figure 5.25 time histories at A2 in Trial 3, A6 and A26 in Trial 5, and A11 and A16 in Trial 6 were closely approximated by the corresponding models. It is noteworthy to mention that another set of analyses were performed considering only the first two identified modes and the response at all sensor locations were predicted using the two-sensor combinations. Overall no remarkable difference was observed between the two cases; however surprisingly no two-sensor combination could result in an acceptable prediction at A2 in the first sand layer. It can

be inferred that the third identified mode played a major role in the response of this sensor. The contributions of individual modes to the overall response at each location are illustrated in Figure 5.26. In spite of the fact that the first mode did not contribute appreciably to the responses at A2, A6, A11 and A16, it predicted the total response at A26 very well. Examination of the transfer functions in Figure 5.26a confirms that first mode is more pronounced in the response of the soil in the upper most layer while in the deeper layers the second and the third modes were more influential.

The most basic use of an identified system is to simulate the system response to various inputs. To validate our identified models in each trial shown in Table 5.6, the response of the soil system to the second and the third shaking events were simulated using the predictive models. The simulated time histories and the corresponding Fourier amplitude spectra are compared against the measured responses in Figures 5.27 and 5.28 for the second and the third events, respectively. The results indicate that the identified models from the first event can predict the soil response at A2, A6 in the dense sand layers, and A11 in the first clay layer very well in the second event while the prediction accuracy is lower for shallower sensors A16 and A26 in the second and fourth clay layers, respectively. For the third event, the models were able to capture the maximum acceleration along with the frequencies carrying the major part of the energy at A2, A6 and A11 very well, the response at A16 and A26 were, however, highly over estimated.

Overall, the prediction capabilities of the models can be considered reasonable except in the upper clay layers and under strong motion such as the third shaking event. It should be pointed out here that the range of application of the identified models is limited to linear systems, while the soil deposit, particularly in the upper layers under

strong excitation, is expected to behave in a nonlinear and time-varying manner. Moreover, relatively higher frequency content of the third event beyond 4 Hz and the absence of the higher modes in this frequency range except the third identified mode at frequency 6.2 Hz is another reason for the poor prediction of response in the Kobe shaking event.

5.7 Summary and conclusions

- Effects of inertial and kinematic interactions on seismic behavior of piles were investigated. In most seismic design codes, pile foundations are designed only against inertial forces of superstructures transmitted to the pile heads where free-field motions are used as superstructure base acceleration. It was shown that the input motion exciting the superstructure could be remarkably different due to the soil-structure interaction. Thus, the free-field motion cannot be used as foundation input motion.
- In the second event, pseudo-flexible transfer functions peaked at about 4 Hz and 6 Hz with nearly the same amplitudes for all piles. The amplitudes increased with the size of the improved zone, except for 6DEF, where the highest amplitude peak occurred at 3.1 Hz close to the second natural frequency of the soil. This might explain the amplified acceleration response of 6DEF in the first and second events.
- The soil fundamental frequency (at 1.2 Hz) played a less significant role in the first and the second events compared to the third event, where it appeared as an influential mode in determining the amplified acceleration response of UIAB.

- In the third event, two major peaks were observed in the pseudo-flexible transfer functions for all piles. The first peak within lower frequencies showed a gradual shift from 2.8 Hz for UIAB, to 3.4 Hz for 6DEF, to 4 Hz for 9DIJ, and finally to 4.2 Hz for 12DMN; this reflects the direct effect of the improvement zone size on the magnitude and frequency of the lower frequency peak. However, the opposite was observed on the second peak as it moved from 8.2 Hz for UIAB towards the lower frequencies to 7 Hz for 12DMN as the improvement zone became larger in size. The results indicated that the lowest natural frequency of the system increased with increasing its stiffness.
- The SDOF model with the lateral stiffness estimated from the pseudo-static tests results over estimated the lowest natural frequency of the soil-pile-top mass systems by 40% for the unimproved soil and about 35% for the improved soils.
- In the unimproved soil the kinematic interaction was more pronounced at the first vibration mode of the soil while in the improved soil the second mode was predominant.
- In spite of the difficulty in obtaining the necessary parameters for the soil analytical model, the first and second identified frequencies matched their counterparts calculated from the analytical model. The identified normal mode shapes of the free-field soil agreed with the analytical solutions in a qualitative sense.
- Comparison of the identified and theoretical amplification functions revealed the weakly excited modes in the identification process due to the insufficient instrumentation and narrow-band frequency content of the excitation motions. A

denser array of accelerometers particularly in the middle and in the surficial layers would have resulted in better estimate of modal quantities

- The assembled state space models using the incomplete set of identified modes were utilized to predict the responses during three shaking events. The models predicted the acceleration-time histories and the corresponding Fourier response spectra reasonably well for the small first and moderate second shaking events. Although the proposed models prediction accuracy was lower in the upper layers for the strong third shaking event, it was still able to predict the behavior of the deeper layers reasonably well.
- Relatively higher frequency content of the third event beyond 4 Hz and the absence of the third analytical mode in the identified modal parameters set is one reason for the poor prediction of response in the third shaking event. It is also believed that the upper soft clay layers behaved in a nonlinear and time-varying manner during the third event.
- The results highlight the benefit in considering a combination of an analytical model and an experimentally identified model for validating the results and thereby avoiding missing modes.

Table 5-1 Input-Output Data Sets Used in Identification of Natural Frequencies of Structures with Different Fixity Conditions at Base

Natural frequencies of	**Input**	**Output**
Flexible-base	free-field ground motion (U_{ff})	total motion at the top mass ($U_{ff}+U_p+\theta_p H_{str}+U_{s,bend}$)
Pseudo flexible-base	total base translation ($U_{ff}+U_p$)	total motion at the top mass ($U_{ff}+U_p+\theta_p H_{str}+U_{s,bend}$)
Fixed-base	total base translation and the contribution of pile rocking at soil surface ($U_{ff}+U_p+\theta_p H_{str}$)	total motion at the top mass ($U_{ff}+U_p+\theta_p H_{str}+U_{s,bend}$)

Table 5-2 Frequencies at Which the Free-Field Motion Was Amplified at the Top Masses

Input: Free-field motion	**Depth of ground improvement**			
	UI	**6D**	**9D**	**12D**
Amplified frequencies Event 1 (Hz)	3.8	2.2 - 3.4	3.5 - 7	3.6 - 4.2
Amplified frequencies Event 2 (Hz)	4.1, 3.4	2.5, 3.4	4.1	4.1-7
Amplified frequencies Event 3 (Hz)	1	2.3	2.8, 3.2	2.8-3.8

Table 5-3 Identified Flexible-Based Natural Frequencies

Events	**Depth of ground improvement**			
	UI	**6D**	**9D**	**12D**
Amplified frequencies Event 1 (Hz)	4, 6.5	3, 3.4, 4.1, 4.6, 6.2	5.9	3.6, 4.1, 6.2
Amplified frequencies Event 2 (Hz)	3.4, 4.1, 6.2	3.1, 4.1	4.2, 6	3.7, 4.2, 5.7
Amplified frequencies Event 3 (Hz)	1.8, 2.8, 6.4, 8.2	2.8, 3.4, 7.5	4, 5, 7, 8.2	4.3, 7

Table 5-4 Fundamental Frequencies of Pile-Soil Systems

Super structure properties	Depth of Ground Improvement			
	UI	**6D**	**9D**	**12D**
m_{str} (kg)	661.5	656.1	661.5	664.2
k_{str} (kN/m)	400	600	760	880
f_{fixed} (Hz)	3.9	4.8	5.4	5.8

Table 5-5 Identified Modal Parameters from Event 1 (4SID Method)

Modes	**First mode**		**Second mode**		**Third mode**	
Undamped frequencies	1.35		2.87		6.20	
Damping ratio	0.13		0.36		0.37	
Sensors	Complex mode shape		Complex mode shape		Complex mode shape	
	Amp.	phase	Amp.	phase	Amp.	phase
A26	1	0	0.67	155.30	0.32	29.88
A16	0.33	19.20	1	0	1	0
A11	0.09	72.29	0.40	48.11	0.37	124.38
A6	0.06	87.65	0.25	61.31	0.22	152.90
A2	0.04	93.00	0.10	72.63	0.08	172.11

Table 5-6 Sensor Configuration

Trials	**Sensor combinations**	**Satisfactory predictions**
Trial 1	Triple (A2, A6, A26)	-
Trial 2	Triple (A2, A11, A26)	-
Trial 3	Triple (A2, A16, A26)	A2
Trial 4	Triple (A6, A11, A26)	-
Trial 5	Triple (A6, A16, A26)	A6, A26
Trial 6	Triple (A11, A16, A26)	A11, A16
Trial 7	Triple (A2, A6, A16)	-
Trial 8	Triple (A2, A11, A16)	-

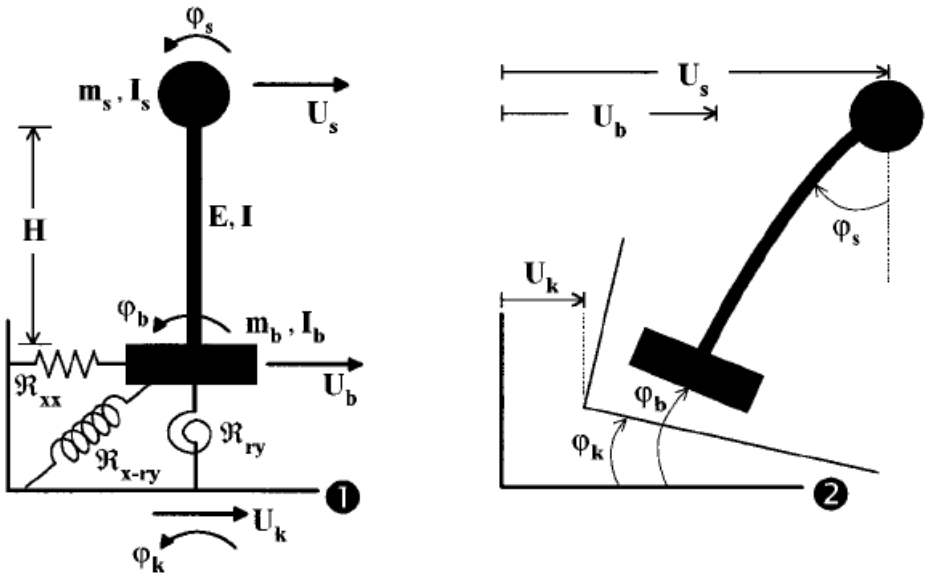

Figure 5.1 Simplified model for analysis of soil-structure interaction (1) model parameters, (2) displacement and rotation with respect to an inertial frame of reference (Mylonakis et al., 1997)

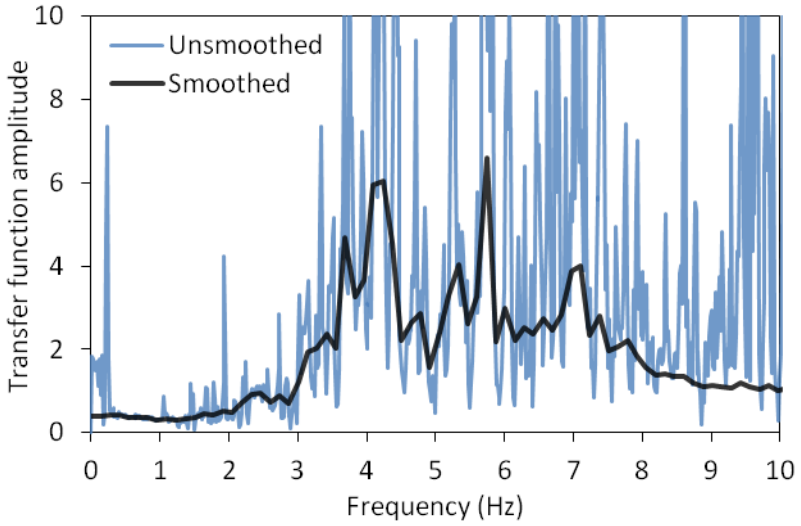

Figure 5.2 Comparison of transfer functions derived with and without smoothing

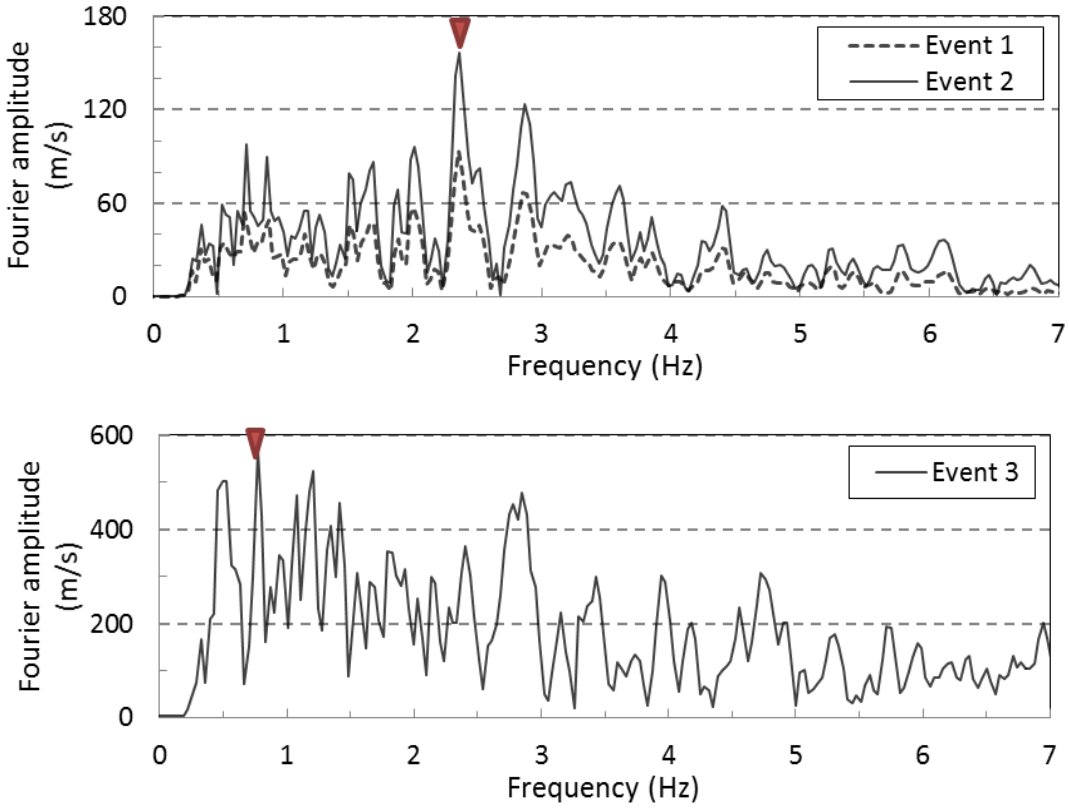

Figure 5.3 Frequency content of the base motion in the shaking events

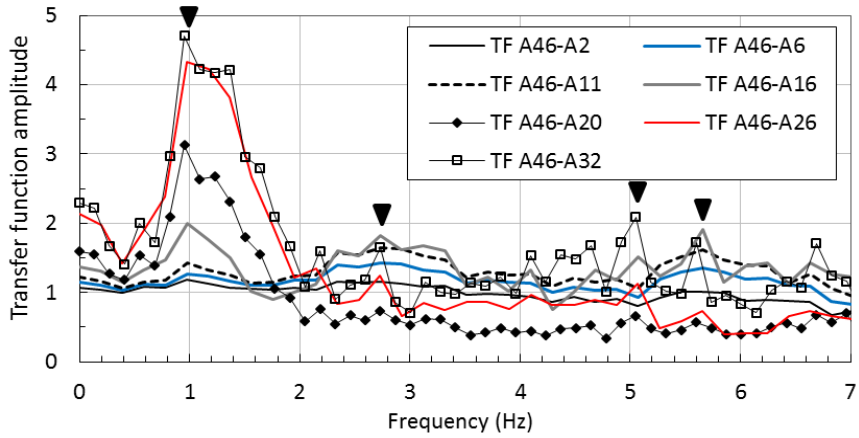

(a)

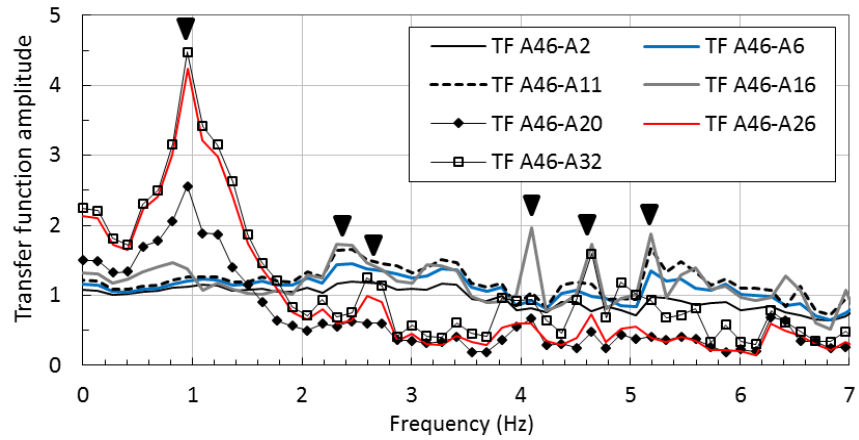

(b)

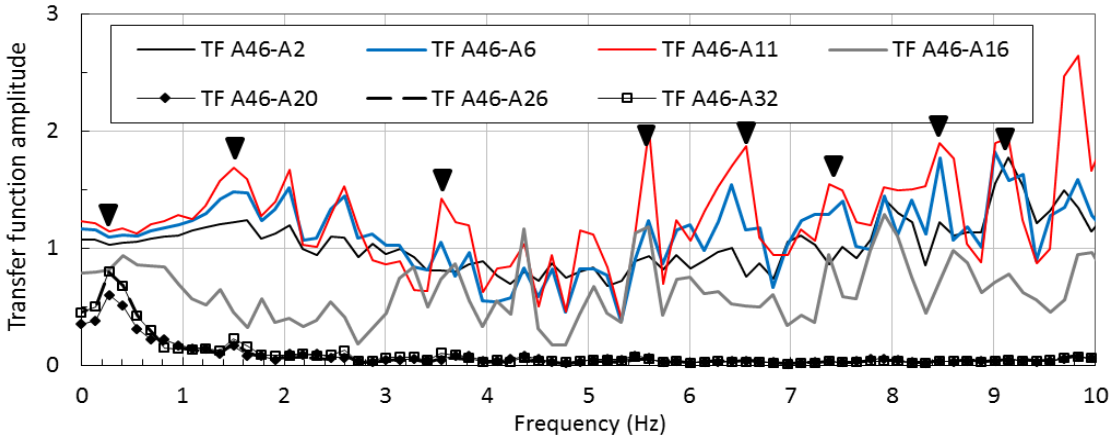

(c)

Figure 5.4 Smoothed transfer functions derived using free-field soil accelerometers in (a) Event 1, (b) Event 2, and (c) Event 3

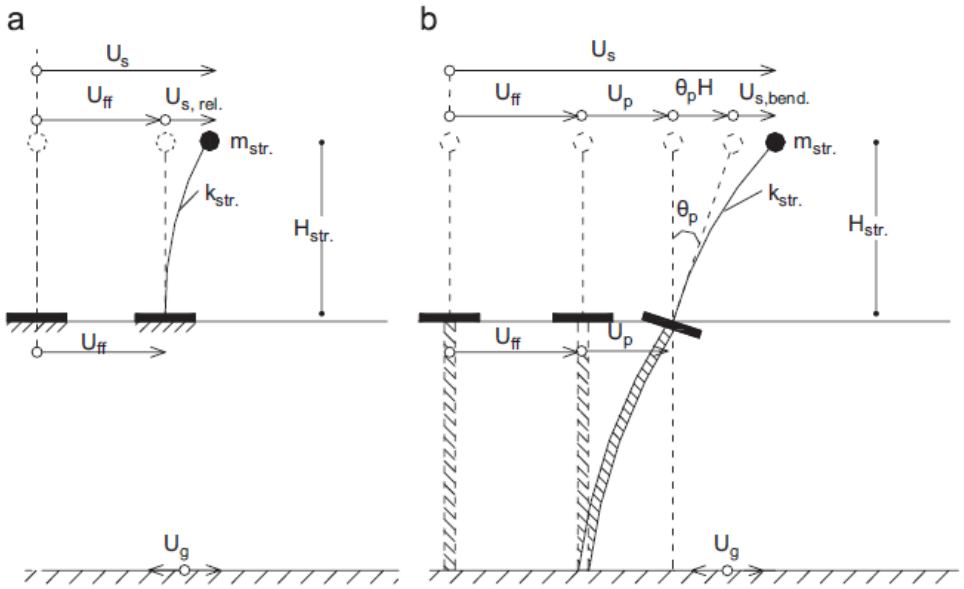

Figure 5.5 Deflection components for a SDOF super structure supported by (a) a fixed foundation and (b) a flexible foundation (Rovithis et al., 2009)

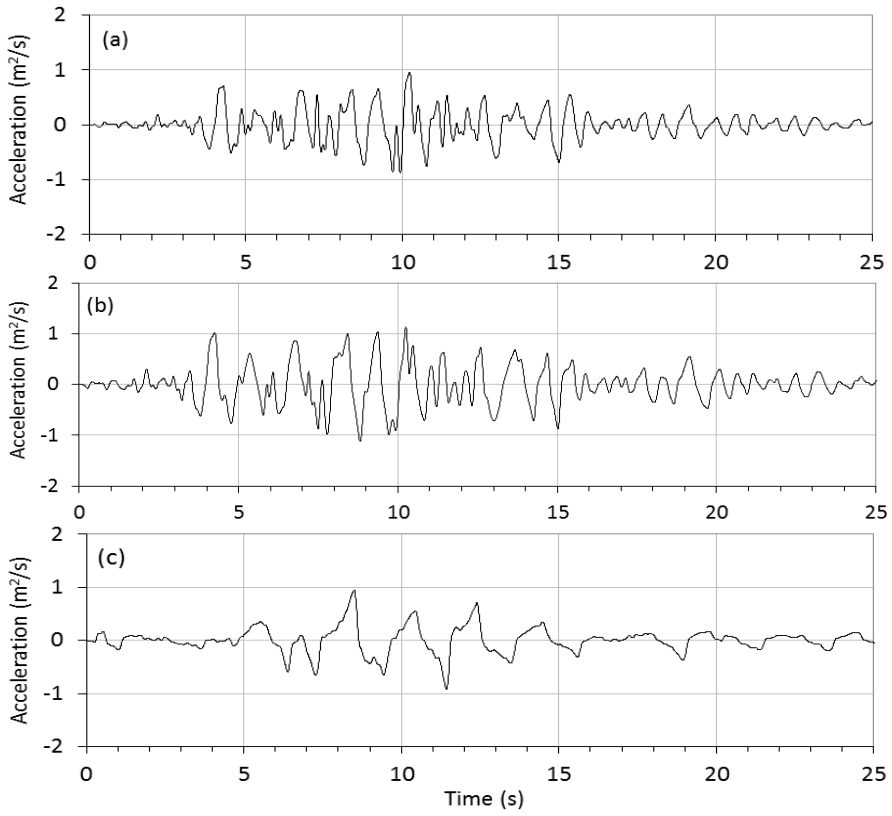

Figure 5.6 Acceleration time histories of the free-field soil surface (A32) (a) Event 1, (b) Event 2, (c) Event 3

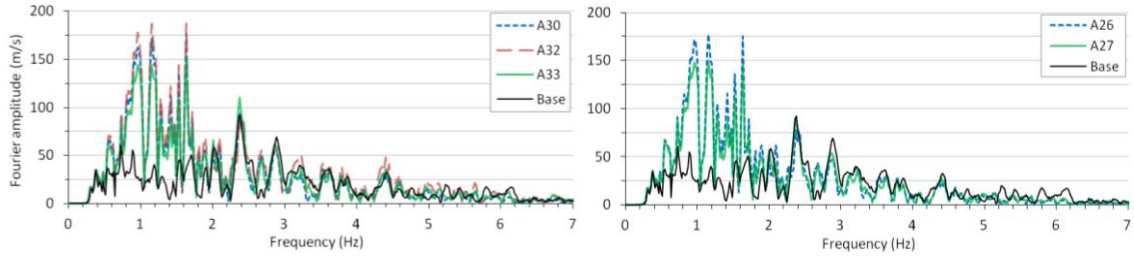

(a) Event 1

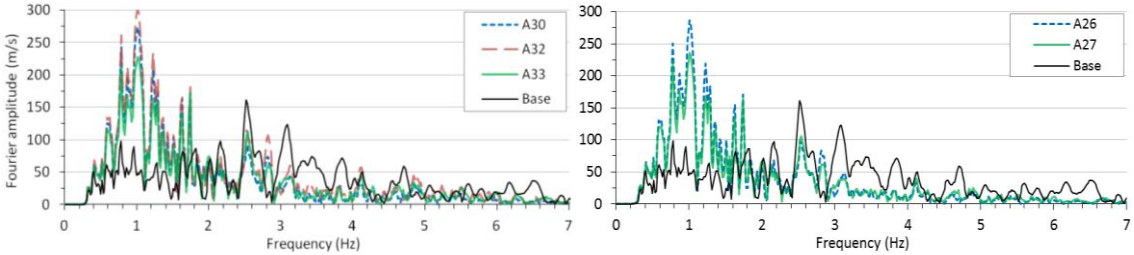

(b) Event 2

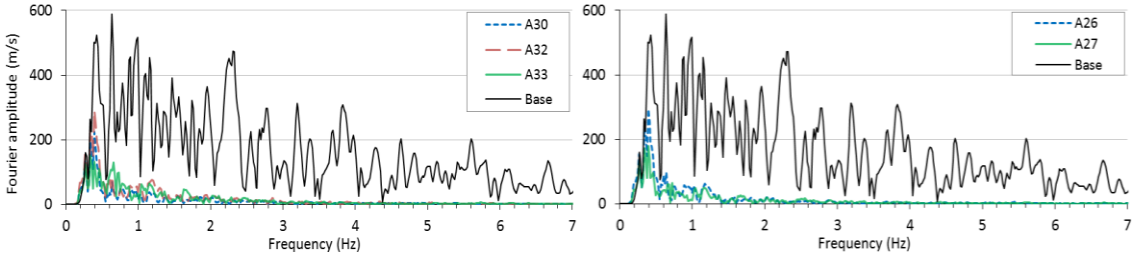

(c) Event 3

Figure 5.7 Frequency content of the soil acceleration close to the soil surface

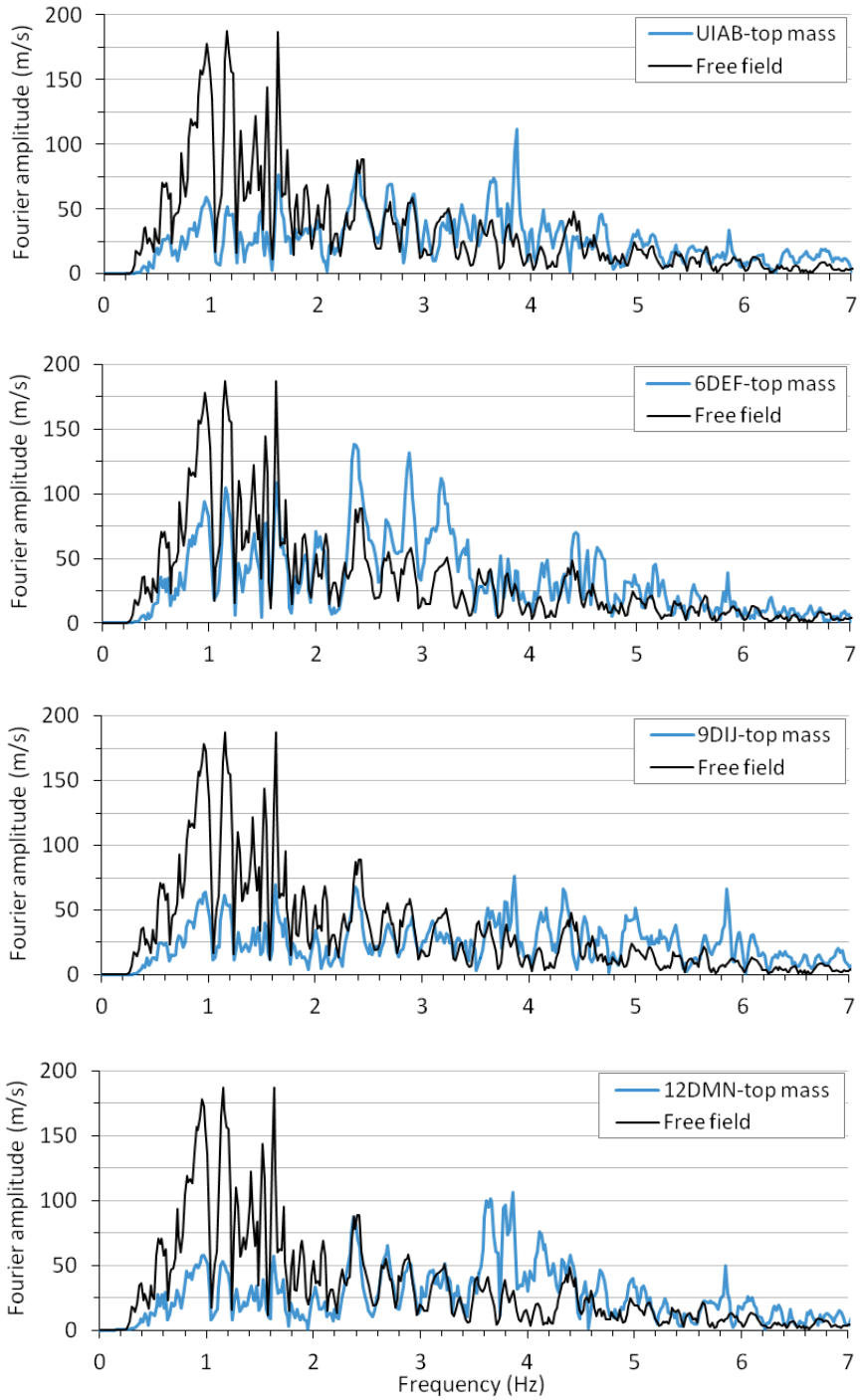

Figure 5.8 Frequency content of the motion recorded by accelerometers on top masses and free-field soil (Event 1)

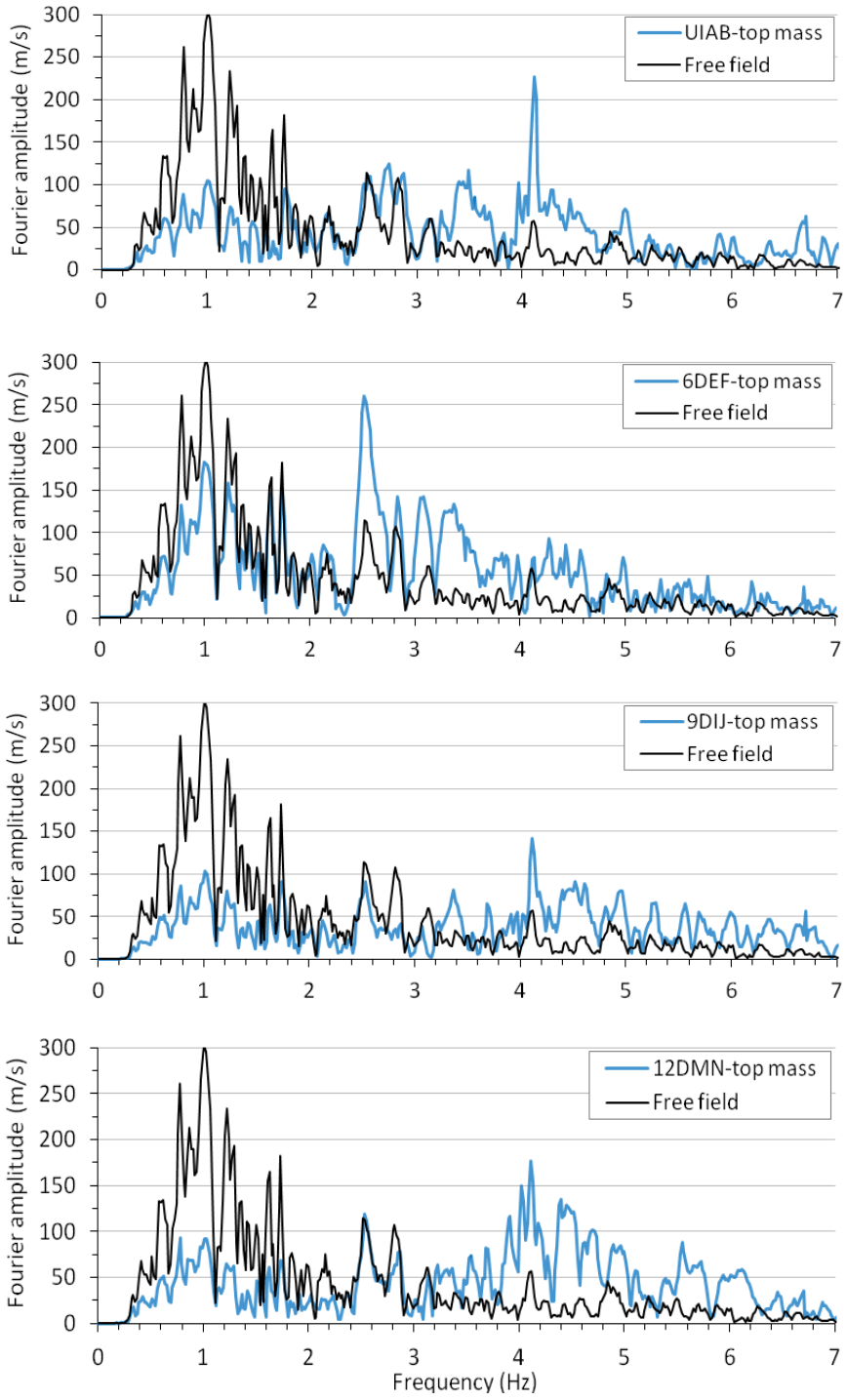

Figure 5.9 Frequency content of the motion recorded by accelerometers on top masses and free-field soil (Event 2)

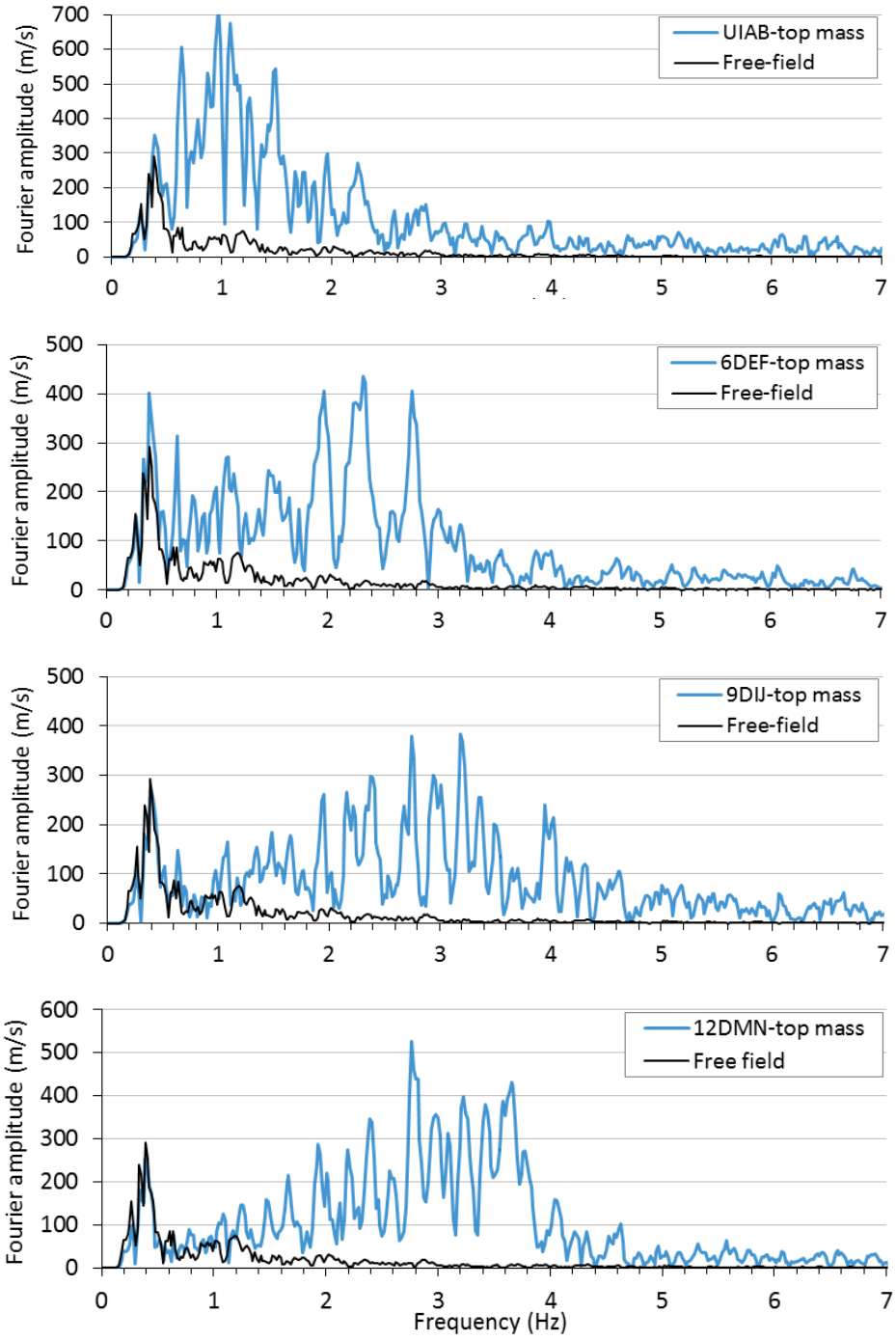

Figure 5.10 Frequency content of the motion recorded by accelerometers on top masses and free-field soil (Event 3)

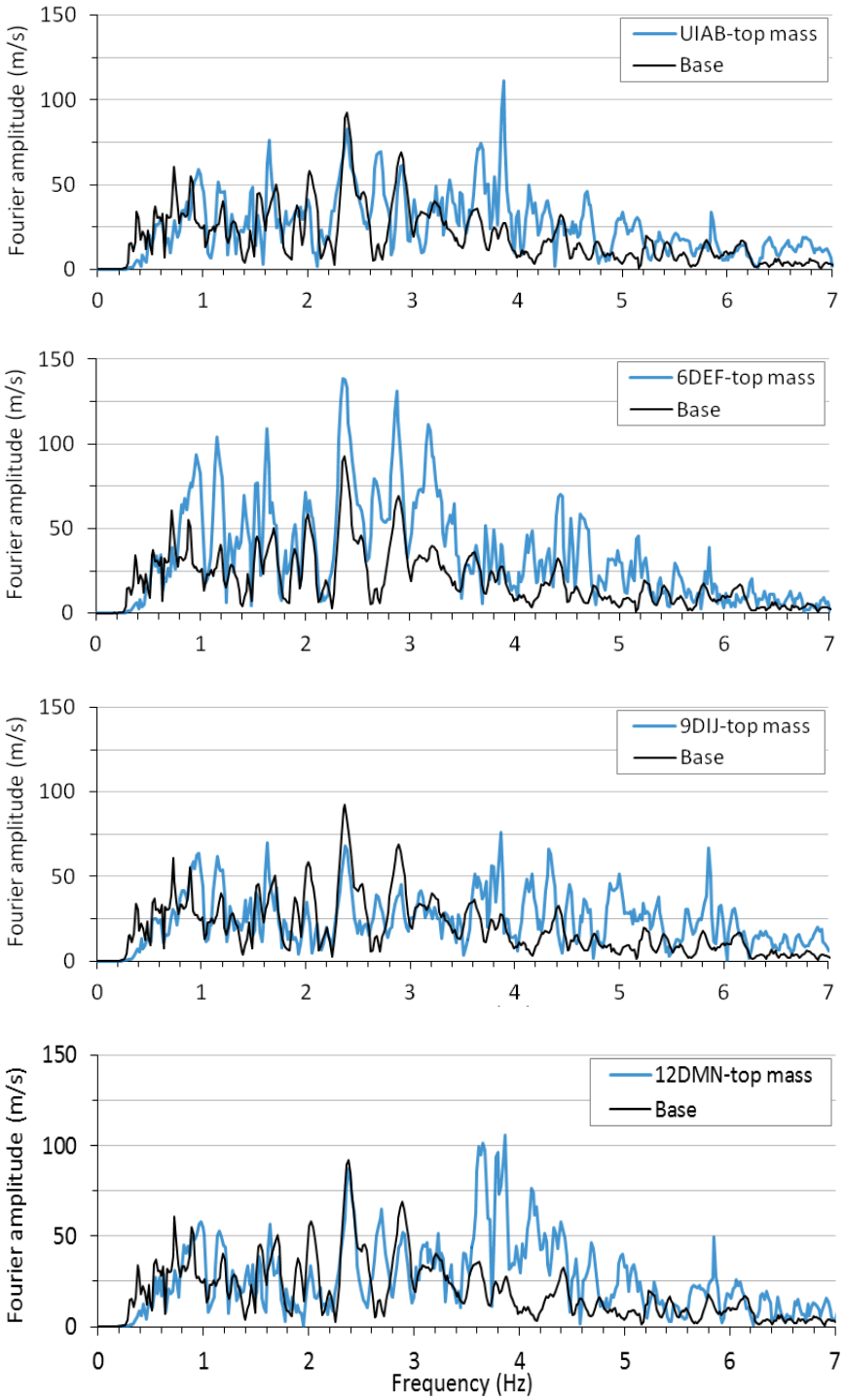

Figure 5.11 Frequency content of the motion recorded by accelerometers on top masses and the model container base (Event 1)

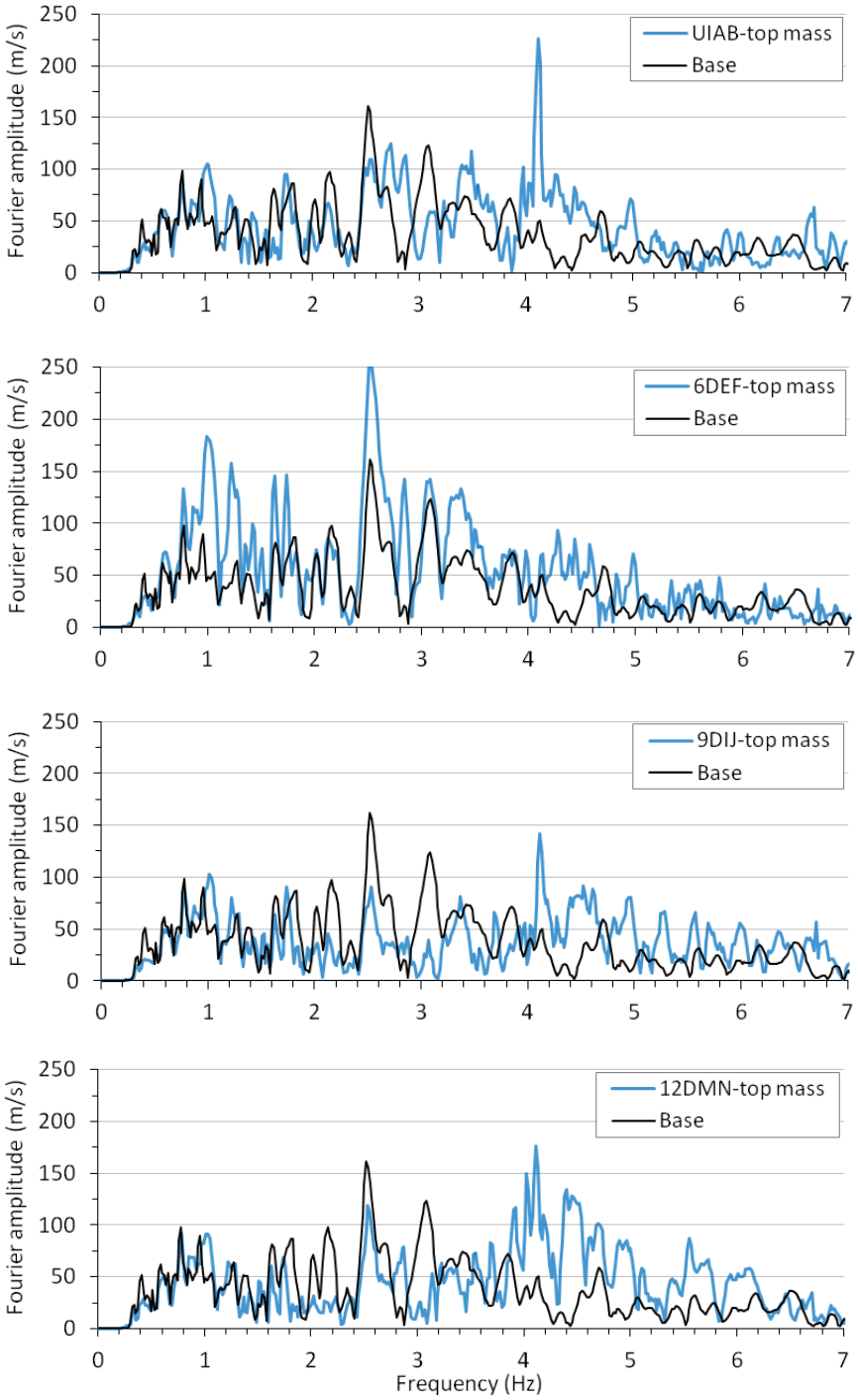

Figure 5.12 Frequency content of the motion recorded by accelerometers on top masses and the model container base (Event 2)

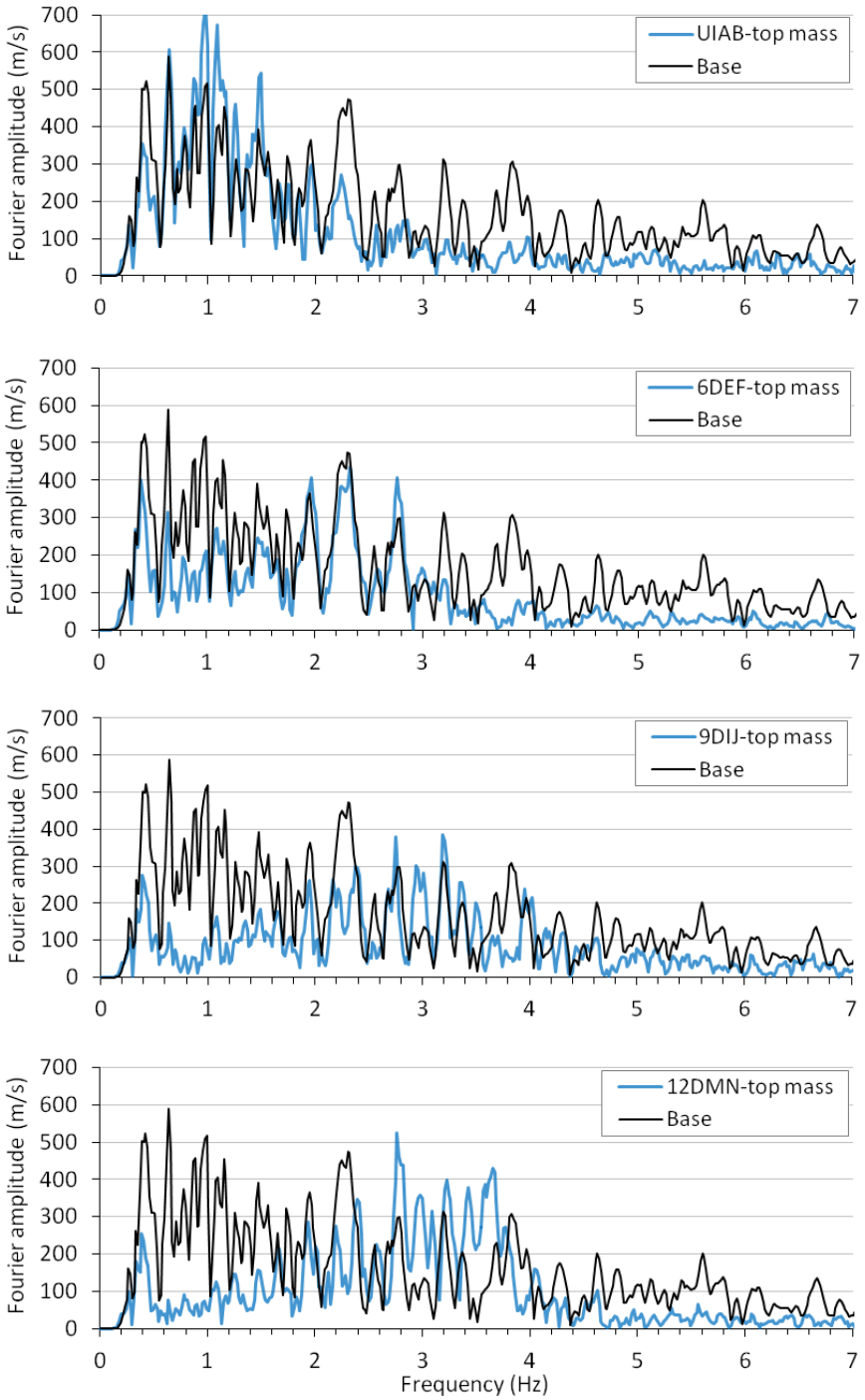

Figure 5.13 Frequency content of the motion recorded by accelerometers on top masses and the model container base (Event 3)

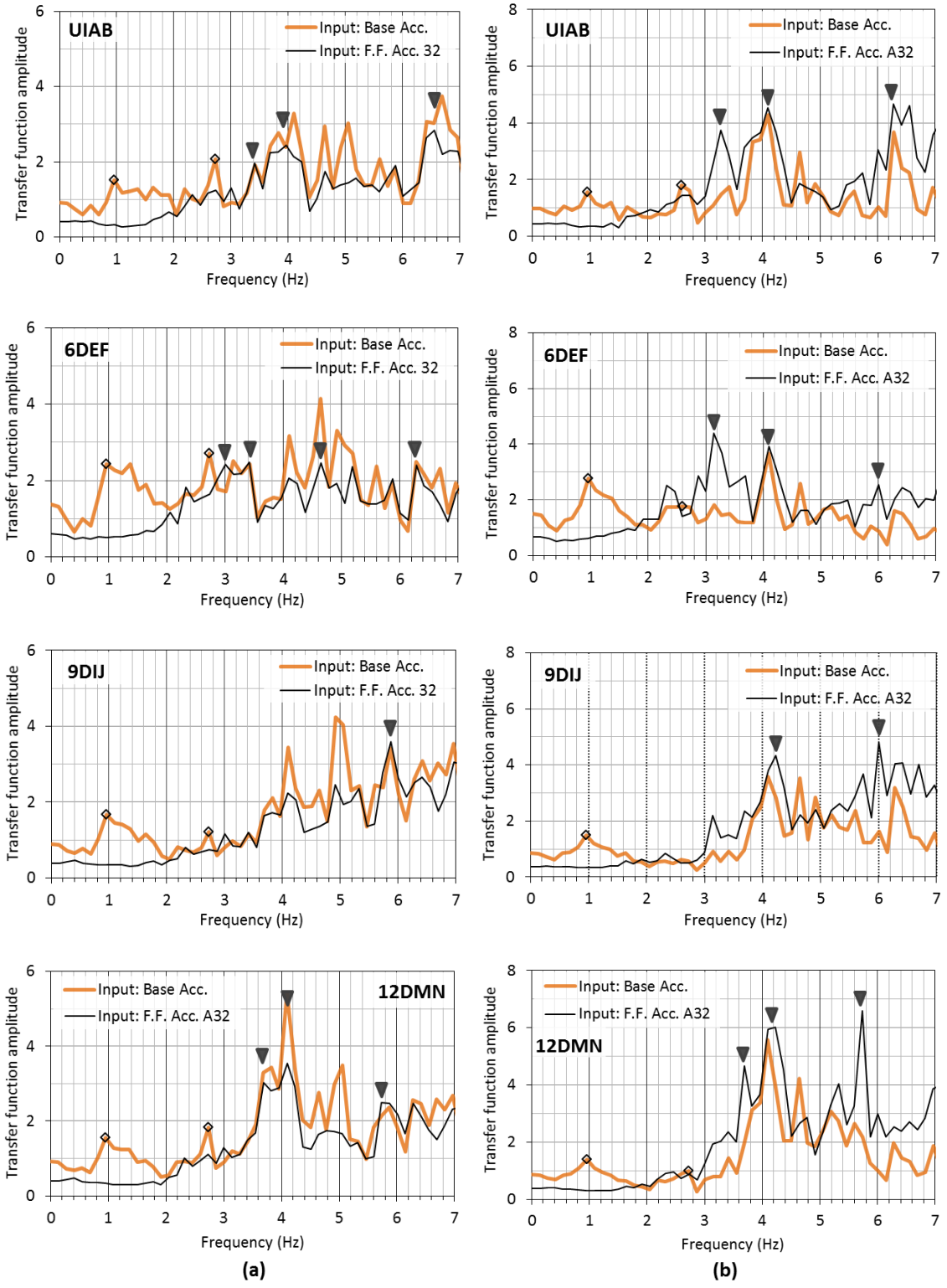

Figure 5.14 Flexible-base transfer functions (a) Event 1, (b) Event 2

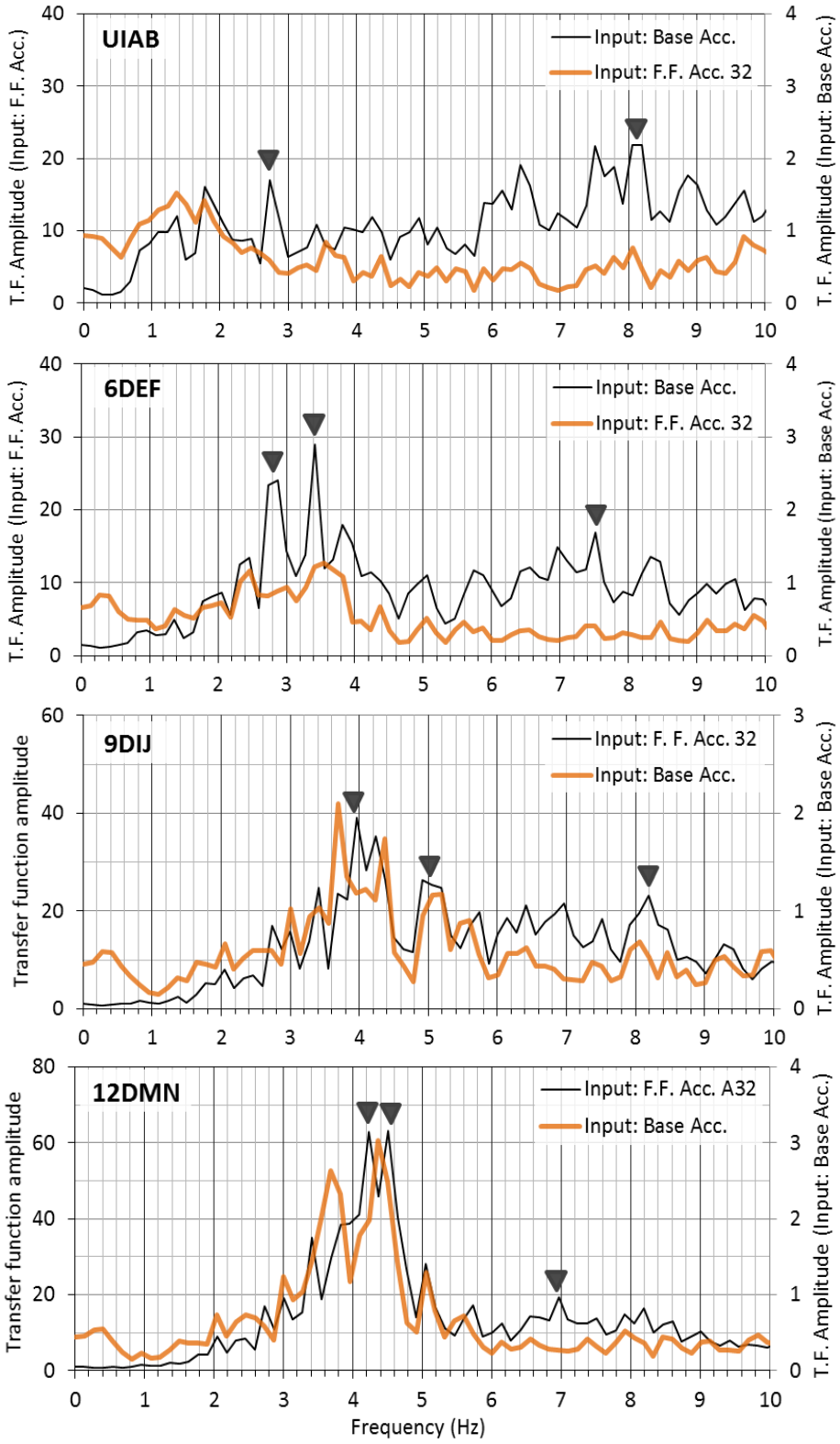

Figure 5.15 Flexible-base transfer functions of Event 3

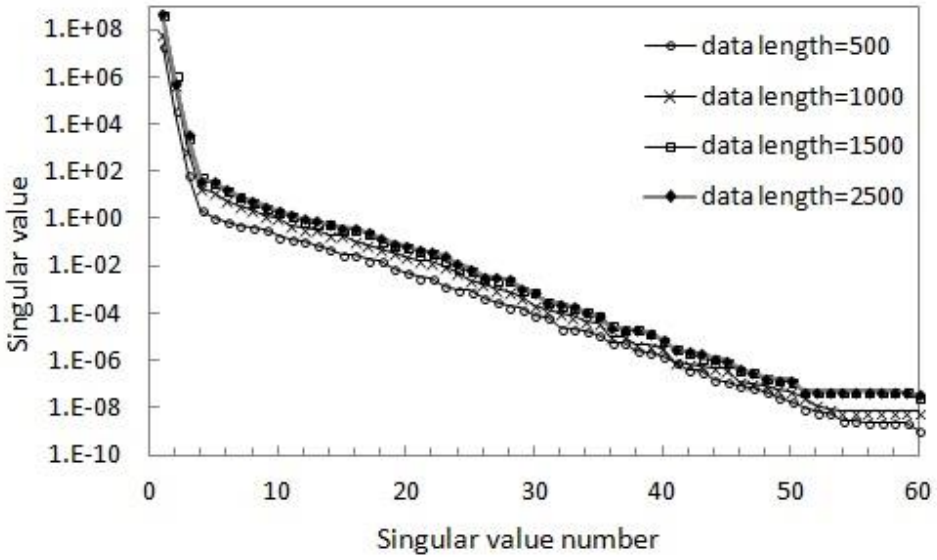

Figure 5.16 Singular values plot (number of row blocks=12)

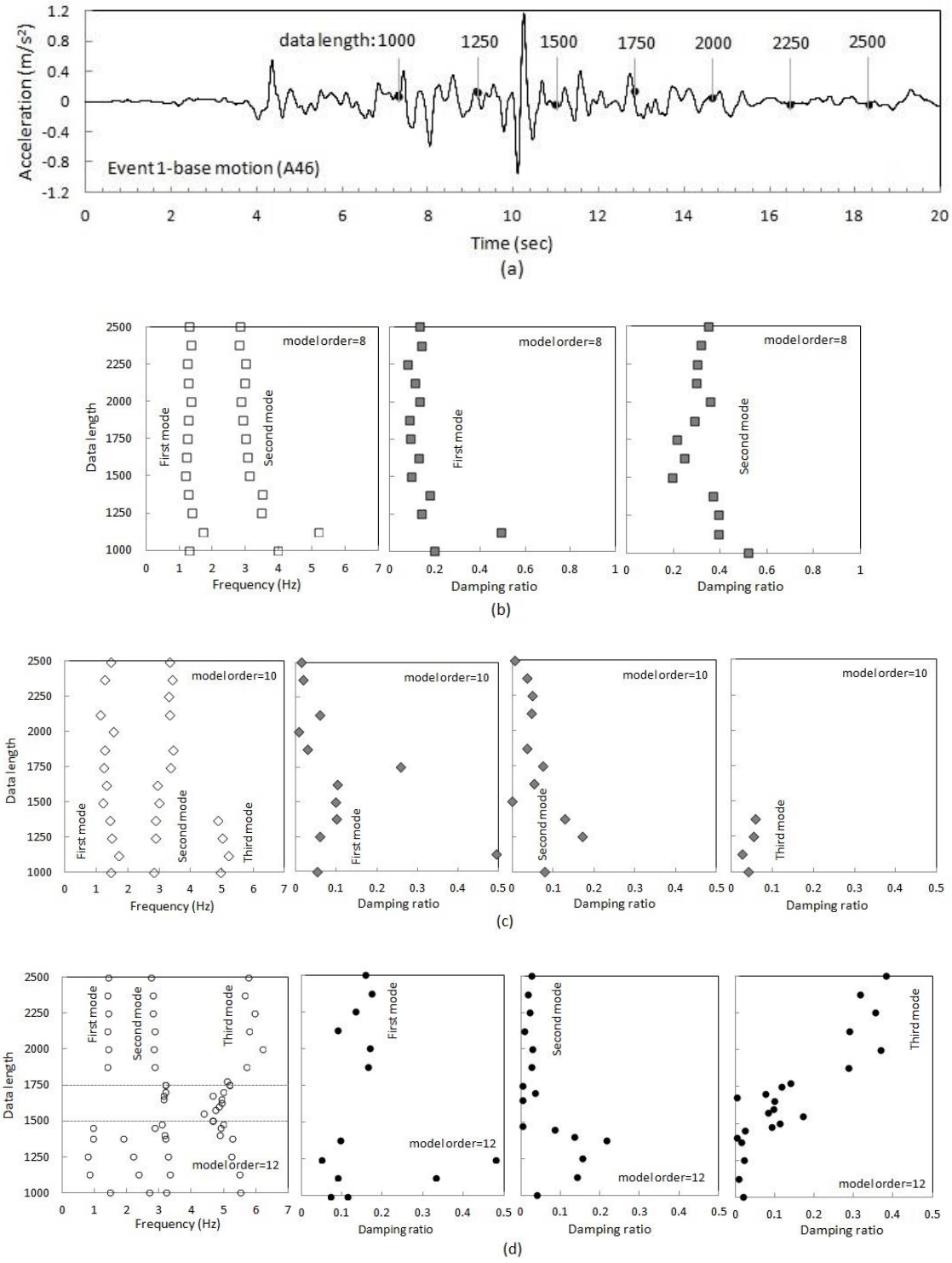

Figure 5.17 Stabilization diagrams of modal frequencies and damping ratios for Event 1
(a) base motion-time history, (b) model order=8, (c) model order=10, (d) model order=12

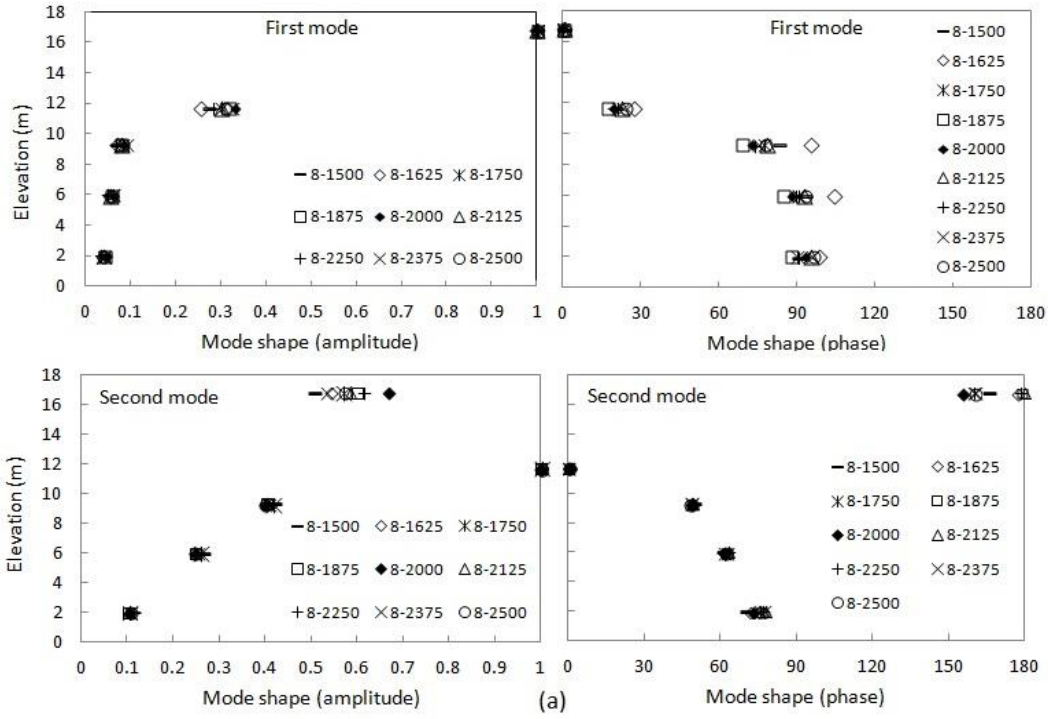
First mode
Elevation (m)
Mode shape (amplitude)
Mode shape (phase)
8-1500
8-1625
8-1750
8-1875
8-2000
8-2125
8-2250
8-2375
8-2500
Second mode

(a)

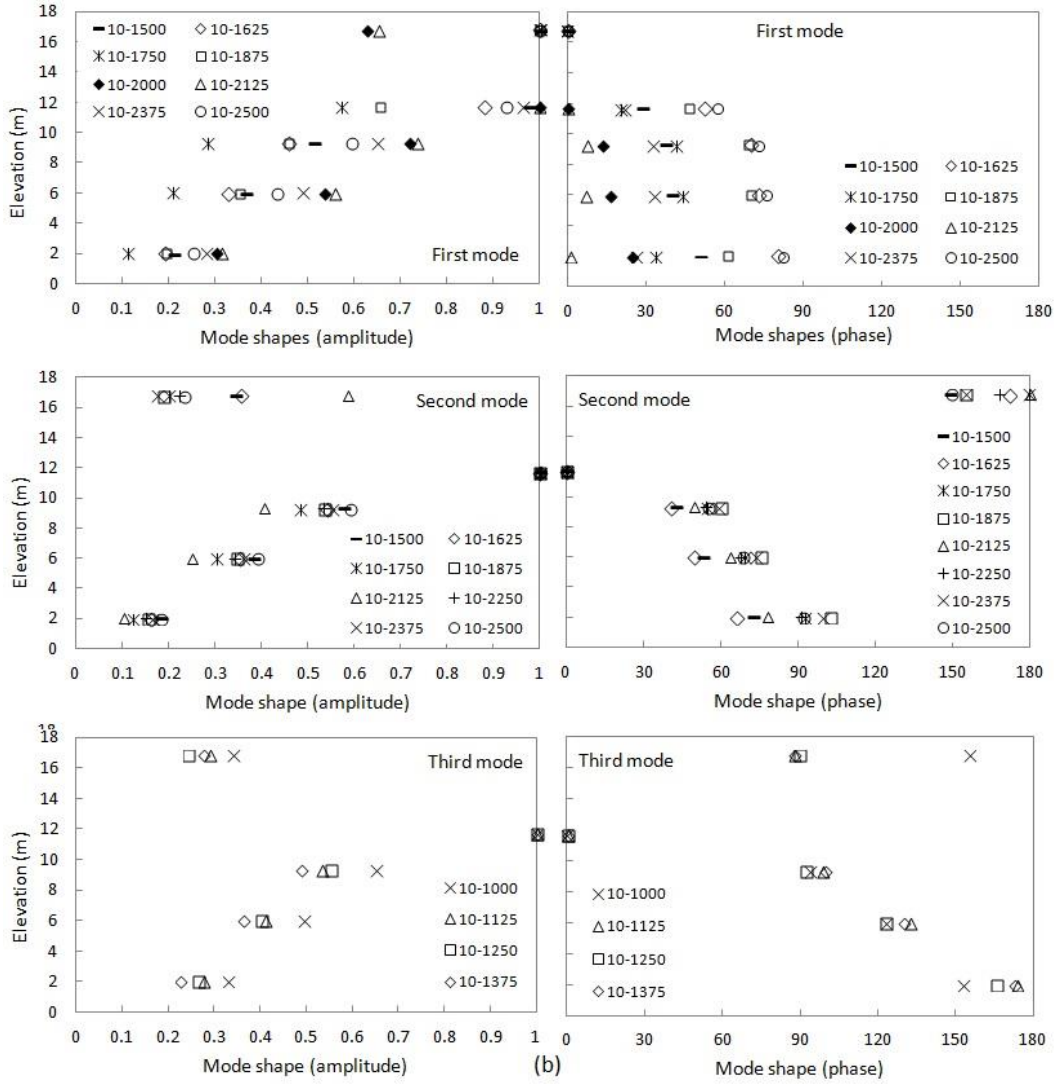
Elevation (m)
Mode shapes (amplitude)
Mode shapes (phase)
First mode
10-1500
10-1625
10-1750
10-1875
10-2000
10-2125
10-2375
10-2500
Second mode
10-2250
Mode shape (amplitude)
Mode shape (phase)
Third mode
10-1000
10-1125
10-1250
10-1375
(b)

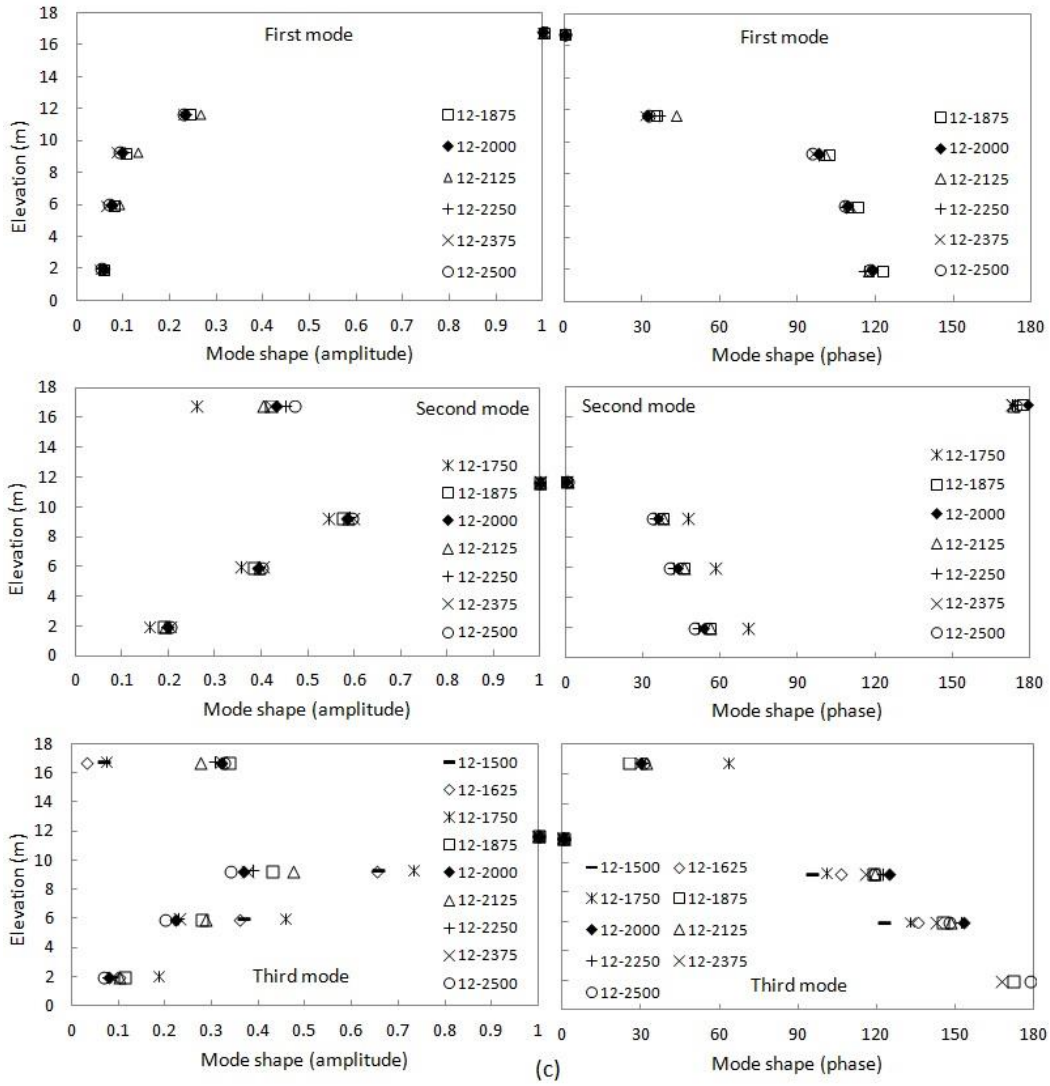

Figure 5.18 Stabilization diagrams of complex mode shapes (First number in the legend specifies the model order and second number specifies the data length), (a) model order=8, (b) model order=10, (c) model order=12

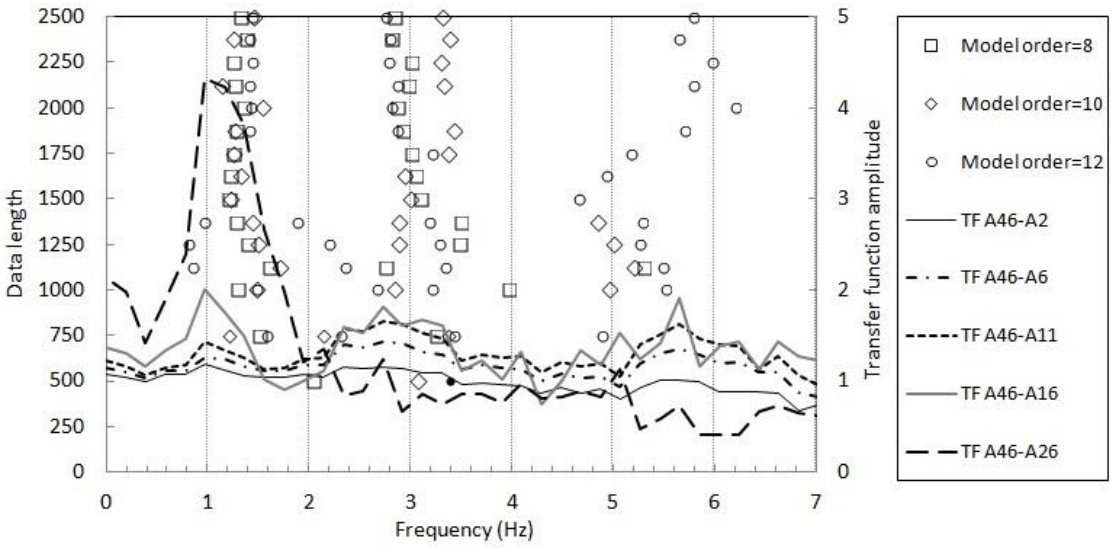

Figure 5.19 Identified natural frequencies of the free-field soil using 4SID method for various data length and model order

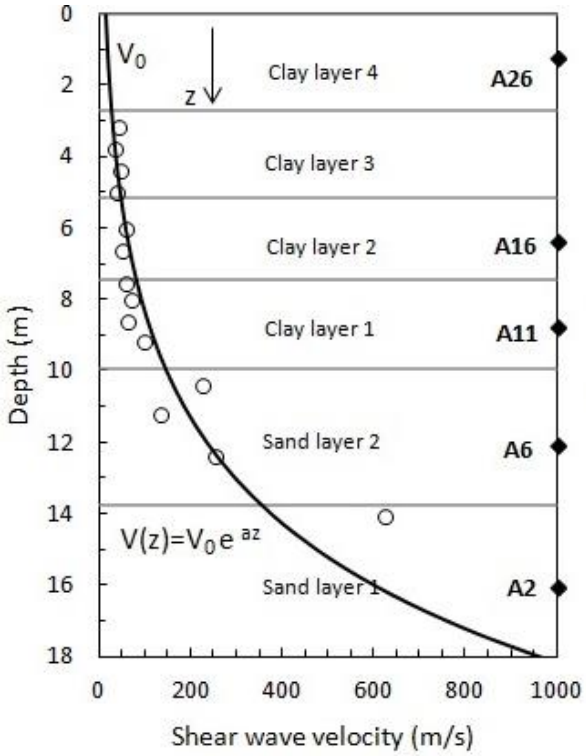

Figure 5.20 Estimated shear wave velocity profile (V_0=11.43 m/s, a =0.24)

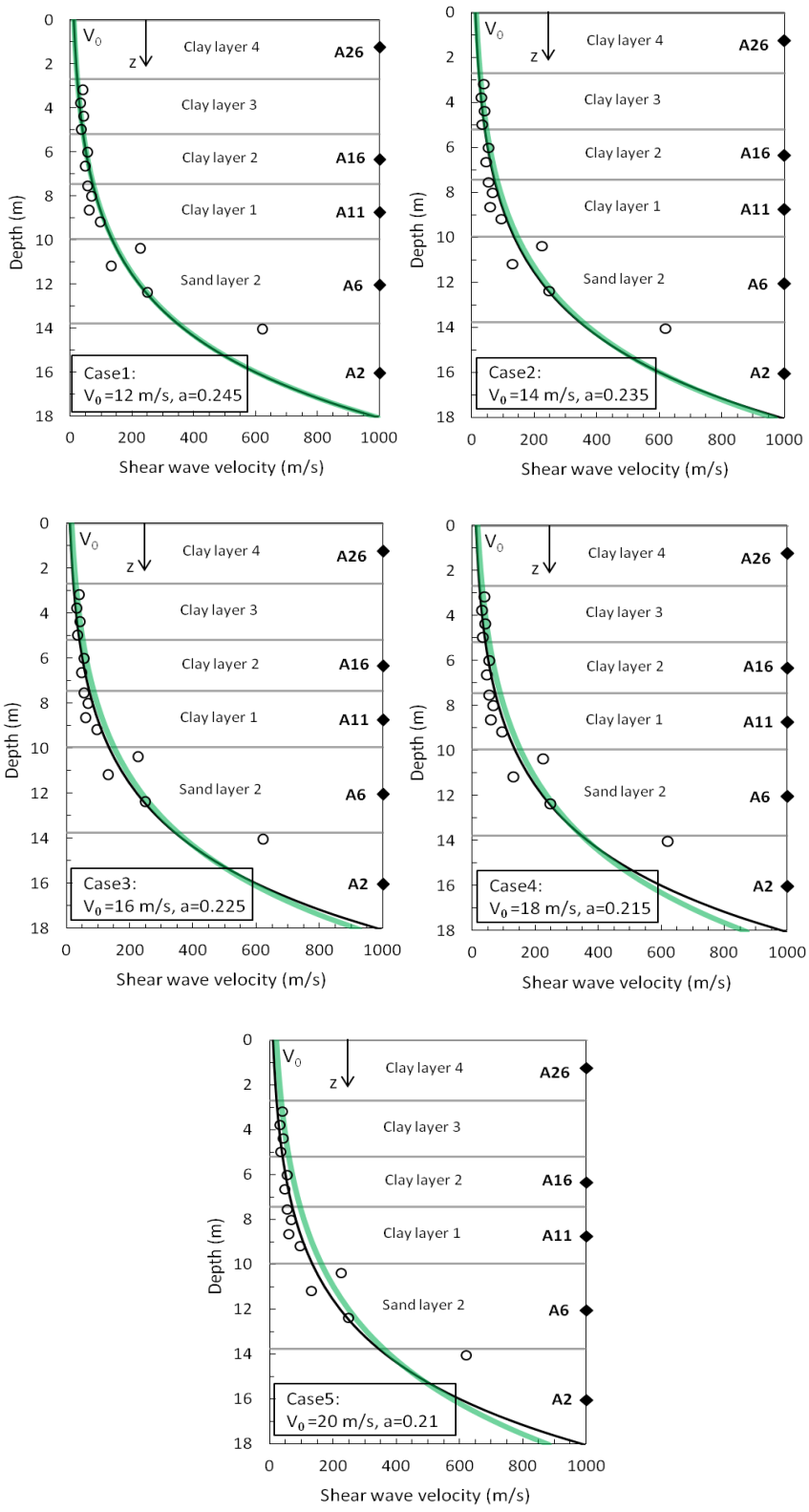

Figure 5.21 Shear velocity profile for five different cases (The solid black line represents the least squares fit.)

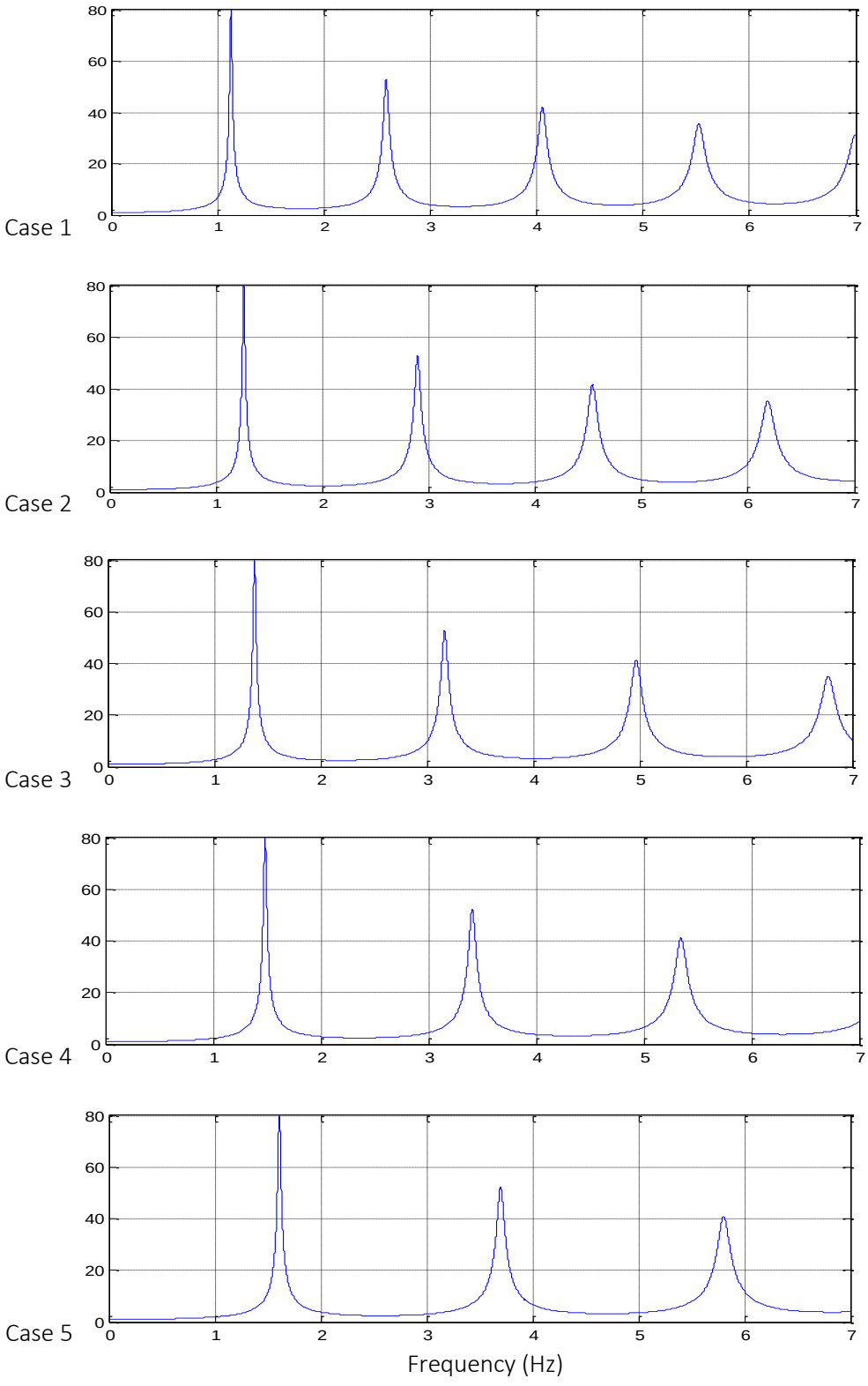

Figure 5.22 Evolution of amplification functions with variations in V_0 and a

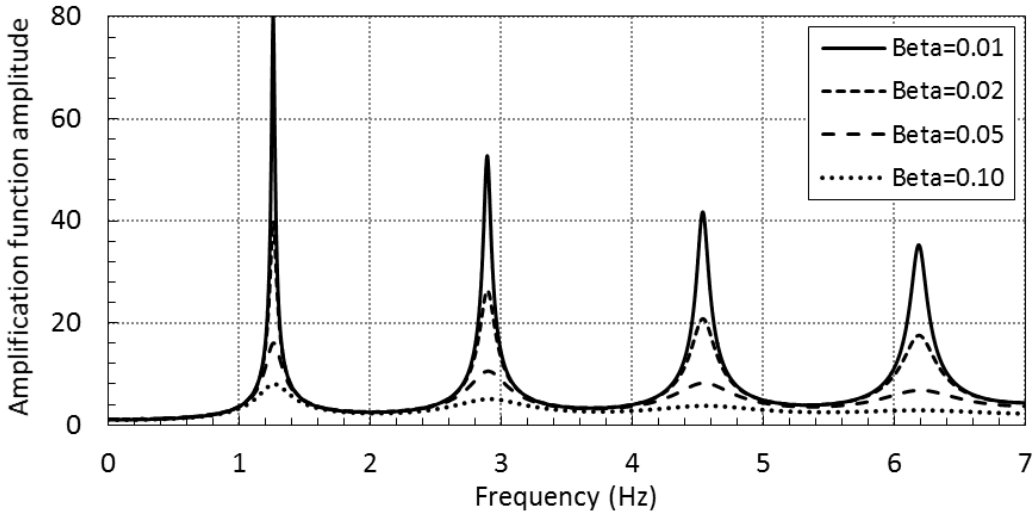

Figure 5.23 Amplification functions of the soil model derived from the analytical solution for various damping ratios

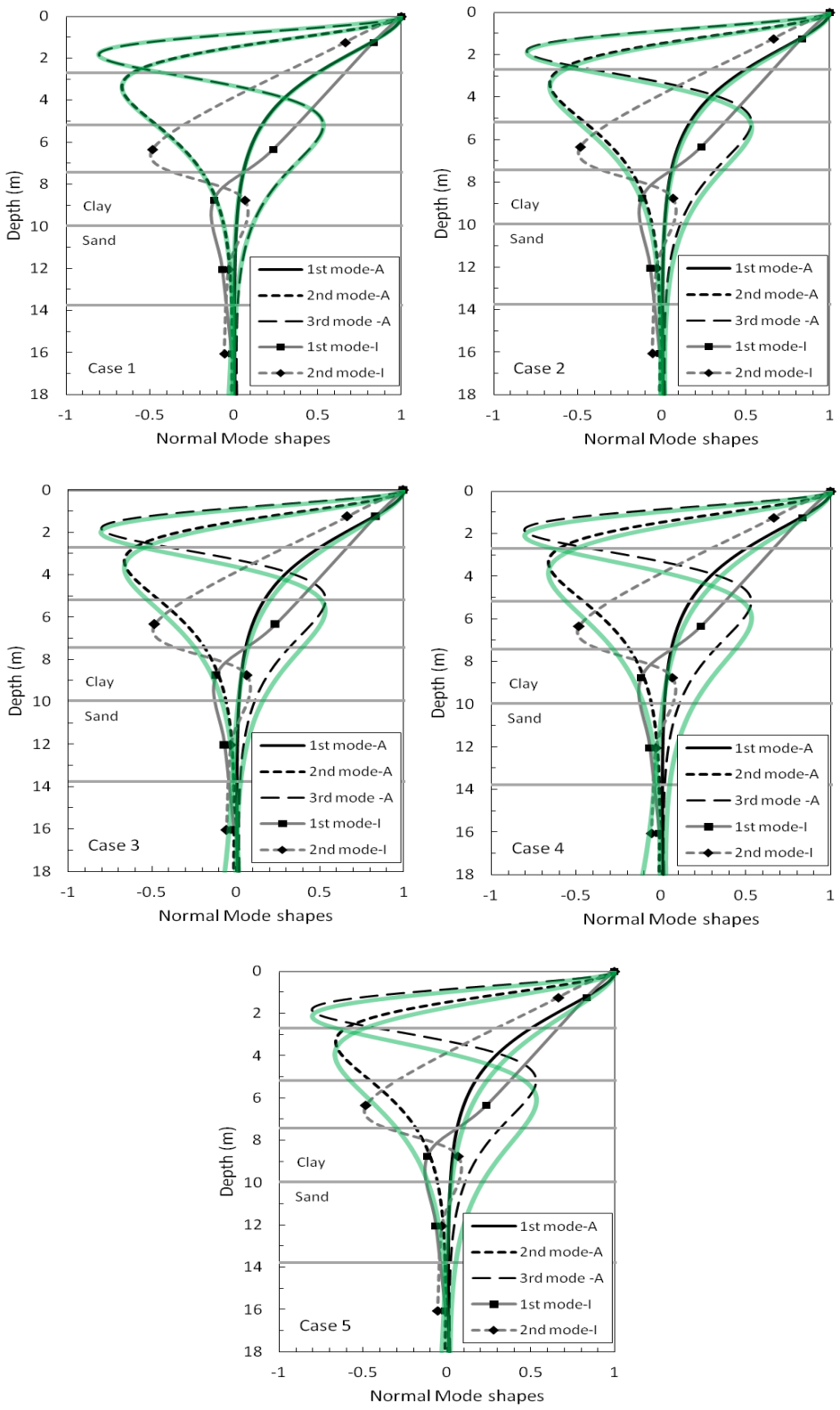

Figure 5.24 Evolution of normal mode shapes with changing V_0 and a shown by green curves
(Damping ratios was assumed for all modes as 1%.)

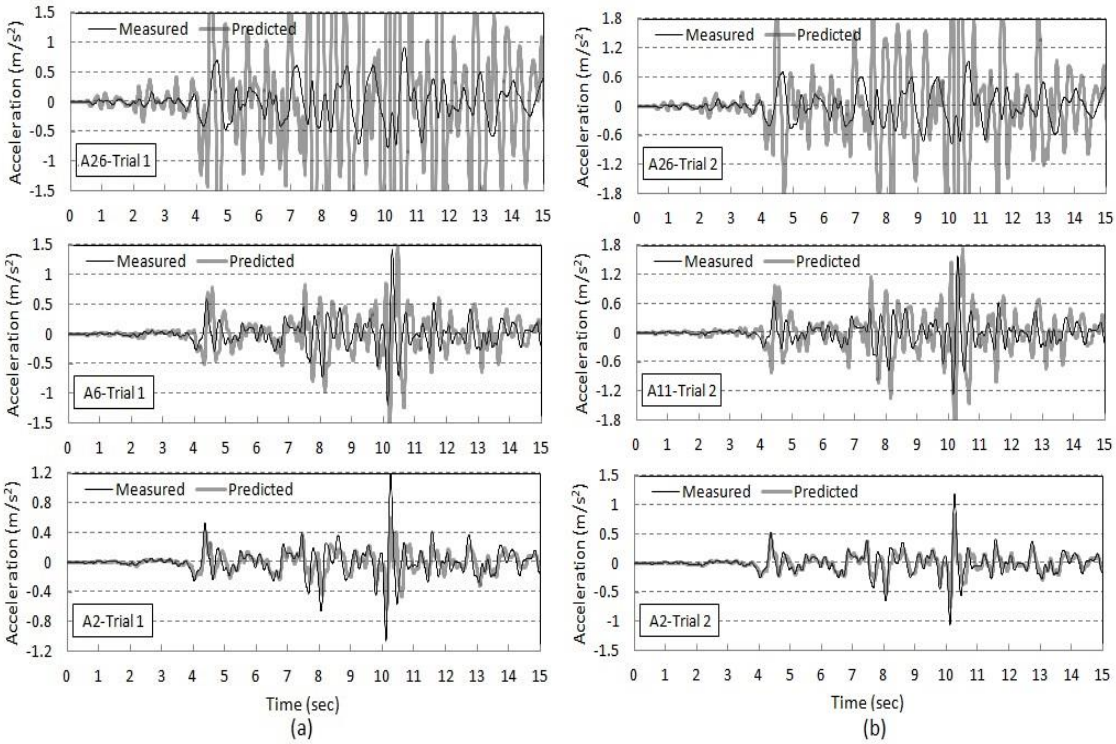
Measured
Predicted
A26-Trial 1
A6-Trial 1
A2-Trial 1
A26-Trial 2
A11-Trial 2
A2-Trial 2
Acceleration (m/s²)
Time (sec)
(a)
(b)

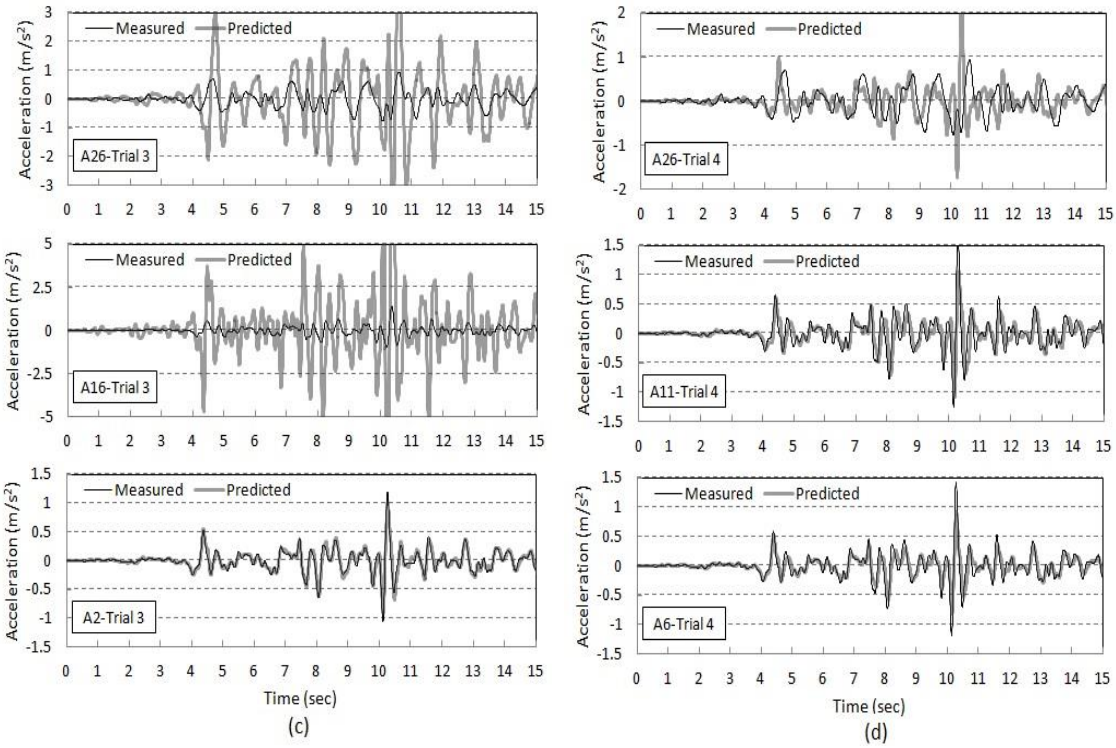
Measured
Predicted
A26-Trial 3
A16-Trial 3
A2-Trial 3
A26-Trial 4
A11-Trial 4
A6-Trial 4
Acceleration (m/s²)
Time (sec)
(c)
(d)

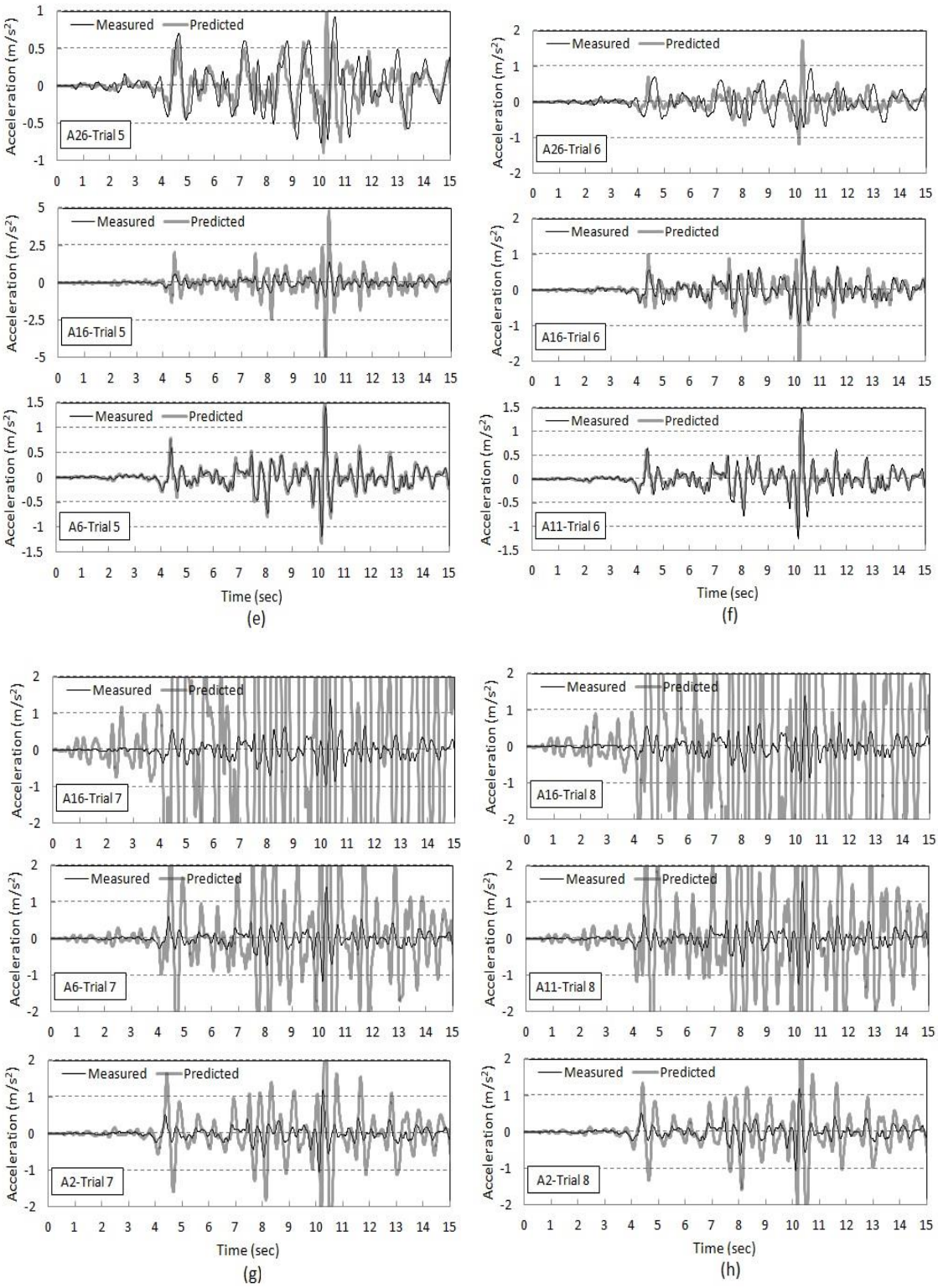

Figure 5.25 Response predictions for Event 1
(a) Trial 1, (b) Trial 2, (c) Trial 3, (d) Trial 4, (e) Trial 5, (f) Trial 6, (g) Trial 7, (h) Trial 8

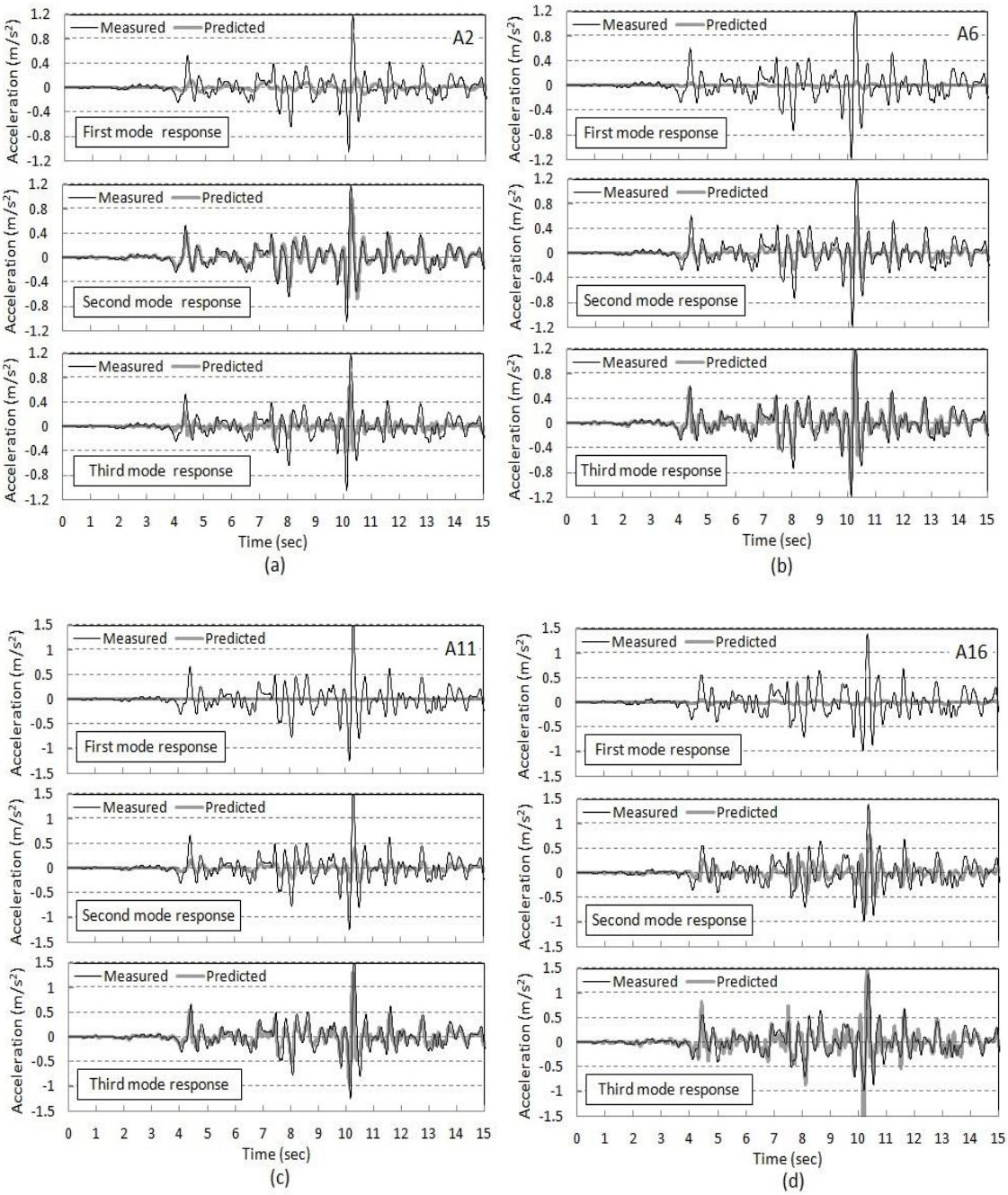
Measured
Predicted
A2
First mode response
Second mode response
Third mode response
Acceleration (m/s²)
Time (sec)
(a)
A6
(b)
A11
(c)
A16
(d)

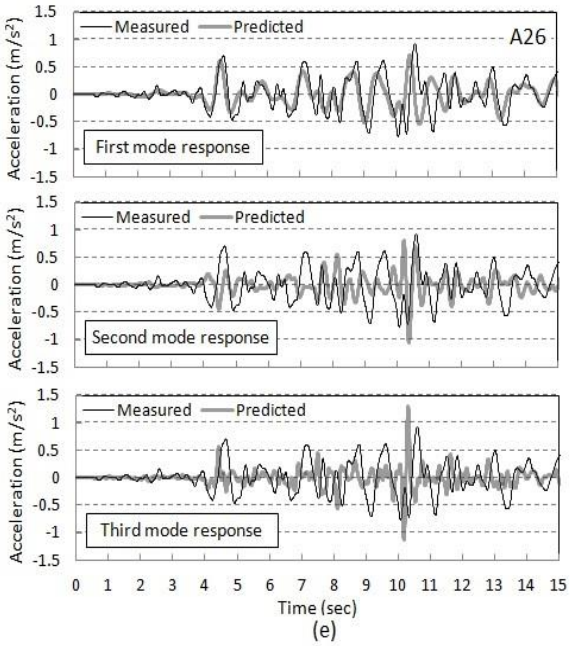

Figure 5.26 Responses of individual modes in Event 1
(a) A2, (b) A6, (c) A11, (d) A16, (e) A26

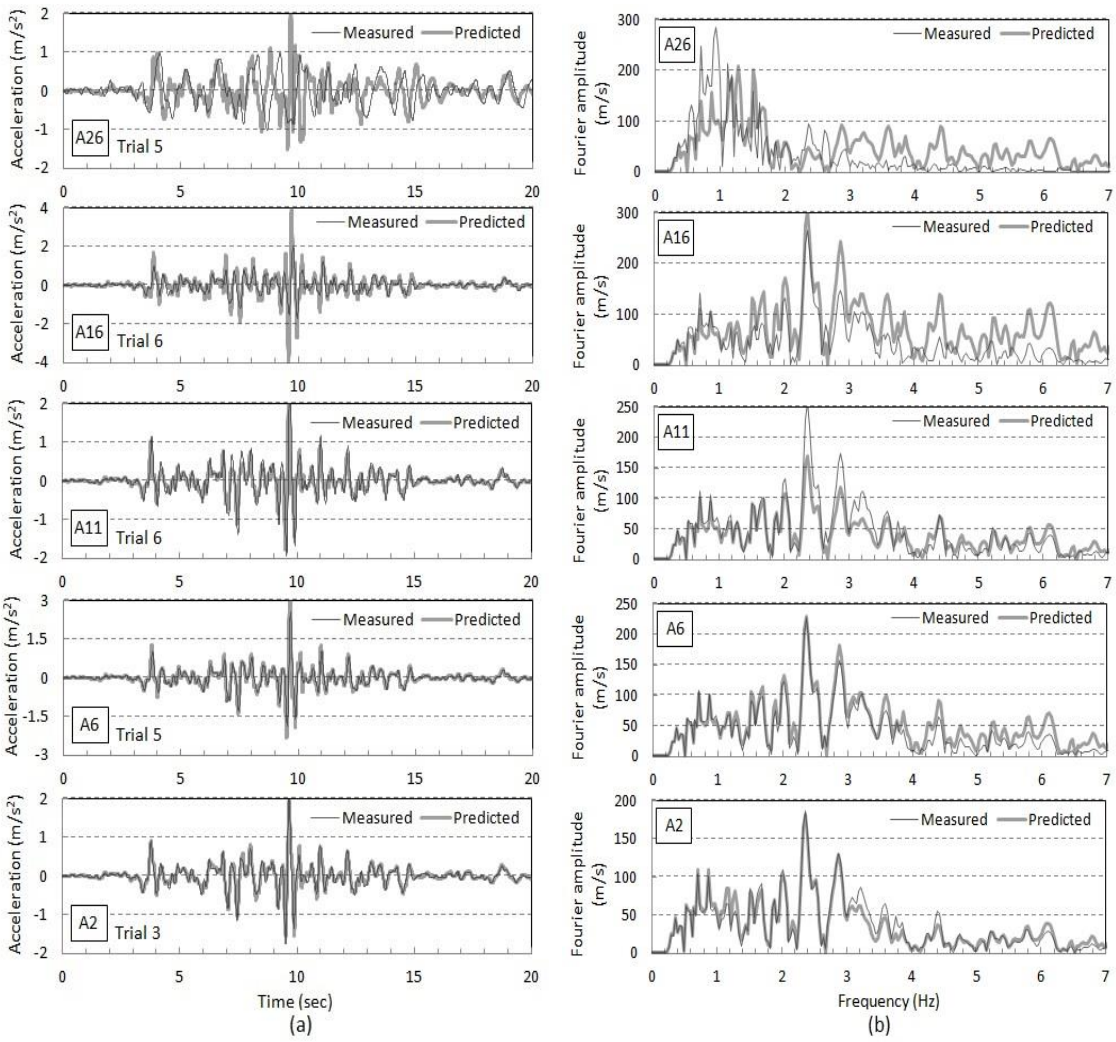

Figure 5.27 Response predictions for Event 2
(a) time histories (b) Fourier amplitude spectra

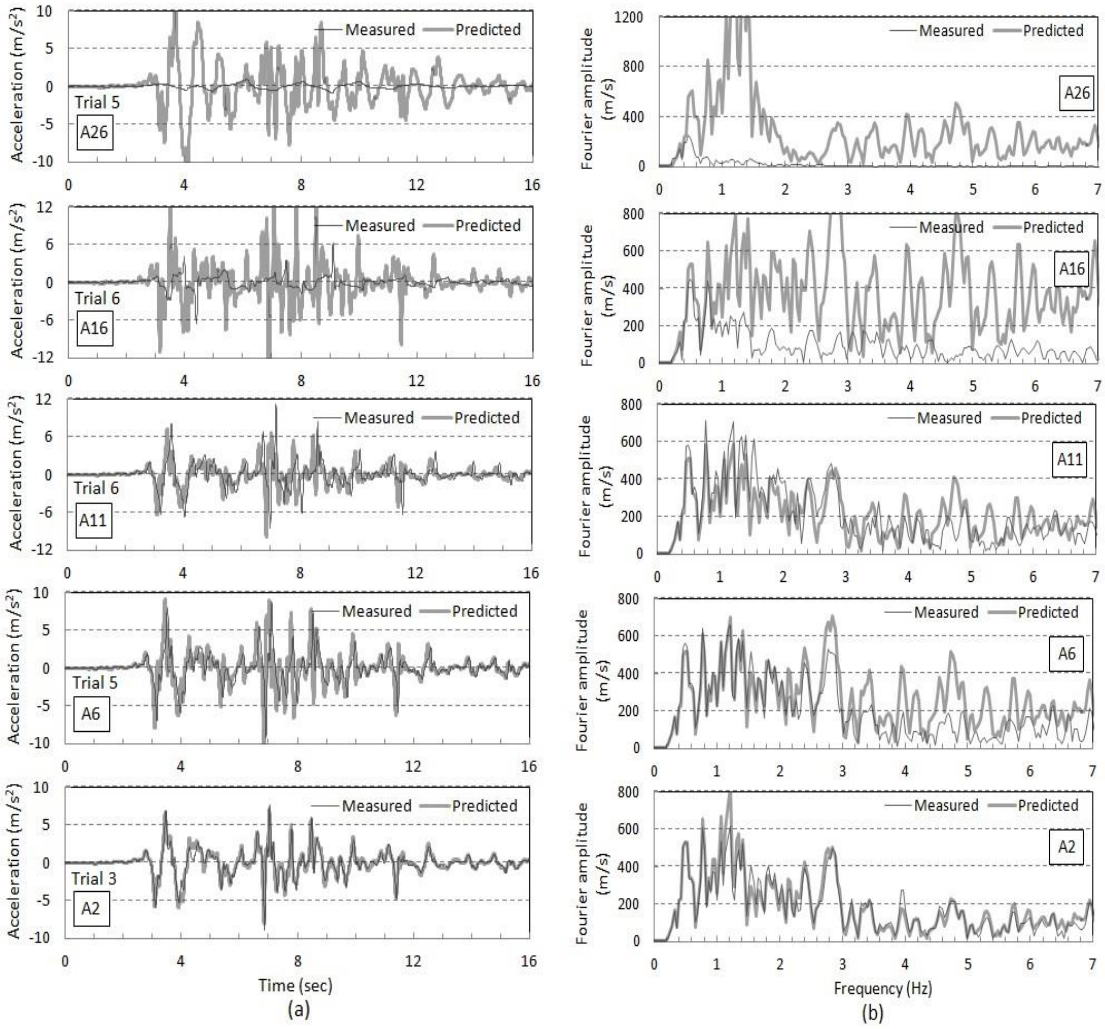

Figure 5.28 Response prediction for Event 3
(a) time histories (b) Fourier amplitude spectra

CHAPTER 6: DEVELOPING A MACRO-ELEMENT FOR SOIL-PILE INTERACTION

6.1 Modification of Winkler springs for dynamic and cyclic lateral loads

The Winkler foundation method can also be considered in modeling the hysteretic reactions between soils and piles, provided that appropriate modifications are applied. In real structures, several mechanisms can generate hysteretic behavior, including friction at connections and joints, friction between the structure and non-structural members, opening and closing of the cracks, and permanent deformations. The response of a hysteretic system depends on both the instantaneous displacement and the history of the displacement. Other components of the dynamic response that should be accounted for in a soil-pile interaction model include 1) formation of a gap between soil and pile, 2) stiffness and strength degradation of soil and pile, 3) the rules for unloading and reloading, 4) rate-dependent radiation damping, and 5) pile inertial effect (Matlock et al., 1978; Badoni and Makris, 1996; Boulanger et al., 1999; Gerolymos and Gazetas, 2005; Allotey and El Naggar, 2008a, 2008b). In the following sections, each component will be discussed briefly.

6.1.1 Inclusion of gap

Gap formation has been modeled in the literature with the aid of detachable Winkler springs at the front and the rear sides of the pile (Matlock et al., 1978; Pranjoto and Pender, 2003; El Naggar and Bentley, 2000). As shown in Figure 6.1, detachment of the springs causes less (or no) resistance against movement of the pile head. Under repeated cyclic loading, springs are repeatedly detached and reattached. As the number of cycles of loading increases, the disengagement position can either move further away from the

initial position, or it can remain unchanged, which determines the gap width at the ground surface and the gap depth from the soil surface. Matlock et al. (1978) considered the depth of the gap to be the same as that defined by Matlock (1970): the depth at which the surface effects no longer influence the pile lateral behavior. As can be seen in Figure 6.1(b), the gap shows up in the load-displacement curves as a flat region with low (or no) resistance.

In cohesive soils, a steady-state gap is likely to form as the number of loading cycles increases. It has been reported that gapping can reduce the lateral stiffness of the pile head by half (Pranjoto and Pender, 2003). Ignoring the soil-pile separation overestimated the ultimate lateral load capacity by about 43% in a single-pile test conducted by Hussien et al. (2010). Formation of a residual gap causes a section of the pile near the ground surface to be unsupported, which produces pinched lateral load-deformation loops in that section. Moreover, gap development transfers the soil resistance from the surface layers to the deeper layers. Gapping in cohesive foundation soils affects not only the soil reaction but also the radiation damping in dynamic loadings, which will be discussed later. Cohesionless soils, on the other hand, tend to flow into the gap, and they sometimes result in stiffness hardening of the pile response under cyclic loading due to densification of the sand (Allotey and El Naggar, 2008b). This behavior is shown schematically in Figure 6.2. In contrast, when liquefied sand fills the separation gap between the pile and soil, the response of the mixture during flow is most likely softer than the original soil.

Interaction elements developed by Blaney (1986) – including viscous dashpot, coulomb blocks, and sliding elements – were used to reproduce the results of a dynamic load test on a full-scale pile with superstructure mass. Nogami et al., (1992) formulated a

model consisting of near-field and far-field elements. The near field was simulated by nonlinear springs and masses representing the soil adjacent to the pile. The far field was modeled with a linear spring in parallel with a dashpot to represent the linear stiffness and radiation damping. Figure 6.3 shows the procedure of modifying the p-y curves to model the gap formation in cyclic loadings.

A nonlinear p-y element was developed by Boulanger et al., (1999) and was incorporated into a finite-element program to study the seismic behavior of single piles in soft clay overlaying a dense sand layer. As depicted in Figure 6.4, this nonlinear p-y element consisted of elastic, plastic, and gap components connected in series. The gap component models the influence of a physical gap and the undrained hysteretic behavior of the soil. The gap applies a residual resistance that acts as a drag force on the sides of the pile when it moves within the gap. The transition from gap behavior to contact behavior was made smooth by including a nonlinear closure spring parallel to a nonlinear drag spring. The resulting p-y curve closely reproduced the backbone curve recommended by Matlock (1970) for soft clay. Although promising in several cases, the implementation, calibration, and numerical robustness of this model for a broad range of soil and pile properties have not been fully addressed. For example, in a study by Rahmani et al. (2012), Boulanger's model resulted in underestimation of the peak bending moments when compared with measured values in two centrifuge experiments.

6.1.2 Inclusion of stiffness and strength degradations

The degradation in the ultimate capacity and stiffness of the p-y elements has been modeled through various methods. Matlock et al. (1978) simulated the strength degradation by applying a degradation factor to the ultimate plastic resistance of each

sub-element. To model strength degradation in cohesive soils, exponential models (Dunnavant and O'Neill, 1989) and hyperbolic models (Georgiadis et al., 1992a) have been adapted, respectively for submerged stiff clay and soft clay. Rajashree and Sundaravadivelu (1996) and Hussien et al. (2010) considered a degradation factor as a function of the number of cycles and the deflection at the first loading cycle. The degradation factor reduced the ultimate resistance of the soil at various depths. Degradation can also be caused by hydraulic scour (Dunnavant and O'Neill, 1989) and the seismically induced pore water pressure, as studied by Varun et al. (2013).

6.1.3 Unloading and reloading curves

Where the virgin loading curve is defined (e.g., by the conventional p-y curves), all subsequent unloading and reloading force-displacement paths afterward can be assumed to follow the extended Masing (1926) criteria. According to Masing's hypothesis, the curve between the reversal points for the positive and negative displacements are the scaled and shifted version of the back-bone curve. Other forms of algebraic nonlinear models that have been proposed for describing the hysteretic behavior include the Ramberg-Osgood model (1943) illustrated in Figure 6.5 and the Menegotto-Pinto model (1973). Multilinear hysteresis models also have been developed; one such model is the Medina-Krawinkler (2003) model illustrated in Figure 6.6. Allotey and El Naggar (2008b) developed a multilinear model with prescribed rules for loading, unloading, and reloading applied to a problem of soil-pile interaction (Figure 6.7).

6.1.4 Radiation damping

Material damping and radiation damping are two fundamentally different damping phenomena associated with soil-pile interaction. Material damping is a measure of the

loss of energy in the soil solely as a function of cyclic strain, independent of the vibration frequency. This type of damping, more pronounced at low frequencies, can be modeled using the area enclosed by the force-displacement loops. Radiation damping on the other hand, represents the loss of energy due to outgoing stress waves transmitted from a vibrating pile to the soil. The relative motion of the pile against the surrounding soil generates stress waves at the contact surface. Radiation damping increases with frequency (Gazetas, 1984). At frequencies below the fundamental frequency of the unperturbed soil deposit, no radiation damping occurs. However, when the loading frequency is increased beyond the fundamental frequency of the soil, the damping ratio increases with depth. Gazetas and Dobry (1984) obtained radiation dashpot coefficients for a linear elastic soil as a function of the loading frequency, the geometry of the soil-foundation system, and the stress-strain behavior of the soil.

In the dynamic BNWF method, energy loss through radiation damping has been modeled by two main approaches. In the first method (Kagawa and Kraft, 1980), the effect of radiation damping on pile response was assessed by including a linear viscous dashpot in parallel with the nonlinear p-y elements, as shown in Figure 6.8(a). In the other approach (Novak and Sheta, 1980; and Nogami et al., 1992), damping in the near field with strong soil nonlinearity was modeled with a nonlinear hysteretic element, while the damping in the far field was modeled with a linear visco-elastic dashpot in series with the hysteretic element (see Figure 6.8b). Using the centrifuge test of a single pile in seismically loaded soft clay and the BNWF method, Wang et al. (1998) compared the two different implementations of the radiation damping. The numerical simulations showed that parallel radiation damping restricts the lateral movement of the pile head and

thus results in a stiffer system response than that for the series radiation damping. However, in series radiation damping, the predicted response is sensitive to the stiffness of the p-y curve, and the dashpot force does not influence the p-y springs. It was concluded that series radiation damping is technically superior to parallel radiation damping because it avoids the unrealistically large damping forces. Further studies showed that radiation damping is strongly influenced by the geometric and material nonlinearity in the soil-pile system. Gerolymos and Gazetas (2005) and Varun et al. (2013) proposed formulations for a visco-plastic dashpot that could capture the coupling between the plastic deformation and the radiation damping.

6.2 Hysteresis Bouc-Wen model overview

The basic version of the Bouc-Wen models was originally proposed by Bouc (1967) and later extended by Wen (1976). It was represented by a first-order nonlinear differential equation that related the input displacement to the output restoring force in a rate-independent way. The Basic Bouc-Wen model (as it has been called in the literature) does not account for the degradation and gapping phenomena occurring in all structures when subjected to cyclic loadings. Evolution and changes in hysteresis loops reflect the degradation in the system. Baber and Wen (1981) were the first researchers to incorporate strength and stiffness degradation into the Basic Bouc-Wen model associated with the energy dissipated in the structure. Sues et al. (1988) added a new feature to the Basic Bouc-Wen model to account for displacement-dependent degrading behavior observed in reinforced concrete structures. Baber and Noori (1985) and Foliente (1995) introduced the pinching effect, a sudden or gradual loss of stiffness due to opening and closing of cracks in wooden, steel, or concrete structures. These extended Bouc-Wen models are

often called Bouc-Wen type models or the Generalized Bouc-Wen (GBW) models. The GBW models have proven capable of reproducing a wide range of displacement-force traces matching the behavior of a variety of hysteretic systems such as wooden structure (Figure 6.9). They have been employed in structural control, damage detection, and health monitoring (Ma et al., 2004; Loh and Chung, 1993; Sengupta and Li, 2013), in addition to being implemented in simulating the seismic and cyclic responses of hysteretic structures.

The GBW models are attractive for behavior prediction of inelastic systems, but calibrating their control parameters is known to be time- and labor-intensive. A common approach in identifying the parameters is to use a set of experimental input-output data and tune the parameters in such a way that the output of the model matches the measured response. Because this model is an empirical one and cannot be derived from the fundamental postulates of mechanics, the exact physical meanings of the parameters are not yet understood fully. Few studies have been performed to clarify their roles in characterizing the response and to identify the degree of their sensitivity (Ajavacom et al., 2008, Sengupta and Li, 2013). The parametric identification methods in the literature include ordinary least squares (Sues et al., 1988), modified Gauss-Newton approach (Kunnath et al., 1997), least-squares-based adaptive identification algorithm (Smyth et al., 1999), Extended Kalman Filter (Hoshiya and Sutoh, 1992; Loh and Chung, 1993; Zhang et al., 2002; Lin and Zhang, 1994), Unscented Kalman Filter (Wu and Smyth, 2008), genetic evolution algorithm (Ajavakom et al., 2008), and multi-objective optimization (Ortiz et al., 2013).

In the area of foundation engineering, the Bouc-Wen model has been of interest in predicting the dynamic nonlinear response of pile foundations under lateral and vertical loads. Trochanis et al. (1991) were the first to implement the GBW model to simulate the pile response to static and cyclic loading. The hysteresis model was used to represent the force-displacement relationship of the nonlinear p-y springs distributed along the pile. Badoni and Makris (1996) simulated the dynamic soil-pile reactions with hysteresis springs and frequency-dependent viscous dashpots connected in parallel in a one-dimensional finite element formulation. The parameters of the model were calibrated using five well-instrumented full-scale experiments. Gerolymos and Gazetas (2005) validated a Bouc-Wen type model by simulating the response of flexible piles under three types of cyclic loadings in a centrifuge test. The developed model was used to model cyclic and dynamic responses of a rigid caisson foundation in soft soil under lateral loading (Gerolymos and Gazetas, 2006). The model was validated against the results of in-situ static load tests and predictions of a 3-D finite element model. No degradation or pile-soil separation were included in the model. Soneji and Jangid (2008) modeled the seismic soil-pile interaction in an isolated cable-stayed bridge by using continuously distributed basic Bouc-Wen hysteretic springs and viscous dashpots placed in parallel. Varun et al. (2013) established a Bouc-Wen type model to predict the behavior of piles in liquefiable soils under seismic motions; this model parameters were calibrated based on experimentally extracted p-y curves and measured soil properties.

As discussed earlier, the parameters of these models can be identified using robust identification methods and data from full-scale and reduced-scale experiments or numerical analysis, but it is desirable to identify the relationship between the model

parameters and the soil properties, such as Young's modulus and undrained shear strength (Badoni and Makris,1996; Gerolymos and Gazetas, 2006). The following sections will discuss formulation of a GBW model and calibration of the shape parameters in a seismic soil-pile interaction problem.

6.3 Formulation

The macro-element representing the seismic soil-pile interaction in this study consists of a hysteresis spring and a viscous dashpot connected in parallel (Figure 6.10). The displacement experienced by this setup is the relative displacement between the pile and the free-field soil y_{p-s} at a given level. The pile displacement with respect to the base, y_p, is obtained from the bending moment curve-fitting already performed for each time instant (detailed in Chapter 4) and the corresponding soil displacement, y_s, derived from double integration of the free-field acceleration relative to the base. The resultant resisting forces induced in the macro-elements, the forces in the nonlinear hysteretic spring F_s, and the forces in the viscous dashpot F_d, are acting as the soil reaction distributed along the pile. Dynamic equilibrium of a pile resting against the interaction elements is given by this fourth-order partial differential equation,

$$EI\frac{\partial^4 y_p(z,t)}{\partial z^4} + m\frac{\partial^2 y_p(z,t)}{\partial t^2} + F_s(z,t) + F_d(z,t) = 0 \qquad (6.1)$$

where EI is the bending stiffness of the pile, m is the mass per unit length of the pile, and z is the location along the pile measured from the soil surface. In this chapter, the inertial force caused by the pile mass is not considered in the formulations. Therefore, the second term in Eq. 6.1 is removed. It is to be noted that in the back-calculation of y_p from the bending moment data, the pile mass was ignored as well. With this assumption, the first term of Eq. 6.1 is the soil reaction per unit length of the pile $p(z,t)$, which has been

estimated already (as reported in Chapter 4) and which is the resultant of the normal and shear stresses along the perimeter for a unit length of the pile. The goal is to calibrate the interaction elements such that the distributed forces in the nonlinear spring and the dashpot would be equal to the soil reaction $p(z,t)$:

$$p(z,t) = -F_s(z,t) - F_d(z,t). \tag{6.2}$$

6.3.1 Formulation of the hysteresis component

The restoring force in the nonlinear spring F_s at depth z is expressed as the sum of an elastic and a hysteretic component:

$$F_s(t) = \alpha k y_{p-s} + (1-\alpha) k y_0 r. \tag{6.3}$$

The restoring force is associated with y_{p-s}, the pile deflection with respect to the free-field at the location of the spring and the dimensionless hysteresis state variable r. The parameter α, sometimes referred to as the rigidity ratio, is the ratio of the post-yield stiffness to the initial elastic stiffness k; therefore, it is dimensionless. Small-amplitude elastic distributed stiffness k has the unit of stiffness per unit length. It corresponds to the traditional subgrade modulus multiplied by the diameter of the pile. The soil reaction and pile deflection at the initiation of yielding in soil, p_0 and y_0, respectively, are related through the initial elastic stiffness as $p_0 = k y_0$. The hysteretic state variable $r(t)$ can be calculated by solving the nonlinear differential equation

$$\dot{r}(t) = h(t) \frac{A\dot{y}_{p-s} - \upsilon(t)(\beta|\dot{y}_{p-s}||r(t)|^{n-1} r(t) + \gamma \dot{y}_{p-s}|r(t)|^n)}{\eta(t)} \tag{6.4}$$

known the time history of y_{p-s} .

$$\upsilon(t) = 1 + \delta_\upsilon \varepsilon(t) \tag{6.5}$$

$$\eta(t) = 1 + \delta_\eta \varepsilon(t). \tag{6.6}$$

Here, $\upsilon(t)$ and $\eta(t)$ are called the degradation shape functions which are controlled by the amount of dissipated energy $\varepsilon(t)$, the rate of strength degradation δ_υ, and the rate of stiffness degradation δ_η. These functions define the progressive loss of stiffness and strength as the cyclic loading proceeds. Because degradation depends on the response duration and the severity of the excitation, the dissipated energy has been selected as a suitable representative in formulation of both stiffness and strength degradations. The area enclosed by a complete hysteresis loop (F_s vs. y_{p-s}) is the measure of the energy dissipated in that cycle, expressed as

$$\varepsilon = (1-\alpha)k\int_{t_0}^{t_c} r\, y_0\, \dot{y}_{p-s}\, dt \tag{6.7}$$

which is a continuous integral of the hysteresis force over the relative displacement y_{p-s}. The dissipated energy ε defined in Eq. 6.7 represents only the loss of energy through hysteresis between the initial time t_0 and the current time t_c and does not include the energy absorbed by the radiation damping through the viscous dashpot. The unit of ε in this formulation is kN.m/m, assuming k is represented in kN/m/m and all the displacement values are measured in meters.

The pinching function $h(t)$ describing growth in the width and severity of the gap between the pile and the soil is defined as follows (Foliente, 1995):

$$h(t) = 1 - \zeta_1(t)\exp\left(-\frac{(r(t)sign(\dot{y}_{p-s})-qr_u)^2}{(\zeta_2(t))^2}\right) \tag{6.8}$$

where

$$r_u = \sqrt[n]{\frac{A}{\upsilon(t)(\beta+\gamma)}} \tag{6.9}$$

$$\zeta_1(t) = \zeta_0(1-\exp(-\rho\varepsilon(t))) \tag{6.10}$$

$$\zeta_2(t) = \left(\psi_0 + \delta_\psi\varepsilon(t)\right)(\lambda+\zeta_1(t)). \tag{6.11}$$

In Eq. 6.8, *sign* is the signum function of $\dot{y_{p-s}}(t)$, and r_u is the ultimate value of r that can be obtained by setting $\dot{r}(t) = 0$. The time-varying parameters $\zeta_1(t)$ and $\zeta_2(t)$ control the progress of pinching. The continuous nature of the pinching function in this formulation allows for a gradual transition from almost zero to maximum stiffness in pinched hysteresis loops without causing any numerical instability. The pinching function includes six control parameters: ζ_0, ψ_0, δ_ψ, λ, ρ, and q, which must be calibrated.

6.3.2 Formulation of the radiation damping

Radiation damping represents loss of energy due to the outgoing stress that a vibrating pile transmits to the soil, and it increases with frequency. In Figure 6.10, radiation damping is modeled by the dashpot placed in parallel with the nonlinear spring. Based on the work of Gazetas and Dobry (1984), the radiation damping can be represented by a linear viscoelastic dashpot as

$$F_d(z,t) = c_x \frac{dy_{p-s}}{dt},\ c_x = 2\left[1 + \frac{3.4}{\pi(1-\upsilon)}\right]^{1.25}\left(\frac{\pi}{4}\right)^{0.75}\left(\frac{\omega d}{V_s}\right)^{-0.25}\rho_s\, V_s\, d, \tag{6.12}$$

where c_x is the damping coefficient for small-amplitude motions, υ is the Poisson's ratio of the soil, V_s is the shear velocity of the soil, d is the pile diameter, and ω is the angular frequency of a harmonic excitation.

Because the gapping not only affects the soil reaction but also has a strong effect on the radiation damping, the coupling between the radiation damping and the hysteretic soil response has been realized by Gerolymos and Gazetas (2006) and Varun et al. (2013). The radiation damping was modified to account for the reduction in damping as a result of prevailing nonlinearity in the soil-pile system. The visco-plastic dashpot force was expressed as

$$F_d(z,t) = c_x \left[\alpha + (1-\alpha) y_0 \frac{dr}{dy_{p-s}}\right]^{c_s} \frac{dy_{p-s}}{dt} \quad (6.13)$$

where c_s is a visco-plastic parameter that controls the coupling between the nonlinearity in the hysteresis spring and the radiation damping. This parameter has been reported by Gerolymos and Gazetas (2006) in the range of [0, 0.5]. As can be deduced from Eq. 6.13, the visco-elastic damping coefficient is modified by the tangent modulus of the hysteresis force-displacement loops (i.e., $\frac{dF_s}{dy_{p-s}} \times \frac{1}{k}$).

6.4 Calibration and implementation of the macro-elements

6.4.1 Interpretation of the GBW model parameters

- The parameter α in Eq. 6.3, as defined earlier, is the post-yield stiffness over the initial elastic stiffness k. Using the experimentally derived p-y curves from the pseudo-static tests and/or the conventional p-y curves, k and α can be properly calibrated. When $\alpha = 0$, no strength hardening develops after the yield point and during soil-pile separation, whereas increasing α introduces strength hardening, as depicted in Figure 6.11. Setting α as zero induces a pure plastic behavior after yielding, which is in compliance with the characteristics of the conventional p-y curves for both soft and stiff clays without free-water.
- In Eq. 6.4, n controls the smoothness of the transition from linear elastic behavior to plastic behavior. As n increases, the transitions becomes sharper (Figure 6.12). A special bilinear case occurs theoretically for n going to infinity; however, in practice, values greater than 10 produce a similar behavior. Wen (1976) assumed integer values for n, but non-integer values have also been reported in literature.

- Parameter A in Eq. 6.4, which was introduced in Bouc and Wen's original paper published in 1981, was proved redundant by Ma et al. (2004). In this chapter, A is assumed to be 1.
- Parameters β and γ in Eq. 6.4 control the size and shape of the unloading and reloading branches of the hysteretic loops. The parameter β must be positive as a necessary condition for the Bouc-Wen model to generate stable hysteretic loops. Thermodynamic admissibility issues require the inequality $\beta \geq \gamma$ to be satisfied (Ismail et al., 2009). Setting $\beta = \gamma = 0.5$ means that the stiffness of the unloading curve after reversal is equal to the initial stiffness, which satisfies the Masing rule (Figure 6.13). The assumption that $\beta + \gamma = 1$ has been used in base isolation problems (Kunnath et al., 1997), simulating a pure visco-plasticity condition on the behavior. Basic hysteresis shapes produced by different interactions of the parameters β and γ are illustrated in Figure 6.14. In this chapter, it is assumed that $\beta = \gamma = 0.5$.
- When the system exhibits no degradation, δ_υ and δ_η can be set to zero. To simplify calibration, it is assumed initially that the degradation in the soil stiffness and strength are negligible. If it is difficult to reproduce the soil reaction, degradation can be incorporated into the model and the associated parameters can be estimated by trial and error.
- The most important part of the calibration process is finding reasonable estimates of the control parameters of the pinching function: ζ_0, ψ_0, δ_ψ, $\lambda, \rho,$ and q. Parameters δ_ψ and λ are the least sensitive parameters, and ζ_0 is the most sensitive parameter, according to the results of studies undertaken by Ma et al. (2004) and

Sengupta and Li (2013), as reported in Table 6.1. The parameter q simulates the drag force on the pile when it moves into the gap. It is expressed as a percentage of the ultimate soil strength. The qualitative roles of all the parameters involved in the GBW model are also included in Table 6.1.

- According to the previous work on the application of Bouc-Wen model for the reinforced concrete structures and wood structures, ranges of the control parameters were reported by Ma et al. (2004) and Sengupta and Li (2013), which are listed in Table 6.2.

6.4.2 Calibration of dampers

Unlike a harmonic motion consisting of one frequency, the applied excitations in the shaking events involved a frequency spectrum that had to be characterized with a single frequency, ω, in Eq. 6.12. Makris et al. (1993) defined the "predominant frequency" f_p of a seismic motion as the frequency at which the amplitude of the Fourier spectrum, as depicted in Figure 5.3 in the previous chapter, reaches its maximum. In another approach, Rathje et al. (1998) defined the predominant frequency as the weighted average of the frequencies in the frequency band of interest, expressed by

$$f_p = \frac{\sum_i {w_i}^2 f_i}{\sum_i {w_i}^2} \tag{6.14}$$

where f_i represents the discrete frequency (which was explained in Section 5.2) and w_i represents the amplitude of the Fourier spectrum at f_i. The fundamental frequencies using the former and latter methods are listed in Table 6.3 under Method 1 and Method 2, respectively.

Soil shear wave velocity V_s is another parameter of Eq. 6.12 that had to be determined *a priori*. Here, the estimated shear wave velocity profile shown in Figure 5.20

was used. The Poisson's ratio of the soil υ was set to 0.4. The density of the improved and unimproved soil ρ_s was estimated as 1.8 ton/m^3. The pile diameter d was 0.286 m.

6.4.3 Implementation

The state variable of the hysteresis spring $r(t)$ was obtained by solving a system of differential equations expressed as

$$\begin{cases} \dot{r}(t) = h(t)\frac{A\dot{y}_{p-s} - \upsilon(t)(\beta|\dot{y}_{p-s}||r(t)|^{n-1}r(t) + \gamma\dot{y}_{p-s}|r(t)|^{n})}{\eta(t)} \\ \dot{\varepsilon}(t) = (1-\alpha)kr\,\dot{y_{p-s}} \end{cases} \quad (6.15)$$

by utilizing numerical integration methods, such as Runge-Kutta method or central finite difference methods. In Eq. 6.14, $y_{p-s}(k)$ was available at each time instant as previously back-calculated (detailed in Chapter 4), and $\dot{y}_{p-s}(k)$ was calculated as

$$\dot{y}_{p-s}(k) = \frac{y_{p-s}(k) - y_{p-s}(k-1)}{T_s},\ T_s = 0.007323 \text{ sec.} \quad (6.16)$$

After the time history of $r(t)$ at each time instant was calculated, the restoring force in the hysteresis spring $F_s(t)$ was obtained by substituting for the values in Eq. 6.3. In deriving the viscous damping force F_d in Eq. 6.13, the term $\frac{dr}{dy_{p-s}}$ was obtained using the numerical differentiation techniques. One approach employed to identify the remaining control parameters was to use trial and error until a good agreement was achieved between the back-calculated (Chapter 4) and the simulated soil reactions using Eq. 6.3. However, this approach did not lead to a unique solution, because a large number of combinations of the parameters could provide a reasonable match with the back-calculated responses.

6.5 Results and discussion

The developed General Bouc-Wen model was used to simulate the soil reaction on pile 6DEF in Event 3 at two depths: 0.2 m within the improved soil and 6.34 m within the soft

clay. The results were compared with their counterparts, which were back-calculated from the bending moment curve-fitting methods detailed in Chapter 4 (Figures 4.27 and 4.35).

6.5.1 Simulated soil reaction in improved soil at z=0.2 m

The parameters y_0 and k were first estimated from the derived p-y curve at the depth of 0.2 m as recommended by Foliente (1995) in Figure 6.15. The initial stiffness was estimated as 7900 kN/m/m close to the Young's modulus of the soil reported in Chapter 3 and the yield displacement was estimated to be about 0.025 m (Figure 6.16). The maximum relative soil-pile displacement, at the depth of 0.2 m, was 0.2 m (Figure 4.35), which is slightly larger than the maximum back-calculated pile deflection in the pseudo-static load test.

The p-y curves derived for the improved soft clay reflected a very small post-yield stiffness. In this case, it was assumed that α=0, similar to the value recommended by Trochanis et al. (1991), Gerolymos and Gazetas (2006), and Varun et al. (2013). To simplify the process of parameter calibration, the other parameters associated with the back-bone curves were set as n=1 and β=γ=0.5.

To investigate the effects of k and y_0 on the resultant force of the macro-element, trials with various combinations of these parameters were conducted as shown in Figure 6.17. The red curve represents the derived p-y curve from the pseudo-static load tests. In this set of simulations, the radiation damping, soil-pile separation, and material degradation were not included. Increasing y_0 while keeping k constant increased the amplitude of the loops. On the other hand, decreasing k while keeping y_0 constant at 0.025 m seemed to reduce the amplitude of the simulated loops and the dissipated energy.

Among these trials, the one with the k and y_0 directly estimated from the pseudo-static p-y curve was selected as the best candidate for investigating the effects of the remaining control parameters of the GBW model and the radiation damping model.

The effects of increasing ζ_0, known as the most sensitive parameter in the pinching function, were investigated next. Figure 6.18 shows that increasing ζ_0 simulated wider slips and thinner loops with smaller amplitudes. According to Foliente (1995), the pinching function is active only during the reloading branches of the loops. Thus, a ζ_0 parameter in the range of 0.9 to 0.95 seemed appropriate. In the following simulations, a constant ζ_0=0.9 was implemented.

The effects of increasing ψ_0, the pinching magnitude and the second most sensitive parameter of the pinching function, was evaluated as shown in in Figure 6.19. Changing ψ_0 from 0.01 to 0.6 squeezed the loops together in the middle. The case with ψ_0=0.4 produced loops with reasonable agreements. At this point, it is noteworthy that the back-calculated loops for the negative displacements in the second and third quadrants appeared with almost no stiffness, which is very close to the characteristic of the behavior inside a gap formed between the improved soil and pile. Figure 6.20 shows the effects of variations in the pinching rate, δ_ψ. The case with δ_ψ=0.01 was selected as the best representative of pinching rate for the subsequent trials.

Degradation of the stiffness δ_η and the strength δ_υ were assessed, as shown in Figure 6.21. The combined effects of both degradation factors were also reported in this figure. The case with δ_υ=δ_η=0.01 was selected for the following simulations.

As explained earlier in this chapter, the residual resistance inside the gap or slip is simulated by the parameter q. The results in Figure 6.22 show that the cases with q=0.1

and q=0.4 produced loops that were the most similar to the measured loops; q selected as 0.1 for the following simulations. The effects of parameter p on the hysteresis loops were evaluated for values changing from 0.5 to 9 as shown in Figure 6.23. A p value of 6 produced the a reasonable match. The last parameter λ was found to be the least sensitive parameter (Figure 6.24); it was set as 0.6 for the rest of the simulations.

Adding viscoelastic and viscoplastic radiation damping to the simulations was performed by activating the dashpot connected in parallel to the hysteresis spring. The coupling between the radiation damping force and the plastic deformation in the spring is controlled by the parameter c_s in Eq. 6.13. Force-displacement loops with lower dissipated energy and thinner shapes corresponded to higher values of c_s, as shown in Figure 6.25. On the other hand, a linear viscoelastic dashpot with c_s=0 produced nearly oval-shaped loops (F_d vs. y_{p-s}).

Table 6.4 shows the list of the parameters used in three trials selected for simulating the improved soil reaction at the depth of 0.2 m. The simulated hysteresis loops along with the time-histories of the simulated soil reaction and the dissipated energy in the macro-element were compared against the corresponding back-calculated values as shown in Figures 6.26 through 6.37. The simulated responses for individual cycles defined in Figure 6.29 were depicted in Figures 6.29, 6.33 and 6.37 for Cases 1, 2 and 3, respectively. Comparing the loops in the first and second cycles reveals an increase in the stiffness in the second cycle which is a sign of material hardening. The developed BW model with the defined progressive degradations in the stiffness and the strength is not able to capture this behavior. However, based on the visual inspections of the plots the

selected models produced some of the peaks and trends in the back-calculated soil reactions.

6.5.2 Simulated soil reaction in improved soil at z=6.3 m

A similar procedure was undertaken for estimating the parameters of the back-bone curves in soft clay. The derived p-y curves inside the soft clay 6.3 m below the soil surface were compared with those from the traditional model (Figure 6.38). Due to the small displacements of pile 6DEF in pseudo-static tests, the derived p-y curve was limited to lateral displacement of 0.01 m while in shaking Event 3, the maximum relative displacement between the pile and the free-field soil reached to 0.15 m. Therefore, the parameters y_0 and k were estimated from the conventional p-y curve for soft clay. The conventional and the experimentally derived p-y curves showed a very close initial stiffness. However, the initial stiffness and the yield displacement were found to be overestimated and underestimated, respectively, and therefore they were adjusted. The pinching function for the soft clay model was set to 1, because formation of any gap between the soil and the pile at 6.3 m depth was expected to be unlikely. The degradation and radiation damping were included in the model. After running many trials, the model parameters were estimated as k=700 kN/m/m, y_0=0.05 m, α=0, β=γ=0.5, n=1, δ_v=δ_η=0.25, C_s=0.25, f_p=2.57 Hz. The simulation results using the winning trial are shown in Figures 6.39 to 6.41, which show that the force-displacement behavior could be characterized with oval shaped loops inside the soft clay 6.34 m below the soil surface. The calibrated model for the soft clay overestimated the soil reaction at the beginning of the excitation; however, it followed the trends and captured the peaks for most parts of the excitation. Another observation made from these figures is that contribution of the

radiation damping in the simulated reaction of the soft clay was much more significant than that of the improved soil.

6.6 Summary and conclusions

- An extended version of the GBW model was employed to simulate the seismic soil-pile reaction in the third shaking event.
- The developed model was capable of simulating gap formation between the improved soil and pile as well as the degradation in the stiffness and strength of the soil.
- Both radiation and material damping in the soil were explicitly accounted for by using distributed dashpots attached in parallel to the hysteresis springs formulated by the GBW model.
- Inclusion of the radiation damping with the hysteresis unit increased the soil resistance especially in soft clay whereas it had a minor effect on simulation of the response in improved soil possibly due to the gap formation.
- Incorporating the coupling between the radiation damping and the hysteresis force was necessary for reproducing the back-calculated soil reactions.
- Uncertainty in the various model parameters influenced the predicted soil reaction to varying degrees. Variations in some input parameters may heavily influence analysis results, while variations in others may affect analysis results very little. Identifying the most influential parameters on the results of the analyses is important because it allows users to focus their efforts on accurately characterizing the most important properties.

- The calibrated model for the soil reaction at a depth of 0.2 m within the improved clay was able to reproduce the soil response in the last three cycles while it was unable to capture the hardening occurred in the second cycle.

Table 6-1 Sensitivity Analyses on the GBW Model Parameters

Parameters	Role	Local sensitivity rank (Ma et al., 2004)	Global sensitivity rank (Ma et al., 2004)	Sensitivity rank (Sengupta and Li, 2013)
α	Ratio of the post yield to pre yield stiffness	1	2	7
β	Hysteresis shape control	5	4	3
γ	Hysteresis shape control	6	5	8
n	Sharpness of the yield	8	7	2
δ_ν	Strength degradation	12	9	6
δ_η	Stiffness degradation	4	8	5
p	Pinching slope	3	10	12
ζ_0	Measure of the total slip	2	1	1
ψ_0	Pinching magnitude	7	3	4
δ_ψ	Pinching rate	11	12	9
λ	Pinching severity. the amount and the spread of pinching in the loop	10	11	10
q	Pinching initiation	9	6	11

Table 6-2 Ranges of Control Parameters Reported by Ma et al. (2004) and Sengupta and Li (2013)

Parameters (reinforced concrete joint) Sengupta and Li (2013)	Parameters (wood structure) Ma et al. (2004)
$0.005<\alpha<0.07$	$0<\alpha<0.1$
$0.04<\beta<0.06$	$0.5<\beta<1.5$
$-0.02<\gamma<-0.01$	$-0.3<\gamma<0.5$
$1<n<1.1$	$0<n<3$
$0.00005<\delta_{\upsilon}<0.00008$	$0<\delta_{\upsilon}<0.05$
$0.005<\delta_{\eta}<0.002$	$0<\delta_{\eta}<0.3$
$0.04<p<0.09$	$0<p<5$
$0.85<\zeta_0<0.98$	$0.7<\zeta_0<1$
$0.75<\psi_0<0.95$	$0<\psi_0<0.2$
$0.1<\delta_{\psi}<0.2$	$0<\delta_{\psi}<0.01$
$0.1<\lambda<0.12$	$0<\lambda<1$
$0.03<q<0.08$	$0<q<0.3$

Table 6-3 Predominant Frequency of Base Motion in Shaking Events

Frequency (Hz) / **Events**	**Method 1**	**Method 2**
Event 1	2.37	2.4
Event 2	2.52	2.56
Event 3	0.64	2.57

Table 6-4 Selected Trials

Parameters	Case 1 Improved clay	Case 2 Improved clay	Case 3 Improved clay	Soft clay
k (kPa)	7900	7900	7900	700
y_0 (m)	0.025	0.025	0.025	0.05
α	0	0	0	0
β	0.5	0.5	0.5	0.5
γ	0.5	0.5	0.5	0.5
n	1	1	1	1
δ_v	0.01	0.05	0.05	0.25
δ_η	0.01	0.05	0.05	0.25
ζ_0	0.9	0.9	0.9	0
ψ_0	0.4	0.4	0.4	-
δ_ψ	0.01	0.01	0.01	-
λ	0.6	0.6	0.6	-
q	0.1	0.1	0.4	-
p	6	6	6	-
υ	0.4	0.4	0.4	0.4
d (m)	0.286	0.286	0.286	0.286
ρ_s (ton/m^3)	1.8	1.8	1.8	1.8
V_s (m/s)	20	20	20	20
f_p (Hz)	2.57	2.57	2.57	2.57
C_s	0.5	0.5	0.5	0.25

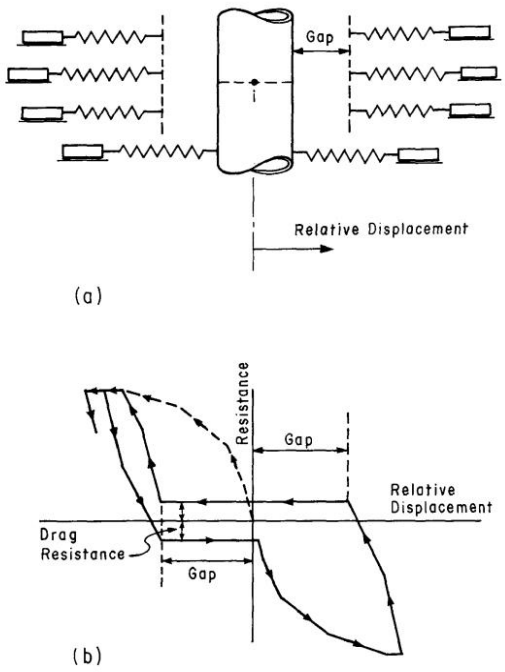

Figure 6.1 Soil reaction model, (a) multiple sub-elements at a single node

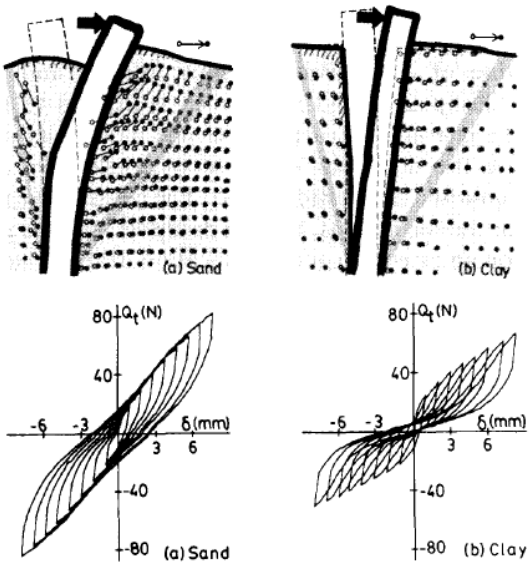

Figure 6.2 Response of a cohessionless soil (left) and a cohesive soil (right) (Gerolymos and Gazetas, 2005)

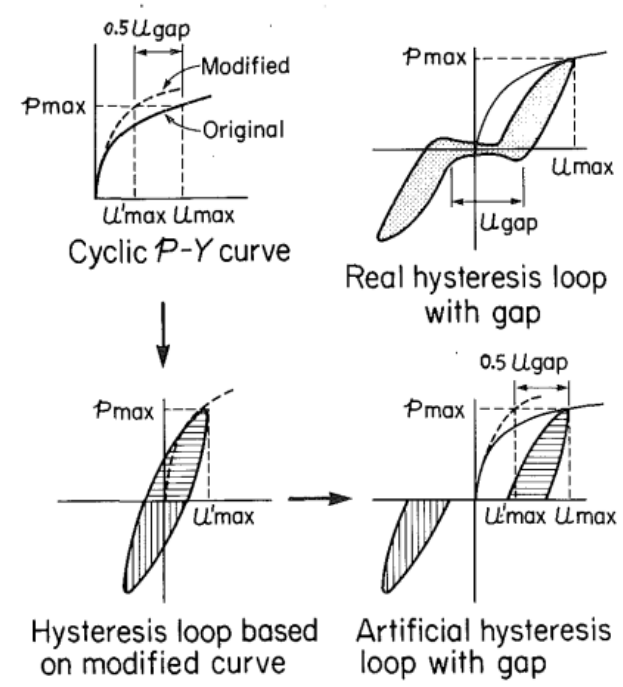

Figure 6.3 Correction of cyclic p-y curves to construct artificial hysteresis loop with gap (Nogami et al., 1992)

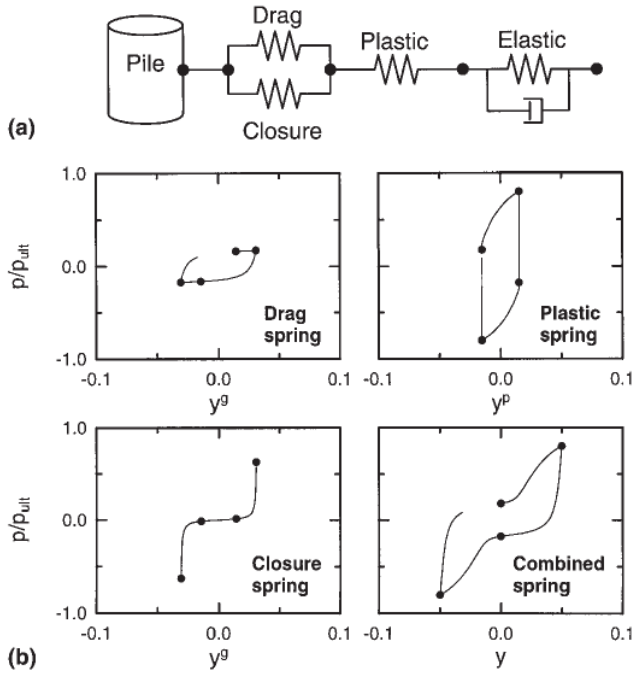

Figure 6.4 Characteristics of non-linear p-y element a) components b) behavior of the components (Boulanger et al. 1999)

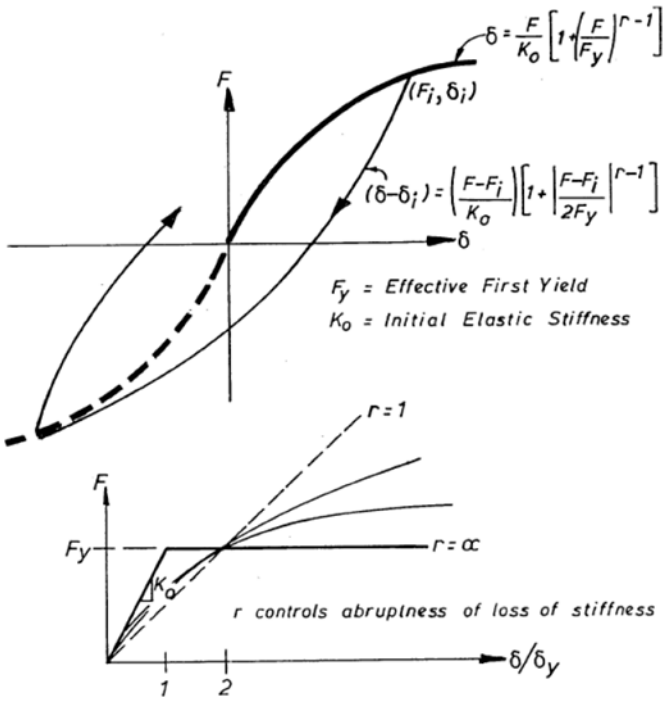

Figure 6.5 Ramberg-Osgood model (Carr, 2003)

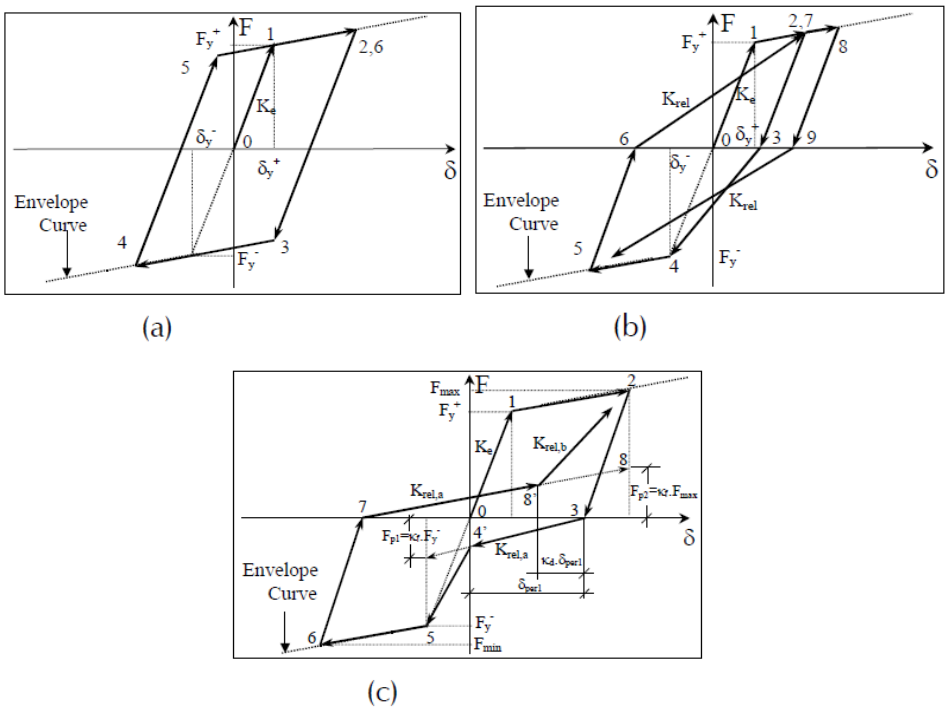

Figure 6.6 Multilinear hysteresis models (a), bilinear (b) peak oriented, (c) pinching model (Medina and Krawinkler, 2003)

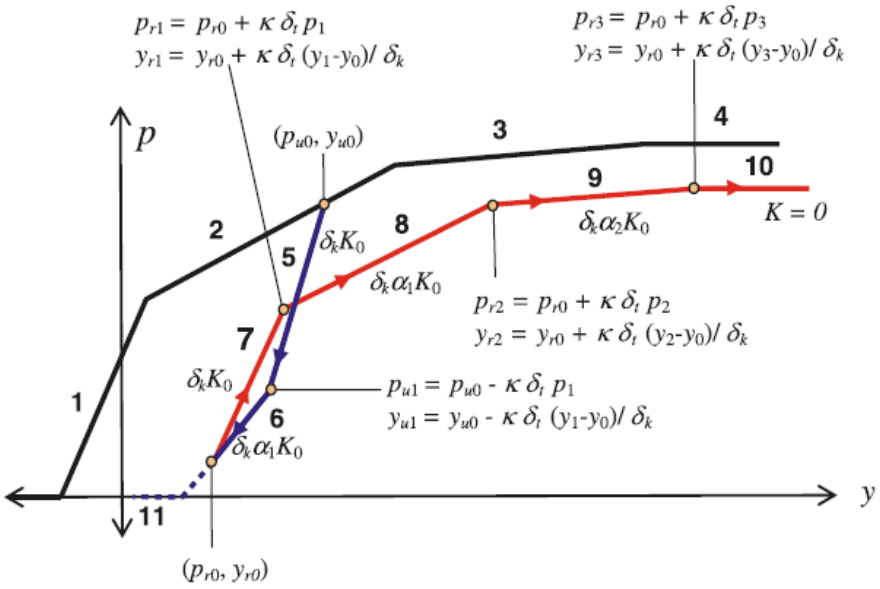

Figure 6.7 Developed model by Allotey and El Naggar (2008b) for cyclic and dynamic soil-pile interaction

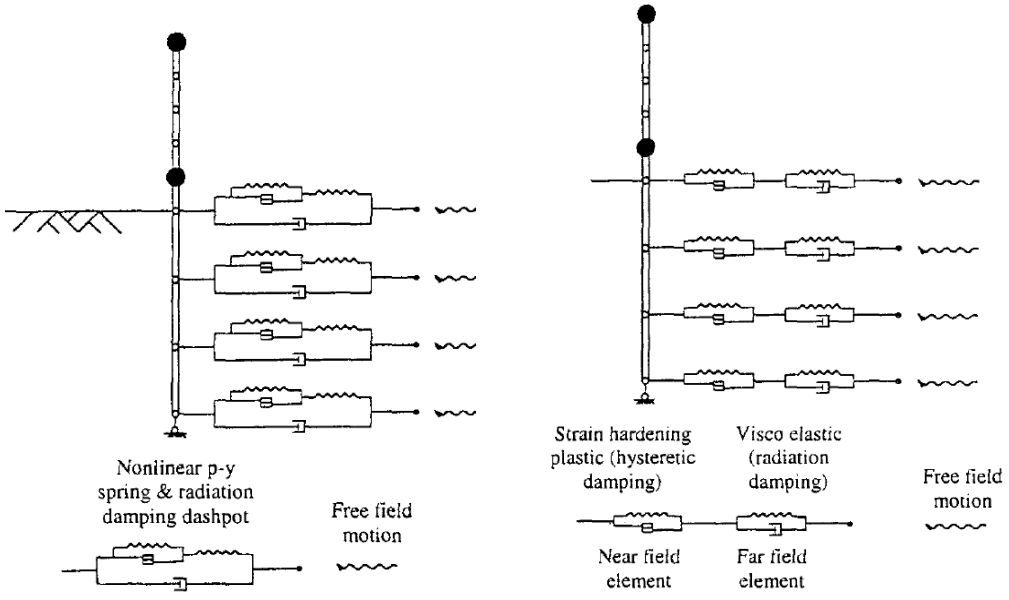

Figure 6.8 Soil-pile-structure model with (a) parallel damping (b) series damping (Wang et al., 1998)

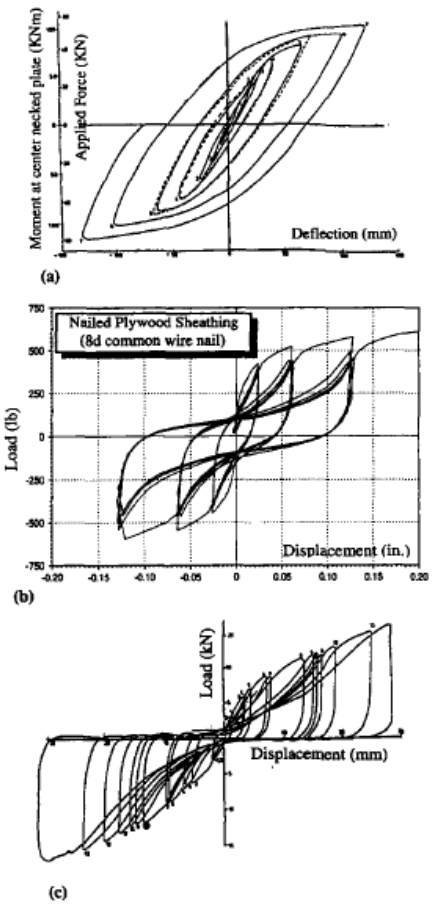

Figure 6.9 Typical hysteresis shapes for wood joints: (a) joint with Yielding Plate, (b) joint with yielding nail, (c) joint with yielding bolt (Dowrick, 1986)

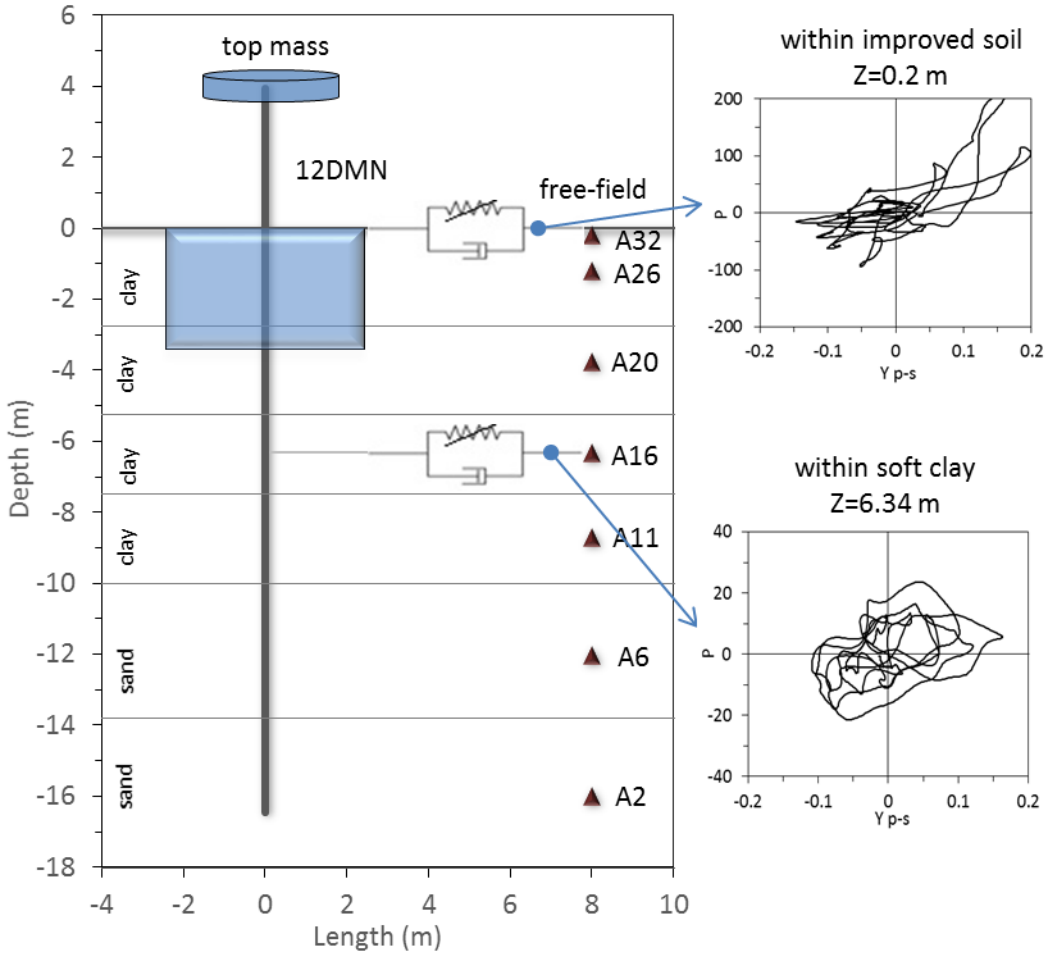

Figure 6.10 Schematic illustration of the macro-elements in the Winkler foundation model

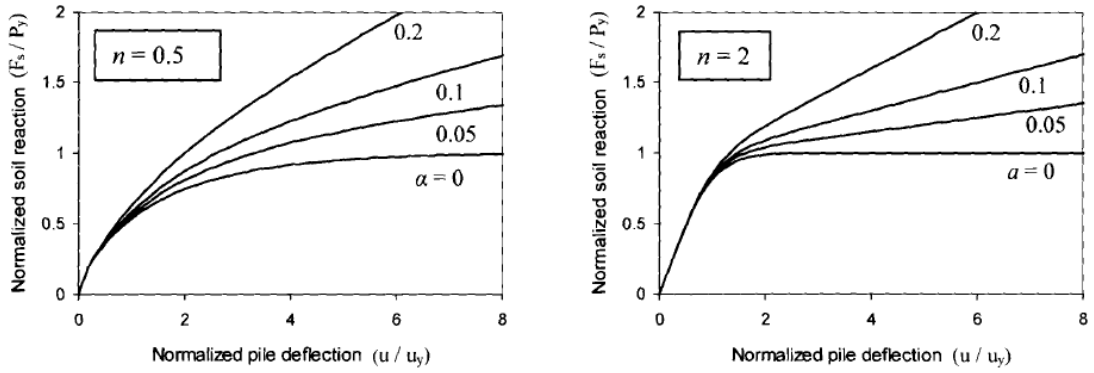

Figure 6.11 Effects of increasing α on the shape of the monotonic loading curve (Gerolymos and Gazetas, 2005)

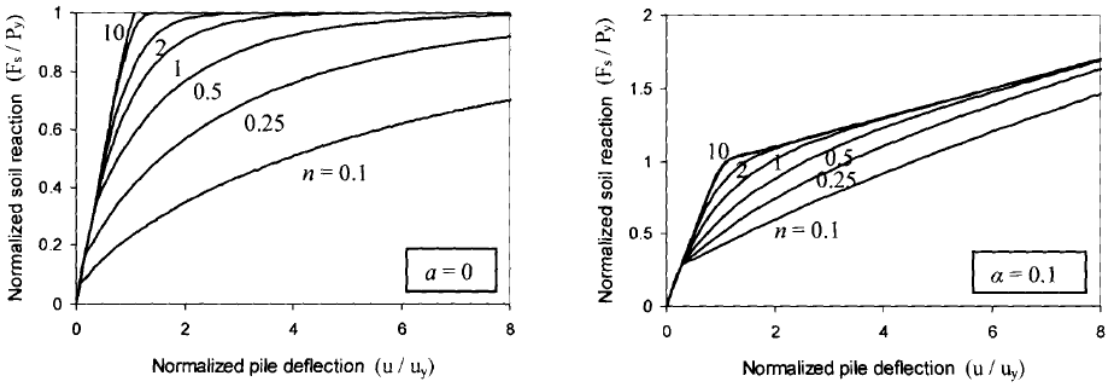

Figure 6.12 Effects of increasing *n* on the shape of the monotonic loading curve (Gerolymos and Gazetas, 2005)

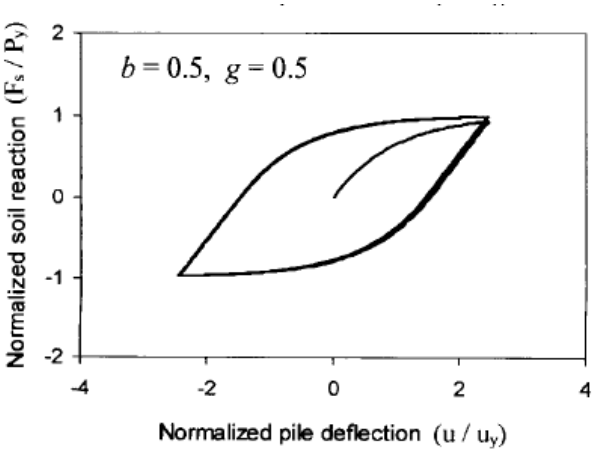

Figure 6.13 Masing rule simulated by β=γ=0.5 (Gerolymos and Gazetas, 2005)

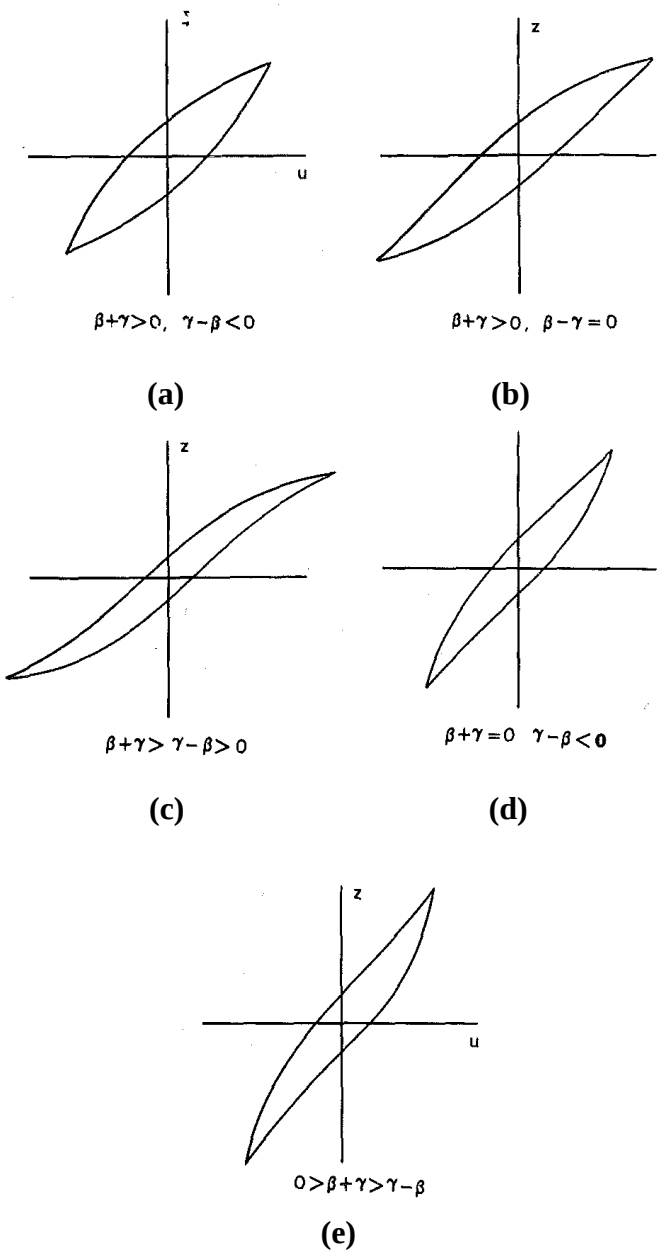

Figure 6.14 Hysteresis shapes for different values of β and γ
(a) weak softening (b) weak softening with mostly linear unloading (c) strong softening (d) weak hardening (e) strong hardening (Baber and Wen, 1980)

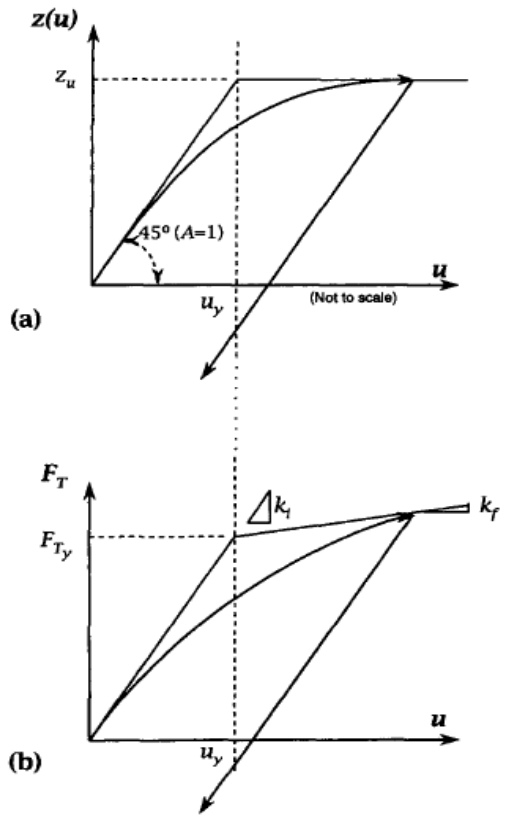

Figure 6.15 Estimation of initial and post-yield stiffness, k_i and k_f, and the yield displacement u_y from the back-bone curves
(a) z- u plane and (b) F_T-u plane (Foliente, 1995). (Note that in these graphs u, u_y, z, and F_T correspond to y_{p-s}, y_0, r, and F_s, respectively.)

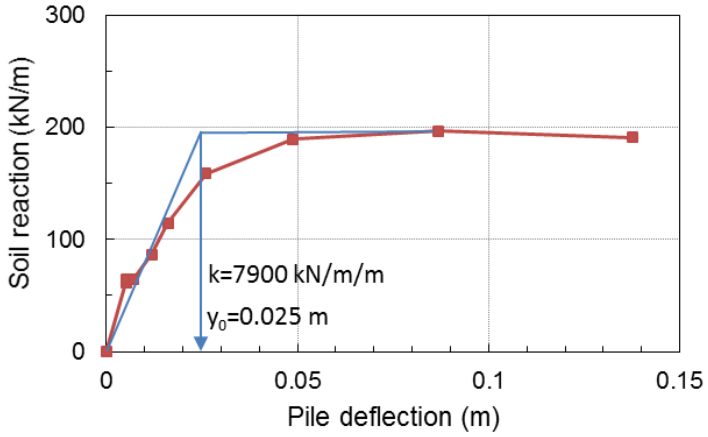

Figure 6.16 Derived p-y curve at z=0.2 m from pseudo-static load tests on pile 6DEF

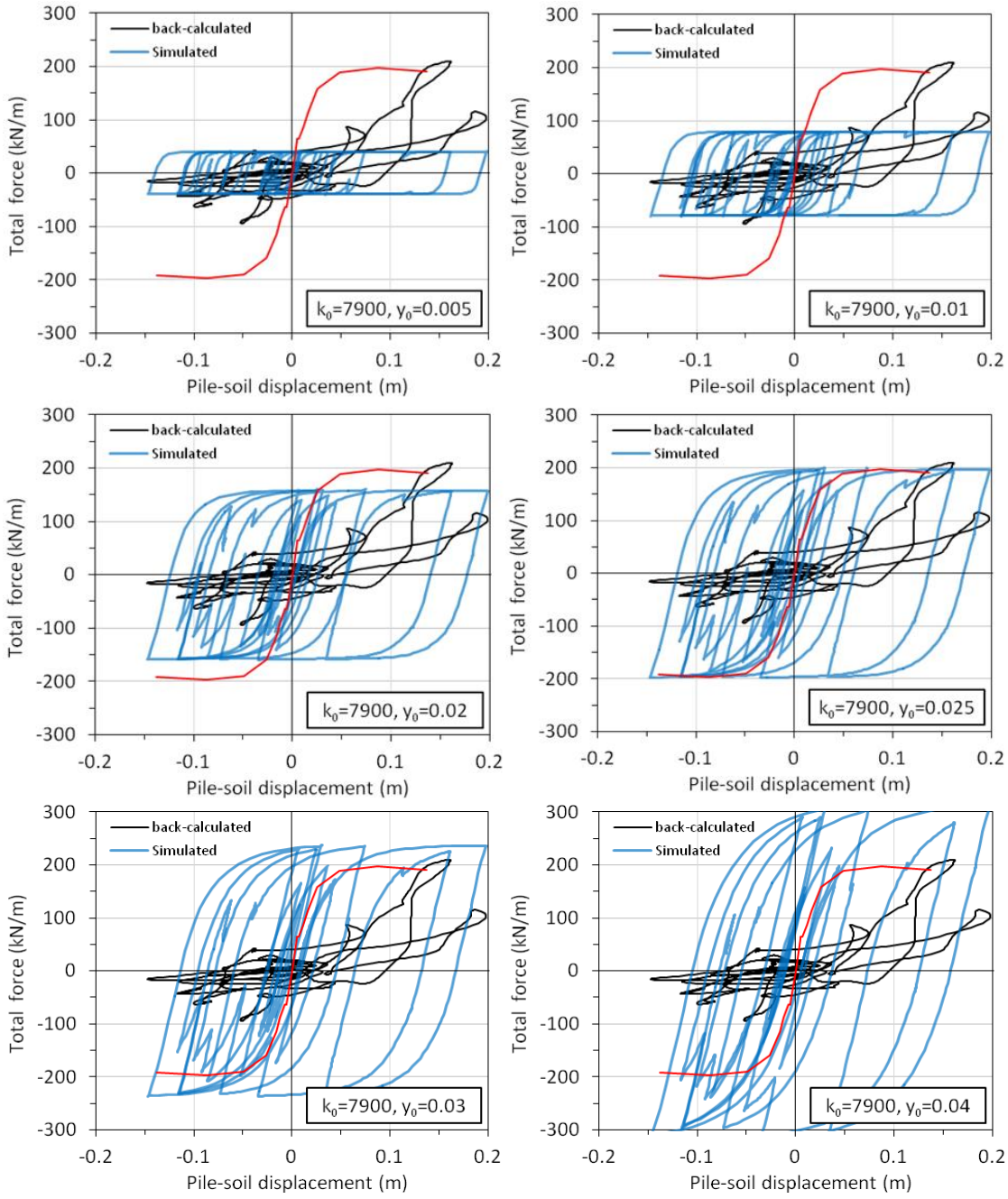
back-calculated
Simulated
Total force (kN/m)
Pile-soil displacement (m)
k0=7900, y0=0.005
k0=7900, y0=0.01
k0=7900, y0=0.02
k0=7900, y0=0.025
k0=7900, y0=0.03
k0=7900, y0=0.04

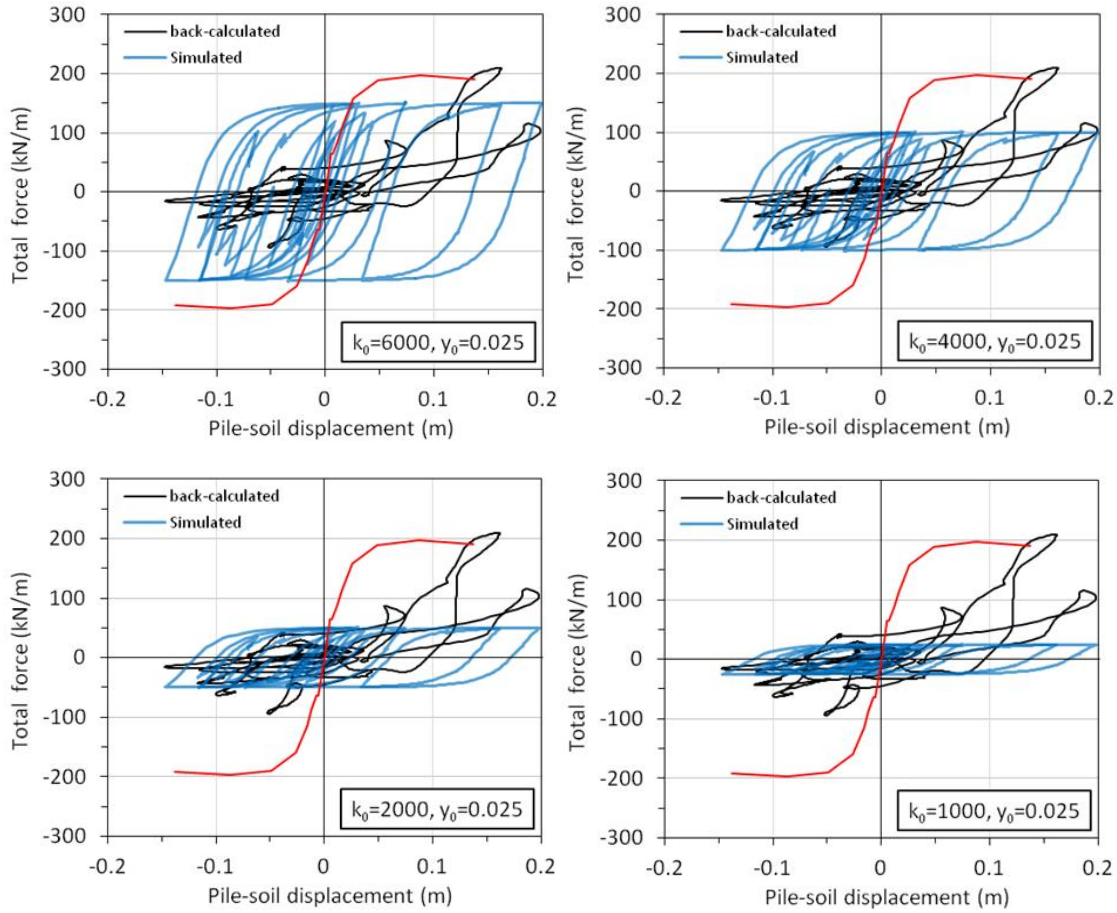

Figure 6.17 Effects of variations in *k* and y_0 on the hysteresis loops at the depth of 0.2 m within the improved soil (pile 6DEF in Event 3)

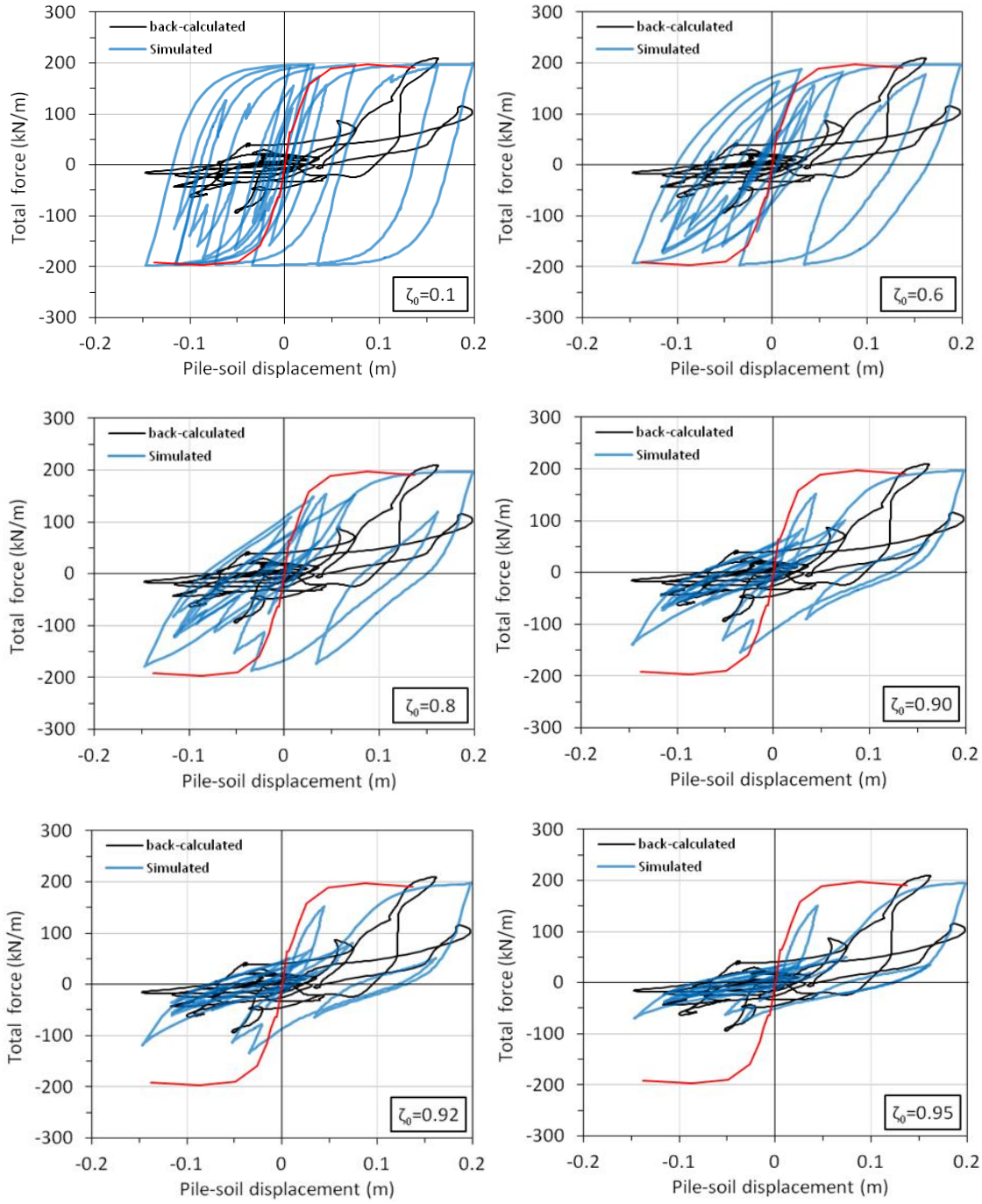

Figure 6.18 Effects of adding pinching to the hysteresis loops, variations in parameter ζ_0
(ψ_0=0.4, δ_ψ=0.01, q=0.1 λ=0.1, ρ=1, δ_v= δ_η=0)

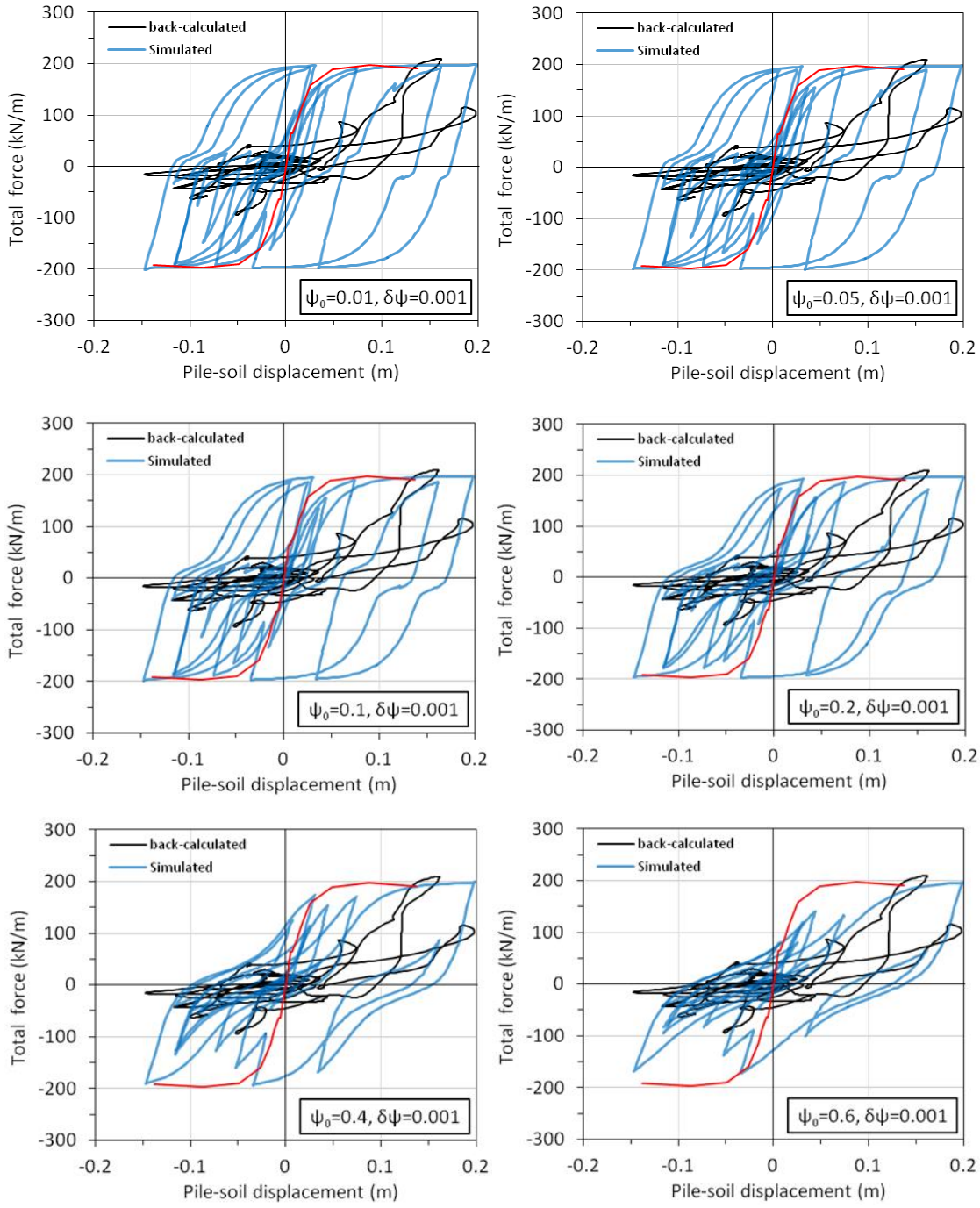

Figure 6.19 Effects of adding pinching to hysteresis loops, variations in parameter ψ_0
(ζ_0=0.9, δ_ψ=0.001, q=0.1, λ=0.1, ρ=1, δ_υ= δ_η=0)

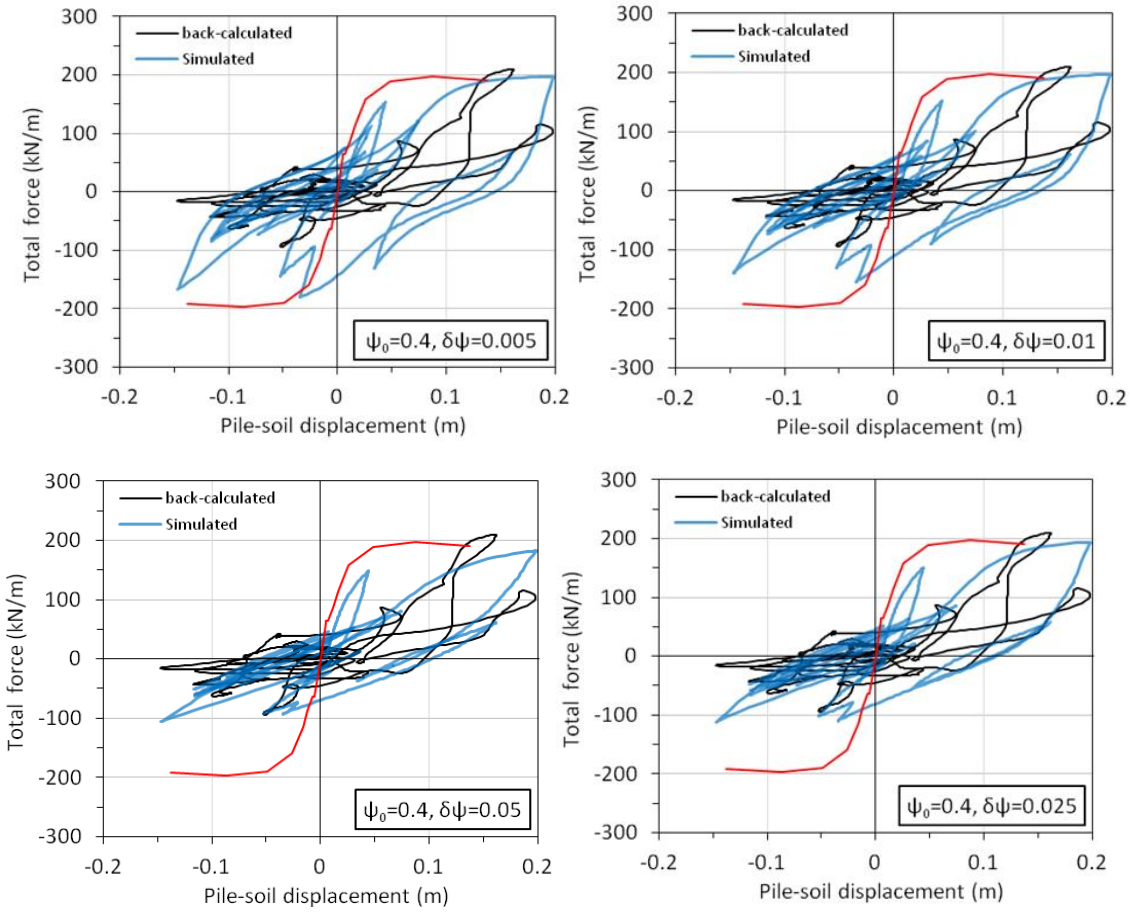

Figure 6.20 Effects of adding pinching to hysteresis loops, variations in parameter δ_ψ
(ζ_0=0.9, ψ_0=0.4, q=0.1, λ=0.1, ρ=1, δ_υ= δ_η=0)

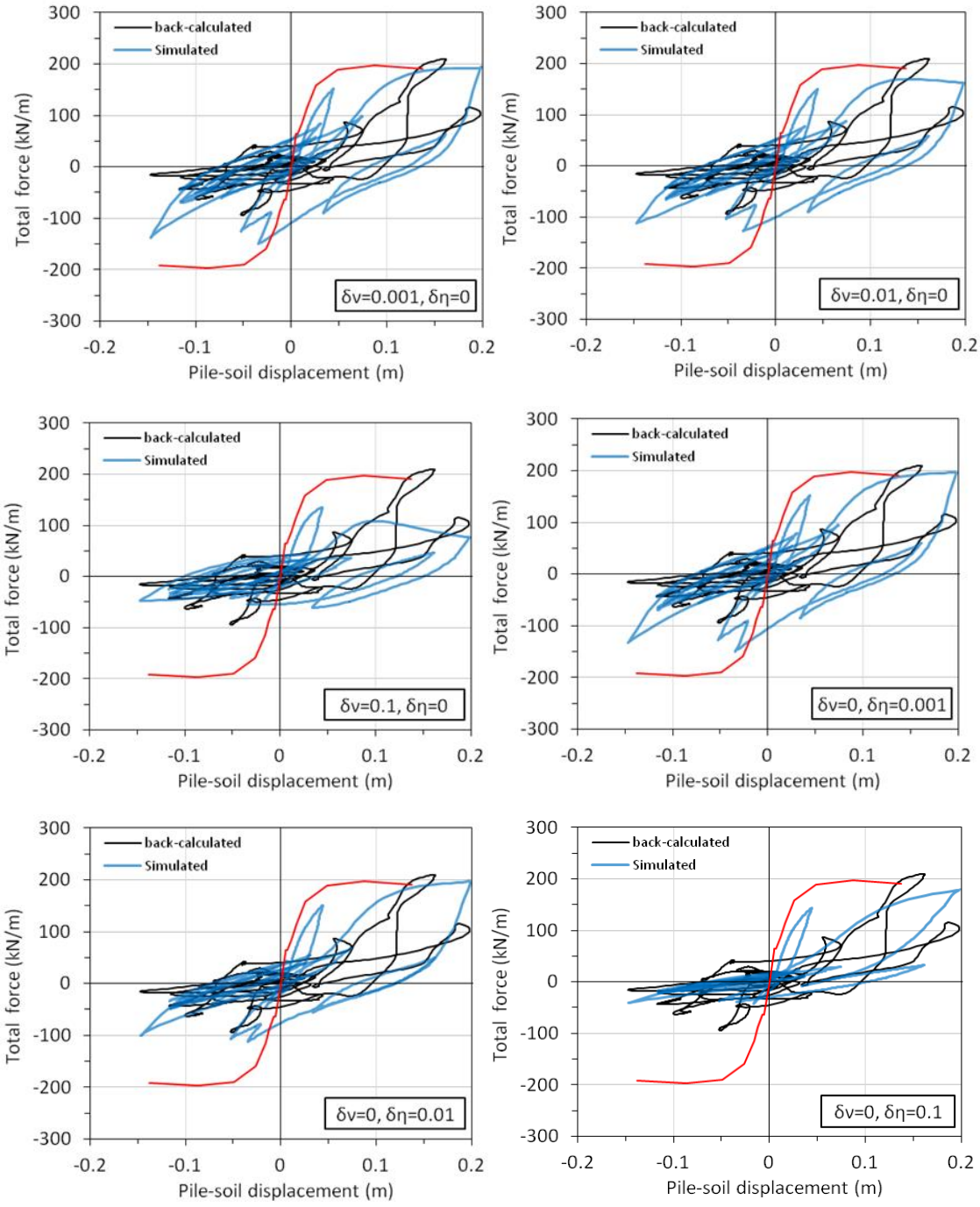
back-calculated
Simulated
Total force (kN/m)
Pile-soil displacement (m)
δv=0.001, δη=0
δv=0.01, δη=0
δv=0.1, δη=0
δv=0, δη=0.001
δv=0, δη=0.01
δv=0, δη=0.1

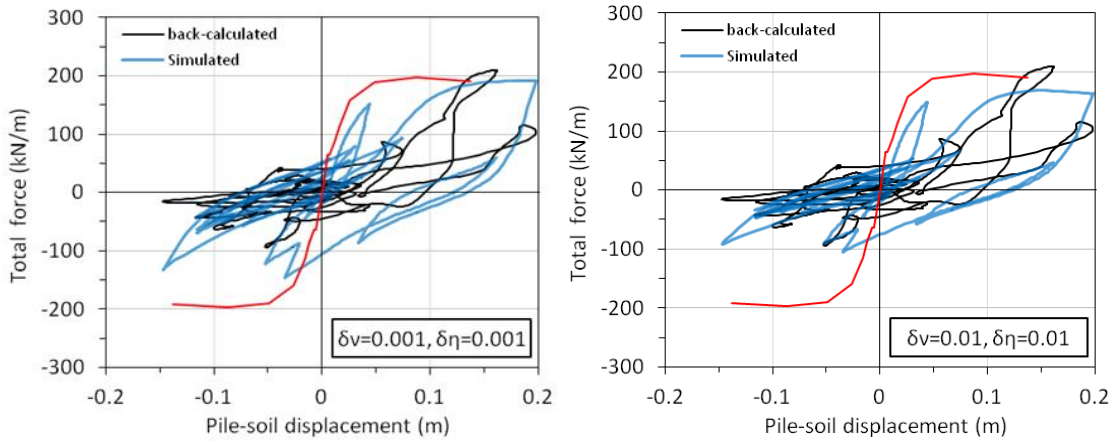

Figure 6.21 Effects of adding pinching and degradation to hysteresis loops, variations in parameters δ_υ and δ_η
(ζ_0=0.9, ψ_0=0.4, δ_ψ=0.01, q=0.1 λ=0.1, ρ=1)

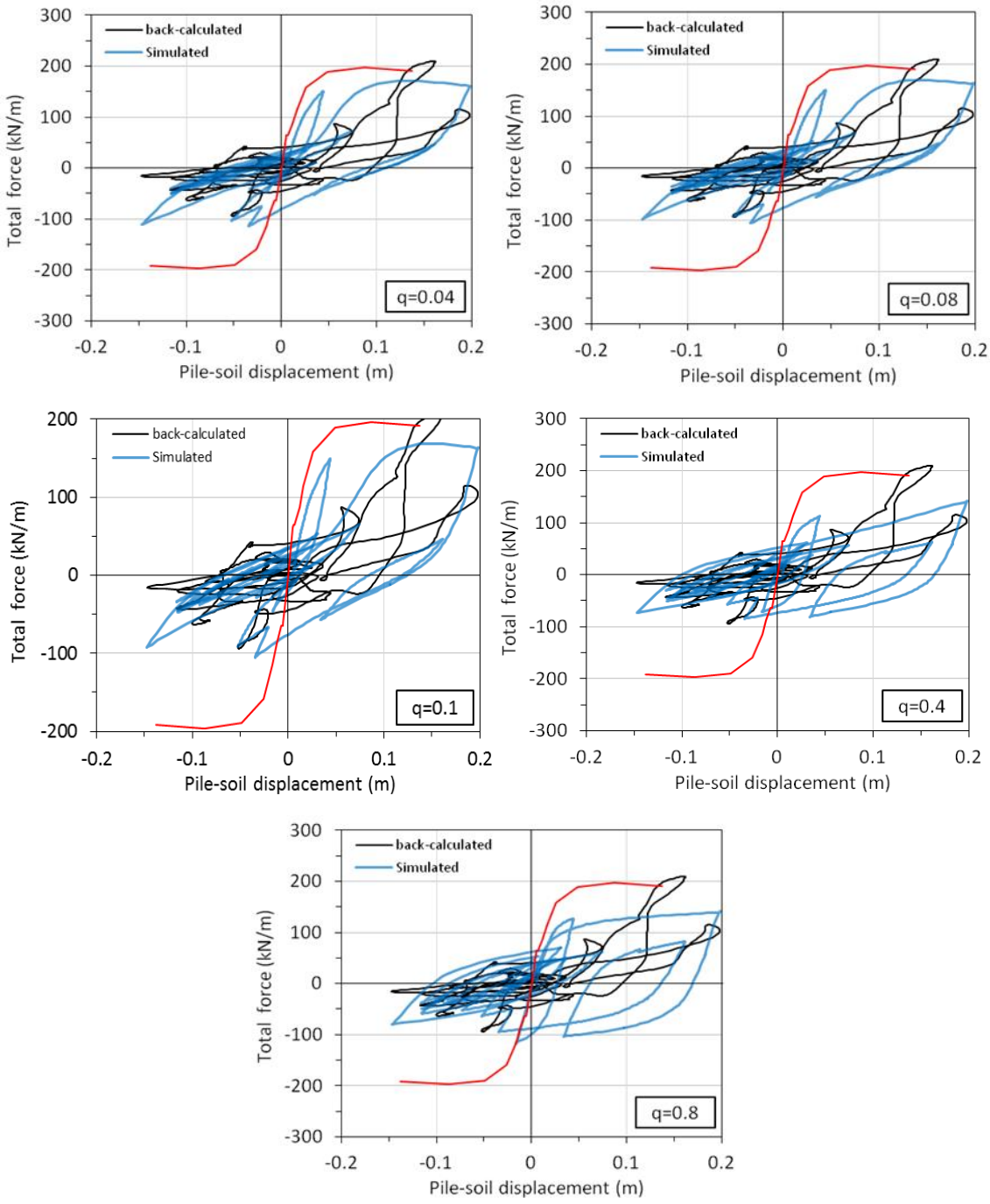

Figure 6.22 Effects of adding pinching and degradation to hysteresis loops, variations in parameter q
(ζ_0=0.9, ψ_0=0.4, δ_ψ=0.01, λ=0.1, ρ=1, δ_υ= δ_η=0.01)

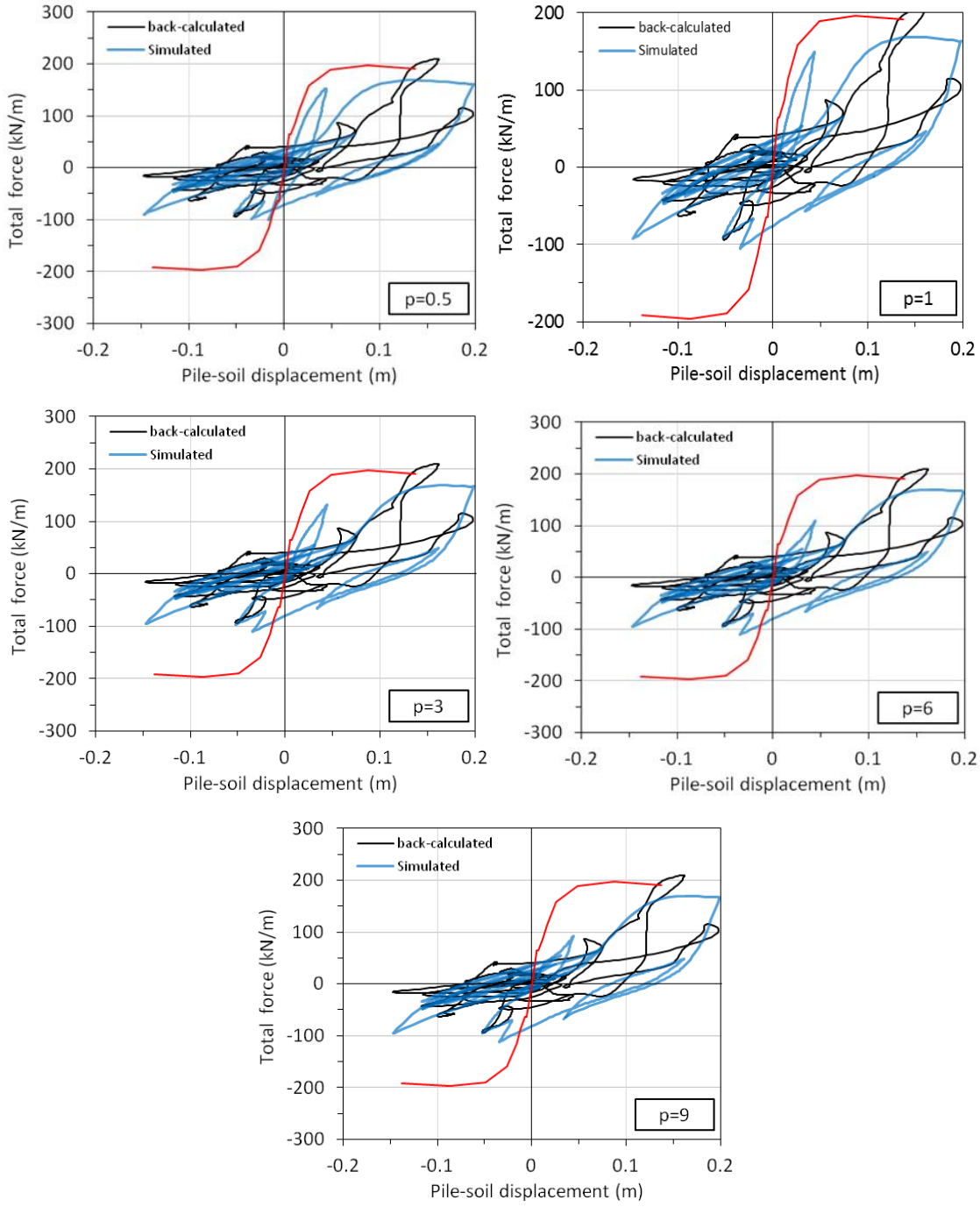

Figure 6.23 Effects of adding pinching and degradation to hysteresis loops, variations in parameter ρ
(ζ_0=0.9, ψ_0=0.4, δ_ψ=0.01, q=0.1, λ=0.1, δ_υ= δ_η=0.01)

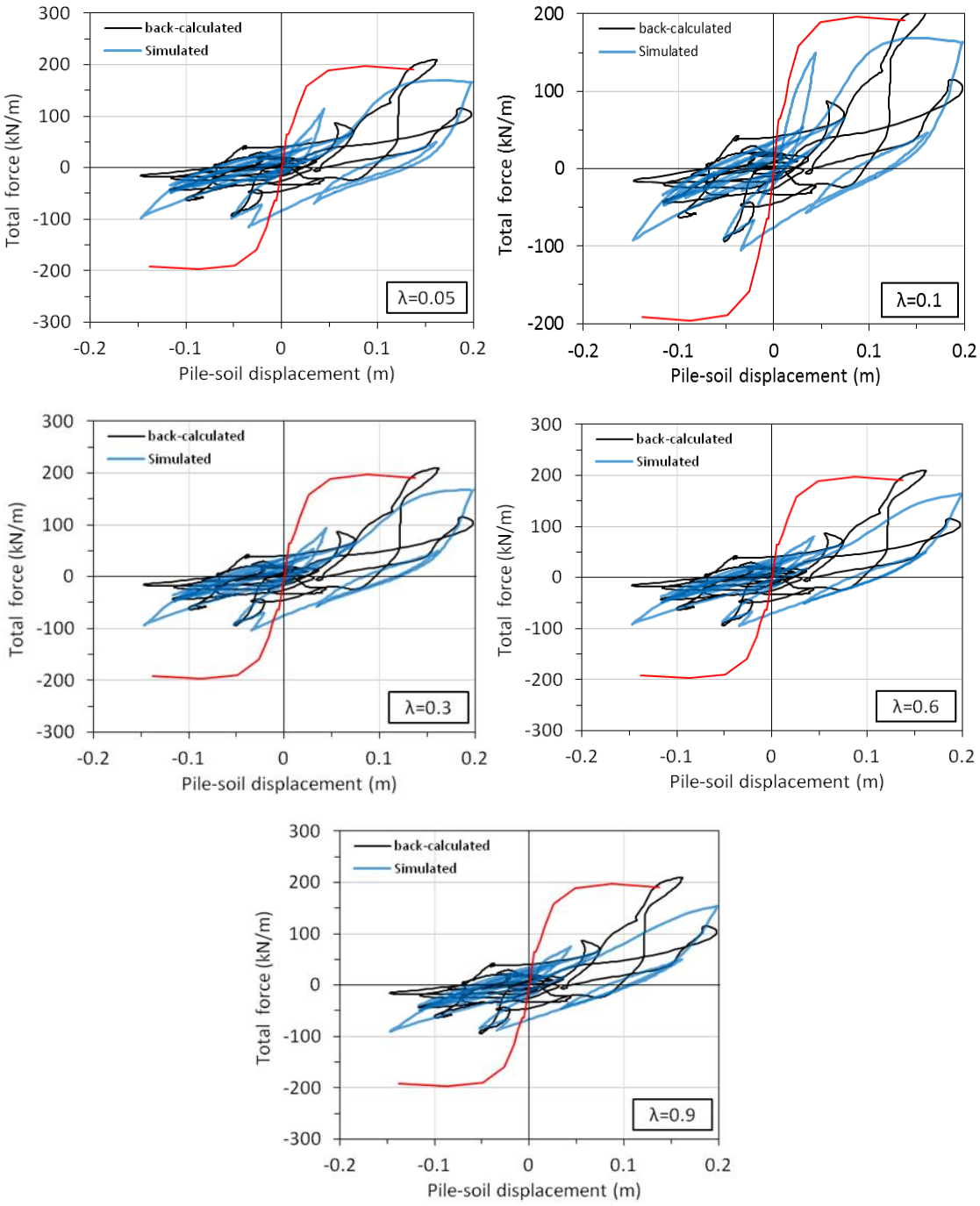

Figure 6.24 Effects of adding pinching and degradation to hysteresis loops, variations in parameter λ
(ζ_0=0.9, ψ_0=0.4, δ_ψ=0.01, q=0.1, ρ=6, δ_v= δ_η=0.01)

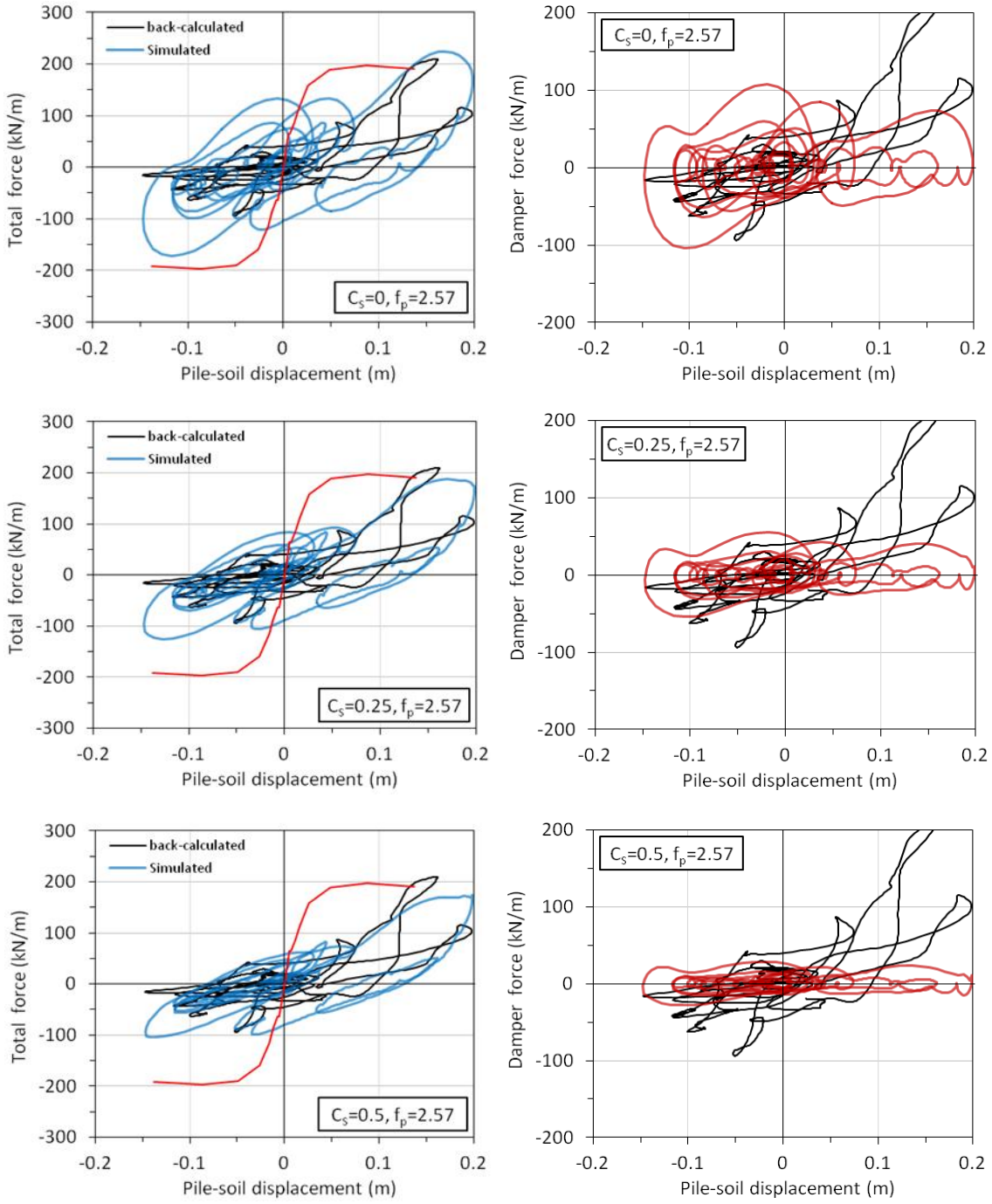

Figure 6.25 Effects of adding radiation damping to the hysteresis loops, variations in parameter c_s
(ζ_0=0.9, ψ_0=0.4, δ_ψ=0.01, q=0.1 λ=0.6, ρ=6, δ_υ= δ_η=0.01)

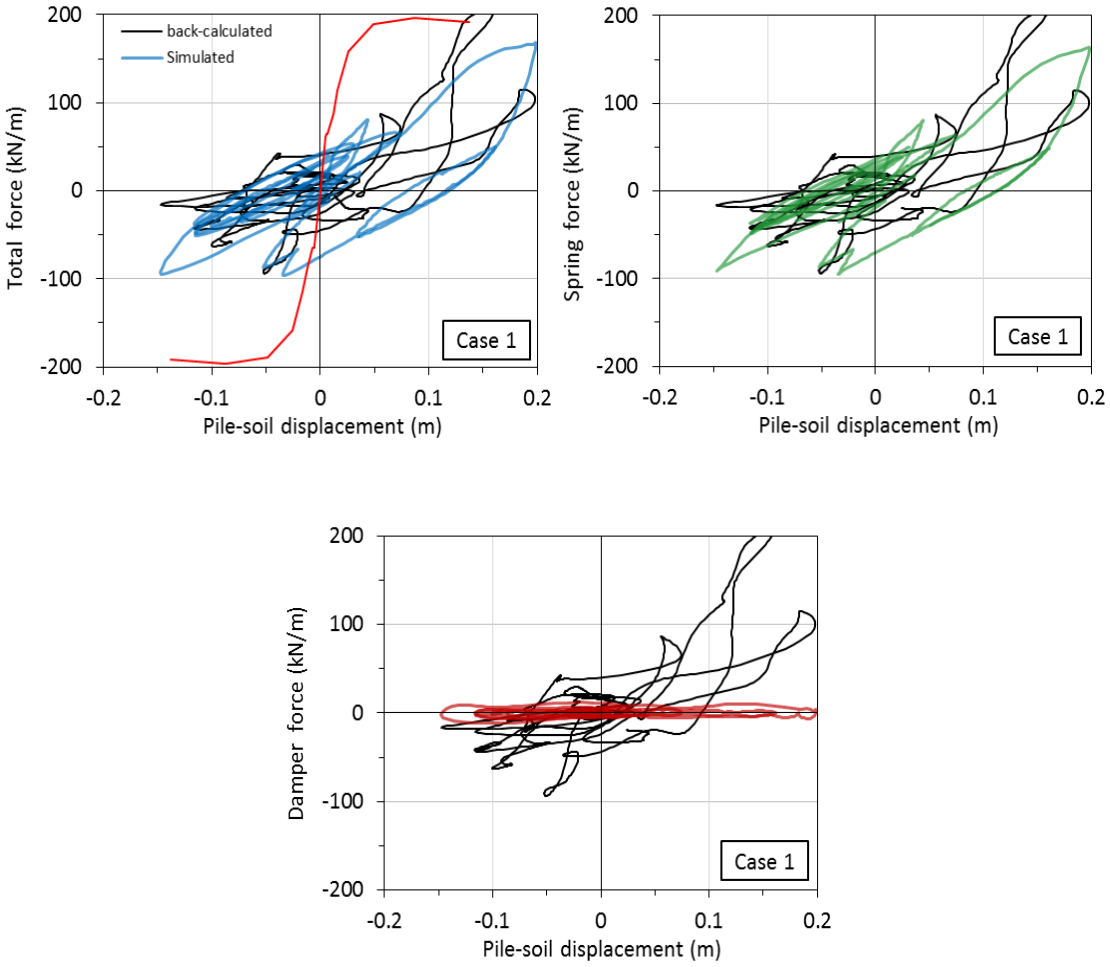

Figure 6.26 Hysteresis loops produced by selected trials (Case 1)

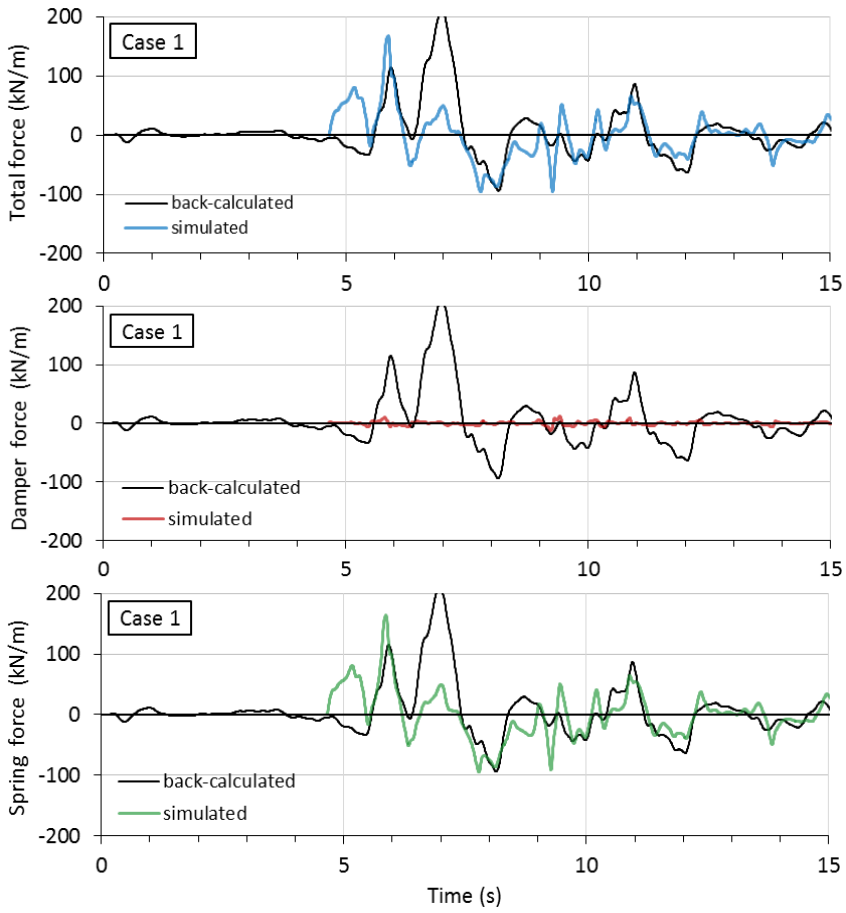

Figure 6.27 Time-histories of the soil reaction produced by different components of the macro-element (Case 1)

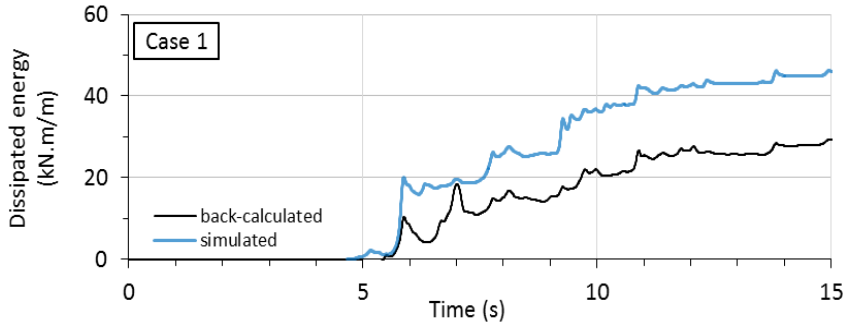

Figure 6.28 Time history of the dissipated energy in the macro-element (Case 1)

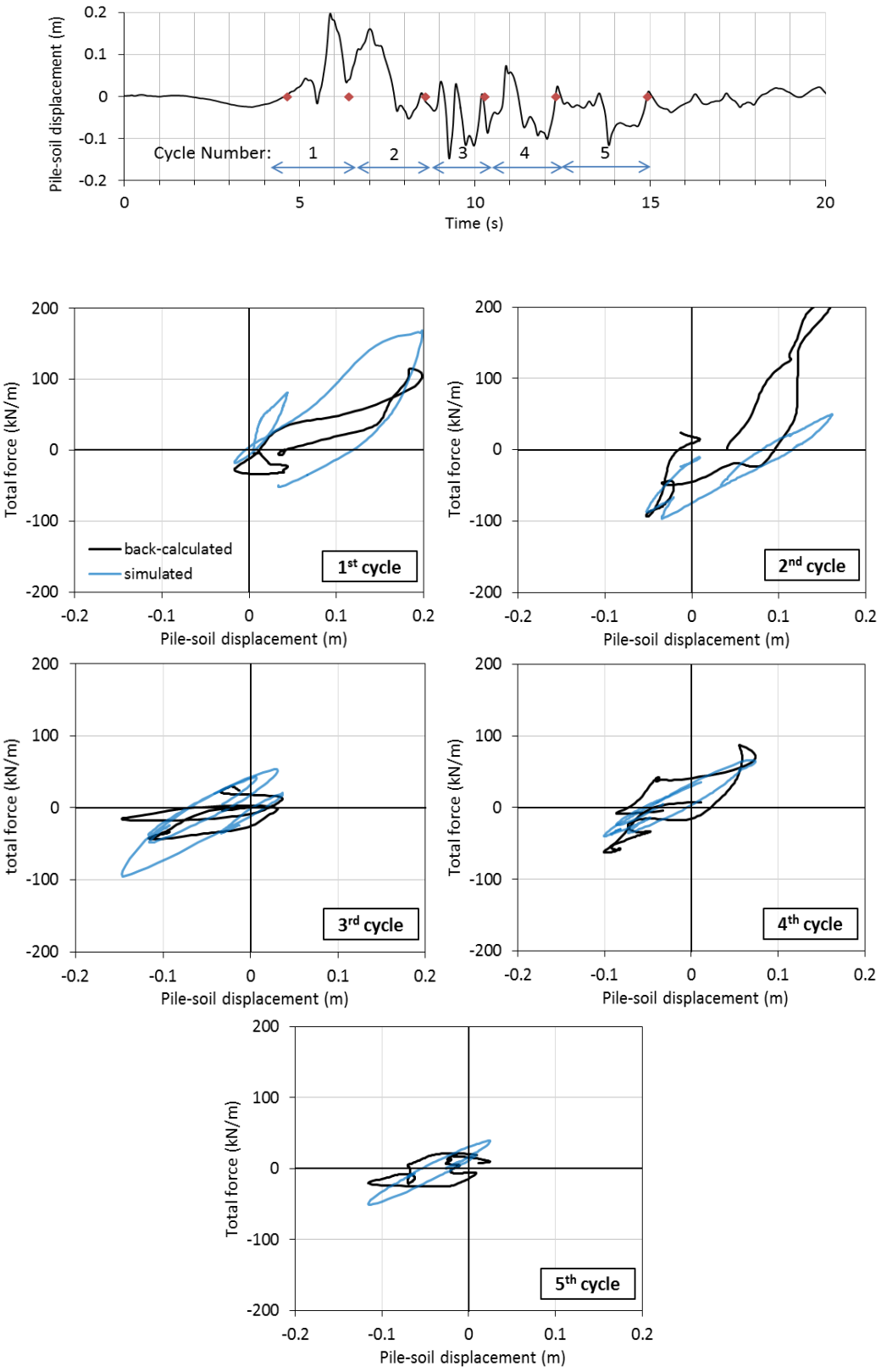

Figure 6.29 Hysteresis loops in the selected cycles (Case 1)

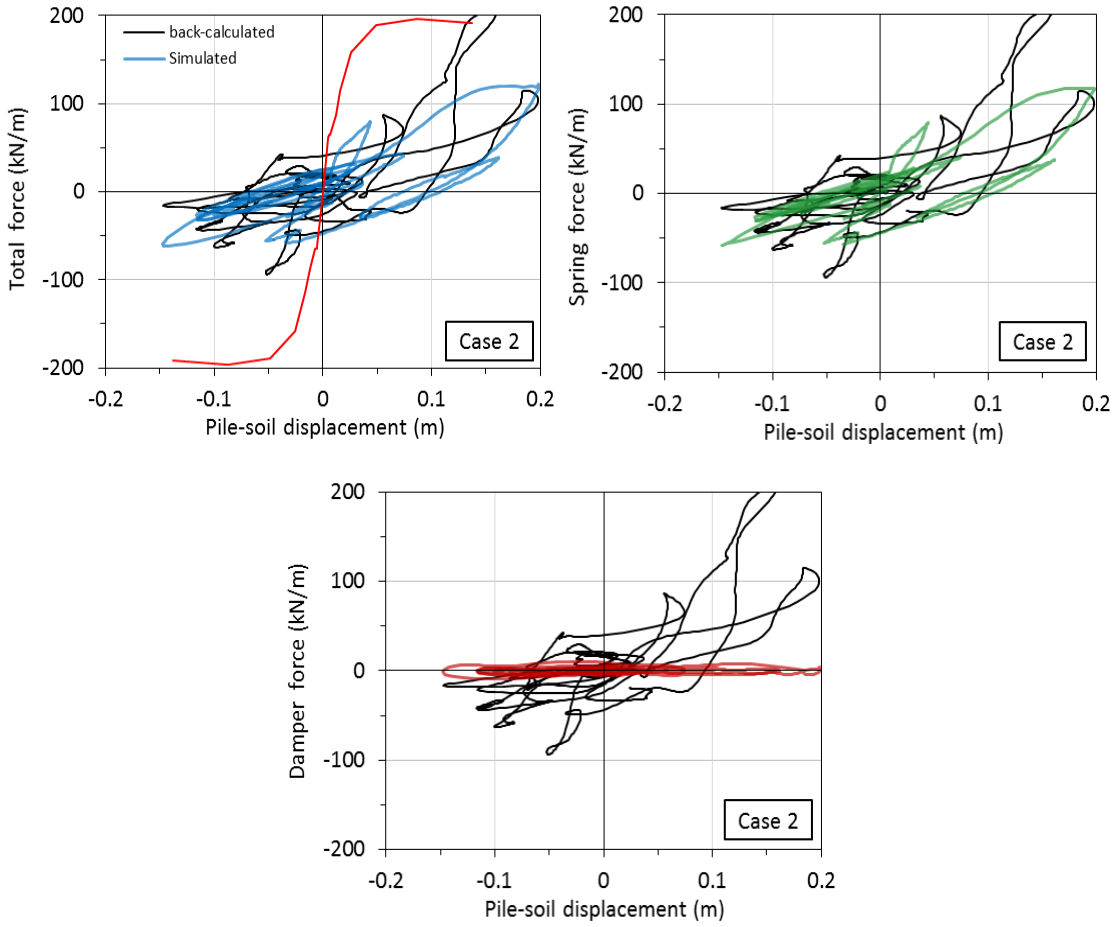

Figure 6.30 Hysteresis loops produced by selected trials (Case 2)

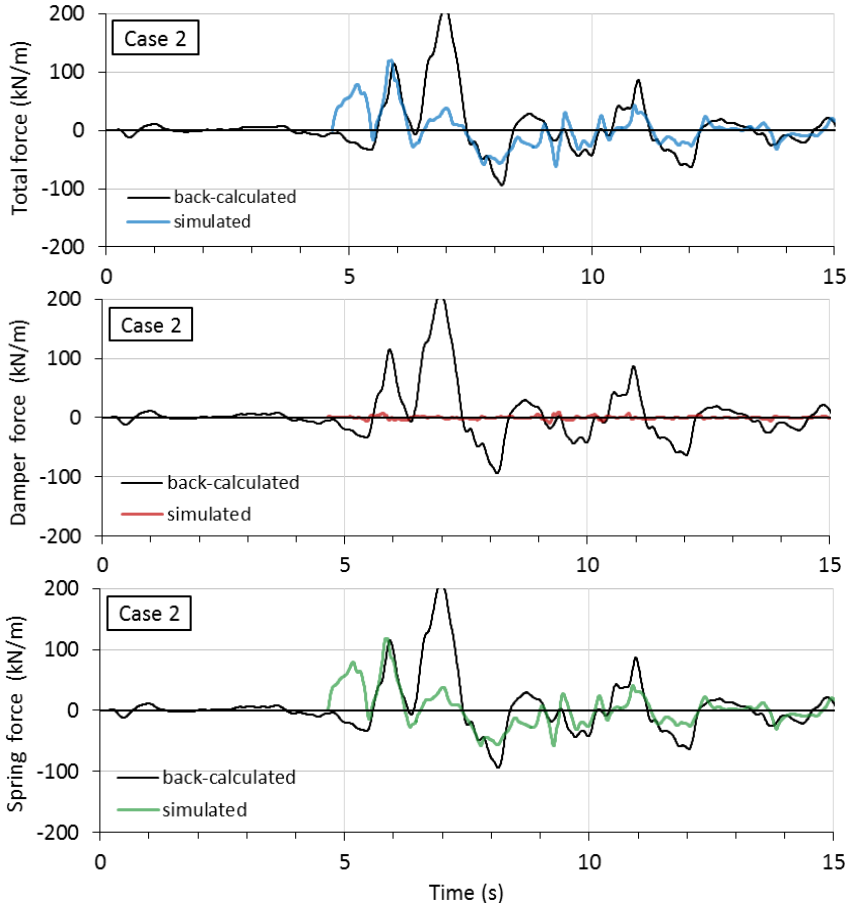

Figure 6.31 Time-histories of the soil reaction produced by different components of the macro-element (Case 2)

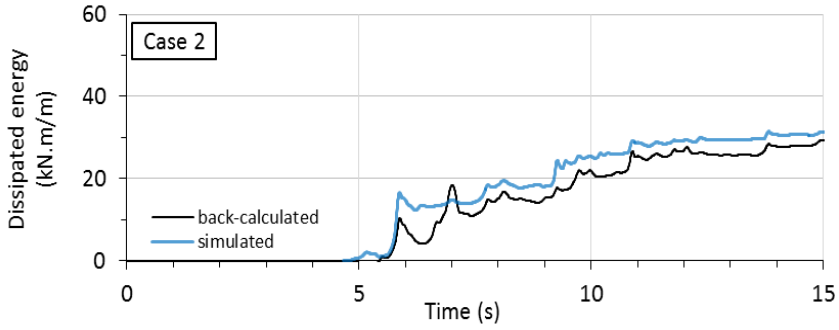

Figure 6.32 Time history of the dissipated energy in the macro-element (Case 2)

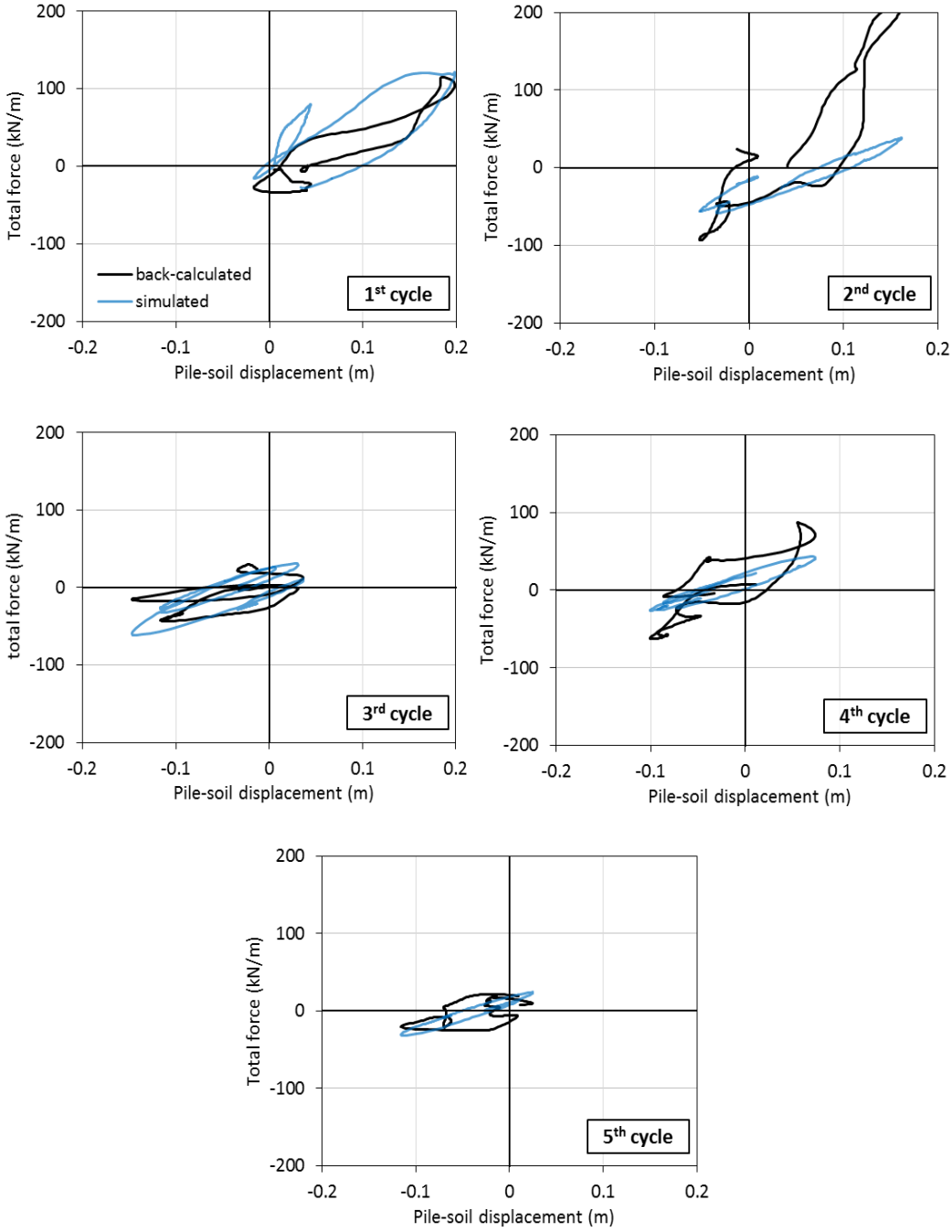

Figure 6.33 Hysteresis loops in the selected cycles (Case 2)

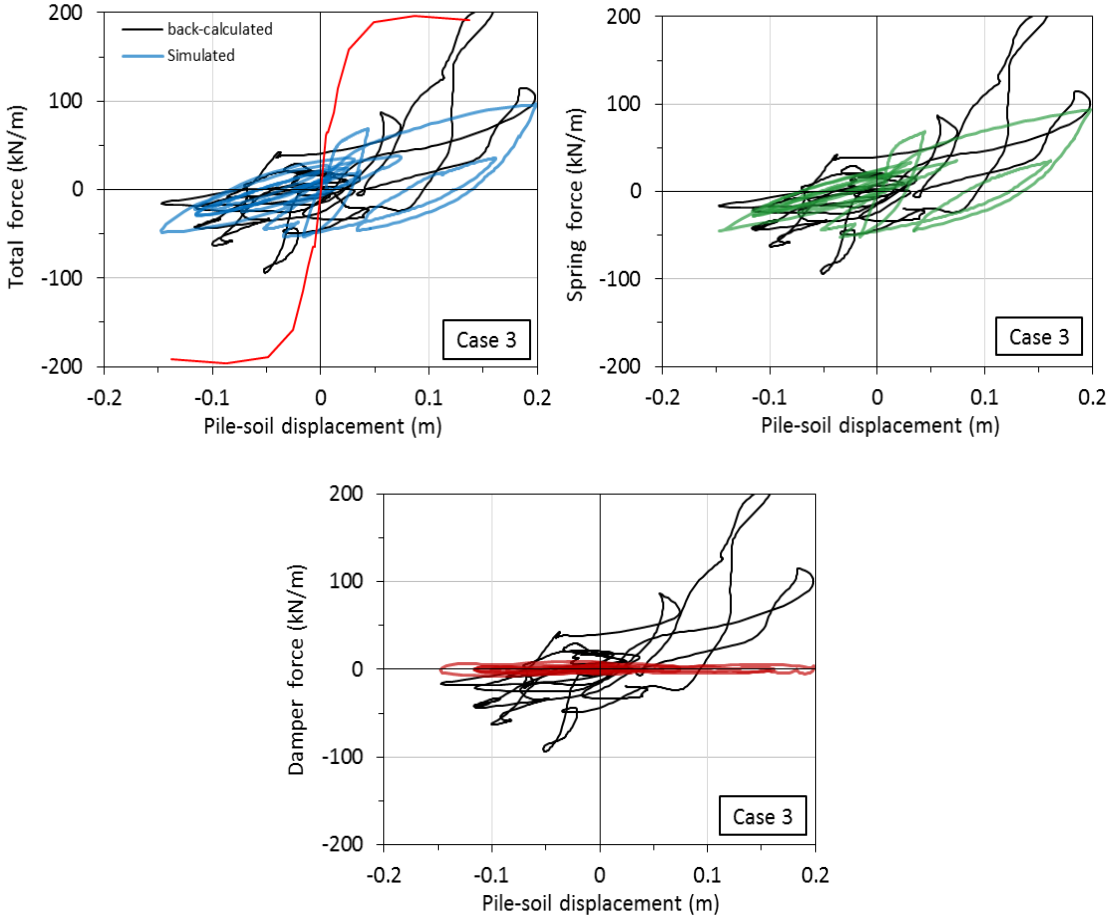

Figure 6.34 Hysteresis loops produced by selected trials (Case 3)

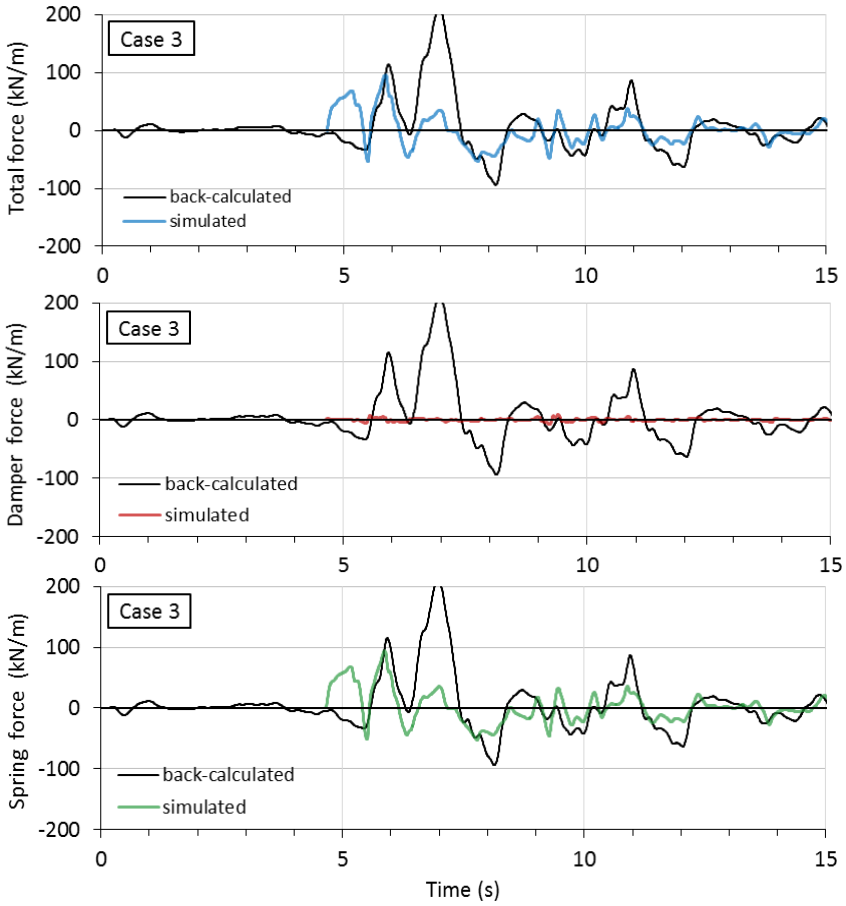

Figure 6.35 Time-histories of the soil reaction produced by different components of the macro-element (Case 3)

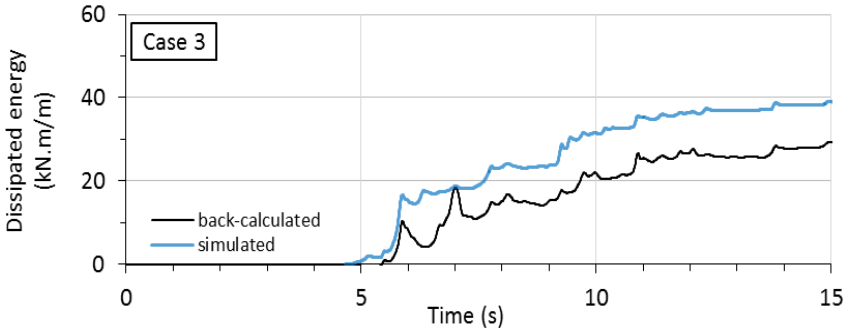

Figure 6.36 Time history of the dissipated energy in the macro-element (Case 3)

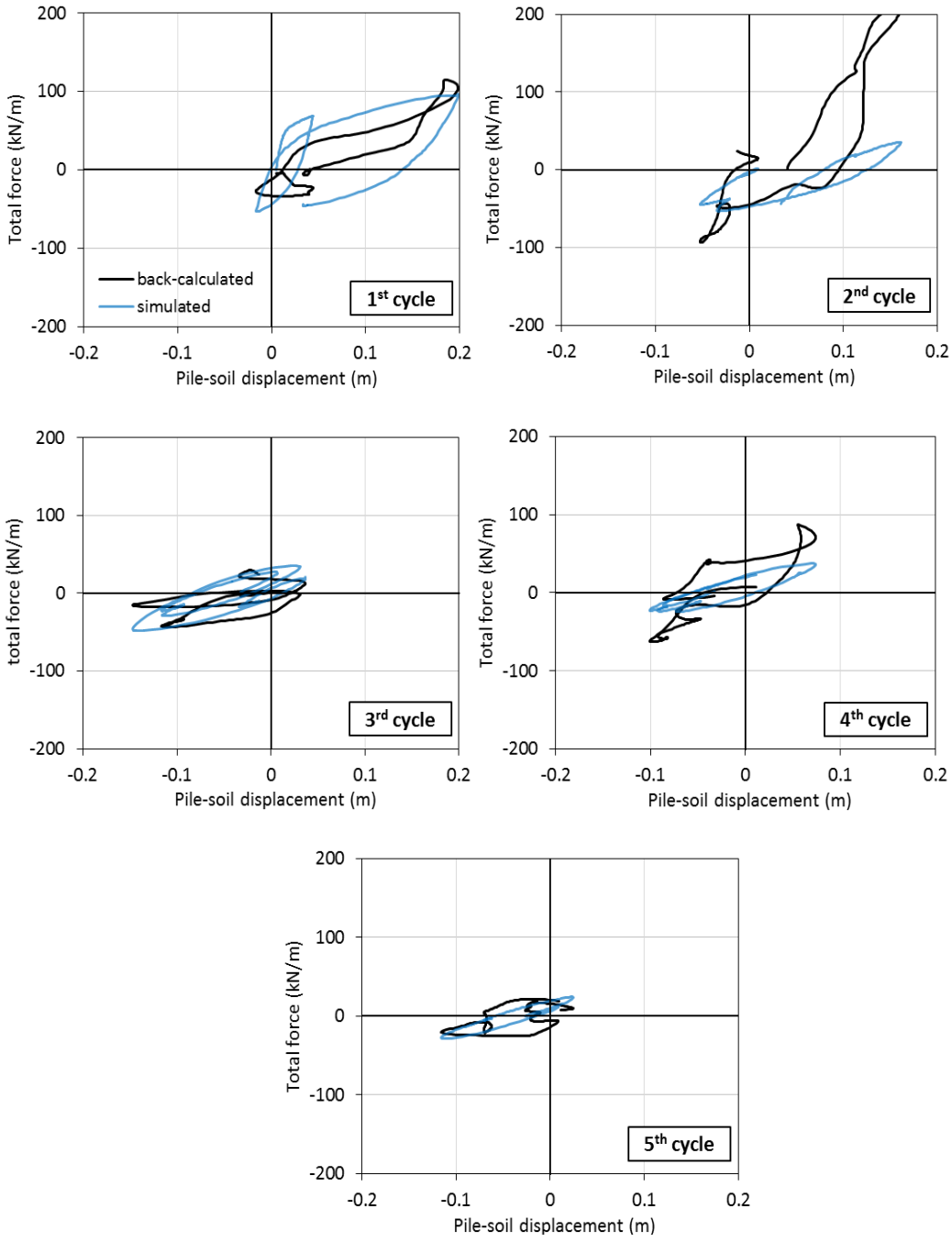

Figure 6.37 Hysteresis loops in the selected cycles (Case 3)

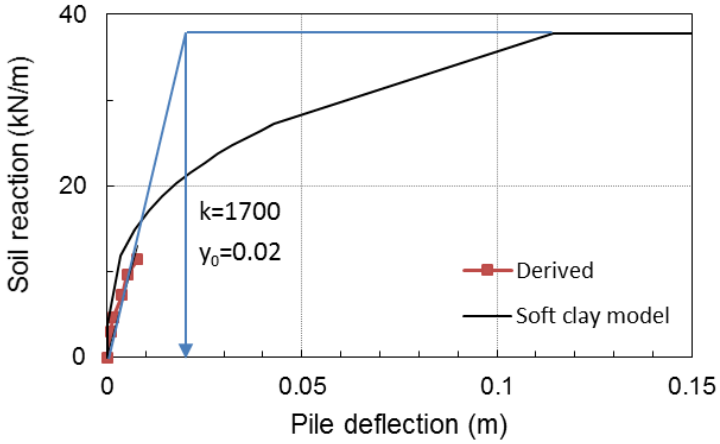

Figure 6.38 p-y curves at z=6.3 m from pseudo-static load tests on pile 6DEF

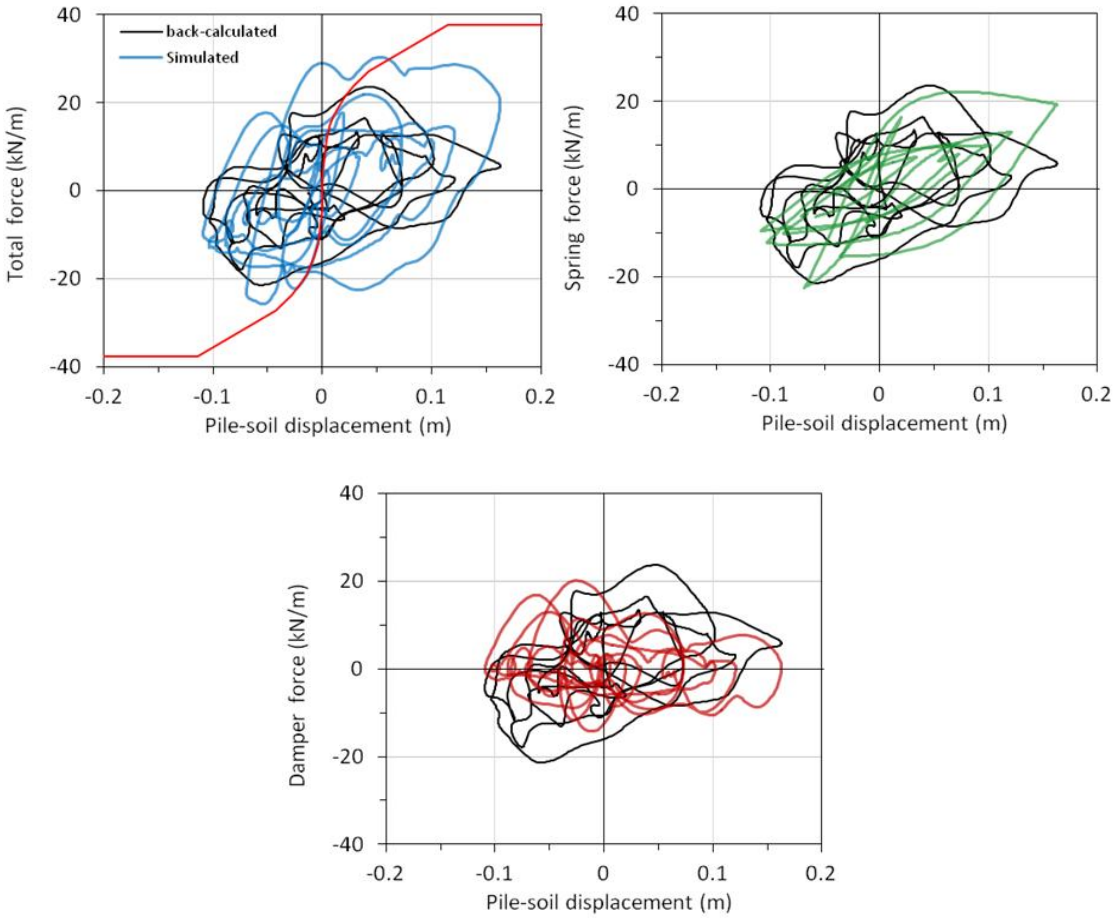

Figure 6.39 Time-histories of the soil reaction produced by different components of the macro-element (soft clay)

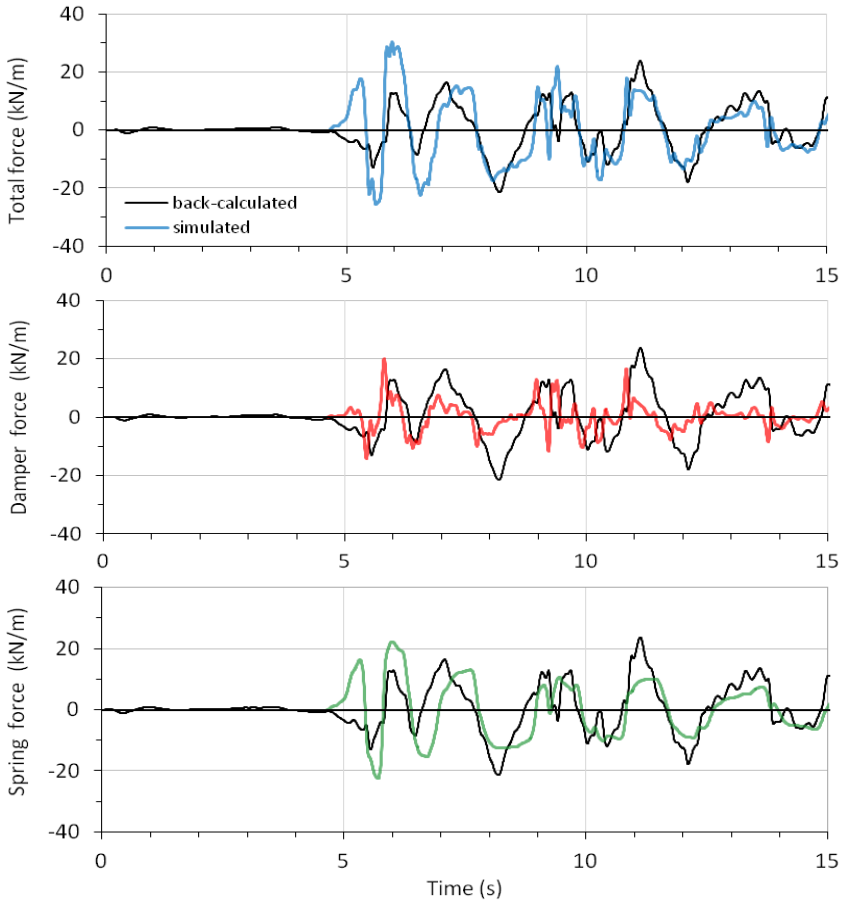

Figure 6.40 Time history of the dissipated energy in the macro-element (Soft clay)

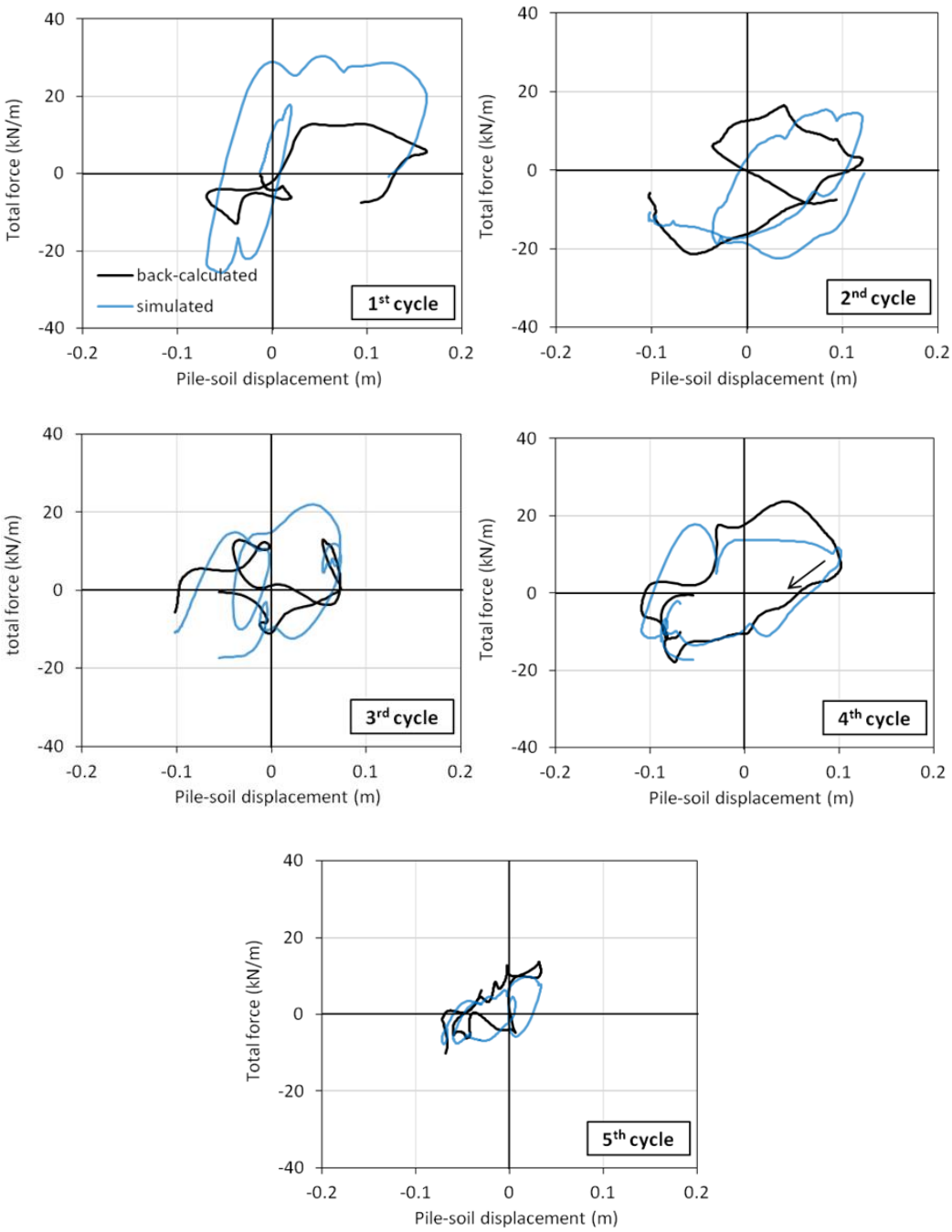

Figure 6.41 Hysteresis loops in the selected cycles (Soft clay)

CHAPTER 7: SUMMARY, CONCLUSIONS AND RECOMMENDATIONS FOR FUTURE WORK

7.1 Summary and conclusions

This research assessed the pseudo-static and seismic responses of single piles in partially improved ground. In professional practice, a variety of strategies are used to address excessive lateral deflection of pile foundations in soft soils. Increasing the number of single piles and using piles with larger diameters or stiffer material are among the more expensive recommended methods. As construction methods develop and contractors' capabilities broaden, engineers and contractors are likely to deploy soil improvement techniques as an alternative to more costly solutions. Such methods also have been considered as options for retrofitting aging structures. However, relatively little is known about the complex behavior of structures supported on improved ground, especially during seismic loading, and this lack of knowledge has impeded the application of such methods in areas with soft or weak soils. In response to this challenge, this project proposed a cement deep soil mixing method and tested it through centrifuge modeling and numerical modeling as a way to strengthen foundations against pseudo-static and seismic lateral loads. Improvements of three different sizes were considered, with the sizes named for the depth of the improvement zone: 6D, 9D, and 12D, with D representing the outside pile diameter. The soil profile consisted of a 10 m soft clay over an 8 m dense sand. The pile tips penetrated into the dense sand layer and the pile heads were free to rotate. The model piles were subjected to a series of pseudo-static and seismic lateral loads. The results of the tests suggested several general guidelines that can be

implemented in the construction of highway bridges, pile-supported wharf structures, oil and gas production platforms, and other offshore structures in seismically active regions.

7.1.1 Single piles subjected to pseudo-static loads

A series of pseudo-static loading tests with increasingly large target displacements at the pile heads were performed on the improved and unimproved piles; these data are presented in Chapter 3. The novel bending moment curve-fitting procedure detailed in Chapter 3 takes into account the soil layering effects by including sharply varying soil reactions at the interface of improved and soft clay layers. Using this method, the pseudo-static p-y curves were back-calculated and compared with the conventional models for soft and stiff clays. The close agreement of the estimated pile deflections with the measurements confirmed that the adopted method for deriving the p-y curves significantly improved the accuracy of the prediction, especially when the spacing between the strain gages was large.

- Some of the software commonly used for analyzing piles response to lateral loads, such as LPILE, are not capable of incorporating limited lateral extents of the improved zones; as a result, they overestimate both the stiffness and the ultimate strength of the improved soft clay. However, the agreement between the simulations and the measurements became closer as the size of the improved zone increased. Close agreements were observed for pile 12DMN. This behavior was expected because the one-dimensional soil model generated by LPILE represented the behavior of the improved soil in the centrifuge experiment more accurately as its lateral extent increased and the influence of the soft clay at deeper depths vanishes.

The experimentally derived p-y curves using the developed curve-fitting method showed similar characteristics, but different values compared with the conventional models for stiff and soft clays. It is therefore recommended that scaling factors be applied to the "p" and "y" values of the conventional models to account for the limited lateral and vertical extents of the improved ground.

Maximum bending moments and shear forces within the piles were observed in the improved soil. The design implication of these findings is that for a given lateral load, ground improvement around a pile in soft clays can lead to considerable reduction in the corresponding cyclic lateral displacement. On the other hand, for a given lateral displacement, the induced bending moments and shear forces can increase significantly, especially within the improved soil regions. Therefore, appropriate dimensions for the piles should be selected so that any significant yielding or premature failure of the pile can be prevented and the full potential of a pile can be realized.

Results of the pseudo-static tests revealed that the small-strain lateral stiffness and load resistance of piles in improved soil increased from 2 to 8 times and 4 to 5 times, respectively, over those of a pile in unimproved soil.

7.1.2 Single piles subjected to seismic loads

Scaled Loma Prieta and Kobe earthquakes were applied in sequence to the centrifuge model of piles that did not experience previous pseudo-static loads. The pile supported by the largest improvement zone was, however, subjected to a small magnitude pile top displacements. The displacements between the pile and the free-field soil were larger than that observed in the pseudo-static load tests at the soil surface. One of the important

findings of this research is that the motions of the piles and the free-field soil in all of the improved cases followed the same pattern and direction.

The distribution of bending moments along the piles during seismic loading showed that the peaks occurred at the interface of the improved and unimproved soil as well as within a region around the interface of the soft clay and dense sand. The maximum moment occurred at the same time as the free-field soil peak displacement. This finding shows that the interaction between the soil and piles was controlled mainly by the kinematic interaction. The inertial interaction caused by the top mass was very small. The location of the maximum pile shear force in the unimproved pile appeared to be close to the clay-sand interface, whereas it moved upward to the middle of the improved zone for the improved piles.

In general, the p-y curves derived experimentally from pseudo-static loading tests in the improved and unimproved soft clay appeared to represent the back-bone curves of the seismic hysteresis loops reasonably well. The study detected an influence of the improved zone on the derived p-y curves of the underlying soft clay layer, and vice versa, suggesting that the p-y springs close to soil layer interfaces functioned as coupled elements.

In the uppermost clay layer, high pore water pressures (PWP) were recorded in all shaking events. Pore pressure records showed that the dense sand layer did not liquefy in all the shaking events.

As detailed in Chapter 6, an extended version of the Bouc-Wen model was employed to simulate the hysteretic seismic reaction between the soil and the pile in the largest improved zone in the third shaking event. The developed model was capable of

simulating gap formation between the improved soil and the pile as well as degradation in the stiffness and strength of the soil; however, it did not capture the hardening behavior of the hysteresis loops in the improved soil at the beginning of the shaking Event 3. Radiation damping was included in the interaction macro-elements using a viscus dashpot in parallel with the hysteresis spring. In modeling the radiation damping in the system, it was found that incorporating the coupling between the radiation damping and the plastic deformations in the hysteresis unit was necessary for reproducing the back-calculated soil reactions. Contribution of the radiation damping in the simulated reaction of the improved soil was almost insignificant compared to that of the soft clay. The discrepancy between the simulated and the derived values in soft clay might be explained by loss of strength due to pore water pressure generation which was not accounted for in the macro-element model. The calibrated model for the soft clay overestimated the soil reaction at the beginning of the excitation; however, it followed the trends and captured the peaks for most parts of the excitation.

7.1.3 Identification of soil-pile-top mass system

To identify the modal frequencies of the soil-pile-top mass system, pseudo-flexible transfer functions were derived utilizing spectral analysis method. In the third event, two major peaks were observed in the pseudo-flexible transfer functions for all piles. The first peak within lower frequencies showed a gradual shift from 2.8 Hz for UIAB, to 3.4 Hz for 6DEF, to 4 Hz for 9DIJ, and finally to 4.2 Hz for 12DMN; this reflects the direct effect of the improvement zone size on the magnitude and frequency of the lower frequency peak. However, the opposite was observed on the second peak as it moved from 8.2 Hz for UIAB towards the lower frequencies to 7 Hz for 12DMN as the

improvement zone became larger in size. The results indicated that the lowest natural frequency of the system increased as its stiffness increased. The SDOF model, with the lateral stiffness estimated from the pseudo-static test results, has been used as a simplified method of estimating the natural frequencies of the soil-pile system. This method overestimated the lowest natural frequency of the soil–pile-top mass systems by 40% for the unimproved soil and about 35% for the improved soils, which is further evidence for the softer behavior of the system in seismic events.

The soil fundamental frequency played a less significant role in the first and the second events than in the third event, where it appeared as an influential mode in determining the amplified acceleration response of the unimproved pile. These findings show that the frequency content of the input motion and the frequencies at which the maximum energy is carried along with the natural frequencies of the free field soil are very effective in the amplification of the motion on the top mass or super structures.

The modal identification results in Chapter 5 highlight the benefits of combining an analytical model and an experimentally identified model for validating the results and thereby avoiding missing modes.

In engineering practice, it is generally desirable to employ the simplest methods possible for achieving a given goal, so it would be beneficial if future investigations sought ways to simplify the design methods for piles in improved soil. Nevertheless, some primary steps towards this goal were taken in this research. Many of the guidelines used in this study were developed by first adopting existing guidelines for static pile loading conditions and subsequently modifying them for seismic loading, as discussed in Chapters 5 and 6 with regard to estimating the natural frequencies of the soil-pile system

and calibrating the Bouc-Wen model. However, the results revealed that the soil-pile system had a less stiff behavior in the seismic events which is possibly due to material degradation, development of the PWP and rigid body movement of the improved zones into the soft clay and following the motion of the surficial soft clay layer.

7.2 Future work

The accuracy of the derived p-y curves could be enhanced considerably by experimenting with denser arrays of strain gages, especially within the improved soil; employing displacement transducers close to the soil surface; and equipping the piles with pressure transducers for direct measurement of the soil pressure. The bending moment curve-fitting method should be modified to account for the inertial effects of the pile. In addition, deploying accelerometers attached to the pile could be considered for direct measurement of the pile acceleration.

Another potential direction for future work is refinement of the generalized Bouc-Wen model developed in this project by calibrating it for several depths in soil and then integrating it into a finite element model to directly predict the pile deflection response for other free-field motions. The parameters of the model for the same kind of soil could be compared for different depths to identify the effect of depth on the parameters.

According to the results reported in Chapter 5, the kinematic interaction was the predominant mechanism in determining the pile response. Experiments with larger top mass could be carried out to provide greater understanding of the induced inertial lateral loads and overturning moments produced by the superstructure dynamic response on the piles.

A comparison of the identified and theoretical amplification functions for the free-field soil revealed that all the vibration modes in the frequency band of interest were not either sufficiently excited or identified due to the insufficient instrumentation and the narrow-band band-limited frequency content of the excitation motions. Therefore, using a denser array of accelerometers, particularly in the middle and in the surficial layers, would provide a better estimate of modal quantities. In addition, the outcomes of the modal identification could be significantly improved by excitations with white noise motions that carry nearly the same amount of energy for the frequencies in the band of interest.

In the current project, the control parameters of the extended Bouc-Wen model were calibrated through trial and error. However, it was found that this approach did not lead to a unique solution, because a large number of combinations of the parameters could provide a reasonable match with the back-calculated or measured responses. Thus, using robust system identification methods for retrieving an optimized set of parameters is recommended, although a preliminary calibration, such as the one detailed in Chapter 6, could provide insight into the possible range of the control parameters. Moreover, efforts should be made to correlate the identified parameters and the physical and mechanical properties of the soil and pile material. The possible influence of PWP on the soil response is another factor that should be considered in modeling the seismic soil-pile interaction. Instrumenting the soil adjacent to the piles with PWP transducers would allow for such analysis.

It would be worthwhile for future research to study the behavior of piles in improved soil under more extreme dynamic loading conditions in which failure of pile

structure or soil system or both could be investigated. The performance of the improved soil under repeated loading and the severity and distribution of damage in the improved soil and piles are the subjects that call for more research.

It is preferable to keep the piles in the elastic range, but when a limited amount of yielding is allowed in the pile, this reduces the cost of material. The present work was limited to linear piles. To provide greater insight for performance-based design, it could be useful to conduct nonlinear analysis of the pile structure for cases where the pile bending moment reaches the yield moment outside but near the soil surface.

References

Abghari, A. and Chai, J. (1995). "Modeling of soil-pile-superstructure interaction for bridge foundations," In proceeding of Performance of Deep Foundations under Seismic Loading, ASCE, pp. 45-49.

Afacan, K. B., Brandenberg, S. J., and Stewart, J. P. (2014). "Centrifuge modeling studies of site response in soft clay over wide strain range," Journal of Geotechnical and Geoenvironmental Engineering, Vol. 140, No. 2, pp.1-13.

Ajavakom, N., Ng, C. H. and Ma, F. (2008). "Performance of nonlinear degrading structures: Identification, validation, and prediction," Computers and Structures, Vol. (86), pp. 652-662.

Allotey, N. and El Naggar, M. H. (2008a). "A numerical study into cyclic nonlinear soil-pile response," Canadian Geotechnical Journal, Vol. 45, pp. 1268-1281.

Allotey, N. and El Naggar, M. H. (2008b). "Generalized dynamic Winkler model for nonlinear soil-structure interaction analysis," Canadian Geotechnical Journal, Vol. 45, pp. 560-573.

Alvin, K. F., and Park, K. C. (1994). "Second-order structural identification procedure via state-space-based system identification," AIAA Journal, Vol. 32, No. 2, pp. 397-406.

Alvin, K. F., Peterson, L.D., and Park, K. C. (1995). "Methods for determining minimum-order mass and stiffness matrices from modal test data," American Institute of Aeronautics and Astronautics Journal, Vol. 33, No., pp. 128-135.

Alvin, K. F., Peterson, L. D., and Park, K. C. (1997). "Extraction of normal modes and full modal damping from complex modal parameters," American Institute of Aeronautics and Astronautics Journal, Vol. 35, No. 7, pp.1187-1194.

Alvin, K. F., Robertson, A. N., Reich, G. W., and Park, K. C. (2003). "Structural system identification: from reality to models," Computers and Structures, Vol. 81, pp. 1149-1176.

Arici, Y. and Mosalam, K.M. (2005). "Modal identification of bridge systems using state-space methods," Structural Control and Health Monitoring, Vol. 12, pp. 381-404.

Ashlock, J. and Pak, R. Y. S. (2009). "Experimental response of piles in sand under compound motion," Journal of Geotechnical and Geoenvironmental Engineering, Vol. 135, No. 6, pp. 799-808.

Ashford, S. A. and Juirnarongrit, T (2003). "Evaluation of pile diameter effect on initial modulus of subgrade reaction, Journal of Geotechnical and Geoenvironmental Engineering, Vol. 129, No. 3, pp. 234-242.

Baber, T. T., and Wen, Y. K. (1981). "Random vibration hysteretic, degrading systems," Journal of the Engineering Mechanics Division, Vol. 107, No. 6, pp. 1069-1087.

Baber, T. T., Noori, M. N. (1985). "Random vibration of degrading, pinching system," Journal of Engineering Mechanics, Vol. 111, No. 8, pp. 1010-1026.

Badoni, D. and Makris, N. (1996). "Nonlinear response of single piles under lateral inertial and seismic loads," Soil Dynamics and Earthquake Engineering, Vol. 15, No. 4, pp. 29-43.

Balmes, E. (1997). "New results on the identification of normal modes from experimental complex modes," Mechanical Systems and Signal Processing, Vol. 11. No. 2, pp.229-243.

Bao, X., Morikawa, Y., Kondo, Y., Nakamura, K., and Zhang, F. (2012). "Shaking table test on reinforcement effect of partial ground improvement for group-pile foundation and its numerical simulation," Soils and Foundations, Vol. 52, No. 6, pp. 1043–1061.

Barron, R. F., Kramer, C., Herlache, W. A. et al. (2006). "Cement deep soil mixing remediation of sunset north basin dam," Proceedings of Dam Safety 2006, the 23rd Annual Conference of the Association of State Dam Safety Officials, Massachusetts, September, pp. 181-199.

Banerjee, S. (2009). "Centrifuge and Numerical Modeling of Soft Clay-Pile-Raft Foundations Subjected to Seismic Shaking," Ph.D. Dissertation, National University of Singapore.

Blaney, G. W. and O'Neill, M. (1986). "Measured lateral response of mass on single pile in clay," Journal of Geotechnical Engineering, Vol. 112, Issue 4, pp. 443-457.

Brandenberg, S. J., Boulanger, R. W., Kutter, B. L. and Change, D. (2005). "Behavior of pile foundations in laterally spreading ground during centrifuge tests," Journal of Geotechnical and Geoenvironmental Engineering, Vol. 131, No. 11, pp. 1378-1392.

Brandenberg, S. J., Wilson, D. W., and Rashid, M. M. (2010). "Weighted residual numerical differentiation algorithm applied to experimental bending moment data," Journal of Geotechnical and Geoenvironmental Engineering, Vol. 136, No. 6, pp. 854-863.

Bouassida, M., and Porbaha, A. (2004). "Ultimate bearing capacity of soft clays reinforced by a group of columns-application to a deep mixing technique," Soils and Foundations, Vol. 44, No.3, pp. 91–101.

Bouc, R. (1967). "Forced vibration of mechanical systems with hysteresis," Proceedings of the Fourth Conference on Nonlinear Oscillation. Prague, Czechoslovakia. p. 315.

Boulanger, R. W., Curras, C. J., Kutter, B. L., Wilson, D. W., and Abghari, A., (1999). "Seismic soil-pile-structure interaction experiments and analyses," Journal of Geotechnical and Geoenvironmental Engineering, Vol. 125, No. 9, pp. 750-759.

Brennan, A. J., Thusyanthan, N. I. and Madabhushi, S. P. G. (2005). "Evaluation of shear modulus and damping in dynamic centrifuge tests," Journal of Geotechnical and Geoenvironmental Engineering, Vol. 131, No. 12, pp. 1488-1497.

Carr, A. J. (2003) "Ruaumoko User Manual", University of Canterbury, New Zealand.

Cho, K. H., Gabr, M. A., Clark, S., and Borden, R. H. (2007) "Field p-y curves in weathered rock," Canadian Geotechnical Journal, Vol. 44, No. 7, pp. 753-764.

Conti, R., and Viggiani, G. M. B. (2012). "Evaluation of soil dynamic properties in centrifuge tests," Journal of Geotechnical and Geoenvironmental Engineering, Vol. 138, No. 7, pp. 850-859.

Damgaard, M., Bayat, M., Andersen, L.V., and Ibsen, L.B. (2014). "Assessment of the dynamic behavior of saturated soil subjected to cyclic loading from offshore monopile wind turbine foundations," Computers and Geotechnics, Vol. 61, pp. 116-126.

De Angelis, M., Lus, H., Betti, R., and Longman, R. W. (2002). "Extracting physical parameters of mechanical models from the identified state-space representations," Journal of Applied Mechanics, Vol. 69, pp. 617-625.

De Angelis, M. and Imbimbo, M. (2012). "A procedure to identify the modal and physical parameters of a classically damped system under seismic motions," Advances in Acoustics and Vibration, Article ID 975125.

Dobry, R. and Whitman, R. V. (1969). "Effect of Local Soil Conditions upon Earthquake Damage," Progress Report, School of Engineering, Department of Civil Engineering, Massachusetts Institute of Technology.

Dobry, R., Oweis, I., and Urzua, A. (1976). "Simplified procedures for estimating the fundamental period of a soil profile," Bulletin of Seismological Society of America, Vol. 66, No. 4, pp. 1293-1321.

Dou, H. and Byrne, P. M. (1996). "Dynamic response of single piles and soil-pile interaction," Canadian Geotechnical Journal, Vol. 33, pp. 80-96.

Douglas, J. and Boore, D. M. (2011). "High-frequency filtering of strong-motion records," Bulletin of Earthquake Engineering, Vol. 9, pp. 395-409.

Dowrick, D. J. (1986). "Hysteresis loops for timber structures," New Zealand Journal of Timber Construction, Vol. 2, No. 3, pp. 14-19.

Dunnavant, W. T., and O'Neill, M. W. (1989). "Experimental p-y model for submerged stiff clay," Journal of Geotechnical Engineering, Vol. 115, pp. 95-114.

Elgamal, A. W., Zeghal, M., Parra, E., Gunturi, R., Tang, H. T., and Stepp, J. C. (1996). "Identification and modeling of earthquake ground response, I. Site amplification," Soil Dynamics and Earthquake Engineering, Vol. 15, pp. 499-522.

El Naggar, M. H. and Wei, J. Q. (1999) "Response of tapered piles to lateral loading," Canadian Geotechnical Journal, Vol. 36, pp.52-71.

El Naggar, M. H. and Bentley, K. J. (2000) "Dynamic analysis for laterally loaded piles and dynamic p-y curves," Canadian Geotechnical Journal, Vol. 37, pp.1166-1183.

Ensoft, Inc. (2004). "LPILE Plus Version 5.0: A Program for the Analysis of Piles and Drilled Shafts under Lateral Load," User's Manual, Austin, Texas.

Finn, W.D.L. & Gohl, W.B. (1987). "Centrifuge model studies of piles under simulated earthquake lateral loading", Geotech. Special Pub. No. 11, ASCE, pp. 21-38.

Finn, W. D. L., (2005) "A study of piles during earthquakes: Issues of design and analysis," Bulletin of Earthquake Engineering, Vol. 3, pp. 141-234.

Fleming, B. J., Sritharan, S., Miller, G. A, and Muraleetharan, K. K. (2015). "Full-scale seismic testing of piles in improved and unimproved soft clay," Earthquake Spectra (In-Press). doi: http://dx.doi.org/10.1193/012714EQS018M.

Flores-Berrones R. and Whitman, R. V. (1982). "Seismic response of end-bearing piles," Journal of the Geotechnical Engineering Division, ASCE, Vol. 108, No. GT4, pp. 554-569.

Foliente, G. C. (1995). "Hysteretic modeling of wood joints and structural systems," Journal of Structural Engineering, Vol. 121, No. 6, pp. 1013-1022.

Fraraccio, G., Brügger. A., and Betti, R. (2008). "Identification and damage detection in structures subjected to base excitation," Experimental Mechanics, Vol. 48, pp. 521-528.

Füellekrug, U. (2008). "Computation of real normal modes from complex eigenvectors," Mechanical System and Signal Processing, Vol. 22, pp. 57-65.

Gazetas, G., (1982). "Vibrational characteristics of soil deposits with variable wave velocity," International Journal for Numerical and Analytical Methods in Geomechanics, Vol. 6, pp. 1-20.

Gazetas, G. and Dobry, R. (1984). "Simple radiation damping model for piles and foundation," Journal of Engineering Mechanics, Vol. 110, No. 6, pp. 937-956.

Gazetas, G. (1984). "Seismic response of end-bearing single piles," Soil Dynamic and Earthquake Engineering, Vol. 3, No. 2, pp.82-93.

Gazioglu S. M. and O'Neill M. W. (1984), "Evaluation of p-y relationships in cohesive soil," Analysis and Design of Pile Foundations, Proceedings, San Francisco, California, pp. 192-213.

Georgiadis, M. (1983). "Development of *p-y* curves for layered soils," Geotechnical Practice in Offshore Engineering, ed. S.G. Wright, ASCE, pp. 536-545.

Georgiadis, M., Anagnostopoulos, C., and Saflekou, S. (1992a). "Centrifugal testing of laterally loaded piles in sand," Canadian Geotechnical Journal, Vol. 29, No. 2, pp. 208-216.

Georgiadis, M., Anagnostopoulos, C., and Saflekou, S. (1992b). "Cyclic lateral loading of piles in soft clay," Journal of Geotechnical Engineering, ASCE, Vol. 23, pp. 47-59.

Gerolymos, N. and Gazetas, G. (2005). "Phenomenological model applied to inelastic response of soil-pile interaction systems," Soils and Foundations, Vol. 45, No. 4, pp.119-132.

Gerolymos, N. and Gazetas, G. (2006). "Development of Winkler model for static and dynamic response of caisson foundations with soil and interface nonlinearities," Soil Dynamics and Earthquake Engineering, Vol. 26, No. 5, pp. 363-376.

Gerolymos, N., Escoffier, S., Gazetas, G., and Garnier, J. (2009). "Numerical modeling of centrifuge cyclic lateral pile load experiments," Earthquake Engineering and Engineering Vibration, Vol. 8, No. 1, pp. 61-76.

Gestel, T. V., Suykens, J. A. K., Van Dooren, P., and De Moor, B. (2001). "Identification of stable models in subspace identification by using regularization," IEEE Transactions on Automatic Control, , Vol. 46(9): 1416-1420.

Glaser, S.D. (1995). "System identification and its application to estimating soil properties," Journal of Geotechnical Engineering, 1995, Vol. 121, No. 7, pp. 553-560.

Glaser, S. D. (1996). "Insight into liquefaction by system identification," Geotechnique, Vol. 46, No. 4, pp. 641-655.

Glaser, S. D. and Baise, L. G., (2000). "System identification estimation of soil properties at Lotung site," Soil Dynamics and Earthquake Engineering, Vol. 19, pp. 521-531.

Hadjian, A. H. (2002) "Fundamental period and mode shape of layered soil profiles," Soil Dynamic and Earthquake Engineering, Vol. 22, pp. 885-891.

He. X., Moaveni, B., Conte, J. P., Elgamal, A. and Masri, S. F. (2009). "System identification of Alfred Zampa Memorial Bridge using dynamic field test data," Journal of Structural Engineering, Vol. 135, No. 1, pp. 54-66.

Hoshiya, M. and Sutoh, A. (1992). "Extended Kalman Filter-weighted local identification method for dynamic structural identification," Earthquake Engineering, 10th World Conference, Balkema, Rotterdam.

Hussien, M. N., Tobita, T. Iai, S., and Rollins, K. M. (2010). "Soil-pile separation effect on the performance of a pile group under static and dynamic lateral loads," Canadian Geotechnical Journal, Vol. 47, pp. 1234-1246.

Ibrahim, S. R. (1983). "Computation of normal modes from identified complex modes," AIAA Journal, Vol. 21, No. 3, pp. 446-451.

Ibrahim, S. R. and Fuellekrug U. (1990) "Investigation into exact normalization of incomplete complex modes by decomposing transformation," Proceeding of the 8th International Modal Analysis Conference, Kissimmee, FL, USA, pp. 205-212.

Ilankatharan, M., and Kutter, B.L. (2008). "Numerical simulation of a soil model-model container-centrifuge shaking table system," In Geotechnical Special Publication No. 181: Geotechnical Earthquake Engineering and Soil Dynamics IV.

Ismail, M., Ikhouane, F., Rodellar. J. (2009). "The hysteresis Bouc-Wen model, a survey," Archives of Computational Methods in Engineering, Vol. 16, pp. 161-188.

Juang, J-N (1993). "Applied System Identification," Prentice Hall.

Kagawa, T. and Kraft, L.M. (1980). "Lateral load deflection relationships of piles subject to dynamic loading," Journal of Soils and Foundations, Vol. 20, No. 4, pp. 19-36.

Kim, Y., Jeong, S. and Won, J. (2009). "Effect of lateral rigidity of offshore piles using proposed p-y curves in Marine clay," Marin Georesources and Geotechnology, Vol. 27, pp. 53-77.

Kim, J. and Lynch J. P. (2012a). "Subspace system identification of support-exited structures-Part I: theory and black-box system identification," Earthquake Engineering and Structural Dynamics, Vol. 41, Issue 15, pp. 2235–2251.

Kim, J. and Lynch J. P. (2012b). "Subspace system identification of support-exited structures-Part II: gray-box interpretations and damage detection," Earthquake Engineering and Structural Dynamics, Vol. 41, Issue 15, pp. 2253–2271.

Kirupakaran, K., Cerato, A.B., Liu, C., Miller, G.A., Muraleetharan, K.K., Pinilla, J.D., Price, S., and Thompson, Z.M. (2010). "Simulation of a centrifuge model test of pile foundations in CDSM improved soft clays." In Geotechnical Special Publication No. 199, GeoFlorida 2010: Advances in analysis, modeling and design, D.O. Fratta, A.J. Puppala and B. Muhunthan (Eds.), pp. 1583-1591.

Kitazume, M. and Terashi, M. (2013). "The Deep Mixing Method," CRC Press.

Kramer, S.L. (1996) "Geotechnical Earthquake Engineering," Prentice Hall, N.J.

Kunnath, S. K., Mander, J. B., and Fang, L. (1997). "Parameter identification for degrading and pinched hysteretic structural concrete systems," Engineering Structures, Vol. 19, pp. 224-232.

Lacy, S. L. and Bernstein, D. S. (2003). "Subspace identification with guaranteed stability using constrained optimization," IEEE Transactions on Automatic Control, Vol. 48, No. 7, pp. 1259-1263.

Lai, Y. P., Bergado, D. T., Lorenzo, G. A., Duangchan, T. (2006). "Full-scale reinforced embankment on deep jet mixing improved ground," Ground Improvement, Vol. 10, No. 4, pp. 153-164.

Lin, J. S. and Zhang, Y. (1994). "Nonlinear structural identification using Extended Kalman Filter," Computers and Structures, Vol. 52, No. 4, pp. 757-764.

Liu, C., Soltani, H., Muraleetharan, K., Cerato, A., Miller, G.A., Sritharan, S. "Cyclic loading of single piles-centrifuge model No.2," Network for Earthquake Engineering Simulation (distributor), Dataset, DOI:10.4231/D35D8NF9W.

Liu, C., Soltani, H., Muraleetharan, K., Cerato, A., Miller, G.A., Sritharan, S. (2014). "Dynamic loading of single piles-centrifuge model No.2," Network for Earthquake Engineering Simulation (distributor), Dataset, DOI:10.4231/D31N7XN5R.

Liyanapathirana, D. S. and Polous, H. G. (2005). "Pseudostatic approach for seismic analysis of piles in liquefying soil," Journal of Geotechnical and Geoenvironmental Engineering, Vol. 131, No. 12, pp. 1480-1487.

Loh, C. H. and Chung, S. T. (1993). "A three-stage identification approach for hysteretic systems," Earthquake Engineering and Structural Dynamics, Vol. 22, pp. 129-150.

Lombardi, D. and Bhattacharya, S. (2014) "Modal analysis of pile-supported structures during seismic liquefaction," Earthquake Engineering and Structural Dynamics, Vol. 43: 119-138.

Lus, H., Betti, R. and Longman R. W. (1999) "Identification of linear structural systems using earthquake-induced vibration data," Earthquake Engineering and Structural Dynamics, Vol. 28, pp. 1449-1467.

Lus, H., De Angelis, M., and Betti, R. (2003a). "A new approach for reduced order modeling of mechanical systems using vibration measurements," Journal of applied mechanics, ASME, Vol. 70, No. 5, pp. 715-723.

Lus, H., De Angelis, M., Betti, R., and Longman, R. W. (2003b). "Constructing second-order models of mechanical systems from identified state space realizations. Part I: Theoretical discussions," Journal of Engineering Mechanics, ASCE, Vol. 129, No. 5, pp. 477-488.

Ma, F., Zhang, H., Bockstedte, A., Foliente, G. C., and Paevere, P. (2004). "On parameter analysis of the differential model of hysteresis," Journal of Applied Mechanics, Vol. 71, Issue, 3, pp. 342-349.

Makris, N and Gazetas, G. (1991). "Dynamic pile-soil-pile interaction - Part II: lateral and seismic response," Journal of Earthquake Engineering and Structural Dynamics Vol. 21, No.2, pp. 145-162.

Makris, N., Tazoh, T., Yun, X. and Fill, A. C. (1997). "Prediction of the measured response of a scaled soil-pile-superstructure system," Soil Dynamics and Earthquake Engineering, Vol. 16, Issue. 2, pp. 113-124.

Masing, G. (1926). "Eigenspannungen and Verfertigung bim Messing," Proceeding of 2nd Int. Congress on Applied Mechanics, Zurich.

Matlock, H. (1970) "Correlations for design of laterally loaded piles in soft clay," Proceeding of 2nd Annual Offshore Technology Conference, Vol. 1, pp. 557-594.

Matlock, H., Foo, S.H., and Bryant, L.L. (1978) "Simulation of lateral pile behavior under earthquake motion," Proceedings of Specialty Conference on Earthquake Engineering and Soil Dynamics, ASCE, Vol. 2, pp. 1065-1084.

Medina, R. and Krawinkler, H. (2003) "Seismic Demands for Nondeteriorating Frame Structures and Their Dependence on Ground Motions," PEER Report 2003/15.

Menegotto, M., and E. Pinto. (1973). "Method of analysis for cyclically loaded reinforced concrete plane frames including changes in geometry and non-elastic behavior of elements under combined normal force and bending," Proceedings, IABSE Symposium. Lisbon, Portugal.

Mikami, A., Stewart, J. P., and Kamiyama, M. (2008). "Effects of time series analysis protocols on transfer functions calculated from earthquake accelerograms," Soil Dynamic and Earthquake Engineering, Vol. 28, pp. 695-706.

Mottershed, J. E. (1993). "Model updating in structural dynamics: A survey," Journal of Sound and Vibration, Vol. 162, No. 2, pp.347-375.

Murchison, J.M. and O'Neill, M. W. (1984). "Evaluation of p-y relationship in cohesionless soils," Analysis and Design of Pile Foundation, ASCE, New York, pp. 174-191.

Mukhopadhyay, S., Lus, H., and Betti, R. (2014). "Modal parameter based structural identification using input-output data: Minimal instrumentation and global identifiability issues," Mechanical System and Signal Processing, Vol. 45, pp. 283-301.

Murff, J. D. and Hamilton J. M. (1993). "P-ultimate for undrained analysis of laterally loaded piles," Journal of Geotechnical Engineering, Vol. 119, No. 1, pp. 91-107.

Murono, Y. and Nishimura, A. (2000). "Evaluation of seismic force of pile foundation induced by inertial and kinematic interaction," 12th World Conference on Earthquake Engineering, Auckland, N.Z. paper No. 1496.

Mylonakis, G., Nikolaou, A., and Gazetas G. (1997). "Soil-pile-bridge seismic interaction: kinematic and inertial effects. Part 1: Soft soil," Earthquake Engineering and Structural Dynamics, Vol. 26, pp. 337-359,

Namikawa, T., Koseki, J., and Suzuki, Y. (2007). "Finite element analysis of lattice-shaped ground improvement by cement-mixing for liquefaction mitigation," Soils and Foundations, Vol. 47, No. 3, pp. 559-576.

Nikolaou, S., Mylonakis, G., Gazetas, G. and Tazoh, T. (2001). "Kinematic pile bending during earthquakes: Analysis and field measurements," Geotechnique, Vol. 51, No.5, pp. 425-440.

Nogami, T., Otani, J., Konagai, K., and Chen, H.-L. (1992). "Nonlinear soil-pile interaction model for dynamic lateral motion," Journal of Geotechnical and Geoenvironmental Engineering, Vol. 118, No. 1, pp. 89-106.

Novak, M. and Sheta, M. (1980). "Approximate approach to contact effects of piles," Proceedings of a Conference on Dynamic Response of Pile Foundation: Analytical Aspects, ASCE, pp. 53-79.

Ohtsuka, S., Yamada, E., and Matsuo, M. (1996). "Bearing capacity analysis of reinforced ground," Proc. of Int. Symp. on Earth Reinforcement. Fukuoda, Vol. 1. pp. 647-652.

Oldham, D. (1984). "Experiments with lateral loading of single piles in sand," Proceeding of the Symposium on the Application of Centrifuge Modeling to Geotechnical Engineering, pp. 121-141.

Ortiz, G. A., Alvarez, D. A. and Bedoya-Ruíz, D. (2013). "Identification of Bouc–Wen type models using multi-objective optimization algorithms," Computers and Structures, Vol. 114-115, pp. 121-132.

Oskay, C., and Zeghal, M. (2011). "A survey of geotechnical system identification techniques," Soil Dynamics and Earthquake Engineering, Vol. 31, No. 4, pp.568-582.

Pandit, S. M. (1991). "Model and Spectrum Analysis: Data Dependent Systems in State Space," John Wiley&Sons, New York, 1991. 131. Sun, R.

Peeters, B. and Ventura, C. E. (2003). "Comparative study of modal analysis techniques for bridge dynamic characteristics," Mechanical Systems and Signal Processing, Vol.17, No. 5, pp: 965-988.

Pranjoto S. and Pender M. J. (2003). "Gapping effects on the lateral stiffness of piles in cohesive soil," Pacific Conference on Earthquake Engineering, Paper Number 96, pp. 1-8.

Poulos, H.G. and Davis, E.H. (1980). "Pile Foundation Analysis and Design," Wiley, New York.

Rahmani, A., Taiebat, M., Finn, W. D. L., and Venura, C. E. (2012). "Determination of dynamic p-y curves for pile foundations under seismic loading," 15 WCEE.

Rajashree, S. S. and Sundaravadivelu, R. (1996). "Degradation model for one-way cyclic lateral load on piles in soft clay," Computers and Geotechnics, Vol. 19, No. 4, pp. 289-300.

Raju, V. R. and Yandamuri, H. K. (2010). "Ground improvement for infrastructure projects in Malaysia," Ground Improvement 163, Issue GI4, pp. 251–263. doi: 10.1680/grim.2010.163.4.251.

Ramberg, W. and Osgood, W. R. (1943). "Description of stress–strain curves by three parameters," Technical Note No. 902, National Advisory Committee for Aeronautics, Washington DC.

Rathje, E. M., Abrahamson, N. A., and Bray, J. D. (1998). "Simplified frequency content estimates of earthquake ground motions," Journal of Geotechnical and Geoenvironmental Engineering, Vol. 124, No. 2, pp. 150-159.

Reese, L.C., Cox, W. and Koop, F.D. (1974). "Analysis of laterally loaded piles in sand," Proceedings of the 6th Offshore Technology Conference, Dallas.

Reese, L. C. and Cox, W. R. (1975). "Field testing and analysis of laterally loaded piles in stiff clay," 7th Annual Offshore Technology Conference, Huston, Texas, pp. 672-690.

Reese, L. C., and Welch, R. C. (1975). "Lateral loading of deep foundations in stiff clay," Journal of Geotechnical Engineering Division, Vol. 101, No. 7, pp. 633 - 649.

Reynders, E. and De Roeck, G. (2008). "Referenced-based combined deterministic-stochastic subspace identification for experimental and operational modal analysis," Mechanical Systems and Signal Processing, Vol. 22, pp. 617-637.

Reynders, E. (2012). "System identification methods for (operational) modal analysis: review and comparison," Archives of Computational Methods in Engineering, Vol. 19, Issue 1, pp. 51-124.

Rollins, K.M., Herbst, M., Adsero, M., Brown, D. (2010). "Jet grouting and soil mixing for increased lateral pile group resistance," Proceedings of GeoFlorida 2010, Advances in Analysis, Modeling and Design, No. 199, ASCE, pp.1563-1572.

Rovithis, E. N., Pitilakis, K. D., and Mylonakis, G.E. (2009). "Seismic analysis of coupled soil-pile-structure systems leading to the definition of a pseudo-natural SSI frequency," Soil Dynamics and Earthquake Engineering, Vol. 29, pp. 1005-1015.

Rovithis, E. and Kirtas, E. (2009). "Experimental p-y loops for estimating seismic soil-pile interaction," Bulletin of Earthquake Engineering, Vol. 7, pp. 719-736.

Rovithis, E. N., Parashakis, H. and Mylonakis, G. E. (2011). "1D harmonic response of layered inhomogeneous soil: Analytical investigation," Soil Dynamic and Earthquake Engineering, Vol. 31, pp. 879-890.

Safak, E. (1997). "Models and methods to characterize site amplification from a pair of records," Earthquake Spectra, Vol. 13, No. 1, pp. 97-129.

Schulze K. (2005). "Vibrational characteristics and seismic response of inhomogeneous soils," MSc thesis, Department of Civil Engineering, City University of New York.

Siringoringo, D. M. and Fujino Y. (2007). "Dynamic characteristics of a curved cable-stayed bridge identified from strong motion records," Engineering Structures, Vol. 29, pp. 2001-2017.

Siringoringo, D. M. and Fujino Y. (2008) "System identification applied to long-span cable-supported bridges using seismic records," Earthquake Engineering and Structural Dynamics," Vol. 37, pp. 361-386.

Scott, R.F. (1979) "Cyclic static model pile tests in a centrifuge," Proceedings of 11th Offshore Technology Conference, pp. 1159-1168.

Scott, R.F. (1981). "Pile testing in a centrifuge," In: Proc. ICSMFE. Stockholm, Sweden, Vol. 2, pp. 839–842.

Sengupta and Li, (2013). "Modified Bouc–Wen model for hysteresis behavior of RC beam–column joints with limited transverse reinforcement," Engineering Structures, Vol. 46, pp. 392-406.

Siddharthan, R. V. and Porbaha, A. (2008). "Seismic response evaluation of sites improved by deep mixing, Part I: Proposed approach," Ground Improvement 161, Issue GI3, pp. 153-162. (doi:10.1680/grim.2008.161.3.153)

Smyth, A. W., Masri, S. F., Chassiakos, A. G., and Caughey, T. K. (1999). "On-Line parametric identification of MDOF nonlinear hysteretic systems," Journal of Engineering Mechanics, Vol. 125, pp. 133-142.

Soltani, H. and Muraleetharan, K. (2015). "Experimental p-y curves for a laterally loaded single pile in cement-improved soft clay," Proceedings of IFCEE 2015, San Antonio, Texas.

Soneji, B. B. and Jangid, R. S. (2008). "Influence of soil-structure interaction on the response of seismically isolated cable-stayed bridge," Soil Dynamic and Earthquake Engineering, Vol. 28, pp. 245-257.

Sousa Coutinho, A. G. F. (2006). "Data reduction of horizontal load full-scale tests on bored concrete piles and pile groups," Journal of Geotechnical and Geoenvironmental Engineering, Vol. 132, No. 6, pp. 752-769.

Stoica, P. and Moses, R. L. (2005). "Spectral Analysis of Signals," Upper Saddle River, N.J., Pearson Prentice Hall.

Stewart, J. P. and Fenves, G. L. (1998) "System identification for evaluating soil-structure interaction effects in building from strong motion recordings," Earthquake Engineering and Structural Dynamics, Vol. 27, pp. 869-885.

Stewart, J. P., Seed, R. B., Fenves, G. L. (1998). "Empirical Evaluation of Inertial Soil-Structure Interaction Effects," Report No. PEER-98/07

Sues, R. H., Mau, S.T., and Wen, Y. K. (1988). "System identification of degrading hysteretic restoring forces," Journal of Engineering Mechanics, Vol. 114, No. 5, pp. 833-846.

Tabesh, A. and Poulos, H. G. (2001). "Pseudostatic approach for seismic analysis of single piles," Journal of Geotechnical and Geoenvironmental Engineering, Vol. 127, No. 9, pp. 757-765.

Taylor, R.N. (Ed.) (1995). "Geotechnical Centrifuge Technology," Chapman & Hall, Glasgow, England.

Ting, J. M., Kauffman, C. R., and Lovicsek, M. (1987). "Centrifuge static and dynamic lateral pile behavior," Canadian geotechnical Journal, Vol. 24, pp. 198-207.

Tobita, T., Kang, G. C., Iai, S., and Rollins, K. M. (2008). "Analysis of statnamic behavior of full-scale pile group in soft clays and silts," Geotechnical Earthquake Engineering and Soil Dynamics IV.

Thompson, Z. M. (2011). "Stress-strain behavior of unimproved and cement-improved soft clay," M. S. Thesis, University of Oklahoma, Norman, OK.

Tomisawa, K. and Miura, S. (2007). "Mechanical behavior of pile foundation constructed in composite ground and its evaluation,"Soils and Foundations, Vol. 47, No. 5, pp. 961-972.

Trochanis, A. M., Bielak, J. and Christiano, P. (1991). "Simplified model for analysis of one or two piles," Journal of Geotechnical Engineering, Vol. 117, No.3, pp. 448-466.

Udwadia, F. (1994). "Methodology for optimum sensor locations for parameter identification in dynamic system,' Journal of Engineering Mechanics, Vol. 20, No. 2, pp. 368-390.

Van Overschee, P. and De Moor, B. (1996). "Subspace Identification for Linear Systems: Theory-Implementation-Application," Dordrecht, Netherlands: Kluwer Academic Publishers.

Varun, Assimaki, D., and Shafieezadeh, A. (2013). "Soil-pile-structure interaction simulations in liquefiable soils via dynamic macroelements: Formulation and validation," Soil Dynamics and Earthquake Engineering, Vol. 47, pp. 92-107.

Viberg, M. (1995). "Subspaced-based methods for the identification of linear time-invariant systems," Automatica, Vol. 31, No. 12, pp. 1835-1851.

Veletsos, A. S. (1977). "Dynamics of structure foundation systems," Structural and Geotechnical Mechanics, A volume honoring N. M. Newmark (W. J. Hall Editor) Prince Hall, pp. 333-361.

Vrettos, C. (2013). "Dynamic response of soil deposits to vertical SH waves for different rigidity depth-gradients," Soil Dynamics and Earthquake Engineering, Vol. 47, pp. 41-50.

Wang, S., Kutter, B. L., Chacko, M. J., Wilson, D. W., Boulanger, R. W., and Abghari, A. (1998). "Nonlinear Seismic Soil-Pile Structure Interaction," Earthquake Spectra, Vol. 14, No. 2, pp. 377-396.

Weng, J., Loh, C., Lynch, J. P., Lu, K., Lin, P., and Wang, Y. (2008). "Output-only modal identification of a cable -stayed bridge using wireless monitoring systems," Engineering Structures, Vol. 30, pp. 1820-1830.

Wen, Y. K. (1976). "Method for random vibration of hysteretic systems". Journal of Engineering Mechanics, Vol. 102, No. 2, pp. 249-263.

Wilson, D. W., Boulanger R. W., Kutter, B. L., Abghari, A. (1997). "Aspects of dynamic centrifuge testing of soil-pile-superstructure interaction," Observation and Modeling in Numerical Analysis and model tests in dynamic soil structure interaction, pp. 47-63.

Wilson D. W. (1998) "Soil-Pile-Structure Interaction in Liquefying Sand and Soft Clay," PhD Thesis, Department of Civil Engineering and Environmental Engineering, University of California, Davis.

Wu, A. and Smyth, A. (2008). "Real-time parameter estimation for degrading and pinching hysteretic models," International Journal of Non-linear Mechanics, Vol. 43, pp. 822-833.

Yamashita, K., Hamada, J., Onimaru, S., and Higashino, M. (2012). "Seismic behavior of piled raft with ground improvement supporting a base-isolated building on soft ground in Tokyo," Soils and Foundations, Vol. 52, No. 5, pp. 1000-1015.

Yang, Z. and Jeremic, B. (2005). "Study of soil layering effects on lateral loading behavior of piles," Journal of Geotechnical and Geoenvironmental Engineering, Vol. 131, No. 6, pp. 762-770.

Zeghal, M. and Elghamal, A. W. (2000) "Site response and vertical seismic arrays," Progress in Structural Engineering and Materials, Vol. 2, No. 1, pp. 92-101.

Zhang, C., White, D., and Randolph, M. (2011). "Centrifuge modeling of the cyclic lateral response of a rigid pile in soft clay," Journal of Geotechnical and Geoenvironmental Engineering, Vol. 137, pp.717-729.

Zhang, H., Foliente, G. C., Yang, Y., and Ma, F. (2002). "Parameter identification if inelastic structures under dynamic loads," Earthquake Engineering and Structural Dynamics, Vol. 31, pp. 1113-1130.